The Dissertation Committee for Gajanan Krishna Choudhary
certifies that this is the approved version of the following dissertation:

Coupled atmospheric, hydrodynamic, and hydrologic models for simulation of complex phenomena

Committee:

Clinton N. Dawson, Supervisor

Corey J. Trahan

Leszek F. Demkowicz

Patrick Heimbach

Tan Bui-Thanh

Coupled atmospheric, hydrodynamic, and hydrologic models for simulation of complex phenomena

by

Gajanan Krishna Choudhary

DISSERTATION

Presented to the Faculty of the Graduate School of

The University of Texas at Austin

in Partial Fulfillment

of the Requirements

for the Degree of

DOCTOR OF PHILOSOPHY

THE UNIVERSITY OF TEXAS AT AUSTIN

December 2019

Dedicated to my parents, Krishna and Kalpana, siblings, Abhinav and Supriya, and wife, Nikita.

Acknowledgments

I will forever be thankful to my advisor, Clint Dawson, for his unwavering professional, financial, and personal support. My graduate student life would have been very different had it been anyone else in his place, so I feel lucky to have worked with him. I am obliged to Corey Trahan, whose past work on Adaptive Hydraulics was crucial to this work. Our discussions and differences always pushed me to produce better work, inspired me to be a better professional, and helped me understand the work culture in the United States that I was not familiar with, being an international student. I am also thankful to the Engineer Research and Development Center (ERDC) for sponsoring various projects, and the Department of Defense for providing funds under the High Performance Computing Modernization Program (HPCMP), that helped finance this work and my education here. I acknowledge the past work of Matthew Farthing from ERDC, which provided guidance for some of this work. Lucas Pettey from Science Applications International Corporation (SAIC) played a significant role by adding to this work and ensuring that it gets carried forward in the future. Hugh Thornburg and Charles Peavey from SAIC read and reviewed several reports on this work that we submitted; their help is much appreciated. It was a pleasure mentoring AJ Inanc, an undergraduate student here at the University of Texas at Austin, who helped in some of this work.

I am indebted to Bhaskaracharya Pratishthana, M. Prakash Academy, IIT Kharagpur, and UT Austin, which provided learning and developmental platforms, and to all my past teachers and professors for shaping my knowledge. There are just no better words than those I used in my master's report to express gratitude to my mathematics teachers, M. Prakash and Leszek Demkowicz, in particular: "They imbibed in me, a deep respect for mathematics through their fiercely passionate teaching, and their rigorous proofs have shaped more than just my mathematical thinking. I look up to them as role models as teachers." I am also obliged to IIT professors Nilanjan Mitra, Lingadahally Ramachandra, Sudhir Kumar Barai, and Dilip Kumar Baidya for writing recommendation letters for my graduate admission application to UT Austin, and to all the professors at the department of Civil Engineering at IIT Kharagpur for helping me grow as an engineer and teaching me the importance of failure. My internship at Himanshu Tulpule and Associates was a turning point that set me down the path of becoming an engineer and a researcher, for which I am thankful to Himanshu Tulpule. I am grateful to Apurba Kar and Karan Doshi from Indian Register of Shipping for mentoring me at my job back in India.

I am lucky to have had Chen Chen, Pushkar Kumar Jain, Vaibhav Bhatia, and many others in my life at Austin, who made living in and adjusting into a new culture easier. I am grateful to each and every one of my friends — too many to list here — whose presence has had a lasting positive impact on my life. I am glad to have Nikita Mathur as my wife, who has been through a lot

of hurdles to ensure that we stay happy and together. Her soothing presence stabilizes my life, particularly while I am working on this dissertation day and night in my last days as a PhD student. Most important of all, I am forever indebted to my parents, Krishna and Kalpana, and my siblings Abhinav and Supriya, whose role in my life is irreplaceable, and without whom, my life would have been colorless. If I could choose my family again, it would be them that I would choose a thousand times over. Their existence, love, care, support, and sacrifices are reasons why I am who I am, and why I was able to produce this work. This work is therefore, dedicated to them from the bottom of my heart.

Last of all, I must acknowledge the hard work of all the scientists before me, "upon whose shoulders I stand to see further," as Sir Isaac Newton would put it. Without their contributions to science, this work would not have been possible.

Coupled atmospheric, hydrodynamic, and hydrologic models for simulation of complex phenomena

Publication No. _____

Gajanan Krishna Choudhary, Ph.D.
The University of Texas at Austin, 2019

Supervisor: Clinton N. Dawson

Simulating the interplay between atmospheric, ocean, and overland physics is often too complicated for any single model to handle due to limitations on developmental and computational costs. A variety of models that specialize in specific physics exist, such as 2D and 3D shallow water and transport models in ADvanced CIRCulation (ADCIRC) and Adaptive Hydraulics (AdH) for ocean and estuarine dynamics, Gridded Surface Subsurface Hydrologic Analysis (GSSHA) and Hydrologic Engineering Center's (HEC) River Analysis System (HEC-RAS) for 2D/1D overland flow, and Global Forecast System (GFS) and North American Mesoscale Forecast System (NAM) for atmospheric physics. This dissertation explores strong and weak coupling between different models to simulate complex phenomena that they cannot individually handle. One-way weak coupling from atmospheric models to ocean or overland flow models is already ubiquitous in the form of usage of meteorological forcing on the flow models. Coupling between 2D and 3D shallow water

models including baroclinic transport, and between shallow water and overland flow models remain relatively unexplored. Strong coupling between 2D and 3D shallow water and baroclinic transport models is the major focus of this work. On studying multiple verification and validation cases, and applications testing the limits of 2D-3D coupling, it is concluded that strongly coupled 2D and 3D shallow water and transport models are conservative, stable, accurate, and convergent in line with theory, and are able to simulate physics that solely 2D or 3D models cannot in general. They also enable building computationally cheaper 3D models by enabling replacement of non-critical 3D regions with 2D subdomains. The second focus of this work is weak one/two-way coupling between 2D shallow water and 2D/1D overland flow models, which are in turn driven by one-way coupling from an atmospheric model. Two-way coupled models are shown to be conservative and capable of simulating compound flooding effects. An application of the coupled models to simulate flooding in Houston, Texas, due to Hurricane Harvey of August 2017 is presented, the results of which demonstrate the suitability of the models for use in high-fidelity forecasts of flooding during hurricanes, after some improvements.

Keywords: 2D-3D coupling, strong and weak coupling, shallow water equations, diffusive wave equations, primitive equations, wetting and drying, baroclinic flow, compound flooding.

Table of Contents

List of Tables

List of Figures

Chapter 1

Introduction

Scientific high-performance computing software are often designed to model specific physics since speed and accuracy in simulating particular phenomena are a greater priority for such codes, in contrast to general purpose engineering software that focus on applicability to a diverse set of problems. When it comes to simulating events beyond their existing capabilities, such models often lack flexibility in expanding their domain of applicability under the strict constraint of maintaining performance. The restrictions are even stricter for simulating extreme atmospheric, hydrodynamic, and hydrologic events such as floods from hurricanes and tsunamis, which require a quick turnaround time of a day or less for chalking out an emergency response, with many lives at stake. Beyond the often-impractical possibility that new capabilities be added to existing scientific codes without adversely affecting performance, coupling well-validated models is an obvious option for enabling simulation of complex physical phenomena. The concept of multi-physics multi-software coupling is already used in a variety of different fields, including Earth system models, global climate models, and fluid structure interaction.

Coupling atmospheric and ocean models is common in Earth system

models in particular. The primitive equations, which are partial differential equations, are commonly used in these cases. In the context of ocean models, these equations, also known as the 3D shallow water equations, are often coupled to transport equations to account for baroclinicity induced by the dependence of density of water on temperature and salinity. The 2D shallow water equations, obtained by depth-integrating the 3D shallow water equations, are simpler to solve. They may also be coupled to transport equations to track constituents, but they are not suitable for use in baroclinic scenarios that quickly result in stratification of flow. The use of 3D shallow water models is unavoidable in such cases. However, for baroclinic flows in estuaries where frequent wetting and drying over land occurs due to tides and wind, a 3D shallow water model that can handle wetting-drying is needed. Although it is possible, in theory, to allow meshes to move in horizontal directions in an arbitrary Lagrangian-Eulerian framework to allow wetting-drying in 3D models, it is extremely complicated and computationally costly. On the other hand, most 2D shallow water models have wetting-drying capabilities without having to move the mesh. Hence, implementing and using non-overlapping coupled 2D-3D shallow water and transport models, explored herein, for leveraging well-tested 2D wetting-drying and 3D baroclinic transport capabilities may be a practical and viable alternative to implementing wetting-drying in 3D shallow water models. Coupled shallow water models may even allow building significantly cheaper computational models in cases where a large domain must be modeled in 3D to study a small region of interest, by allowing replacement

of non-critical areas with 2D subdomains. The theory, verification, validation, and applications of strongly coupled 2D and 3D shallow water models is the primary focus of this work.

Although the 2D-3D coupled models can additionally be driven by one-way coupling from an atmospheric model, the test cases presented herein are meant to isolate the behavior of 2D-3D coupling and hence do not include atmospheric forcing. The atmospheric model is instead included in the second focus of this work on exploring weak coupling between atmospheric, shallow water and diffusive wave equation based overland flow models. The study of compound flooding phenomena, which are exacerbated floods due to occurrence of at least two of coastal, pluvial, or fluvial flooding effects simultaneously in a given area, is becoming increasingly important given the recent occurrences of extreme events. An example of that is Hurricane Harvey of August 2017, one of the costliest hurricanes to hit the United States. Computational models designed to handle such extreme events are often designed to focus on only one aspect of flooding and not others. Since expanding the applicability of existing models to simulate compound flooding events is not an easy task, coupled models taking advantage of existing software may be a possible solution. Accordingly, shallow water and overland flow models are coupled one-way and two-way herein, driven by one-way meteorological forcing from an atmospheric model.

1.1 Literature review

The shallow water equations are partial differential equations that govern flows in rivers, lakes, estuaries, and oceans. These equations are typically applicable in scenarios where horizontal scales are much larger than the vertical one, allowing scaling approximations to the Navier-Stokes equations. Although analytical solutions to these equations exist in specific cases [87], it is difficult to find them in the general. Numerical methods are therefore employed to solve the equations approximately. Various finite difference models [9, 15, 16, 46], finite volume models [2, 7, 18, 58], continuous Galerkin finite element models [6, 10, 44, 50, 64, 85, 89, 90], discontinuous Galerkin finite element models [21, 22, 72], and hybrid models such as [57] have been used over the years to solve these equations for studying ocean and estuary dynamics. Either 2D or 3D shallow water models may be used to study ocean dynamics, with the choice dependent on computational cost and physical phenomena under consideration. 2D shallow water models are computationally cheaper as well as easier to implement, whereas 3D shallow water models can provide more accurate information about the variation of flow in the vertical direction. Most 3D shallow water models use natural z coordinates, transformed σ coordinates [68], or transformed p (pressure) coordinates [84] in the vertical direction. 3D models using z coordinate must be treated in an arbitrary Lagrangian-Eulerian (ALE) framework [38, 39, 41] to keep track of mesh movement in the vertical direction. The σ coordinate used in 3D models is essentially equivalent to the ALE method [24].

It is common for estuary and ocean models to include effects of wind, pressure, temperature, salinity, sedimentation, wetting and drying, or other relevant governing physics. Constituent transport is particularly important in ocean dynamics, since flow in oceans is baroclinic, i.e., the density of the water depends on salinity and temperature. Such flows cannot be modeled using 2D shallow water models since they cannot capture vertically varying horizontal pressure gradients arising from spatial density differences. 3D shallow water models, on the other hand, can handle baroclinicity accurately. However, it is challenging to implement wetting-drying in 3D models, which is movement of water over dry land due to wind and tides, for example. Wetting-drying in 2D shallow water models can be dealt with using a variety of methods [3, 30, 37, 40]. One way of dealing with wetting and drying is to use an ALE framework to move the mesh horizontally, possibly re-meshing the models on-the-go. A more common way is to use an Eulerian approach, with a fixed mesh covering even dry regions that are either excluded during calculations or are kept wet numerically with a thin layer of fluid [12]. 3D shallow water models on the other hand, generally do not use horizontal mesh movement for wetting and drying due to the complexity in implementation and high computational cost. Only a few 3D shallow water models with meshes fixed in the horizontal plane can handle 3D wetting and drying, and these are mainly geared at σ coordinate based models [47, 98]. Wetting-drying for 3D z-coordinate based models remains a challenge.

Flows in estuaries, which is where a river meets the ocean, is generally

baroclinic due to mixing of fresh river water and saline sea water, resulting in salinity shocks moving out into the ocean [35] or up rivers. 3D models are needed to simulate the flow in such cases. Since wetting and drying in estuaries due to tides and winds, or inundation due to extreme events like hurricanes and tsunamis poses a challenge for 3D models, coupled 2D-3D models may be a way around implementation of wetting-drying in 3D models. Related past coupling efforts involve weak coupling of 1D and 2D shallow water models [19], and weak coupling between 2D shallow water models and 3D Navier Stokes equations [59], with both works focused on the finite volume method. The foundations of 2D-3D strongly coupled shallow water models which form the basis of this work were laid in [20] against a backdrop of the stabilized continuous Galerkin finite element framework. CG FEM has been successfully applied to efficiently solve the shallow water equations over domains with complex boundaries and bathymetry in a high-performance computing setting. Multiscale computational models involving unstructured meshes with element sizes varying from a few meters near the coast to a few kilometers in deep oceans have been used in the past to simulate complex phenomena such as hurricane storm surge [77], oil spills [26], and tsunamis [49].

Although shallow water models help in predicting coastal flooding during hurricanes, they may not be enough since many of the models do not account for flooding from inland precipitation [61]. The number of extreme rainfall events along the coast of Gulf of Mexico are on the rise [91]. The number of compound flooding events, which are incidents characterized by

coastal inundation combined with pluvial flooding from inland precipitation during hurricanes, have also increased at many of the coastal cities in the United States over the last century [94]. Hurricane Harvey, which made landfall along the coast of Texas, United States, in August 2017, was accompanied by a record amount of rainfall [76]. The compound flooding during Hurricane Harvey [99] was a factor in making it one of the costliest hurricanes on record to hit the US [17]. A possible way to predict overland flooding during such extreme events may be to couple shallow water models that can handle storm surge simulations with surface/subsurface flow models that can handle pluvial/fluvial flooding. These models may additionally be supplied with wind and precipitation forcing via one-way coupling from atmospheric models in order to enable high fidelity actionable forecasts of compound flooding events. Preliminary work on coupling a 2D shallow water model and a 2D/1D overland flow model based on diffusive wave equations, driven by one-way coupling from an atmospheric model, is presented to hindcast the flooding due to Hurricane Harvey. Several improvements are still needed in the coupled models, including additional boundary condition coupling options, before the model can be used for real-world scenarios. The lessons learned in coupling the models, however, are important for future work.

The first and major focus of this dissertation is on strongly coupled 2D-3D shallow water and transport finite element models. This is done to enable simulations simultaneously incorporating wetting-drying as well as baroclinicity, and to enable selectively replacing non-critical regions of 3D models with

2D subdomains for reducing computational cost. The second part of this work touches upon beginnings of multi-software multi-physics weak coupling between atmospheric, hydrodynamic (shallow water) and hydrologic (overland flow/diffusive wave) models in order to enable quick turn-around forecasts during extreme events.

1.2 Approaches to coupling models

As is the case with domain decomposition problems, models may be coupled by having them interact with each other over either a shared boundary between non-overlapping regions, or through shared elements over an overlapping region. There are two broad categories of coupling 2D and 3D shallow water models, viz., algebraic/strong coupling [20], or flux/weak coupling motivated by the additive Schwarz method [75]. A general discussion of methods of strong and weak coupling of multi-physics models wherein different types of partial differential equations are being solved, for instance in the case of fluid-structure interaction, is given in [97]. In the former approach, a monolithic, coupled system of equations is built, which must be solved once per time step. In the latter approach, separate systems corresponding to each of the component models are solved iteratively at each time step by exchanging information of solution and boundary conditions till some condition is satisfied, which may be convergence of the interface solutions as well as fluxes, or a limit on the maximum number of iterations. At least in case of 2D and 3D shallow water finite element models, strong coupling in a conform-

ing continuous Galerkin setting mathematically guarantees that the solution variables as well as fluxes are continuous, and hence mass and momentum are conserved across the interface at each instant in time [20]. Weak coupling can further be classified into two categories of iterative methods based on the way information is exchanged between models. Gauss-Seidel iterative method solves the models serially within each time step, whereas Gauss-Jacobi iterative method allows models to be solved simultaneously in parallel within each time step [97]. Gauss-Seidel iterations use the latest available solutions of submodels/subsystems to set appropriate interface conditions on the current subsystem, which prevents models from being solved simultaneously in parallel. Gauss-Jacobi iterations use solutions of all subsystems from the previous Gauss-Jacobi iterations to set interface conditions of all subsystems in the current iteration, allowing parallel solution. Gauss-Seidel iterations are observed to have a better convergence behavior than Gauss-Jacobi iterations [80, 97]. Weak coupling can be advantageous in a practical scenario if the subsystems involved are solved in parallel, with a limit on the number of iterations allowed within each time step instead of indefinitely iterating till convergence is achieved. They can also be useful over strong coupling due to the key possibility of subcycling, in which the models can run for multiple time steps or cycles before exchanging information. However, in weak coupling, using fewer iterations results in truncation errors, leading to a discontinuity in either the solution or the fluxes at the interface, and even instabilities.

In the context of coupling 2D and 3D shallow water models imple-

mented in a single computational software using similar methodologies, strong coupling makes more sense due to compatibility, and since multiple iterations for solving a time step are not required. In case of multiphysics coupling of atmospheric, shallow water and overland flow models which may be part of different software, using different programming languages, and solving different sets of equations with distinct methods for spatial and temporal discretization, however, weak coupling appears to be the better, if not the only, way to go. Also factored into the choice is that the software source codes must be accessible and significantly modifiable in case of strong coupling, whereas for weak coupling, the source codes may need relatively less modification and the new coupling code that must be written can be kept separate from them.

As mentioned previously, the mathematical foundations of 2D-3D coupled shallow water models were laid in [20], which presented the theory and two simple verification test cases. This dissertation revisits the coupling theory in new light of conformity, presents improvements to some of the previous shortcomings by correcting vertical velocities at the interface through addition of a vertical velocity coupling stage, and builds upon the past work to include 2D-3D transport coupling in order to enable simulation of baroclinic flows. Many examples testing the limits of baroclinic 2D-3D coupling are presented, along with a comparison of solutions against those of usual 2D-only or 3D-only models. Numerical temporal and spatial convergence analysis are performed. Two validation test cases are included and lastly, two applications of 2D-3D coupled models are demonstrated, involving baroclinicity as well as

wetting-drying. For the sake of completeness, however, some of the work presented in [20] is reproduced in this work, and every effort is made to cite that past work. Lastly, although the concept of multi-physics weak coupling itself is nothing new, its application in the context of atmospheric, shallow water, and overland flow coupling for simulating extreme flooding events such as that from Hurricane Harvey appears to be the first.

Coupled 2D-3D shallow water models are implemented in Adaptive Hydraulics (AdH) [5,6,89], a multi-physics software suite comprised of 2D and 3D shallow water (SW) and constituent transport models, among others. The models use a CG FE engine with streamline upwind Petrov-Galerkin (SUPG) stabilization [11]. As the name suggests, AdH supports adaptivity in both space and time. AdH shallow water models use triangular meshes in 2D, and tetrahedral or prismatic meshes in 3D. First and second-order implicit time-stepping are supported. 2D SW models in AdH are based on an Eulerian treatment of physics on an unstructured mesh, including wetting and drying. AdH 3D SW models use the natural z coordinate in an ALE framework to move the mesh only in the vertical direction. They can handle baroclinic flows including vertical mixing, but they cannot handle wetting and drying at this time. 3D meshes are generated by extruding the 2D unstructured meshes in the vertical direction, so that they are semi-structured with nodes aligned in the vertical direction into what are referred to as 'node columns' hereafter. These node columns are useful for coupling with 2D shallow water models as they allow preserving conformity.

For coupling atmospheric, shallow water, and surface/subsurface flow models, different codes are used. The atmospheric model is the North American Mesoscale Forecast System (NAM), run daily by the National Centers for Environmental Prediction (NCEP), United States [45]. The 2D shallow water model from AdH is utilized, and the diffusive wave equation based coupled 1D channel and 2D overland flow models from Gridded Surface Subsurface Hydrologic Analysis (GSSHA) [31, 32] are used. GSSHA uses a finite volume method for overland flow and channel routing, with Manning's formula being used to relate depth to discharge. GSSHA also has 1D infiltration and 2D groundwater simulation capabilities, with full coupling between groundwater, infiltration, streams and overland flow. Specifically, for this work, AdH 2D shallow water models are weakly coupled to GSSHA watershed models at a connected portion of the AdH domain boundary and a single GSSHA watershed 1D channel outlet cell, which is coupled to the 2D overland flow model. AdH and GSSHA model domains are assumed to be non-overlapping. Weak coupling is used in this case, with options of unidirectional as well as bidirectional information exchange between AdH and GSSHA. The case of zero Gauss-Seidel iterations is currently used for coupling the models, with plans to allow multiple Gauss-Seidel iterations in the future. Since the coupling from NAM to AdH and NAM to GSSHA is one-way, and since NAM is run daily by NCEP, producing new forecasts every six hours, the NAM code itself is not coupled to AdH and GSSHA, and instead, the publicly available NAM output files are used to obtain relevant data for coupling with AdH and GSSHA. AdH

uses winds, and GSSHA uses precipitation forecasts from NAM output files.

The NAM-AdH-GSSHA coupling presented herein is only preliminary and should be considered as a proof-of-concept, with many improvements still possible. In particular, overland flow coupling over multiple GSSHA domain boundary cells, which would be important for practical use in compound flooding predictions, is currently pending and may be pursued in the future. Implementing complicated coupled models such as 2D-3D strongly coupled AdH models coupled to GSSHA watershed models with full internal coupling of groundwater, infiltration, stream, and overland flow, all of which are driven by atmospheric forcing from NAM, is also straightforward with the present work in place, but has not been pursued due to time constraints.

The remainder of this dissertation is arranged as follows. Table 1.1 gives the terminology used herein. Chapter 2 introduces the shallow water equations and gives an overview of the SUPG FE methodology used in AdH for numerical solution of the shallow water equations. Chapter 3 revisits the theory behind 2D-3D strong coupling from [20], improves it, and adds transport coupling considerations to it. Chapter 4 gives four verification test cases, chapter 5 gives two validation test cases, and chapter 6 gives two large-scale applications of 2D-3D shallow water coupling. Chapter 7 touches upon the weak coupling between atmospheric, hydrodynamic, and hydrologic models in order to produce forecasts requiring quick turn-around times. NAM, AdH, and GSSHA are respectively the candidates for coupling in this case. Lastly chapter 8 summarizes and concludes the work.

Table 1.1: Terminology.

Item	Description
(x, y, z, t)	Cartesian coordinates and time
b	Bed coordinates, assumed fixed
η	Water surface elevation
$h = \eta - b$	Water depth
$\boldsymbol{u} = \{u, v, w\}$	Velocity vector
$\bar{\boldsymbol{u}} = \{\bar{u}, \bar{v}\}$	Depth-averaged horizontal velocities
ρ, ρ_0	Density of fluid (water)
$\boldsymbol{S} = \{S_x, S_y\}$	Horizontal bottom friction and wind stress
$\boldsymbol{T}_x, \boldsymbol{T}_y, \overline{\boldsymbol{T}}_x, \overline{\boldsymbol{T}}_y$	Reynold's stresses
μ	Dynamic viscosity
$\sigma_{xx}, \sigma_{xy}, \sigma_{yy}, \sigma_{xz}, \sigma_{yz}$	Eddy viscosity coefficients
g	Acceleration due to gravity ($9.81\,\mathrm{m/s^2}$)
f	Coriolis parameter
p, P	Pressure
p_a	Atmospheric pressure, assumed constant
$\Omega^{2\mathrm{D}}, \Omega^{3\mathrm{D}}$	2D and 3D domains
$\partial\Omega^{2\mathrm{D}}, \partial\Omega^{3\mathrm{D}}$	2D and 3D domain boundaries
$\boldsymbol{R}^*$	Global weak residual vector, continuous in time
$\boldsymbol{R}$	Global weak residual vector, discrete in time
$\boldsymbol{r}^i$	Weak residual vector at node i, discrete in time
$r^{mx,i}, r^{my,i}$	Discrete horizontal momentum residuals at node i
$r^{c,i}$	Discrete continuity residual at node i
$\boldsymbol{s}$	Global solution vector of the model
$\boldsymbol{s}_i$	Solution vector at node i
$\mathcal{N}^{2\mathrm{D}}$, $\mathcal{N}^{3\mathrm{D}}$	Sets of all nodes in the 2D and 3D models
$\mathcal{J}^{2\mathrm{D}}$	Set of interface nodes that belong to the 2D model
$\mathcal{J}^{3\mathrm{D}}$	Set of interface nodes that belong to the 3D model
$\Gamma^{2\mathrm{D}}$	2D model interface (1D curve)
$\Gamma^{3\mathrm{D}}$	3D model interface (2D surface)
N	Number of nodes in the model (2D or 3D)
M	Number of elements in the model (2D or 3D)
Δt	Time step size
$\hbar$	Mesh size (not to be confused with the depth, h)

Chapter 2

2D and 3D shallow water models

Shallow water (SW) equations are coupled nonlinear partial differential equations, first order in time and second order in space. The primitive equations for the ocean, or the 3D SW equations as they are referred to herein, can be derived directly from conservation principles or from the Navier-Stokes equations under scaling, hydrostatic, and Boussinesq assumptions [93]. The 2D SW equations can be derived from the 3D SW equations by integrating them over the fluid depth. A brief introduction on the theory relevant to this work is presented.

Let t denote the time and (x, y, z) denote the position of a point in the usual three-dimensional mutually orthogonal Cartesian coordinate system. The x and y directions are often referred to as horizontal directions and the z direction as the vertical one. Since this work is mainly concerned with large water bodies on the Earth's surface like lakes and oceans, consider an analogous water body (or fluid) with a freely moving surface contained in a connected domain Ω. The boundary $\partial\Omega$ of the domain has two to three parts: the top, bottom, and side portions. The top boundary $\partial\Omega_{\mathrm{s}}$ corresponds to the freely moving water surface, the bottom part $\partial\Omega_{\mathrm{b}}$ is called the bed or bathymetry,

and the side portion $\partial\Omega_{\mathrm{v}}$, which is optional for 2D models and required for 3D models used herein due to lack of wetting-drying implementation in 3D, is a boundary aligned vertically, connecting the surface and the bed. The assumptions or approximations leading to the shallow water equations are as follows.

1. The *flow* is isochoric (i.e., incompressible), with density possibly allowed to vary spatially with dependence on salinity and temperature.

2. Reynold's time averaging is performed, which results in Reynold's stress and the standard turbulence closure problem. The eddy viscosity model is used for closure. The eddy viscosity may be specified as a constant or may be calculated using the Smagorinsky-Lilly model [81], with the Smagorinsky coefficient C_s being specified.

3. Horizontal scales are assumed to be much larger than vertical scales of the problem. This is the basic scaling assumption that leads to shallow water equations. In particular, vertical accelerations are negligible, resulting in pressure being hydrostatic.

4. Boussinesq approximation is made, which assumes density variations (due to salinity and temperature) to be small enough to not affect the flow field, except for giving rise to buoyancy forces. Hence for all equation terms containing the density, a constant density ρ_0 is used, except for terms involving acceleration due to gravity g, for which spatially varying density ρ is used.

Additional assumptions not related to the shallow water ones given above are also made. The bathymetry is assumed to vary over space, but is fixed in time, and sedimentation is not considered. Precipitation and evaporation are not included. The water can move under different possible forces, which include gravity, wind, friction, and atmospheric pressure. Coriolis force is also included since the Earth is a rotating frame of reference, but for the scale of the models considered herein, the Coriolis parameter is considered constant at $f = 2\alpha \sin \phi$, where α is the rotation rate of the Earth, and ϕ is the latitude of the domain location. A detailed derivation of the shallow water equations from the Navier-Stokes equations is given in [93]. Lastly, if the density depends on salinity and/or temperature resulting in baroclinicity, then transport equations must be additionally included for tracking salinity and/or temperature, and a state equation is used to relate density with them. The following sections give a short, informal mathematical description of the shallow water and transport equations, along with the numerical scheme used for solving them.

2.1 Shallow water equations

The 3D and 2D shallow water equations are respectively explained in the following sections.

2.1.1 3D shallow water equations

The solution variables for the 3D shallow water equations are the depth, h, and the velocity, $\boldsymbol{u} = \{u, v, w\}$. The equations are comprised of conservation of mass, horizontal momentum in x and y directions, and (simplified) vertical momentum in the z direction, respectively given by,

$$\nabla \cdot \boldsymbol{u} = 0, \tag{2.1}$$

$$\frac{Du}{Dt} + \frac{1}{\rho_0}\frac{\partial p}{\partial x} - fv - \frac{1}{\rho_0}\nabla \cdot \boldsymbol{T}_x = 0, \tag{2.2}$$

$$\frac{Dv}{Dt} + \frac{1}{\rho_0}\frac{\partial p}{\partial y} + fu - \frac{1}{\rho_0}\nabla \cdot \boldsymbol{T}_y = 0, \tag{2.3}$$

$$p = p_a + \int_z^\eta g\rho \, dz. \tag{2.4}$$

Here, $\nabla = \{\partial/\partial x, \partial/\partial y, \partial/\partial z\}$ represents the gradient operator and $D/Dt = (\partial/\partial t + \boldsymbol{u} \cdot \nabla)$ represents the total derivative operator. The Reynold's stress vectors $\boldsymbol{T}_x$ and $\boldsymbol{T}_y$ include dynamic viscosity and turbulence effects, and are given by,

$$\{\boldsymbol{T}_i\}_j = \left\{ (\sigma_{ij} + \mu) \left(\frac{\partial u_i}{\partial x_j} + \frac{\partial u_j}{\partial x_i} \right) \right\}, \quad i \in \{x, y\}, j \in \{x, y, z\}, \quad \text{no sum},$$

where σ_{ij} are eddy viscosity coefficients for turbulence closure and μ is the dynamic viscosity. σ_{ij} may be specified as constants or may be calculated with the Smagorinsky-Lilly scheme [81], not covered herein.

There are kinematic boundary conditions on the free surface and the

bed, respectively given by,

$$\frac{\partial \eta}{\partial t} + u(x,y,\eta,t)\frac{\partial \eta}{\partial x} + v(x,y,\eta,t)\frac{\partial \eta}{\partial y} - w(x,y,\eta,t) = 0, \tag{2.5a}$$

$$\frac{\partial b}{\partial t} + u(x,y,b,t)\frac{\partial b}{\partial x} + v(x,y,b,t)\frac{\partial b}{\partial y} - w(x,y,b,t) = 0, \tag{2.5b}$$

which state that water cannot cross the surface and bed boundaries, $\partial\Omega_{\mathrm{s}}$ and $\partial\Omega_{\mathrm{b}}$. The vertical side boundaries $\partial\Omega_{\mathrm{v}}$ may have one of Dirichlet/Neumann elevation or normal flow boundary conditions specified. Bottom friction and wind may also be specified as boundary conditions and enter the numerical scheme in the weak form. Wall friction, however, is currently not considered herein. Initial conditions on the solution variables $\{h, u, v, w\}$ are also required.

Note that an additional equation for tracking the free surface is needed, which is usually obtained by depth-integrating (2.1). In this work, however, the depth-integrated equation is not directly used; instead, a different method is employed to obtain a 'numerical water surface equation,' explained in section 2.3.4.2. This equation and the horizontal momentum equations together form a prognostic set for predicting $\{h, u, v\}$ first, after which the continuity equation (2.1) is used as a diagnostic equation to calculate w. These two stages of solving for the water depth and horizontal velocities first followed by finding the vertical velocity are respectively referred to as HVEL and WVEL stages herein.

2.1.2 2D shallow water equations

Depth-integrating (2.1)–(2.3) leads to the 2D shallow water equations. The solution variables for these equations are the depth, h, and the depth-averaged velocity, $\bar{\boldsymbol{u}} = \{\bar{u}, \bar{v}\}$. The conservation equations are comprised of a depth-integrated continuity equation, hereafter referred to as the water surface equation, and depth-integrated horizontal momentum equations, respectively given by,

$$\frac{\partial h}{\partial t} + \frac{\partial h\bar{u}}{\partial x} + \frac{\partial h\bar{v}}{\partial y} = 0, \tag{2.6}$$

$$\begin{aligned}\frac{\partial h\bar{u}}{\partial t} + \frac{\partial h\bar{u}\bar{u}}{\partial x} + \frac{\partial h\bar{v}\bar{u}}{\partial y} + \frac{\partial}{\partial x}\left(\frac{1}{2}gh^2\right) + \frac{h}{\rho_0}\frac{\partial p_a}{\partial x} \\ +gh\frac{\partial b}{\partial x} - fh\bar{v} - \nabla\cdot\left(\frac{h}{\rho_0}\overline{\boldsymbol{T}}_x\right) + S_x = 0,\end{aligned} \tag{2.7}$$

$$\begin{aligned}\frac{\partial h\bar{u}}{\partial t} + \frac{\partial h\bar{v}\bar{u}}{\partial x} + \frac{\partial h\bar{v}\bar{v}}{\partial y} + \frac{\partial}{\partial y}\left(\frac{1}{2}gh^2\right) + \frac{h}{\rho_0}\frac{\partial p_a}{\partial y} \\ +gh\frac{\partial b}{\partial y} + fh\bar{u} - \nabla\cdot\left(\frac{h}{\rho_0}\overline{\boldsymbol{T}}_y\right) + S_y = 0.\end{aligned} \tag{2.8}$$

In the above equations, turbulence and dynamic viscosity effects are represented by the Reynold's stress vectors $\overline{\boldsymbol{T}}_x$ and $\overline{\boldsymbol{T}}_y$, which are given by,

$$\left\{\overline{\boldsymbol{T}}_i\right\}_j = \left\{(\sigma_{ij} + \mu)\left(\frac{\partial u_i}{\partial x_j} + \frac{\partial u_j}{\partial x_i}\right)\right\}, \quad \{i,j\} \in \{x,y\}, \quad \text{no sum},$$

with the eddy viscosities σ_{ij} specified as constants or calculated using the Smagorinsky-Lilly model [81]. S_x and S_y, represent forces due to wind and bottom friction, and are given by,

$$S_i = \frac{1}{2}c_f|\bar{\boldsymbol{u}}|\bar{u}_i - \frac{\rho_{\text{air}}}{\rho_0}c_d|\boldsymbol{U}|U_i, \quad i \in \{x,y\}, \tag{2.9}$$

where c_f is the coefficient of bottom friction calculated as given in [89], $\rho_{\text{air}} = 1.225\,\text{kg/m}^3$ is the density of air, $\boldsymbol{U} = \{U_x, U_y\}$ is the wind velocity close to the water surface (generally obtained from an atmospheric model or observations), and c_d is the wind drag coefficient calculated according to [86].

In case of 2D shallow water equations, the boundary conditions for the surface and bottom (2.5) are already built into the water surface equation. The 2D domain may have wetting-drying fronts in part of or the entire boundary or may have boundary edges corresponding to vertical side boundaries of 3D models $\partial\Omega_{\text{v}}$, with Dirichlet/Neumann boundary conditions specified on the elevation or velocity, similar to the 3D shallow water equations. Initial conditions on $\{h, \bar{u}, \bar{v}\}$ are also specified.

The 2D shallow water equations have no dependence on the vertical velocity w. Unlike in the 3D shallow water models, solving for the vertical velocity after solving the 2D shallow water equations is not required, so the 2D models generally do not have a WVEL stage. However, in past work on 2D-3D coupling [20], problems were encountered when solving for vertical velocities in the WVEL stage for coupled models, in which equations were only available on the 3D side and not the 2D side. In order to alleviate the problem, it is proposed herein that the 2D models also be allowed to have a WVEL stage. On solving the 2D shallow water equations in the HVEL stage, the kinematic boundary conditions (2.5) are used as diagnostic equations in the WVEL stage to calculate the vertical velocity at the surface and the bed, assuming that the horizontal velocities are constant along the depth. This

allows a 2D-3D coupled WVEL stage, in which the equations on the 2D side are also available, avoiding the ambiguity explained in [20].

2.2 Transport equations

In many situations, particularly in estuaries, the transport of sediments, contaminants, salinity, or temperature is of importance. The constituents may be dilute with concentrations small enough to not alter the density of water, or they may affect it as in the case of salinity and temperature. Regardless of the case, additional equations must be included to track the constituents. The conservation statement for constituents leads to the classic advection-diffusion equation (assuming non-reactive constituents). The equation for each constituent is given by,

$$\frac{\partial c}{\partial t} + \nabla \cdot (\boldsymbol{u}c) - \nabla \cdot \left(\overline{\overline{\boldsymbol{D}}}^{3D} \nabla c\right) = 0, \tag{2.10}$$

in case of 3D models. For 2D models, depth-integration of the above equation and ignoring some terms (which cannot be ignored in case of baroclinicity) leads to,

$$\frac{\partial h\bar{c}}{\partial t} + \nabla^{2D} \cdot (h\bar{\boldsymbol{u}}\bar{c}) - \nabla^{2D} \cdot \left(\overline{\overline{\boldsymbol{D}}}^{2D} \nabla^{2D}(h\bar{c})\right) = 0. \tag{2.11}$$

Here, c and $\bar{c}$ are respectively 3D and depth-averaged constituent concentrations, $\boldsymbol{u}$ and $\bar{\boldsymbol{u}}$ are 3D and depth-averaged 2D velocities of water, $\nabla = \{\partial/\partial x, \partial/\partial y, \partial/\partial z\}$ and $\nabla^{2D} = \{\partial/\partial x, \partial/\partial y\}$ represent the 3D and 2D gradient operators. $\overline{\overline{\boldsymbol{D}}}^{3D}$ and $\overline{\overline{\boldsymbol{D}}}^{2D}$ are 3D and 2D eddy diffusivity tensors of the constituent, in which off-diagonal terms are zero, and only $\overline{\overline{\boldsymbol{D}}}^{3D}_{ii}$ and $\overline{\overline{\boldsymbol{D}}}^{2D}_{jj}$ (no

sum), for $i \in \{x, y, z\}$ and $j \in \{x, y\}$ may be user specified. Boundary and initial conditions on the constituent concentrations must be specified.

Note that although the 2D transport equation can be used to transport salinity and temperature, only the 3D equations are accurate for such baroclinic transport. This is because in case of 2D models, depth-integration leads to differential advection terms which are ignored assuming the flow to be barotropic (i.e., not baroclinic), which is obviously invalid if salinity or temperature transport are involved, whereas in the 3D models, no such assumption is made; see [93] for a discussion on differential advection terms.

In case of baroclinic transport, an equation of state must be included to calculate the density from the concentrations. Only baroclinicity due to temperature and salinity is included in the current work. The equation of state taken from [69, 89] is given by,

$$\begin{aligned}\rho(S,T,0) = \rho_w &+ \left(b_0 + b_1 T + b_2 T^2 + b_3 T^3 + b_4 T^4\right) S \\ &+ \left(c_0 + c_1 T + c_2 T^2\right) S^{3/2} + d_0 S^2,\end{aligned}$$

where $\rho(S,T,0)$ is the density of water at a salinity of $S\,\mathrm{g/kg}$, temperature of $T\,^\circ\mathrm{C}$, and pressure of $0\,\mathrm{bars}$. The reference density ρ_w of pure water is given by,

$$\rho_w = a_0 + a_1 T + a_2 T^2 + a_3 T^3 + a_4 T^4 + a_5 T^5.$$

The empirical constants in the above equations are given by,

$$
\begin{aligned}
a_0 &= 9.998\,425\,94 \times 10^{2}, & b_0 &= 8.244\,93 \times 10^{-1}, & c_0 &= -5.724\,66 \times 10^{-3},\\
a_1 &= 6.793\,952 \times 10^{-3}, & b_1 &= -4.0899 \times 10^{-3}, & c_1 &= 1.0277 \times 10^{-4},\\
a_2 &= -9.095\,290 \times 10^{-3}, & b_2 &= 7.6438 \times 10^{-5}, & c_2 &= -1.6546 \times 10^{-6},\\
a_3 &= 1.001\,685 \times 10^{-4}, & b_3 &= -8.2467 \times 10^{-7}, & & \\
a_4 &= -1.200\,83 \times 10^{-6}, & b_4 &= 5.3875 \times 10^{-9}, & & \\
a_5 &= 6.536\,332 \times 10^{-9}, & & & d_0 &= 4.8315 \times 10^{-4}.
\end{aligned}
$$

2.3 Numerical solution

Although known analytic solutions to the shallow water equations do exist in some cases [87], they must be solved numerically for all realistic scenarios. The streamline upwind Petrov-Galerkin (SUPG) finite element method [11] is employed for the numerical solution of these equations in the Adaptive Hydraulics software suite, which has been used in the present work. The weak formulation, numerical schemes, and other details about the theory implemented within AdH are given in [4–6] for its 2D shallow water model and [89] for its 3D one. As mentioned in section 2.1.1, the shallow water equations are solved in two stages, HVEL and WVEL. In the HVEL stage, depth and horizontal velocities are solved for. In the WVEL stage, the vertical velocities are obtained. In case of constituent transport, the advection-diffusion equations given in the previous section are solved thereafter. If salinity and/or temperature are being transported, then the equation of state is used after that to calculate the density of water for the next time step. Instead of solving all

the equations in a monolithic manner, the equations are solved one after the other in a split-operator fashion. Since the SUPG formulation in AdH is neither a contribution, nor a focus of this work, the derivation is not included herein, but is given in [89].

An overview of the solution methodology for the finite element method is given in Figure 2.1. A semi-discrete continuous Galerkin formulation with streamline upwind Petrov-Galerkin (SUPG) stabilization is used to first discretize the equations in space. This leads to a set of coupled first order nonlinear ordinary differential equations in time. These equations are then discretized in time using first or second order backward difference formulas, leading to a system of nonlinear equations represented abstractly as $\boldsymbol{R}(\boldsymbol{s}) = 0$, which must be solved at each time step. Newton-Raphson iterations are used to solve the nonlinear equations.

2.3.1 Spatial discretization

For spatial discretization, the standard space of continuous piecewise linear polynomials is chosen as the trial space U^h, with the well-known Lagrange 'hat' functions being a basis. The resulting discretization is hence triangular in 2D, and tetrahedral in 3D. In the usual SUPG method, the test functions are basis functions of the trial space plus an additional term dependent on the gradient of the basis function. The semi-discrete formulation

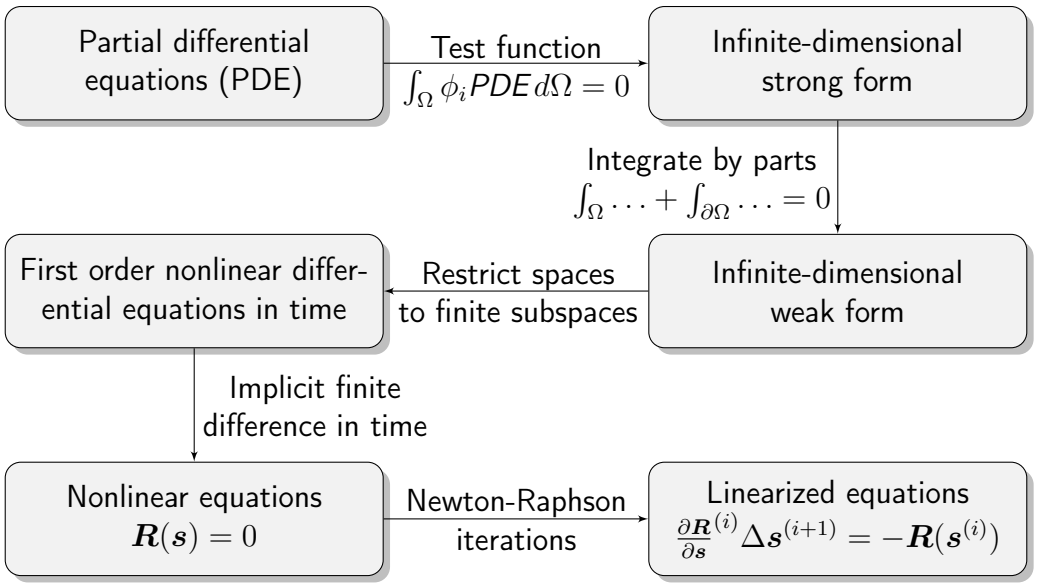

Figure 2.1: Overview of the semi-discrete finite element method.

assumes the solution to be of the form,

$$s^h(\boldsymbol{x}, t) = \sum_{i=1}^{N} \phi_i(\boldsymbol{x}) s_i(t), \quad \forall \boldsymbol{x} \in \Omega^h, t \in [0, T], \tag{2.12}$$

where N is the number of nodes, $\phi_i \in U^h$ are the piecewise linear basis functions, s_i are temporally varying nodal unknowns, T is the final time, $\boldsymbol{x}$ is $\{x, y, z\}$ for 3D models and $\{x, y\}$ for 2D models, and $s^h \in U^h \times [0, T]$ is a solution variable representative of each of $\{h, u, v, w, c\}$ for 3D models and $\{h, \bar{u}, \bar{v}, w^{\mathrm{s}}, w^{\mathrm{b}}, \bar{c}\}$ for 2D models. For convenience in notation, $\boldsymbol{s}^h = \sum_{i=1}^{N} \phi_i(\boldsymbol{x}) \boldsymbol{s}_i(t) \in \boldsymbol{U}^h \times [0, T]$ is used to represent the solution variables of the equation being solved, where $\boldsymbol{s}_i$ is used to represent the n degrees of freedom at a given node i, and $\boldsymbol{U}^h = (U^h)^n$ is the trial space of appropriate dimensions. In the HVEL stage, each node has three degrees of freedom, viz., $\{h, u, v\}$ in

3D models and $\{h, \bar{u}, \bar{v}\}$ in 2D models. In the WVEL stage, each node has one degree of freedom, w. Note that for the WVEL stage of 2D models, the vertical velocities $\{w^{\mathrm{s}}, w^{\mathrm{b}}\}$ at the surface and the bed correspond to different locations and are technically calculated as if there were a mesh each on the surface and the bed. In case of constituent transport, the advection-diffusion equation is solved for each constituent separately using a single degree of freedom each time, which is c for 3D models and $\bar{c}$ for 2D ones. In case of baroclinic transport, the density ρ is also interpolated linearly within the domain, although it does not have to be solved for using FEM given the split-operator strategy and availability of the equation of state. Lastly, the nodal unknowns, which are a function of time, are represented as $\boldsymbol{s}(t) = \{\boldsymbol{s}_i(t)\}_{i=1}^{N}$, not to be confused with the spatiotemporal solution, $\boldsymbol{s}^{\hbar}(\boldsymbol{x}, t)$.

In the classical continuous Galerkin FE method, the semi-discrete weak form in the HVEL, WVEL, and transport stages is to find $\boldsymbol{s}^{\hbar} \in \boldsymbol{U}^{\hbar} \times [0, T] \subset \left(H_0^1(\Omega^{\hbar})\right)^n \times [0, T]$ (assuming zero Dirichlet BCs for simplicity,) such that,

$$\boldsymbol{R}_i^*(\boldsymbol{s}) = \boldsymbol{b}_{\mathrm{CG}}\left(\boldsymbol{s}^{\hbar}, \boldsymbol{\phi}_i\right) = \boldsymbol{0}, \quad \forall \boldsymbol{\phi}_i \in \boldsymbol{U}^{\hbar} \subset \left(H_0^1(\Omega^{\hbar})\right)^n, t \in [0, T],$$

where n is the number of degrees of freedom per node, which are 3, 1, and 1 respectively in the HVEL, WVEL, and transport stages, and $\boldsymbol{b}_{\mathrm{CG}} : (\boldsymbol{U}^{\hbar} \times [0, T]) \times \boldsymbol{U}^{\hbar} \ni (\boldsymbol{s}^{\hbar}, \boldsymbol{\phi}_i) \to \boldsymbol{b}_{\mathrm{CG}}(\boldsymbol{s}^{\hbar}, \boldsymbol{\phi}_i) = \boldsymbol{R}^*(\boldsymbol{s}(t)) \in \mathbb{R}^n$ represents the final semi-discrete weak form of the partial differential equations. Due to the semi-discrete nature, the result $\boldsymbol{R}^*(\boldsymbol{s}(t))$, referred to as the continuous-in-time weak residual, is a system of first order nonlinear ordinary differential equations. Obtaining this form involves steps shown in Figure 2.1, which are multiplying the

differential equation(s) under consideration with a test function, integrating over the domain, integrating relevant terms by parts, applying boundary conditions, and finally, restricting the infinite dimensional trial and test spaces, $\left(H_0^1(\Omega^\hbar)\right)^n$, to finite dimensional ones, $\boldsymbol{U}^\hbar$. $\boldsymbol{b}_{\mathrm{CG}}$ is linear in its second argument and nonlinear in its first one.

The test and trial spaces are the same in case of the classical continuous Galerkin FEM, but when using SUPG stabilization, additional terms are added to the weak form. An excellent review of the method is given in [42]. SUPG terms perturbing the test space, depending on the local velocity, gradient of the test function, and an element-dependent stabilizing parameter, are added. Complete details of the added terms for the 2D and 3D shallow water as well as transport models used herein are given in [89] and are omitted here for brevity. The terms are represented abstractly as $\boldsymbol{b}_{\mathrm{PG}}\left(\boldsymbol{s}, \boldsymbol{\phi}_i\right)$. This appropriately modifies the finite element statement, which now states: Find $\boldsymbol{s} \in \boldsymbol{U}^\hbar \times [0, T]$ such that,

$$\boldsymbol{R}_i^*(\boldsymbol{s}) = \boldsymbol{b}_{\mathrm{SUPG}}\left(\boldsymbol{s}, \boldsymbol{\phi}_i\right) = \boldsymbol{b}_{\mathrm{CG}}\left(\boldsymbol{s}, \boldsymbol{\phi}_i\right) + \boldsymbol{b}_{\mathrm{PG}}\left(\boldsymbol{s}, \boldsymbol{\phi}_i\right) = \boldsymbol{0}, \quad \forall \boldsymbol{\phi}_i \in \boldsymbol{U}^\hbar, t \in [0, T],$$

where $\boldsymbol{b}_{\mathrm{SUPG}}$ still remains linear in the second argument and nonlinear in the first, and $\boldsymbol{R}^*(\boldsymbol{s}(t)) = \{\boldsymbol{r}_i^*(\boldsymbol{s})\}_{i=1}^N$ is still the continuous-in-time weak residual vector corresponding to a system of first order nonlinear ordinary differential equations. $\boldsymbol{R}^*(\boldsymbol{s}(t))$ is thus, a function of time alone, with all the spatial variables removed through integration. The next step is to discretize the equations in time, covered in the next section.

2.3.2 Temporal discretization

Spatial discretization using the semi-discrete formulation results in the weak residual $\boldsymbol{R}^*(\boldsymbol{s}(t))$, which is continuous in time and contains first order time derivatives of the solution vector $\boldsymbol{s}(t)$. Backward difference formulas (BDF) [43] are used for approximating these temporal derivatives at this stage, given by,

$$\frac{d\boldsymbol{s}}{dt} = (1-\theta)\left(\frac{\boldsymbol{s}^{k+1}-\boldsymbol{s}^{k}}{\Delta t}\right) + \theta\left(\frac{3\boldsymbol{s}^{k+1}-4\boldsymbol{s}^{k}+\boldsymbol{s}^{k-1}}{2\Delta t}\right),$$

where θ is a user-specified parameter for choosing the time stepping order, Δt is the time step size, $\boldsymbol{s}$ is the solution vector, $\boldsymbol{s}^{k+1} = \boldsymbol{s}(t^{k+1})$ is the unknown being solved for at time $t = t^{k+1}$, and $\boldsymbol{s}^{k} = \boldsymbol{s}(t^{k})$ and $\boldsymbol{s}^{k-1} = \boldsymbol{s}(t^{k-1})$ are known solutions of previous timestamps $t = t^{k}$ and $t = t^{k-1}$. Note that $\theta = 0$ and $\theta = 1$ respectively correspond to first order backward Euler and second order time stepping methods. Here, the time range $[0, T]$ has been divided into equally sized time slabs for illustration, $\{[t^{k-1}, t^{k}]\}_{k=1}^{k=T/\Delta t}$. In actual simulations, however, the time step size may change adaptively for the first order time stepping, but for second order time stepping, the current implementation requires a constant time step. It is also noted that using the second order time stepping procedure requires two initial conditions, or if one is unavailable, then it must be approximated by using first order time stepping with a much smaller time step size ($\mathcal{O}(\Delta t^2)$). The BDF convert the nonlinear ordinary differential equations, $\boldsymbol{R}^*(\boldsymbol{s}(t)) = \boldsymbol{0}$, to a system of nonlinear equations, $\boldsymbol{R}(\boldsymbol{s}(t^{k+1})) = \boldsymbol{0}$, that must be solved at each time step, which is explained next.

2.3.3 Solution of nonlinear equations

The nonlinear equations obtained after spatial and temporal discretization can be written abstractly for any of the HVEL, WVEL, or transport stages as,

$$\boldsymbol{R}(\boldsymbol{s}(t^{k+1})) = \left\{\{\boldsymbol{r}^j(\boldsymbol{s}(t^{k+1}))\}_{j=1}^{N}\right\} = \boldsymbol{0}, \tag{2.13}$$

where $\boldsymbol{r}^j$ is the nodal residual at node j. The Newton-Raphson method used for solving the nonlinear equations gives rise to,

$$\left(\frac{\partial \boldsymbol{R}}{\partial \boldsymbol{s}_{k+1}}\right)^{(i)} \Delta \boldsymbol{s} = -\boldsymbol{R}\left(\boldsymbol{s}_{k+1}^{(i)}\right), \tag{2.14a}$$

$$\boldsymbol{s}_{k+1}^{(i+1)} = \boldsymbol{s}_{k+1}^{(i)} + \Delta \boldsymbol{s}. \tag{2.14b}$$

being solved repeatedly (over the index, i, with an initial guess, say, $\boldsymbol{s}_{k+1}^{(i=0)} = \boldsymbol{s}_k$), until either (2.13) is satisfied to some user defined 'nonlinear residual' tolerance, or the maximum change in the solution vector over an iteration falls below a user specified 'solution increment' tolerance. If the solver fails to converge within a third user specified limit on the number of solver iterations, then the time step is reduced to one-fourth of its value, and the solution is reattempted. If the solver is successful, the time is incremented, the time step size may possibly be doubled, and the entire process is repeated, thus marching forward in time till the user specified final time T is reached.

2.3.4 Special considerations

In this section, some topics relevant to the numerical solution of the equations are covered.

2.3.4.1 Meshes, node columns, and depth-summing

Due to the choice of continuous piecewise linear polynomials as the trial space, the resulting meshes used herein have 3-noded triangular elements in 2D models, and 4-noded tetrahedral elements in 3D ones. Support for 6-noded bilinear wedge elements for 3D models has also been added, and although it is not covered herein, the 2D-3D coupling theory given in the next chapter remains completely unchanged even with the bilinear elements. The 3D meshes used in this work are extruded from 2D unstructured meshes, resulting in meshes that are unstructured horizontally, but have nodes aligned vertically into what are referred to hereafter as 'node columns.' An example is shown in Figure 2.2, which shows a Galveston Bay 2D mesh and a 3D mesh extruded from it. An important feature of such 3D meshes is depth-summability of the basis functions ϕ_i of the trial space. This property is used not only in deriving a numerical water surface equation for 3D models as explained in the next section, but also for proving discrete mass and momentum conservation node-column-wise across a 2D-3D interface in case of 2D-3D strongly coupled models. The depth-summability and a reduction operator is explained next.

Consider a 2D mesh in the x-y plane, Ω^{2D}, and a 3D mesh Ω^{3D} obtained from extrusion of Ω^{2D}. Continuous piecewise linear polynomial trial spaces U^h_{2D} and U^h_{3D} from section 2.3.1 are defined on the domains, with basis functions $\phi_I \in U^h_{\text{2D}}$ and $\phi_i \in U^h_{\text{3D}}$ defined classically such that they have a value of 1 at the location of nodes I and i respectively, and 0 at all other nodes in the meshes. Each node I in the 2D mesh generates a corresponding column of

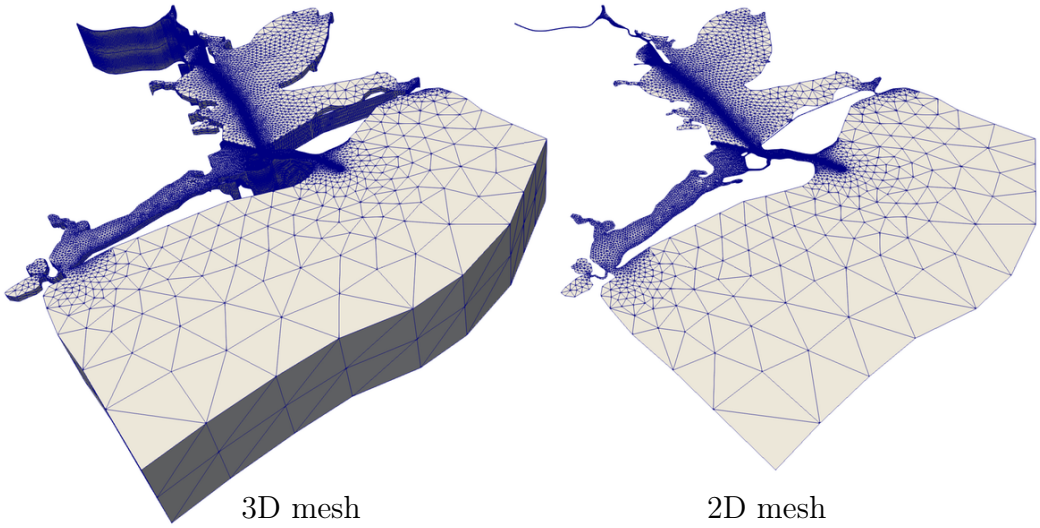

Figure 2.2: 2D Galveston Bay mesh (right) and the 3D mesh (left) extruded from it. (Figure not drawn to scale)

nodes in the 3D mesh, denoted as the set $\mathcal{C}(I)$. The following is formally stated without proof as it is obvious to see but perhaps tedious to prove rigorously,

$$\sum_{i \in \mathcal{C}(I)} \phi_i(x, y, z) = \phi_I(x, y). \tag{2.15}$$

This states that for the column of nodes $i \in \mathcal{C}(I)$ of the extruded 3D mesh, the result of summing the corresponding 3D basis functions ϕ_i, referred to as 'depth-summing' herein, is a function independent of z, and is equal to $\phi_I \in U^h_{2\mathrm{D}}$ formally (since technically these are defined on two different domains). This also applies to the respective gradients. Therefore, if two interrelated sets of operators are defined, $\mathcal{O}^{3\mathrm{D}} = \{id, \partial/\partial x, \partial/\partial y, \partial/\partial z, \nabla\}^\intercal$ and $\mathcal{O}^{2\mathrm{D}} = \{id, \partial/\partial x, \partial/\partial y, 0, \nabla\}^\intercal$, acting on basis functions in the respective spaces, where id is the identity operator, and ∇ is the 3D gradient operator then the depth-summing property of the operators can be formally stated

as,

$$\sum_{i \in \mathcal{C}(I)} \mathcal{O}^{3\mathrm{D}} \phi_i = \mathcal{O}^{2\mathrm{D}} \phi_I. \tag{2.16}$$

Now, consider any continuous function, $f(x, y, z)$, over $\Omega^{3\mathrm{D}}$, with its depth-averaged value $\bar{f}(x, y)$ over the $\Omega^{2\mathrm{D}}$ being defined as,

$$\bar{f}(x, y) = \frac{1}{h} \int_{z=b}^{z=\eta} f(x, y, z)\, dz. \tag{2.17}$$

It is seen that,

$$\sum_{i \in \mathcal{C}(I)} \int_{\Omega^{3\mathrm{D}}} f \mathcal{O}^{3\mathrm{D}} \phi_i \, d\Omega^{3\mathrm{D}} = \int_{\Omega^{2\mathrm{D}}} \int_{z=b}^{z=\eta} f \sum_{i \in \mathcal{C}(I)} \left(\mathcal{O}^{3\mathrm{D}} \phi_i \right) dz \, d\Omega^{2\mathrm{D}} \tag{2.18a}$$

$$= \int_{\Omega^{2\mathrm{D}}} \mathcal{O}^{2\mathrm{D}} \phi_I \left(\int_b^{\eta} f \, dz \right) d\Omega^{2\mathrm{D}} \tag{2.18b}$$

$$= \int_{\Omega^{2\mathrm{D}}} h \bar{f} \mathcal{O}^{2\mathrm{D}} \phi_I \, d\Omega^{2\mathrm{D}}, \tag{2.18c}$$

where the i-independence of f is used to obtain (2.18a), followed by depth-summing property (2.16) and z-independence to get (2.18b), and lastly, the definition of depth-averaged value (2.17) to get (2.18c). An analogous result involving the exact same steps is also available for depth-summing integrals over the vertical boundaries $\partial\Omega_{\mathrm{v}}^{3\mathrm{D}}$ of the 3D domain (comprising of 2D element faces), which correspond to the boundary $\partial\Omega^{2\mathrm{D}}$ of the 2D domain (comprising of 1D edges) since the 3D mesh is extruded from it. The two results hold importance particularly in proving discrete consistency in the HVEL and WVEL stages through the use of a numerical water surface equation and proving mass

and momentum conservation across the 2D-3D interface in 2D-3D strong coupling. The two results are summarized below.

$$\sum_{i\in\mathcal{C}(I)}\int_{\Omega^{3D}} f\mathcal{O}^{3D}\phi_i\, d\Omega^{3D} = \int_{\Omega^{2D}} h\bar{f}\mathcal{O}^{2D}\phi_I\, d\Omega^{2D}, \tag{2.19a}$$

$$\sum_{i\in\mathcal{C}(I)}\int_{\partial\Omega_v^{3D}} f\mathcal{O}^{3D}\phi_i\, d\partial\Omega_v^{3D} = \int_{\partial\Omega^{2D}} h\bar{f}\mathcal{O}^{2D}\phi_I\, d\partial\Omega^{2D}. \tag{2.19b}$$

2.3.4.2 Numerical water surface equation for 3D models

As noted in section 2.1.1, the 3D shallow water equations (2.1)–(2.4) need an additional equation to allow the 3D mesh to track the water surface. Although one possibility is to use the 2D water surface equation (2.6) for that purpose, a different approach is adopted, as given in [20, 89]. A numerical water surface equation is used to maintain discrete consistency between the HVEL and WVEL stages. In particular, the discrete consistency between the numerical water surface equation used in the HVEL stage and the weak form of the 3D continuity equation (2.1) used in the WVEL stage is maintained by employing the depth-summing property to arrive at the numerical water surface equation. The continuous-in-time weak residual of the 3D continuity equation (2.1), $R^{*c,i}_{3D,WVEL}$, used in the WVEL stage, is depth summed over node columns to obtain continuous-in-time weak residual, $\overline{R}^{*c,\mathcal{C}}_{3D,HVEL}$, used as the numerical water surface equation in the HVEL stage. For the classical continuous Galerkin case, the weak form of the 3D continuity equation (2.1)

is given by,

$$
\begin{aligned}
R^{*c,i}_{\mathrm{3D,WVEL}} = &- \int\limits_{\Omega^{\mathrm{3D}}} \boldsymbol{u} \cdot \nabla \phi_i \, d\Omega^{\mathrm{3D}} + \int\limits_{\partial\Omega^{\mathrm{3D}}_{\mathrm{v}}} \phi_i \boldsymbol{u} \cdot \boldsymbol{n} \, d\partial\Omega^{\mathrm{3D}}_{\mathrm{v}} \\
&+ \int\limits_{\partial\Omega^{\mathrm{3D}}_{\mathrm{b}}} \phi_i \boldsymbol{u} \cdot \boldsymbol{n}^{\mathrm{b}} \, d\partial\Omega^{\mathrm{3D}}_{\mathrm{b}} + \int\limits_{\partial\Omega^{\mathrm{3D}}_{\mathrm{s}}} \phi_i \frac{\partial \eta}{\partial t} n^{\mathrm{s}}_z \, d\partial\Omega^{\mathrm{3D}}_{\mathrm{s}},
\end{aligned}
\tag{2.20}
$$

where $\boldsymbol{n}$ is the normal to the boundary pointing out of the domain, and the surface and bed boundary conditions (2.5) have been used after rewriting them as,

$$
\frac{\partial \eta}{\partial t} n^{\mathrm{s}}_z - \boldsymbol{u} \cdot \boldsymbol{n}^{\mathrm{s}} = 0, \tag{2.21a}
$$

$$
-\frac{\partial b}{\partial t} n^{\mathrm{b}}_z + \boldsymbol{u} \cdot \boldsymbol{n}^{\mathrm{b}} = 0, \tag{2.21b}
$$

knowing that the outward normals at the surface and bed are respectively given by,

$$
\begin{aligned}
\boldsymbol{n}^{\mathrm{s}} &= \left\{ n^{\mathrm{s}}_x, n^{\mathrm{s}}_y, n^{\mathrm{s}}_z \right\}^{\intercal} = \frac{\{-\partial\eta/\partial x, -\partial\eta/\partial y, +1\}^{\intercal}}{\left[(\partial\eta/\partial x)^2 + (\partial\eta/\partial y)^2 + 1 \right]^{1/2}}, \\
\boldsymbol{n}^{\mathrm{b}} &= \left\{ n^{\mathrm{b}}_x, n^{\mathrm{b}}_y, n^{\mathrm{b}}_z \right\}^{\intercal} = \frac{\{+\partial b/\partial x, +\partial b/\partial y, -1\}^{\intercal}}{\left[(\partial b/\partial x)^2 + (\partial b/\partial y)^2 + 1 \right]^{1/2}}.
\end{aligned}
$$

Only one of the boundary conditions (2.21a) has been used in (2.20) since the 3D continuity equation (2.1) is a first order equation, which allows using only one of the BCs to keep the problem well-posed. In this case, the surface kinematic BC is used in (2.20), whereas the other boundary condition at the bed should automatically be satisfied in the WVEL stage if all calculations are correct and the code is working properly.

In the HVEL stage of 3D models, the water depth is an unknown at any given horizontal location, i.e., for any given column of nodes $\mathcal{C}(I)$, where I follows the definition from the previous section of being the node in the 2D mesh from which the column of nodes has been generated through extrusion. There are as many depth unknowns as there are node columns in the 3D mesh, which is the same as the number of nodes on the surface or bed boundaries of the 3D model. The WVEL continuity residual (2.20) is used in conjunction with the depth-summing property (2.19) from the previous section to define the HVEL residual for each column of nodes $\mathcal{C}$ as,

$$\begin{aligned} 0 = \overline{R}^{*c,\mathcal{C}(I)}_{\text{3D,HVEL}} = & \sum_{i\in\mathcal{C}(I)} R^{*c,i}_{\text{3D,WVEL}} \\ = & -\sum_{i\in\mathcal{C}(I)} \int_{\Omega^{\text{3D}}} \boldsymbol{u}\cdot\nabla\phi_i \, d\Omega^{\text{3D}} + \int_{\Omega^{\text{2D}}} \phi_I \frac{\partial h}{\partial t} \, d\Omega^{\text{2D}} \\ & + \sum_{i\in\mathcal{C}(I)} \int_{\partial\Omega^{\text{3D}}_{\text{v}}} \phi_i \boldsymbol{u}\cdot\boldsymbol{n} \, d\partial\Omega^{\text{3D}}_{\text{v}}, \end{aligned} \tag{2.22}$$

in which the boundary condition at the bed (2.21b) has also been substituted along with the relation, $n^{\text{s}}_z \, d\partial\Omega^{\text{3D}}_{\text{s}} = -n^{\text{b}}_z \, d\partial\Omega^{\text{3D}}_{\text{b}} = d\Omega^{\text{2D}}$. This equation is the discrete analog to depth integration of the strong form of the 3D continuity equation (2.1) used to obtain the 2D water surface equation (2.6) and is referred to as the numerical water surface equation herein. It can be shown that it is equivalent to the weak form of the water surface equation (2.6), at least in case of CG FEM [20]. For SUPG FEM, both (2.20) and (2.22) have additional PG terms, and care has been taken to check that this depth-summing equivalence also holds for the SUPG terms [89]. In the code implementation, the

numerical water surface equation is assigned to the surface node as the third equation (apart from momentum). The third equation for sub-surface nodes enforces accordion-like mesh movement in the vertical direction, so that the ratio of the depths between nodes in a node column remains the same as the initial one, throughout the simulation. These sub-surface displacement equations are additionally eliminated by hand in advance since they have a simple linear for, and are replaced with dummy equations. This is done because of the use of ALE method for tracking mesh movement; the surface nodes must move with the surface, whereas the movement of the sub-surface nodes is specified to let the depth ratios remain constant throughout the simulation, given by,

$$\frac{z(t) - b(t)}{h(t)} = \frac{z(0) - b(0)}{h(0)},$$

where z is the elevation of the node, and z, b, and h all correspond to the same horizontal location (x, y). In fact, in the code, the nodal unknowns are changed from the depth h to displacement d of mesh nodes in the z direction with respect to their initial locations at time $t = 0$, using the simple linear transformation, $z(t) = z(0) + d(t)$, which for the surface nodal unknown h translates to,

$$h(t) = h(0) + d(t).$$

Summarizing, in the HVEL stage of the 3D shallow water models used herein, the final set of unknowns in the code are $\{d, u, v\}$ instead of $\{h, u, v\}$. All nodes have horizontal momentum equations, but the third equation is the numerical water surface equation (2.22) in case of surface nodes, and dummy

equations ($R^{c,i}_{\text{3D,HVEL}}(\boldsymbol{s}(t)) = d_i(t) = 0$) in case of sub-surface nodes. The numerical water surface equation used in the HVEL stage is discretely consistent with the residuals used in the WVEL stage. Lastly, it is noted that since using $\{h, u, v\}$ and $\{d, u, v\}$ are equivalent through a simple linear transformation, the 2D-3D coupling theory explained in the next chapter is explained in the context of using $\{h, u, v\}$ as the solution variables.

2.3.4.3 WVEL stage of 2D shallow water models

In past work [4–6, 20, 89], 2D shallow water models only had the HVEL stage and did not solve for vertical velocities. As a result, for coupled 2D-3D shallow water models, there was ambiguity at the 2D-3D interface in the coupled WVEL stage, which involved a non-unique way of distributing the 2D side HVEL residuals among the 3D side nodes [20] in order to maintain discrete consistency. The present work alleviates the problem by adding a WVEL stage in 2D shallow water models, which is explained next.

After the HVEL stage of 2D models, the depth-averaged horizontal velocities and water surface elevations are known (whereas the bathymetry b is already known since sedimentation is not considered herein). Using this known HVEL solution, denoted by $\bar{\boldsymbol{u}}^{\text{HVEL}}$ and η^{HVEL} in this section, the weak form of the kinematic boundary conditions (2.5) are used as equations in the WVEL stage to obtain vertical velocities at the surface and bed. The calculated depth-averaged horizontal velocity $\bar{\boldsymbol{u}}^{\text{HVEL}}$ is used instead of the 3D velocities $\boldsymbol{u}$ contained in (2.5). The assumption here is that the 2D horizontal velocities are

nearly constant down the water column, which, if invalid, makes the 2D shallow water equations themselves inapplicable anyway. Moreover, the 2D WVEL stage only matters for coupled 2D-3D models, since in solely 2D simulations, the vertical velocities are not used anywhere.

The weak formulation of the kinematic BCs states: Find $w^{\mathrm{s}}, w^{\mathrm{b}} \in U^{\hbar}$ such that $\forall \phi_i \in U^{\hbar}$,

$$R^{\mathrm{s},i}_{\mathrm{2D,WVEL}} = \int\limits_{\Omega^{\mathrm{2D}}} \phi_i \left(\frac{\partial \eta^{\mathrm{HVEL}}}{\partial t} + \bar{\boldsymbol{u}}^{\mathrm{HVEL}} \cdot \nabla^{\mathrm{2D}} \eta^{\mathrm{HVEL}} - w^{\mathrm{s}} \right) d\Omega^{\mathrm{2D}} = 0, \quad \text{(2.23a)}$$

$$R^{\mathrm{b},i}_{\mathrm{2D,WVEL}} = \int\limits_{\Omega^{\mathrm{2D}}} \phi_i \left(\bar{\boldsymbol{u}}^{\mathrm{HVEL}} \cdot \nabla^{\mathrm{2D}} b - w^{\mathrm{b}} \right) d\Omega^{\mathrm{2D}} = 0. \quad \text{(2.23b)}$$

Equations (2.23a) and (2.23b) are solved together in spite of being decoupled systems. Although the implication for code implementation is that there are two degrees of freedom on each node, theoretically they are still treated as if there were two separate meshes on the surface and bed with corresponding single degrees of freedom w^{s} and w^{b}, respectively. Since η^{HVEL} and b are known in the WVEL stage, the above equations essentially act like Dirichlet BCs on the surface and bed vertical velocities. At the 2D-3D interface in 2D-3D strong coupling, the theoretically different nodes for the surface and bed on the 2D model side are coupled with the surface and bed nodes on the 3D model side. More on coupling is explained in the next chapter on 2D-3D strong coupling.

Chapter 3

Strongly coupled 2D and 3D shallow water models

Consider a scenario being simulated using the shallow water equations, in which the 3D solution is of interest in a relatively small region, but a large domain is needed for accuracy. For example, in order to study the 3D effects of hurricanes hitting a coastal region like Galveston Bay, a much larger region containing at least the track and extent of the hurricane, along with surrounding areas must generally be modeled, which in this case would be the entire Gulf of Mexico. 3D models are significantly computationally expensive. A 2D-3D coupled model can save computational cost by enabling simulations in which only the region of interest is modeled as 3D with the rest of the region modeled as 2D. Another possible use of 2D-3D coupled models is to combine the strengths of 2D wetting-drying and 3D baroclinic transport, which 3D and 2D models alone respectively cannot handle in most cases, into a single model that is able to handle both. Coupled 2D-3D shallow water models could possibly be explored for studying baroclinic flow in estuaries, or for studying the combined effect of hurricane storm surge and torrential coastal rainfall on salinity and temperature distribution, which are of importance to coastal ecosystems [56].

As explained in section 1.2, there are two broad approaches to coupling 2D and 3D shallow water models, viz., strong and weak coupling. Although both ways were initially pursued and a basic setup of weak coupling was also completed, only strongly coupled 2D-3D models, which were tested extensively, are presented herein. Another reason for that was that the 2D and 3D shallow water models used herein are highly compatible in their formulation, making 2D-3D strong coupling the natural course to pursue. Limited work on coupled 2D and 3D shallow water models was presented in past work [20], but did not include transport coupling, convergence studies, validation, and applications, all of which are presented herein. There were also unresolved problems in vertical velocity coupling in the past work that have now been alleviated.

One way to approach 2D-3D coupled models in terms of coding implementation is to directly support mixed 2D and 3D meshes such that full-2D or full-3D meshes would follow the 2D and 3D shallow water formulations touched upon in the previous chapter, whereas mixed meshes would follow a coupled formulation. However, due to several reasons, it is saner, more practical, and much cleaner to build finite element engines for 2D and 3D models separately, and then couple 2D and 3D models through the engines while keeping the models and all their data separate. This is because although it is theoretically possible have 2D and 3D elements mixed randomly in the domain for the sake of having a mixed grid, such grids would only serve an academic purpose, and practical problems would seldom, if at all, warrant the use of a complicated mixed grid. Therefore, strong 2D-3D coupling is introduced in the context

of a single 2D and a single 3D model, although they would be applicable, in theory, to any reasonable mixed grids satisfying the restrictions given in this chapter. The 2D and 3D model grids are thus stored separately even when coupling them. Each model can run its own functions relevant to building 2D and 3D systems of equations respectively. The models are non-overlapping, sharing a boundary with no gaps in between. Even at the shared boundary, called the 2D-3D interface herein, each model has its own sets of nodes and elements. Each model calculates its own residuals and Jacobian and sends its own contributions in assembling the monolithic coupled system, which is solved using Newton-Raphson iterations explained in section 2.3.3. In terms of coding implementation, strong coupling occurs at the level of residuals and Jacobian. All that is needed to build a monolithic system is to send the residual and Jacobian contributions of 2D-3D interface nodes to the right locations, requiring minimal intrusion into and changes in the original implementation of the coupled 2D and 3D shallow water models. That is why, strong coupling may also be referred to as algebraic coupling. Theoretically, however, the coupled models are a natural outcome of a correct choice of trial and test spaces for the coupled models. In the theory presented in this chapter, an attempt has been made to balance explanation between theory and coding implementation with the hope that a clear picture of both is available. The following sections lay down the background definitions, give the assumptions of the 2D-3D coupled models, build the coupled system, and give the key steps for proving conservation of mass and momentum across the 2D-3D interface.

Lastly, a brief note on the relation between 2D-3D strong coupling to 2D-2D or 3D-3D strong coupling is given.

3.1 Background definitions

Figure 3.1 shows an example of a coupled 2D-3D model. Recall that the 3D shallow water models used herein are necessarily surrounded by vertical boundaries $\partial\Omega_{\mathrm{v}}$ between the surface and the bed ones since they are generated by extruding 2D meshes (see section 2.3.4.1). The 2D and 3D domains are non-overlapping but share a share a common boundary without gaps in between in the sense that the intersection of the projections of the 3D and 2D models on the x-y plane is a continuous curve. Another way to look at it is that elements in selective regions of an entirely 2D mesh are extruded to form a 3D mesh, creating two coupling-ready meshes that satisfy the conformity requirement explained in the next section. The partial extrusion process also results in an appropriate 'shared' boundary, $\Gamma = \Gamma^{3\mathrm{D}} \cup \Gamma^{2\mathrm{D}}$, as shown in the figure.

Let $\mathcal{N}^{2\mathrm{D}}$ and $\mathcal{N}^{3\mathrm{D}}$ respectively denote the sets of all nodes in the 2D and 3D submodels. The sets of nodes lying on the 2D-3D interface on the 2D and 3D sides as are denoted as $\mathcal{I}^{2\mathrm{D}}$ and $\mathcal{I}^{3\mathrm{D}}$, respectively. The sets of non-interface nodes of the models are therefore given by the set difference $\mathcal{N}^{n\mathrm{D}} - \mathcal{I}^{n\mathrm{D}}$, $n \in \{2, 3\}$. In Figure 3.1, for example, the set of 2D model interface nodes is $\mathcal{I}^{2\mathrm{D}} = \{1, 2, 3\}$, whereas the set of 3D model interface nodes is $\mathcal{I}^{3\mathrm{D}} = \{4, 5, \ldots, 12\}$. For maintaining conformity explained in the next section, the interface nodes must be aligned into node columns as shown, in

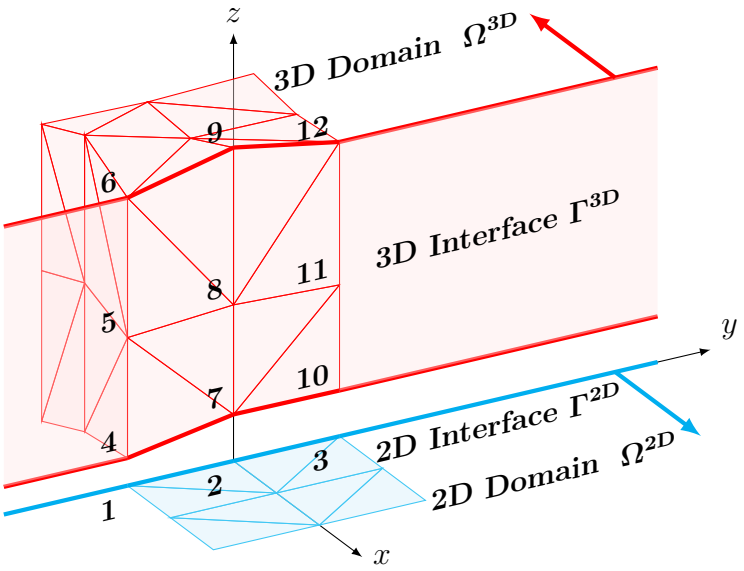

Figure 3.1: Example of a coupled 2D-3D model.

the sense that they have the same horizontal locations. This also results in 1D boundary edges constituting Γ^{2D} being perfectly aligned with columns of 2D boundary faces constituting Γ^{3D}.

In the example shown in Figure 3.1, the plan is to couple node 1 to node column $\mathcal{C}(1) = \{4, 5, 6\}$, node 2 to node column $\mathcal{C}(2) = \{7, 8, 9\}$, and 3 to node column $\mathcal{C}(3) = \{10, 11, 12\}$. Thus, in terms of coding implementation, the idea is to couple 2D nodes I with corresponding 3D node columns $\mathcal{C}(I)$ by enforcing specific relations between solution variables among the coupled nodes. This is done in HVEL, WVEL as well as transport solution stages mentioned in the previous chapter. The relations enforced between the solution variables within coupled node columns are mutual equality in case of coupled HVEL

and transport solution stages, whereas in the coupled WVEL stage, they are equality only at the bed and surface nodes with linear variation in between. For example, for the 3D nodes $\mathcal{C}(2) = \{7, 8, 9\}$ coupled to the 2D node 2, the HVEL and transport stages enforce $h_2^{2D} = h_9^{3D}$, $\bar{u}_2^{2D} = u_7^{3D} = u_8^{3D} = u_9^{3D}$, $\bar{v}_2^{2D} = v_7^{3D} = v_8^{3D} = v_9^{3D}$, and $\bar{c}_2^{2D} = c_7^{3D} = c_8^{3D} = c_9^{3D}$, and the WVEL stage enforces $w_2^{s,2D} = w_9^{3D}$ and $w_2^{b,2D} = w_7^{3D}$, with w_8 chosen so that the vertical velocity is linear over the node column. With these key ideas in place, the assumptions of and restrictions on 2D-3D strongly coupled models are explained in the next section.

3.2 Model requirements for 2D-3D coupling

Strong coupling between non-overlapping 2D and 3D models sharing a common boundary is the focus of this work. Continuity of the solution, mass flux, horizontal momentum fluxes, and constituent fluxes across the 2D-3D interface are enforced at all times in a conforming continuous Galerkin FE setting. Two requirements are imposed on the models, one is on the applicability of the 2D-3D coupled model to enforce its sensible use, and another is a conformity requirement to ensure discrete conservation of mass and momentum across the 2D-3D interface. The qualitative applicability requirement is a caution on the possible pitfalls of incorrectly using 2D-3D coupled models (irrespective of the type of coupling, strong or weak,) whereas the conformity requirement naturally leads to a monolithic 2D-3D coupled system (irrespective of its applicability). The two requirements complement each other.

3.2.1 Applicability

In order to be on the safer side, coupled 2D-3D models should only be used where they are applicable and would likely be accurate. Therefore, an obvious restriction on 2D-3D coupled models is that the 2D region and the 2D-3D interface should be placed in a region where 2D models may be used to capture relevant physics. It is necessary to use engineering sense before deciding on the location and arrangement of the 2D and 3D models since it is just as easy to combine the worst of both worlds as it is to incorporate the best of both. Placing either the 2D subdomain or the 2D-3D interface in a location where a 3D region is needed for capturing physics would result in an inaccurate solution, at least close to the 2D-3D interface. In case of baroclinic transport simulations, for example, the 2D subdomain and the 2D-3D interface should be placed in a region in which the water is well-mixed not only vertically, but also horizontally throughout the duration of the simulation. Nevertheless, it may be still possible that users of 2D-3D coupled models are forced to place the 2D-3D interface in a baroclinic region due to lack of any other option, which would violate the restrictions placed in this section. That is why, in the numerous test cases given herein, many are baroclinic test cases specifically meant for testing the limits of 2D-3D strong coupling by violating the applicability recommendation in order to understand the solution behavior in such scenarios. Since this condition on applicability does not prevent one from coupling 2D and 3D models, it is more of an engineering guideline than an assumption of or restriction on 2D-3D coupling.

3.2.2 Conformity

Discrete mass and momentum conservation across element boundaries in classical 1D, 2D, and 3D continuous Galerkin FEM is a natural outcome of conformity. The definition of conformity over a mesh essentially requires that the trial space U^h be a subspace of $H^1(\Omega)$, which is the space of square integrable functions in $L^2(\Omega)$ such that their first order derivatives are also in $L^2(\Omega)$. In most cases, however, by approximating domain boundaries, 'variational crimes' are committed in that U^h ends up being a subspace of $H^1(\Omega^h)$ on the discretized domain Ω^h instead of the actual domain Ω; these are ignored herein. The conditions for conformity in relation to the H^1 space is stated in the following lemma taken from [82].

Lemma 3.2.1 (Conformity requirements of the Sobolev space H^1)**.** *If $\mathcal{T}_h$ represents the triangulation of the domain Ω^h, i.e., the set of element domains Ω^{el} in the mesh, then a function $f : \Omega^h \to \mathbb{R}$ belongs to $H^1(\Omega^h)$ if and only if,*

1. *$f\big|_{\Omega^{el}} \in H^1(\Omega^{el})$, for each element $\Omega^{el} \in \mathcal{T}_h$, and*
2. *For each common face $\partial\Omega^{el} = \overline{\Omega}_1^{el} \cap \overline{\Omega}_2^{el}$, where $\Omega_1^{el}, \Omega_2^{el} \in \mathcal{T}^h$ and $\overline{(\cdot)}$ represents the closure operator, the trace of $f\big|_{\Omega_1^{el}}$ and $f\big|_{\Omega_2^{el}}$ on $\partial\Omega^{el}$ is the same, or in other words, the jump of the function f across any face $\partial\Omega^{el}$, defined by,*

$$[\![f]\!]_{\partial\Omega^{el}}(\boldsymbol{x}) = f\big|_{\Omega_2^{el}}(\boldsymbol{x}) - f\big|_{\Omega_1^{el}}(\boldsymbol{x}) \quad a.e.\ on\ \partial\Omega^{el},$$

vanishes, i.e., $[\![f]\!]_{\partial\Omega^{el}}(\boldsymbol{x}) = 0$ a.e. on $\partial\Omega^{el}$.

In case of solely 2D or 3D meshes that use the classical space $U^\hbar$ of continuous piecewise linear polynomials as the trial space, the conformity conditions in the above lemma are satisfied by the manner of construction of basis functions $\phi_i \in U^\hbar$. The 2D-3D strong coupling approach proposed in [20] and carried forward herein requires conformity in the coupled models as well. This requirement itself hints at the choice of trial space that naturally leads to a monolithic strongly coupled system. It is unknown if there are multiple ways to satisfy the above conformity requirement in the context of 2D-3D coupling, but at least one known way is presented herein. The next section presents strong coupling for the HVEL and transport stages, whereas the section after that presents strong coupling for the WVEL stage.

3.3 HVEL and transport stage coupling

By starting with a fully 2D mesh and extruding different regions of the mesh into 3D domains, a coupling-ready, part-2D, part-3D mesh is created, in which nodes at the 2D-3D interface are aligned into node columns without any gaps between (the x-y-plane projections of) the 2D and 3D models. With the 3D model being a result of extrusion, there are exactly as many nodes I lying on Γ^{2D} as there are node columns $\mathcal{C}(I)$ lying on Γ^{3D}, as shown in Figure 3.1.

As noted in the previous section, the classical trial space of continuous piecewise linear polynomials satisfies the conditions of Lemma 3.2.1 by construction of a particular basis to define the space. An appropriate basis is constructed for the trial space $U^\hbar_{\text{2D-3D}}$ 2D-3D strongly coupled models as well,

starting with the classical trial spaces of the 2D and 3D regions of the hybrid mesh, denoted as $U^{\hbar}_{\text{2D}}$ and $U^{\hbar}_{\text{3D}}$, respectively.

To that end, let Ω^{2D} and Ω^{3D} respectively denote the 2D and 3D regions of the hybrid 2D-3D domain $\Omega^{\text{2D-3D}} = \Omega^{\text{2D}} \cup \Omega^{\text{3D}}$. The sets $\mathcal{N}^{\text{2D}}$, $\mathcal{N}^{\text{3D}}$, $\mathcal{I}^{\text{2D}}$ and $\mathcal{I}^{\text{3D}}$ are defined as given in section 3.1. Let ϕ_i^{2D} and ϕ_i^{3D} respectively be the original, classical 'hat' basis functions of $U^{\hbar}_{\text{2D}}(\Omega^{\text{2D}})$ and $U^{\hbar}_{\text{3D}}(\Omega^{\text{3D}})$, defined as continuous piecewise linear functions with $\phi_i(\boldsymbol{x}_j) = \delta_{ij}$, where i is the node corresponding to the basis function ϕ_i, $\boldsymbol{x}_j$ is the location of any node j in the respective mesh, and δ_{ij} is the Kröenecker delta function with value 1 if $i = j$ and 0 otherwise. The basis functions for $U^{\hbar}_{\text{2D-3D}}(\Omega^{\text{2D-3D}})$ are constructed as follows.

First off, intermediate functions $\iota_i^{\text{2D}}, \iota_i^{\text{3D}} : \Omega^{\text{2D-3D}} \to \mathbb{R}$ are defined as possibly discontinuous trivial extensions of ϕ_i^{2D} and ϕ_i^{3D} corresponding to all nodes $i \in \mathcal{N}^{\text{2D}}$ and $i \in \mathcal{N}^{\text{3D}}$ of the parent meshes onto the entire coupled domain $\Omega^{\text{2D-3D}}$, written as,

$$\begin{aligned} \iota_i^{\text{2D}}(\boldsymbol{x}) &= \begin{cases} \phi_i^{\text{2D}}(\boldsymbol{x}), & \boldsymbol{x} \in \Omega^{\text{2D}} \\ 0, & \boldsymbol{x} \in \Omega^{\text{3D}} \end{cases}, \quad \forall i \in \mathcal{N}^{\text{2D}} \\ \iota_i^{\text{3D}}(\boldsymbol{x}) &= \begin{cases} 0, & \boldsymbol{x} \in \Omega^{\text{2D}} \\ \phi_i^{\text{3D}}(\boldsymbol{x}), & \boldsymbol{x} \in \Omega^{\text{3D}} \end{cases}, \quad \forall i \in \mathcal{N}^{\text{3D}} \end{aligned} \tag{3.1}$$

Note that the intermediate functions corresponding to the non-interface nodes $i \in \mathcal{N}^{\text{2D}} - \mathcal{I}^{\text{2D}}$ or $i \in \mathcal{N}^{\text{3D}} - \mathcal{I}^{\text{3D}}$ in the coupled domain are continuous throughout, and satisfy the conditions of Lemma 3.2.1 by default. It is the intermediate functions at the 2D-3D interface nodes $i \in \mathcal{I}^{\text{2D}}$ or $i \in \mathcal{I}^{\text{3D}}$ that are discontinuous. Using these intermediate functions, however, functions continuous across

the 2D-3D interface, to be included in the basis, are constructed. The number of basis functions at the 2D-3D interface is the same as the number of sets of coupled nodes at the interface, which is $|\mathcal{I}^{\text{2D}}|$. The final basis functions $\phi_i^{\text{2D-3D}} \in U^h_{\text{2D-3D}}(\Omega^{\text{2D-3D}})$ can be defined as,

$$\phi_i^{\text{2D-3D}} = \begin{cases} \iota_i^{\text{2D}}, & \forall i \in \mathcal{N}^{\text{2D}} - \mathcal{I}^{\text{2D}} \\ \iota_i^{\text{3D}}, & \forall i \in \mathcal{N}^{\text{3D}} - \mathcal{I}^{\text{3D}} \\ \iota_i^{\text{2D}} + \sum\limits_{j \in \mathcal{C}(i)} \iota_j^{\text{3D}}, & \forall i \in \mathcal{I}^{\text{2D}} \end{cases} \tag{3.2}$$

where continuity of $\phi_i^{\text{2D-3D}}$ is guaranteed by the depth-summability property of the basis functions (2.15). This is because according to (3.1) and (2.15), depth-summing ϕ_j^{3D} over coupled node columns $\mathcal{C}(i)$ would result in the function ϕ_I on the 3D side, where I is the 2D node that generates the node column $\mathcal{C}(I)$ on extrusion, which is the 2D interface node i itself. The function $\phi_I \cup \phi_i^{\text{2D}}$, obtained by joining ϕ_I and ϕ_i^{2D}, is a basis function of the original full-2D mesh from which the 2D-3D hybrid mesh is generated, and is continuous by construction. In particular,

$$\iota_i^{\text{2D}}\big|_{\Gamma^{\text{2D}}}(\boldsymbol{x}) = \left(\sum_{j \in \mathcal{C}(i)} \iota_j^{\text{3D}} \right) \Bigg|_{\Gamma^{\text{3D}}} (\boldsymbol{x}), \quad \forall i \in \mathcal{I}^{\text{2D}}, \forall x \in \Gamma. \tag{3.3}$$

Thus, the functions $\phi_i^{\text{2D-3D}}$ satisfy the second condition of Lemma 3.2.1 by construction. They also satisfy the first condition by construction, since the restriction of the functions $\phi_i^{\text{2D-3D}}\big|_{\Omega^{\text{el}}}$ to any 2D or 3D element Ω^{el} is ultimately either ϕ_i^{2D} or a linear combination of ϕ_i^{3D}, all of which satisfy the lemma. The test spaces are defined analogously as in (3.2), with the trial functions replaced with test functions.

Further arguments may be required to prove that the basis functions defined in (3.2) do, in fact, form a basis on the space $U^h_{\text{2D-3D}}(\Omega^{\text{2D-3D}})$, and that the space is complete. The analysis, however, has not been performed at present, and it is assumed that the rest of the things fall into place with these definitions of trial and test spaces. The functions in (3.2) satisfy both the conditions of Lemma 3.2.1, and under the conjectures that they do also form a basis on the space $U^h_{\text{2D-3D}}$ and that the space is complete, all functions f in the constructed space satisfy the conformity conditions of Lemma 3.2.1. Hence, the 2D-3D strongly coupled models presented herein and in [20] are conforming. The above steps apply for HVEL and transport stages of the 2D-3D strongly coupled models. The solution variables $\{h^{\text{3D}}, u^{\text{3D}}, v^{\text{3D}}, c^{\text{3D}}\}$ on the 3D side and $\{h^{\text{2D}}, \bar{u}^{\text{2D}}, \bar{v}^{\text{2D}}, \bar{c}^{\text{2D}}\}$ on the 2D side are defined according to (2.12), using the trial basis (3.2). Note that there is no ambiguity at the 2D-3D interface due to conformity, which ensures that the solution there is continuous and single-valued, given by,

$$\begin{pmatrix} h^{\text{2D}} \\ \bar{u}^{\text{2D}} \\ \bar{v}^{\text{2D}} \\ \bar{c}^{\text{2D}} \end{pmatrix}\Bigg|_{\Gamma^{\text{2D}}} = \begin{pmatrix} h^{\text{3D}} \\ u^{\text{3D}} \\ v^{\text{3D}} \\ c^{\text{3D}} \end{pmatrix}\Bigg|_{\Gamma^{\text{3D}}}. \tag{3.4}$$

The system is square since the trial and test space dimensions are equal by construction. Due to the nature of the trial functions, the HVEL/transport solution variables on the 2D and 3D sides of the interface are effectively set to be equal, as given by (3.4). Theoretically, the degrees of freedom for the entire column of nodes are the same. In a code, however, as is explained later in the comments in section 3.6, the 2D and 3D meshes may be using different degrees

of freedom on both sides of the interface and calculating their own residual and Jacobian contributions to build the system of equations. In terms of the code, then, coupling involves setting those extra degrees of freedom per coupled set of nodes to be equal to those of one of the nodes.

3.4 WVEL stage coupling

In order to maintain discrete consistency between HVEL and WVEL stages, the 3D models used herein generate a numerical water surface equation for the HVEL stage by depth-summing the WVEL residuals. The individual continuity equation residuals that have been depth-summed for the HVEL stage are driven to zero in the WVEL stage. In the past work on 2D-3D strong coupling [20], however, 2D models did not have a WVEL stage, so the WVEL stage in coupled models was effectively a 3D-only WVEL stage. Attempts were made to maintain the same discrete consistency between the coupled HVEL stage and the 3D-only WVEL stage, but that brought in ambiguity in the residual calculations in the WVEL stage.

The 2D WVEL stage introduced herein allows a coupled 2D-3D WVEL stage instead of the 3D-only WVEL stage of past work [20]. The WVEL stage coupling is slightly different compared to HVEL and transport coupling stages, because in this stage, using the same trial functions from the previous section would mean that on the 3D side, the vertical velocity is constant along the z-direction, which in turn creates flow across the bed and surface, violating the kinematic boundary conditions (2.5).

Moreover, since two equations per node are available on the 2D side for the WVEL stage given by (2.23), enforcing linear variation of w along the z direction becomes possible. Since the coupling idea is still similar to that of the HVEL stage, mathematical analysis for the WVEL stage is not presented herein. For clarity in the proceeding explanation, however, recall that the weak forms used in the 2D WVEL stage given by (2.23a) and (2.23b) respectively for the vertical velocities at the surface and the bed are theoretically considered to be over two separate meshes for the surface and the bed, although they are actually on the same 2D mesh. The key ideas in case of a coupled WVEL stage can then be stated as follows, noting that the coupled HVEL solution is known at this stage.

1. The surface and bed nodes on the 2D side of the interface are coupled respectively to the surface and bed nodes on the 3D side of the interface. This means that the vertical velocities at the surface on the 2D and 3D sides of the interface are set to be equal, and likewise in the case of bed velocities, as explained with an example at the end of section 3.1. The trial functions restricted to the surface and bed are continuous in a 2D sense.

2. Equations (2.23a) and (2.23b) from the 2D WVEL stage are used for obtaining residual/Jacobian contributions from the 2D side of the surface and bed nodes, respectively. At the surface and bed nodes on the 3D side of the interface, the WVEL residual/Jacobian contributions are calculated using a weak form analogous to the 2D WVEL stage (2.23). The

usual WVEL residuals (2.20) are not used for the 3D interface surface and bed nodes. This effectively enforces a Dirichlet boundary condition at the surface and bed.

3. On the 3D side of the interface, the residuals for the vertical velocities for all nodes between the surface and bed (exclusive) are replaced with equations enforcing linear variation from the bed to the surface. The equation for enforcing this linear variation of vertical velocities between the bed and surface is given by,

$$w(x,y,z,t) = \left(\frac{\eta - z}{h}\right) w(x,y,b,t) + \left(\frac{z-b}{h}\right) w(x,y,\eta,t), \qquad (3.5)$$

and is implemented in a Dirichlet manner.

3.5 Conservation across the 2D-3D interface

Due to the nature of the defined basis functions, conservation across any two 2D or two 3D elements in a coupled 2D-3D model is already guaranteed; what remains is to prove that mass, horizontal momentum, and transported constituents are conserved on crossing the 2D-3D interface. As in the case of solely 2D or 3D models, discrete conservation even in strongly coupled 2D-3D models across the 2D-3D interface is a natural consequence of conformity. Since the meshes on the sides of the 2D-3D interface are of different dimensions, the strictest level of conservation of quantities in the continuous sense would be column-wise, i.e., vertically integrated quantities would have to be conserved

ideally at every horizontal location $\boldsymbol{x} = (x, y) \in \Gamma^{2\mathrm{D}}$. This can be stated as,

$$\begin{pmatrix} h^{2\mathrm{D}} \\ h^{2\mathrm{D}}\bar{u}^{2\mathrm{D}} \\ h^{2\mathrm{D}}\bar{v}^{2\mathrm{D}} \\ h^{2\mathrm{D}}\bar{c}^{2\mathrm{D}} \end{pmatrix} \bar{\boldsymbol{u}}^{2\mathrm{D}} \cdot \boldsymbol{n}^{2\mathrm{D}} = -\int_{b^{3\mathrm{D}}}^{\eta^{3\mathrm{D}}} \begin{pmatrix} 1 \\ u^{3\mathrm{D}} \\ v^{3\mathrm{D}} \\ c^{3\mathrm{D}} \end{pmatrix} \boldsymbol{u}^{3\mathrm{D}} \cdot \boldsymbol{n}^{3\mathrm{D}}\, dz, \tag{3.6}$$

for all $(x, y) \in \Gamma^{2\mathrm{D}}$, which are four different equations written in short-hand, with the first one being, for example,

$$h^{2\mathrm{D}}\bar{\boldsymbol{u}}^{2\mathrm{D}} \cdot \boldsymbol{n}^{2\mathrm{D}} = -\int_{b^{3\mathrm{D}}}^{\eta^{3\mathrm{D}}} 1 \cdot \boldsymbol{u}^{3\mathrm{D}} \cdot \boldsymbol{n}^{3\mathrm{D}}\, dz.$$

Here, each solution variable has been tagged as 2D or 3D to make it clear which side of the 2D-3D interface it comes from. It can also be shown using (3.2) and (3.3) that,

$$\phi_I^{2\mathrm{D}} \begin{pmatrix} h^{2\mathrm{D}} \\ h^{2\mathrm{D}}\bar{u}^{2\mathrm{D}} \\ h^{2\mathrm{D}}\bar{v}^{2\mathrm{D}} \\ h^{2\mathrm{D}}\bar{c}^{2\mathrm{D}} \end{pmatrix} \bar{\boldsymbol{u}}^{2\mathrm{D}} \cdot \boldsymbol{n}^{2\mathrm{D}} = -\sum_{i \in \mathcal{C}(I)} \int_{b^{3\mathrm{D}}}^{\eta^{3\mathrm{D}}} \phi_i^{3\mathrm{D}} \begin{pmatrix} 1 \\ u^{3\mathrm{D}} \\ v^{3\mathrm{D}} \\ c^{3\mathrm{D}} \end{pmatrix} \boldsymbol{u}^{3\mathrm{D}} \cdot \boldsymbol{n}^{3\mathrm{D}}\, dz, \tag{3.7}$$

for all $(x, y) \in \Gamma^{2\mathrm{D}}$ and $I \in \mathcal{I}^{2\mathrm{D}}$. This gives conservation on the discrete level, which is less strict and requires that for all $I \in \mathcal{I}^{2\mathrm{D}}$,

$$\int_{\Gamma^{2\mathrm{D}}} \phi_I^{2\mathrm{D}} \begin{pmatrix} h^{2\mathrm{D}} \\ h^{2\mathrm{D}}\bar{u}^{2\mathrm{D}} \\ h^{2\mathrm{D}}\bar{v}^{2\mathrm{D}} \\ h^{2\mathrm{D}}\bar{c}^{2\mathrm{D}} \end{pmatrix} \bar{\boldsymbol{u}}^{2\mathrm{D}} \cdot \boldsymbol{n}^{2\mathrm{D}}\, d\Gamma^{2\mathrm{D}} = -\sum_{i \in \mathcal{C}(I)} \int_{\Gamma^{3\mathrm{D}}} \phi_i^{3\mathrm{D}} \begin{pmatrix} 1 \\ u^{3\mathrm{D}} \\ v^{3\mathrm{D}} \\ c^{3\mathrm{D}} \end{pmatrix} \boldsymbol{u}^{3\mathrm{D}} \cdot \boldsymbol{n}^{3\mathrm{D}}\, d\Gamma^{3\mathrm{D}}. \tag{3.8}$$

These are four equations as well, corresponding to mass, horizontal momentum, and constituent conservation across the interface. The following facts ensure that all the above conservation conditions are satisfied in case of the strongly coupled models presented herein.

1. For all points $\boldsymbol{x}$ on the 2D-3D interface Γ, $\boldsymbol{n}^{3D}(\boldsymbol{x}) = -\boldsymbol{n}^{2D}(\boldsymbol{x})$ holds for the outward pointing normals independent of z since there are no gaps in the 2D-3D interface.

2. The solution variables u^{3D}, v^{3D}, and c^{3D} are independent of z at the 2D-3D interface by the choice of the trial function.

3. Although w^{3D} is z-dependent, its contribution in $\boldsymbol{u}^{3D} \cdot \boldsymbol{n}^{3D}$ is zero since the normal at the 2D-3D interface is orthogonal to the z direction.

4. Conformity implies that $\phi_I^{2D}\big|_{\Gamma^{2D}} = \left(\sum_{i \in \mathcal{C}(I)} \phi_i^{3D}\right)\Big|_{\Gamma^{3D}}$ and (3.4) hold.

3.6 Code aspects of strong coupling

Although the coupled system is a natural consequence of the right choice of trial and test spaces, the actual coupling in a code can be implemented directly in the Newton-Raphson iteration stage (2.14) by monolithically building the residual and solution vectors as well as the Jacobian matrix. The number of coupled basis functions defined in (3.2) for the HVEL and transport stages, and in section 3.4 for the WVEL stage, which is also the effective number of nodes for those stages, is given by,

$$N_{\text{eff}}^{\text{2D-3D}} = \begin{cases} |\mathcal{N}^{2D}| & + |\mathcal{N}^{3D} - \mathcal{I}^{3D}|, & \text{HVEL stage,} \\ 2|\mathcal{N}^{2D} - \mathcal{I}^{2D}| & + |\mathcal{N}^{3D}|, & \text{WVEL stage,} \\ |\mathcal{N}^{2D}| & + |\mathcal{N}^{3D} - \mathcal{I}^{3D}|, & \text{Transport stage.} \end{cases} \tag{3.9}$$

The size of the coupled system is this effective number of nodes times the number of degrees of freedom per node, which are 3, 1, and 1 respectively

in case of HVEL, WVEL and transport stages. However, as noted in the beginning of this chapter, the 2D and 3D models are stored separately, and a monolithic coupled system must be built from them. This means that at the 2D-3D interface, each model has its own set of nodes, and each of those nodes has its own degrees of freedom, even though from the theory presented in section 3.3, there is supposed to be just one set of degrees of freedom per coupled node column in HVEL and transport coupling. This discrepancy between the code and theory must be circumvented. It would be good to allow the functions of the 2D and 3D models to be called independently and in any order to build the final monolithic system of equations. That way, the coupling can be made agnostic, allowing an array of not only 2D-3D coupled models, but also 2D-2D and 3D-3D coupled ones, in which each submodel would be called within a loop to assemble the monolithic system of equations. To that end, instead of the 2D and 3D models building separate systems of equations and then assembling a monolithic system from that, all memory accesses to the Jacobian, residual, and solution vectors pass through a mask vector μ that maps each node simultaneously to an equation and its set of degrees of freedom. Thus, instead of accessing, say, the continuity residual at node i as r_i^c, the residual is accessed as $r_{\mu(i)}^c$, and instead of accessing some Jacobian row/column as $\partial R_i^{mx}/\partial v_j$, it is obtained as $\partial R_{\mu(i)}^{mx}/\partial v_{\mu(j)}$. Using the mask μ, minimal modifications to the existing 2D and 3D finite element engines are required. The major effort in coding then goes into adding support for input and output of arrays of 2D and 3D models, their coupling interfaces, redefining

the memory used by the monolithic system of equations, and creating the mask vector μ.

The mask vector maps each node to its degrees of freedom or equivalently, its set of equations. In case of solely 2D or 3D models, it is just an identity map. In case of multiple 2D and 3D models being solved together without any coupling, it maps each node successively to a distinct number from 1 to the total number of nodes across the models. In case of 2D-3D coupled models, the mask vector maps all the 2D and 3D non-interface nodes to distinct numbers, but the mapping for the interface nodes must be dealt with separately, with some nodes having a common number that they are mapped to. The sets of coupled nodes are the same in case of HVEL and transport, so they use the same mask vector, μ^{HVEL}. The coupled nodes in the WVEL stage are different from those in HVEL and transport stages, so a second mask vector μ^{WVEL} is required. The definitions of the two mask vectors given below are valid irrespective of whether a single, multiple non-coupled, or an array of 2D-3D coupled models are being run.

An HVEL 'equation map,' given by $\varepsilon^{\text{HVEL}} : \mathcal{N}^{\text{2D}} \cup (\mathcal{N}^{\text{3D}} - \mathcal{I}^{\text{3D}}) \rightarrow \{1, 2, \ldots, |\mathcal{N}^{\text{2D}}| + |\mathcal{N}^{\text{3D}} - \mathcal{I}^{\text{3D}}|\})$ is defined first, which maps all nodes in the 2D model, and all non-interface nodes in the 3D model to distinct numbers between 1 and $\mathcal{N}_{\text{eff}}^{\text{2D-3D}}$, given by (3.9). These effectively act like equation numbers (triplets in case of HVEL stage and single in case of transport stage). Since any ordering is possible, the map $\varepsilon^{\text{HVEL}}$ itself is not unique, but any given choice must be a bijection by construction. Next, define $\xi^{\text{HVEL}} : \mathcal{I}^{\text{3D}} \rightarrow \mathcal{I}^{\text{2D}}$,

which maps each node on the 3D interface node to the 2D node it must be coupled with. This means that $\xi^{\text{HVEL}}(i) = I$, for all $i \in \mathcal{C}(I)$, where $I \in \mathcal{I}^{\text{2D}}$. This map is obviously not a bijection since all nodes in a 3D node column $\mathcal{C}(I)$ are mapped to a single 2D node I. The HVEL/transport mask map, $\mu^{\text{HVEL}} : \mathcal{N}^{\text{2D}} \cup \mathcal{N}^{\text{3D}} \to \{1, 2, \ldots, N_{\text{eff}}^{\text{2D-3D}}\}$, can then be defined as,

$$\mu^{\text{HVEL}}(i) = \begin{cases} \varepsilon^{\text{HVEL}}(i), & i \in \mathcal{N}^{\text{2D}} - \mathcal{I}^{\text{2D}}, \\ \varepsilon^{\text{HVEL}}(i), & i \in \mathcal{N}^{\text{3D}} - \mathcal{I}^{\text{3D}}, \\ \varepsilon^{\text{HVEL}}(i), & i \in \mathcal{I}^{\text{2D}}, \\ \varepsilon^{\text{HVEL}}\left(\xi^{\text{HVEL}}(i)\right), & i \in \mathcal{I}^{\text{3D}}. \end{cases} \tag{3.10}$$

Likewise, for the WVEL mask vector, a different WVEL equation map is first defined, $\varepsilon^{\text{WVEL}} : (\mathcal{N}_{\text{s}}^{\text{2D}} - \mathcal{I}_{\text{s}}^{\text{2D}}) \cup (\mathcal{N}_{\text{b}}^{\text{2D}} - \mathcal{I}_{\text{b}}^{\text{2D}}) \cup \mathcal{N}^{\text{3D}} \to \{1, 2, \ldots, 2|\mathcal{N}^{\text{2D}} - \mathcal{I}^{\text{2D}}| + |\mathcal{N}^{\text{3D}}|\})$, which maps all nodes in the 3D submodel and all non-interface nodes in the (hypothetically different) 2D submodels for the surface and the bed to distinct numbers from 1 to $\mathcal{N}_{\text{eff}}^{\text{2D-3D}}$, given by (3.9). Like $\varepsilon^{\text{HVEL}}$, the map $\varepsilon^{\text{WVEL}}$ is also not unique, but any choice is a bijection by construction. Next, $\xi^{\text{WVEL}} : (\mathcal{I}_{\text{s}}^{\text{2D}} \cup \mathcal{I}_{\text{b}}^{\text{2D}}) \to \mathcal{I}^{\text{3D}}$ is defined, which maps the 2D interface surface and bed nodes to the 3D interface surface and bed nodes, respectively. The WVEL

mask vector, $\mu^{\text{WVEL}} : \mathcal{N}^{\text{2D}} \cup \mathcal{N}^{\text{3D}} \rightarrow \{1, 2, \ldots, N_{\text{eff}}^{\text{2D-3D}}\}$, can then be defined as,

$$\mu^{\text{WVEL}}(i) = \begin{cases} \varepsilon^{\text{WVEL}}(i), & i \in \mathcal{N}_{\text{s}}^{\text{2D}} - \mathcal{I}_{\text{s}}^{\text{2D}}, \\ \varepsilon^{\text{WVEL}}(i), & i \in \mathcal{N}_{\text{b}}^{\text{2D}} - \mathcal{I}_{\text{b}}^{\text{2D}}, \\ \varepsilon^{\text{WVEL}}(i), & i \in \mathcal{N}^{\text{3D}} - \mathcal{I}^{\text{3D}}, \\ \varepsilon^{\text{WVEL}}\left(\xi^{\text{WVEL}}(i)\right), & i \in \mathcal{I}_{\text{s}}^{\text{2D}}, \\ \varepsilon^{\text{WVEL}}\left(\xi^{\text{WVEL}}(i)\right), & i \in \mathcal{I}_{\text{b}}^{\text{2D}}, \\ \varepsilon^{\text{WVEL}}(i), & i \in \mathcal{I}^{\text{3D}}. \end{cases} \tag{3.11}$$

With these masks in place, all the residual and Jacobian contributions, and solution accesses pass through the mask vector, resulting in a correctly built monolithic system of equations (2.14). In the coupled HVEL and transport stages, calling the 2D and 3D model functions in a loop in any order to build the system of equations automatically results in a correctly built monolithic system. For the coupled WVEL stage, however, the following slightly different steps are carried out.

1. Only the 3D model(s) are called first to assemble their contributions into the system of equations. Once all the 3D models have assembled their contributions, the interface node contributions are all zeroed out.

2. All the 2D models are then called to assemble their contributions into the system of equations according to (2.23).

3. The contributions of the 3D model surface and bed nodes are reassembled into the system of equations using the weak form of the kinematic BCs on the surface and bed, on the lines of the 2D WVEL equations (2.23).

4. The contributions of all the 3D interface nodes between the surface and bed (exclusive) are assembled into the system of equations after relevant manipulations to (3.5).

3.7 A note on 2D-2D and 3D-3D strong coupling

The theory for 2D-3D conforming strong coupling can be modified appropriately for non-overlapping 2D-2D and 3D-3D conforming strong coupling as well. Once again, conformity requires the interface nodes and edges to be aligned in case of 2D-2D coupling, and the interface nodes and faces to be aligned in case of 3D-3D coupling. The trial and test spaces for 2D-2D and 3D-3D coupled models then happen to be exactly the same as the full-2D and full-3D counterparts, where full-2D model is one obtained by taking the union of the two 2D models, and the full-3D model is created by taking the union of the two 3D models. 2D-2D and 3D-3D strong coupling are nothing but the usual 2D and 3D finite element method in disguise. Strong 2D-3D coupling in a conforming framework can be thought of as a generalization of the usual finite element method for mixed dimension models. Although there seems no benefit in implementing 2D-2D and 3D-3D coupling, these are obtained practically for free when implementing 2D-3D coupling, and more importantly, they are an intermediate step in the verification of the coupling methodology, explained in the next chapter.

Chapter 4

Verification of 2D-3D coupling

Verification is an important step in the development of any scientific software. It ensures that the theory has been correctly implemented in a computer code. For the finite element method, verification involves comparison of finite element solutions against analytic ones where available, comparing spatial and temporal convergence rates with theoretical estimates, and so on. Particularly in case of 2D-3D coupling, one of the first steps to confirm the correctness of the method and its code implementation would be to compare 2D-2D and 3D-3D strong coupling solutions with those of full-2D and full-3D models. This allows verifying that the coupling approach is agnostic and that the code modules relevant to coupling are working properly. Since 2D-2D and 3D-3D coupled models are equivalent to full-2D and full-3D models, the node numbering in the models can be done in a manner that ensures that for even the most general simulations, the system of equations generated by the 2D-2D and 3D-3D coupled systems respectively matches those of the full-2D and full-3D models to near machine precision. In such a case, the solutions must also match for all time steps to machine precision. It was verified that the code satisfied the above criteria. The results for 2D-2D and 3D-3D strong coupling have not been presented, however, since no new information is obtained.

The second stage in verification of 2D-3D coupled models is comparing their results to their full-2D and full-3D counterparts (or equivalently, 2D-2D and 3D-3D coupled counterparts), keeping the common parameters between all the models the same wherever possible. For test cases in which a full-2D model would generally suffice, it is expected that the solution of full-3D and 2D-3D coupled models would be similar to (and possibly lie 'between') that of full-2D and full-3D models. Verifying this would be in support of the claim that 2D-3D coupling is a generalization of the finite element method for mixed dimension grids.

To that end, four verification test cases that include the results of full-2D, 2D-3D coupled, and full-3D models are presented, viz., small- and large-amplitude slosh, baroclinic flume, and baroclinic lock-exchange. For the slosh test cases, the analytical solution for the linearized shallow water equations for small-amplitude case is known. For the flume test case, the steady state solution is known. The lock-exchange test case is a part-verification, part-validation test case. The flume and lock-exchange test cases also help in observing the behavior of baroclinicity in the vicinity of the 2D-3D interface. Although section 3.2.1 recommends that the 2D-3D interface be placed in a region far away from baroclinicity, it may not always be possible to do so in practical scenarios. Understanding the effect of baroclinicity near 2D-3D interfaces is therefore important, which is why the baroclinic flume and lock-exchange test cases have been included. Past work on 2D-3D strong coupling [20], which did not include transport coupling and had problems in the

coupled WVEL stage, presented results of a simple flume test case and the small-amplitude slosh test case. The simple flume test case has not been repeated herein for brevity, but the slosh test case is revisited, and extensive analysis is performed on it herein, which was not done in [20]. The test cases and results are described in the following sections.

4.1 Small-amplitude slosh test case

Conservation, accuracy, and convergence are important considerations for any FEM-based code. A detailed analysis of the spatial and temporal convergence rates of 2D, 3D, and 2D-3D coupled models is given this section. Mass conservation across the 2D-3D interface is tested for the 2D-3D coupled model.

In the small-amplitude slosh test case, water is filled in a rectangular domain given by $\Omega = (0, L) \times (0, W)$, where the length L and width W are 25.6 km, 6.4 km, respectively, as shown in Figure 4.1 later in section 4.1.3. The bed elevation is $b(x, y) = -H = -82.5\,\text{m}$, and the at-rest water depth is H, corresponding to a water surface elevation of 0 m. Density is constant at $990\,\text{kg/m}^3$ throughout the domain, and the total volume of fluid contained in the domain is $L \times W \times H = 13.5168\,\text{km}^3$. The boundary conditions specified on all vertical boundaries are no-normal-flow, i.e., $\boldsymbol{u} \cdot \boldsymbol{n} = 0$. The water is initially at rest throughout the domain. An initial condition on the depth is specified, given by,

$$h(x, y, 0) = H + a\cos(\pi x/L), \tag{4.1}$$

which is an east-west varying perturbation in the form of a cosine wave of amplitude $a = 0.01\,\mathrm{m}$ and wavelength $2L$. There is no viscosity, bottom friction, wind, or air pressure. Under these conditions, the 2D SWE (2.6)–(2.8) are simplified to,

$$\begin{aligned} \frac{\partial h}{\partial t} + \frac{\partial h\bar{u}}{\partial x} + \frac{\partial h\bar{v}}{\partial y} &= 0, \\ \frac{\partial h\bar{u}}{\partial t} + \frac{\partial h\bar{u}\bar{u}}{\partial x} + \frac{\partial h\bar{v}\bar{u}}{\partial y} + \frac{\partial}{\partial x}\left(\frac{1}{2}gh^2\right) &= 0, \\ \frac{\partial h\bar{u}}{\partial t} + \frac{\partial h\bar{v}\bar{u}}{\partial x} + \frac{\partial h\bar{v}\bar{v}}{\partial y} + \frac{\partial}{\partial y}\left(\frac{1}{2}gh^2\right) &= 0, \end{aligned} \tag{4.2}$$

and the 3D SWE (2.1)–(2.4) reduce to,

$$\begin{aligned} \frac{\partial u}{\partial x} + \frac{\partial v}{\partial y} + \frac{\partial w}{\partial z} &= 0, \\ \frac{\partial u}{\partial t} + u\frac{\partial u}{\partial x} + v\frac{\partial u}{\partial y} + w\frac{\partial u}{\partial z} + \frac{1}{\rho_0}\frac{\partial p}{\partial x} &= 0, \\ \frac{\partial v}{\partial t} + u\frac{\partial v}{\partial x} + v\frac{\partial v}{\partial y} + w\frac{\partial v}{\partial z} + \frac{1}{\rho_0}\frac{\partial p}{\partial y} &= 0, \\ p &= \rho_0 g(\eta - z) \end{aligned} \tag{4.3}$$

The analytical solution to the above equations is unknown in most cases, including this one. However, the analytical solution for linearized SWE with advection terms neglected is available. Small perturbations are assumed when linearizing the SWE about the steady state solution ($h = H, \boldsymbol{u} = \mathbf{0}$). The linearized 2D SWE are given by,

$$\begin{aligned} \frac{\partial h}{\partial t} + H\frac{\partial \bar{u}}{\partial x} + H\frac{\partial \bar{v}}{\partial y} &= 0, \\ \frac{\partial \bar{u}}{\partial t} + g\frac{\partial h}{\partial x} &= 0, \\ \frac{\partial \bar{v}}{\partial t} + g\frac{\partial h}{\partial y} &= 0, \end{aligned} \tag{4.4}$$

and the linearized 3D SWE are given by,

$$\begin{aligned} \frac{\partial u}{\partial x} + \frac{\partial v}{\partial y} + \frac{\partial w}{\partial z} &= 0, \\ \frac{\partial u}{\partial t} + g\frac{\partial h}{\partial x} &= 0, \\ \frac{\partial v}{\partial t} + g\frac{\partial h}{\partial y} &= 0. \end{aligned} \tag{4.5}$$

The boundary conditions on the surface (2.5a) and the bed (2.5b) must also be linearized, and are given by,

$$\begin{aligned} \frac{\partial \eta}{\partial t} - w(x, y, \eta, t) &= 0, \\ - w(x, y, b, t) &= 0. \end{aligned} \tag{4.6}$$

The 2D as well as 3D linearized systems (4.4)–(4.6) have the same analytical solution,

$$\begin{aligned} h^{lin}(x, y, t) &= H + a\cos\left(\frac{\pi}{L}x\right)\cos\left(\frac{\pi\sqrt{gH}}{L}t\right), \\ u^{lin}(x, y, z, t) &= \frac{a\sqrt{gH}}{H}\sin\left(\frac{\pi}{L}x\right)\sin\left(\frac{\pi\sqrt{gH}}{L}t\right), \\ v^{lin}(x, y, z, t) &= 0, \\ w^{lin}(x, y, z, t) &= -\left(\frac{a\pi\sqrt{gH}}{L}\right)\left(\frac{z-b}{H}\right)\cos\left(\frac{\pi}{L}x\right)\sin\left(\frac{\pi\sqrt{gH}}{L}t\right), \end{aligned} \tag{4.7}$$

as given in [95], which can be verified by substituting (4.7) in (4.4)–(4.6). Note that the above analytical solution (4.7) is not the analytical solution to the full nonlinear SWE, (4.2) and (4.3), that are effectively being solved herein, which can also be verified by substituting (4.7) in (4.2) and (4.3). Assuming that the FE method used converges to the true solution upon mesh refinement and time step reduction, the finite element solution of a model

with sufficiently small mesh size and time step can be considered to be an approximation to the unknown analytical solution of the full nonlinear SWE. In this case, the solution of the finest mesh with the smallest time step is used as an approximation. Hereafter, the unknown analytical solution of the full nonlinear SWE (4.2) and (4.3) is referred to as the 'true solution', the finest mesh, smallest time step FE solution is called the 'approximate true solution', the solution (4.7) to the linearized SWE is the 'analytical solution', and any other mesh/time step solution is referred to as a 'finite element (FE) solution', in order to distinguish between them. The true, approximate true, analytical, and FE solutions are denoted by $\boldsymbol{s} = (h, \boldsymbol{u})$, $\tilde{\boldsymbol{s}} = (\tilde{h}, \tilde{\boldsymbol{u}})$, $\boldsymbol{s}^{lin} = (h^{lin}, \boldsymbol{u}^{lin})$, and $\boldsymbol{s}^{\hbar} = (h^{\hbar}, \boldsymbol{u}^{\hbar})$, respectively.

4.1.1 Error definitions

In order to analyze the error plots and convergence results, additional terminology is introduced. The temporally varying spatial L^2 norm for a scalar $f = f(\boldsymbol{x}, t)$ and a vector $\boldsymbol{v} = \boldsymbol{v}(\boldsymbol{x}, t)$ is defined as,

$$\begin{aligned} \|f\|^2(t) &= \int_{\Omega} f^2 \, d\Omega, \\ \|\boldsymbol{v}\|^2(t) &= \int_{\Omega} (\boldsymbol{v} \cdot \boldsymbol{v}) \, d\Omega. \end{aligned} \tag{4.8}$$

The FE solution errors are defined as,

$$\boldsymbol{e}^{\hbar} = \{e_h^{\hbar} \ , \boldsymbol{e}_{\boldsymbol{u}}^{\hbar} \ \} = \{h - h^{\hbar} \ , \boldsymbol{u} - \boldsymbol{u}^{\hbar} \ \} = \boldsymbol{s} - \boldsymbol{s}^{\hbar}, \tag{4.9a}$$

$$\boldsymbol{e}^{lin,\hbar} = \{e_h^{lin,\hbar}, \boldsymbol{e}_{\boldsymbol{u}}^{lin,\hbar}\} = \{h^{lin} - h^{\hbar}, \boldsymbol{u}^{lin} - \boldsymbol{u}^{\hbar}\} = \boldsymbol{s}^{lin} - \boldsymbol{s}^{\hbar}, \tag{4.9b}$$

$$\tilde{\boldsymbol{e}}^{\hbar} = \{\tilde{e}_h^{\hbar} \ , \tilde{\boldsymbol{e}}_{\boldsymbol{u}}^{\hbar} \ \} = \{\tilde{h} - h^{\hbar} \ , \tilde{\boldsymbol{u}} - \boldsymbol{u}^{\hbar} \ \} = \tilde{\boldsymbol{s}} - \boldsymbol{s}^{\hbar}, \tag{4.9c}$$

and it is noted that these functions depend on $\hbar$ and Δt. On the other hand, the (unknown) method-, $\hbar$- and Δt-independent difference between the true and analytical solutions is defined as,

$$\boldsymbol{e}^{lin} = \{e_h^{lin} \ , \boldsymbol{e}_{\boldsymbol{u}}^{lin} \ \} = \{h - h^{lin} \ , \boldsymbol{u} - \boldsymbol{u}^{lin} \ \} = \boldsymbol{s} - \boldsymbol{s}^{lin}. \tag{4.9d}$$

Although the approximate true solution $\tilde{\boldsymbol{s}}$ depends on the mesh and time step sizes, it can be considered as $\hbar$- and Δt-independent for a sufficiently fine mesh using a sufficiently small time step. Therefore, the error between the true solution and the approximate true solution is defined as,

$$\tilde{\boldsymbol{e}} = \{\tilde{e}_h \ , \tilde{\boldsymbol{e}}_{\boldsymbol{u}} \ \} = \{h - \tilde{h} \ , \boldsymbol{u} - \tilde{\boldsymbol{u}} \ \} = \boldsymbol{s} - \tilde{\boldsymbol{s}}, \tag{4.9e}$$

and is treated as if it is $\hbar$- and Δt-independent. Lastly, the error (4.9d) between the analytical solution and the true solution can be approximated using the error between the approximate true solution and the analytical solution, defined as,

$$\tilde{\boldsymbol{e}}^{lin} = \{\tilde{e}_h^{lin} \ , \tilde{\boldsymbol{e}}_{\boldsymbol{u}}^{lin} \ \} = \{\tilde{h} - h^{lin} \ , \tilde{\boldsymbol{u}} - \boldsymbol{u}^{lin} \ \} = \tilde{\boldsymbol{s}} - \boldsymbol{s}^{lin}. \tag{4.9f}$$

In general, convergence behavior should be analyzed by calculating $\boldsymbol{e}^{\hbar}$, which is unknown in this case since the true solution $\boldsymbol{s}$ is unknown. The

quantities that can be calculated are $\boldsymbol{e}^{lin,\hbar}$, $\tilde{\boldsymbol{e}}^{\hbar}$, and $\tilde{\boldsymbol{e}}^{lin}$. $\boldsymbol{e}^{lin,\hbar}$ and $\tilde{\boldsymbol{e}}^{\hbar}$ are approximations to $\boldsymbol{e}^{\hbar}$, whereas $\tilde{\boldsymbol{e}}^{lin}$ approximates $\boldsymbol{e}^{lin}$, as is explained later. For both temporal and spatial convergence analyses, the maximum-over-time values of the calculable L^2 errors are defined as,

$$\begin{aligned} E_h^{lin,\hbar} &= \max_{t\in[0,T]} \|e_h^{lin,\hbar}\|, \qquad \tilde{E}_h^{\hbar} = \max_{t\in[0,T]} \|\tilde{e}_h^{\hbar}\|, \qquad \tilde{E}_h^{lin} = \max_{t\in[0,T]} \|\tilde{e}_h^{lin}\|, \\ E_{\boldsymbol{u}}^{lin,\hbar} &= \max_{t\in[0,T]} \|\boldsymbol{e}_{\boldsymbol{u}}^{lin,\hbar}\|, \qquad \tilde{E}_{\boldsymbol{u}}^{\hbar} = \max_{t\in[0,T]} \|\tilde{\boldsymbol{e}}_{\boldsymbol{u}}^{\hbar}\|, \qquad \tilde{E}_{\boldsymbol{u}}^{lin} = \max_{t\in[0,T]} \|\tilde{\boldsymbol{e}}_{\boldsymbol{u}}^{lin}\|. \end{aligned} \tag{4.10}$$

Instead of performing the exact integration in (4.8) to calculate the L^2 norm of errors, the root mean square (RMS) value is used, which is an approximation to the L^2 norm up to a constant multiplier dependent upon the area and volume of the 2D and 3D domains, respectively. The integral can be approximated by using the simplest Gauss-Lobatto quadrature rule for integrating linear polynomials, given by,

$$\int_{\Omega^{\mathrm{el}}} f \, d\Omega^{\mathrm{el}} = (f_1 + f_2 + f_3)|\Omega^{\mathrm{el}}|/3,$$

For example, in case of the uniform, structured, 2D triangular meshes used in this test case with each interior node attached to 6 elements as shown in Figure 4.1 later in section 4.1.3, the integral can be estimated as,

$$\begin{aligned} \|f\|_{L^2}^2 = \int_{\Omega} |f|^2 \, d\Omega &\approx \sum_{\Omega^{\mathrm{el}}} \frac{|\Omega^{\mathrm{el}}|}{3} \left(|f_1^{\mathrm{el}}|^2 + |f_2^{\mathrm{el}}|^2 + |f_3^{\mathrm{el}}|^2\right) \\ &\approx \left(6 \sum_{i=1}^{N} |f_i|^2\right) \frac{|\Omega^{\mathrm{el}}|}{3} = \sum_{i=1}^{N} |f_i|^2 (2|\Omega^{\mathrm{el}}|) = \sum_{i=1}^{N} |f_i|^2 \left(\frac{2|\Omega|}{M}\right) \\ &\approx |\Omega| \left(\sum_{i=1}^{N} \frac{|f_i|^2}{N}\right). \end{aligned} \tag{4.11}$$

Here, $|\Omega^{\text{el}}|$ and $|\Omega|$ are the element and domain areas, and M and N are respectively the number of elements and nodes (with $M \approx 2N$). Note that the boundary errors, introduced by assuming that each node is attached to 6 elements even at the boundary instead of just the interior, have been ignored when bringing in the factor of 6 in the above steps. Thus, from (4.11), it is seen that,

$$\|f\|_{L^2} \approx |\Omega|^{1/2} \left(\sum_{i=1}^{N} \frac{|f_i|^2}{N} \right)^{1/2} = |\Omega|^{1/2} \text{RMS}(f). \tag{4.12}$$

The $|\Omega|^{1/2}$ factor does not matter for getting the convergence rates, so the RMS error (RMSE) suffices for analysis. With this notation in place, the behavior of errors and simulation results are analyzed in the following sections.

4.1.2 Convergence behavior of errors

The optimal convergence rate of the L^2 norm of the error $\boldsymbol{e}^h$ at the final time for parabolic equations for the case of piecewise linear polynomials and second order time stepping is $\mathcal{O}(h^2 + \Delta t^2)$ [96], i.e., second order in space and time in general. The spatial convergence rate in H^1 norm for SUPG FEM applied to SWE is first order [23], but the error estimate in the L^2 norm for SUPG FEM applied to SWE appears to be unexplored in literature. The convergence rate for SUPG FEM applied to the advection-dominated case of the advection-diffusion equation, using continuous, piecewise linear polynomials is 1.5 [4, 48, 65]. The optimal convergence rate in the L^2 norm for linear elements and second order time stepping is generally second order for

the finite element method, i.e.,

$$\begin{aligned} \|h - h^{\hbar}\|(T) &\leq C_1 \hbar^2 + C_2 \Delta t^2, \\ \|\boldsymbol{u} - \boldsymbol{u}^{\hbar}\|(T) &\leq C_3 \hbar^2 + C_4 \Delta t^2, \end{aligned} \tag{4.13}$$

where T is the final time, and C_1, C_2, C_3, and C_4 are constants independent of the mesh size $\hbar$ and time step Δt. Since $\boldsymbol{e}^{\hbar}$ is unknown here, convergence analysis must be performed using $\boldsymbol{e}^{lin,\hbar}$ and $\tilde{\boldsymbol{e}}^{\hbar}$ which can both be calculated. In the next two sections, the convergence behavior using $\boldsymbol{e}^{lin,\hbar}$ and $\tilde{\boldsymbol{e}}^{\hbar}$ is analyzed.

4.1.2.1 Using the analytical solution to linearized SWE

For coarse meshes with small time step size in case of spatial convergence analysis, and fine meshes with large time step size in case of temporal convergence analysis, $\boldsymbol{e}^{lin,\hbar}$ is a good approximation to $\boldsymbol{e}^{\hbar}$. Specifically, the approximation holds when the error $\|\boldsymbol{e}^{\hbar}\|$ dominates the error $\|\boldsymbol{e}^{lin}\|$, or in other words using their approximations, when $\|\boldsymbol{e}^{lin,\hbar}\| \gg \|\boldsymbol{e}^{lin}\| \approx \|\tilde{\boldsymbol{e}}^{lin}\|$. This is because,

$$\begin{aligned} \boldsymbol{e}^{\hbar} &= \boldsymbol{s} - \boldsymbol{s}^{\hbar} \\ &= \boldsymbol{s} - \boldsymbol{s}^{lin} + \boldsymbol{s}^{lin} - \boldsymbol{s}^{\hbar} \\ &= \boldsymbol{e}^{lin} + \boldsymbol{e}^{lin,\hbar} \\ &\approx \boldsymbol{e}^{lin,\hbar}, \quad \text{if } \|\boldsymbol{e}^{lin,\hbar}\| \gg \|\boldsymbol{e}^{lin}\|. \end{aligned}$$

Since $\boldsymbol{e}^{lin}$ is unknown, $\tilde{\boldsymbol{e}}^{lin}$ can be used as an approximation to $\boldsymbol{e}^{lin}$ for a sufficiently accurate $\tilde{\boldsymbol{s}}$, since

$$\begin{aligned}
\boldsymbol{e}^{lin} &= \boldsymbol{s} - \boldsymbol{s}^{lin} \\
&= \boldsymbol{s} - \tilde{\boldsymbol{s}} + \tilde{\boldsymbol{s}} - \boldsymbol{s}^{lin} \\
&= \tilde{\boldsymbol{e}} + \tilde{\boldsymbol{e}}^{lin} \\
&\to \tilde{\boldsymbol{e}}^{lin}, \quad \text{since } \tilde{\boldsymbol{e}} \to 0 \text{ as } (\hbar, \Delta t) \to 0.
\end{aligned}$$

On the other hand, $\boldsymbol{e}^{lin,\hbar}$ is not a good approximation to $\boldsymbol{e}^{\hbar}$ for sufficiently fine meshes with a small time step size, since $\boldsymbol{e}^{lin,\hbar} \to -\boldsymbol{e}^{lin}$ and $\boldsymbol{e}^{lin,\hbar} \nrightarrow \boldsymbol{e}^{\hbar}$. This is because $\boldsymbol{s}^{\hbar} \nrightarrow \boldsymbol{s}^{lin}$ and $\boldsymbol{s}^{\hbar} \to \boldsymbol{s} \implies \boldsymbol{e}^{\hbar} \to \boldsymbol{0}$ as $\hbar \to 0$, so that,

$$\begin{aligned}
\boldsymbol{e}^{lin,\hbar} &= \boldsymbol{s}^{lin} - \boldsymbol{s}^{\hbar} \\
&= \boldsymbol{s}^{lin} - \boldsymbol{s} + \boldsymbol{s} - \boldsymbol{s}^{\hbar} \\
&= -\boldsymbol{e}^{lin} + \boldsymbol{e}^{\hbar} \\
&\to -\boldsymbol{e}^{lin}, \quad \text{since } \boldsymbol{e}^{\hbar} \to 0 \text{ as } (\hbar, \Delta t) \to 0.
\end{aligned}$$

In the convergence plots, the expected behavior of $E_h^{lin,\hbar}$ and $E_{\boldsymbol{u}}^{lin,\hbar}$ is that convergence could possibly be seen initially for coarser meshes or larger time steps specifically if $\|\boldsymbol{e}^{lin,\hbar}\| \gg \|\tilde{\boldsymbol{e}}^{lin}\|$, which are both calculable. However, successive refinements leading to a sufficiently small mesh or time step size would result in those values becoming nearly a constant, given approximately by $\tilde{E}_h^{lin}$ and $\tilde{E}_{\boldsymbol{u}}^{lin}$, since $\boldsymbol{e}^{lin,\hbar} \to -\boldsymbol{e}^{lin} \to -\tilde{\boldsymbol{e}}^{lin}$. This is verified in the convergence plots for $E_h^{lin,\hbar}$ and $E_{\boldsymbol{u}}^{lin,\hbar}$ versus either $\hbar$ or Δt, given later. Thus, although an analytical solution is available, extracting the asymptotic spatial

or temporal convergence rates for the models using $\boldsymbol{e}^{lin,\hbar}$ as the approximation to the true error $\boldsymbol{e}^{\hbar}$ might not be straightforward as $\boldsymbol{s}^{\hbar} \nrightarrow \boldsymbol{s}^{lin} \implies \boldsymbol{e}^{lin,\hbar} \nrightarrow \boldsymbol{0}$ as $(\hbar, \Delta t) \to 0$. This is precisely the reason why further analysis using the approximate true solution $\tilde{\boldsymbol{s}}$ instead of the analytical solution $\boldsymbol{s}^{lin}$ becomes necessary.

4.1.2.2 Using the approximate true solution

Under the assumption that $\boldsymbol{s}^{\hbar} \to \boldsymbol{s}$, it is seen that $\tilde{\boldsymbol{e}}^{\hbar}$ is an approximation to $\boldsymbol{e}^{\hbar}$ for any mesh or time step size, so long as a sufficiently accurate approximate true solution $\tilde{\boldsymbol{s}}$ is chosen using small enough time step and mesh sizes for the calculation of $\tilde{\boldsymbol{e}}^{\hbar}$ in (4.9c). Specifically, this approximation holds when $\|\boldsymbol{e}^{\hbar}\|$ dominates $\|\tilde{\boldsymbol{e}}\|$, or in other words, when $\|\tilde{\boldsymbol{e}}^{\hbar}\| \gg \|\tilde{\boldsymbol{e}}\|$, since,

$$\begin{aligned}
\boldsymbol{e}^{\hbar} &= \boldsymbol{s} - \boldsymbol{s}^{\hbar} \\
&= \boldsymbol{s} - \tilde{\boldsymbol{s}} + \tilde{\boldsymbol{s}} - \boldsymbol{s}^{\hbar} \\
&= \tilde{\boldsymbol{e}} + \tilde{\boldsymbol{e}}^{\hbar} \\
&\approx \tilde{\boldsymbol{e}}^{\hbar}, \quad \text{if } \|\tilde{\boldsymbol{e}}^{\hbar}\| \gg \|\tilde{\boldsymbol{e}}\|.
\end{aligned}$$

Convergence guarantees that sufficiently small mesh and time step sizes can be used for choosing $\tilde{\boldsymbol{s}}$ arbitrarily close to the true solution $\boldsymbol{s}$, so that the errors of coarse meshes result in an error $\|\boldsymbol{e}^{\hbar}\| \approx \|\tilde{\boldsymbol{e}}^{\hbar}\| \gg \|\tilde{\boldsymbol{e}}\|$. However, how fine a mesh or how small a time step results in this condition is not straightforward to calculate. Moreover, unlike in the case of the analytical solution where the approximation $\tilde{\boldsymbol{e}}^{lin}$ to $\boldsymbol{e}^{lin}$ is straightforward to calculate,

the approximation to the unknown $\tilde{\boldsymbol{e}}$ is not available with any of the previously defined calculable errors. In this work, it was assumed that the finest mesh with the smallest time step satisfies the requirements for it to be considered as the approximate true solution. The results given in the following sections indicate that this may not be the case. It appears in this case that the errors of at least the second finest mesh should be excluded in obtaining spatial convergence rates, and those of the smallest and second smallest time steps should be excluded in obtaining the temporal convergence rates. This also relates to the above condition $\|\tilde{\boldsymbol{e}}^{\hbar}\| \gg \|\tilde{\boldsymbol{e}}\|$ required for $\|\tilde{\boldsymbol{e}}^{\hbar}\| \approx \|\boldsymbol{e}^{\hbar}\|$ to hold, which is likely invalidated if the mesh and time step sizes are close to those used for obtaining the approximate true solution $\tilde{\boldsymbol{s}}$. Lastly, since $\tilde{\boldsymbol{s}}$ can be chosen so that $\tilde{\boldsymbol{e}}^{\hbar}$ is an approximation to $\boldsymbol{e}^{\hbar}$, it is expected that the convergence plots using $\tilde{E}_h^{\hbar}$ and $\tilde{E}_{\boldsymbol{u}}^{\hbar}$ versus either $\hbar$ or Δt can be used to extract asymptotic convergence rates, unlike in the convergence plots of $E_h^{lin,\hbar}$ and $E_{\boldsymbol{u}}^{lin,\hbar}$ wherein the graphs flatten out to a constant.

4.1.3 Model parameters

The results of the 2D-3D coupled model are compared with equivalent full-2D and full-3D models defined in section 3.7. In the 2D-3D coupled model, the eastern model is the 3D model and the western model is the 2D model, with the 2D-3D interface located at $x = L/2 = 12.8\,\text{km}$. The total simulation time is set to 3 hours, corresponding to 6 oscillation cycles, since the time period of sinusoidal oscillations in the domain, according to the analyt-

ical solution (4.7) with $g = 9.81\,\mathrm{m/s^2}$ is $2L/\sqrt{gH} = 1799.7\,\mathrm{s}$, which is nearly 0.5 hours. Simulation output is written at 30 s intervals to preserve computer memory, since the solution output files with that interval are already over 2 gigabytes in size for the finest mesh. The error norm time series are calculated at these intervals. The approximate true solution $\tilde{\boldsymbol{s}}$ is set to be the FE solution of a model with mesh size 50 m and time step 1 s, which is the finest mesh and smallest time step chosen for this test case since the simulation run time for this model running on 10 processors in parallel is more than 2 days. For spatial convergence, the FE solutions $\boldsymbol{s}^{\hbar}$ of seven coarser meshes with horizontal node spacing $\hbar = \Delta x = \Delta y = \{6400, 3200, 1600, 800, 400, 200, 100\}\,\mathrm{m}$ are used. The full-2D, 2D-3D coupled, and full-3D meshes are shown in Figure 4.1 for the case of $\hbar = 1600\,\mathrm{m}$. In case of all 3D models, a single layer of elements is used in the vertical direction, and the meshes are refined only in the horizontal plane. For spatial convergence analysis, second order time stepping is used with a time step of 1 s determined after temporal convergence analysis in order to reduce time discretization errors. This means that the errors are predominantly due to mesh discretization according to (4.13), allowing the extraction of the spatial convergence rate. For temporal convergence, the second finest mesh ($\Delta x = \Delta y = 100\,\mathrm{m}$) is used, with time step sizes $\Delta t = \{30, 15, 10, 6, 3, 1\}\,\mathrm{s}$, so that time discretization errors dominate the mesh discretization errors, allowing extraction of temporal convergence rates. As explained in the previous section, however, for temporal convergence, it appears that for this test case, the results of simulations using 3 s and 1 s time

steps might need to be excluded for obtaining temporal convergence rates as the approximate true solution should have been obtained using an even smaller time step and finer mesh.

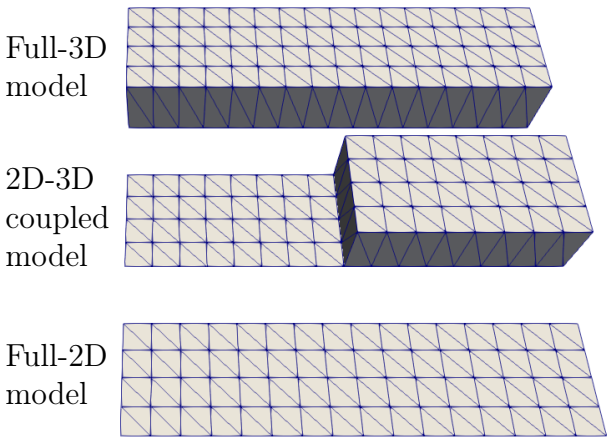

Figure 4.1: Slosh test case meshes, $\Delta x = \Delta y = 1600\,\mathrm{m}$ (scaled by a factor of 50 in the z direction).

For spatial convergence analysis, two sets of simulations are run, one excluding the SUPG terms, and one including the SUPG terms. For low amplitudes, the simulations excluding SUPG terms still run successfully without resulting in typical node-to-node oscillations usually seen in advection-dominated problems. The maximum-over-time errors with respect to the analytical and approximate true solutions, i.e., $\{E_h^{lin,\hbar}, E_{\boldsymbol{u}}^{lin,\hbar}\}$ and $\{\tilde{E}_h^{\hbar}, \tilde{E}_{\boldsymbol{u}}^{\hbar}\}$ are used for convergence analysis, and the units of the errors are dropped. Before proceeding with the convergence analysis, the maximum-over-time value of the error norm of the analytical solution with respect to the approximate true solution, $\tilde{E}_h^{lin}$ and $\tilde{E}_{\boldsymbol{u}}^{lin}$ are obtained. For full-2D, 2D-3D coupled and

full-3D model simulations, both with and without SUPG terms, $\tilde{E}_h^{lin}$ and $\tilde{E}_{\boldsymbol{u}}^{lin}$ are observed to be approximately $(1.4 \pm 0.2) \times 10^{-5}$ and $(5 \pm 1) \times 10^{-6}$, respectively. If $\tilde{\boldsymbol{s}}$ is sufficiently accurate, then it is expected that in both spatial as well as temporal convergence analyses respectively using a fine time step and fine mesh,

$$\begin{aligned} E_h^{lin,\hbar} &\to \tilde{E}_h^{lin} \approx (1.4 \pm 0.2) \times 10^{-5}, \\ E_{\boldsymbol{u}}^{lin,\hbar} &\to \tilde{E}_{\boldsymbol{u}}^{lin} \approx (5 \pm 1) \times 10^{-6}. \end{aligned} \tag{4.14}$$

Obviously, the above numbers only hold for the chosen parameters such as domain dimensions, perturbation amplitude, simulation duration, and so on.

4.1.4 Temporal convergence

For temporal convergence analysis, the errors $\boldsymbol{e}^{lin,\hbar}$ and $\tilde{\boldsymbol{e}}^{\hbar}$ of the finite element solutions $\boldsymbol{s}^{\hbar}$ of the second finest mesh of size 100 m and time steps $\Delta t = \{30, 15, 10, 6, 3, 1\}$ s are used. Figures 4.2 and 4.3 plot the RMS errors of depth and velocity versus time step for the full-2D, 2D-3D and full-3D models, with the top and bottom subfigures respectively corresponding to simulations excluding and including SUPG terms. The dashed lines in the figures correspond to errors with respect to $\boldsymbol{s}^{lin}$, and the solid lines are for comparison against $\tilde{\boldsymbol{s}}$. In case of comparison against the analytical solution $\boldsymbol{s}^{lin}$, the errors flatten out to the values given by (4.14) on time step refinement, as expected. Excluding two of the leftmost points in the figures for reasons explained in the section 4.1.2.2, the temporal convergence rate using comparison with $\tilde{\boldsymbol{s}}$ is seen to be second order as expected.

Note that temporal convergence rates should be extracted after en-

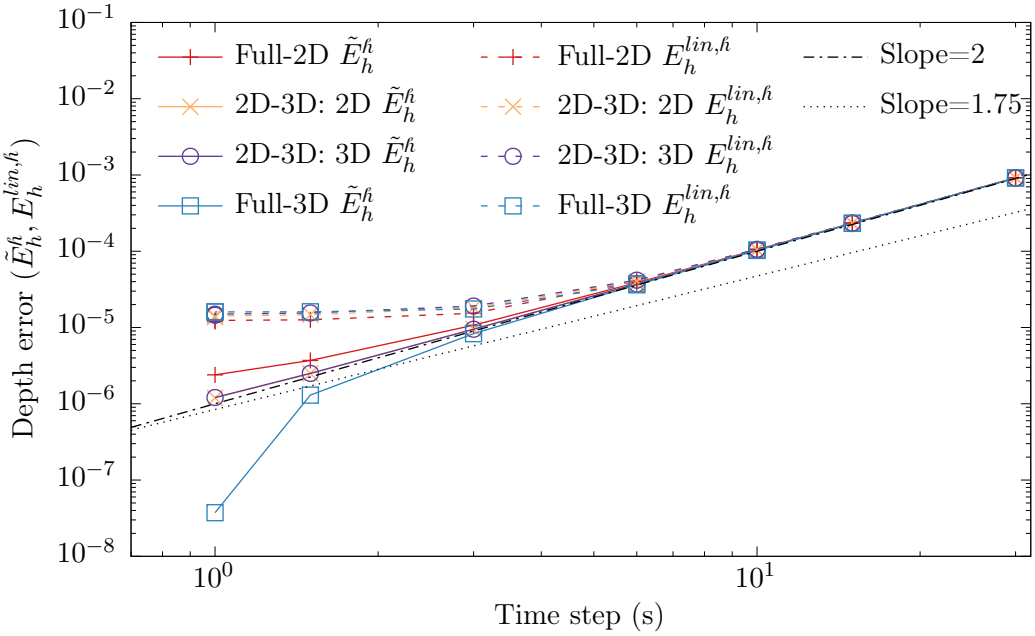

(a) Depth errors in simulations excluding SUPG terms

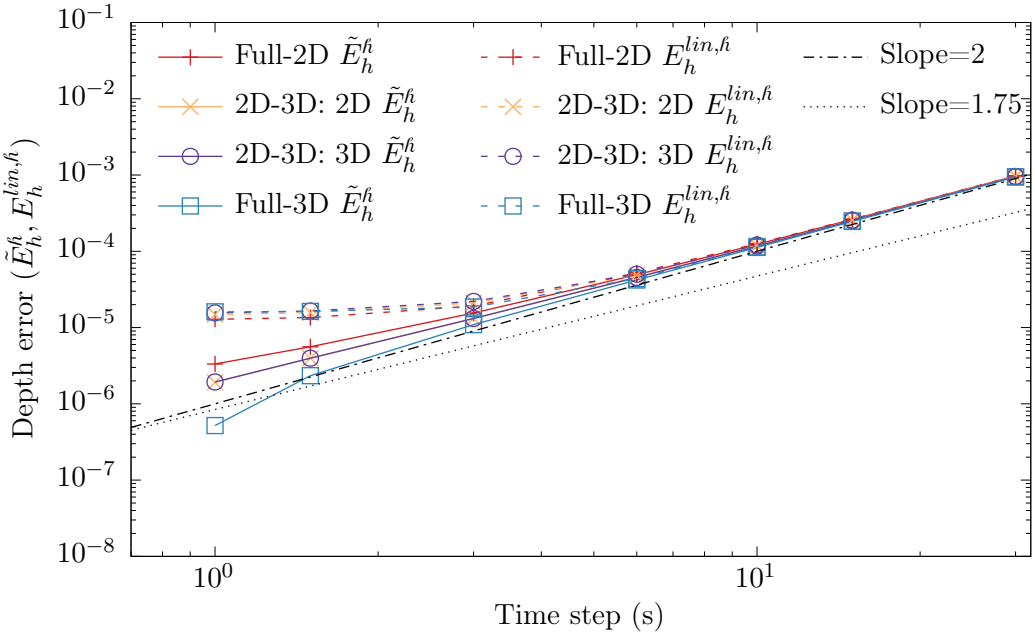

(b) Depth errors in simulations including SUPG terms

Figure 4.2: Small-amplitude slosh test: Temporal convergence of depth using mesh 7, $\hbar = 100\,\mathrm{m}$.

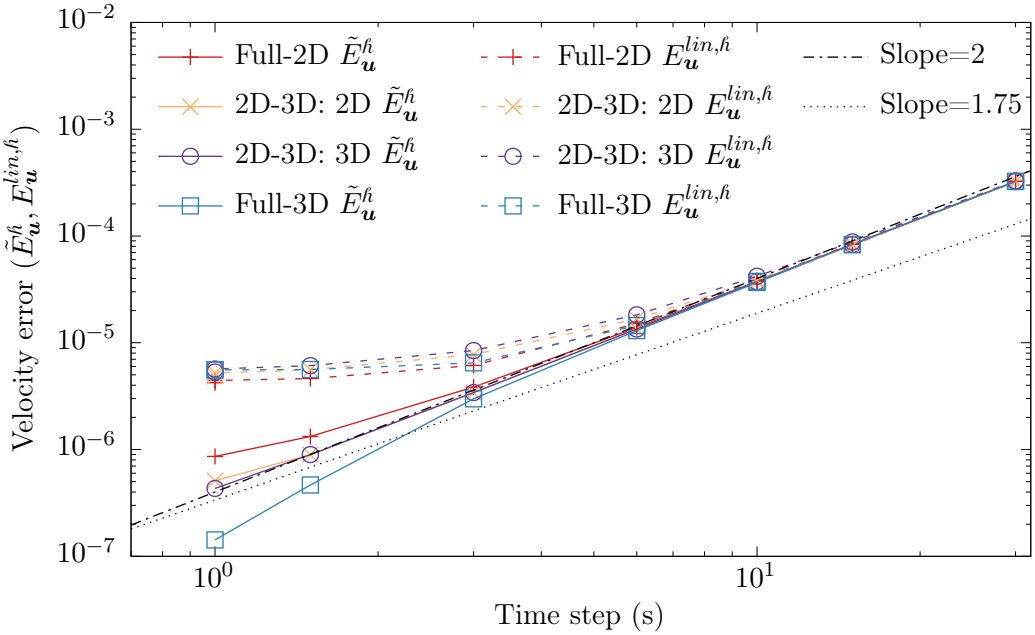

(a) Velocity errors in simulations excluding SUPG terms

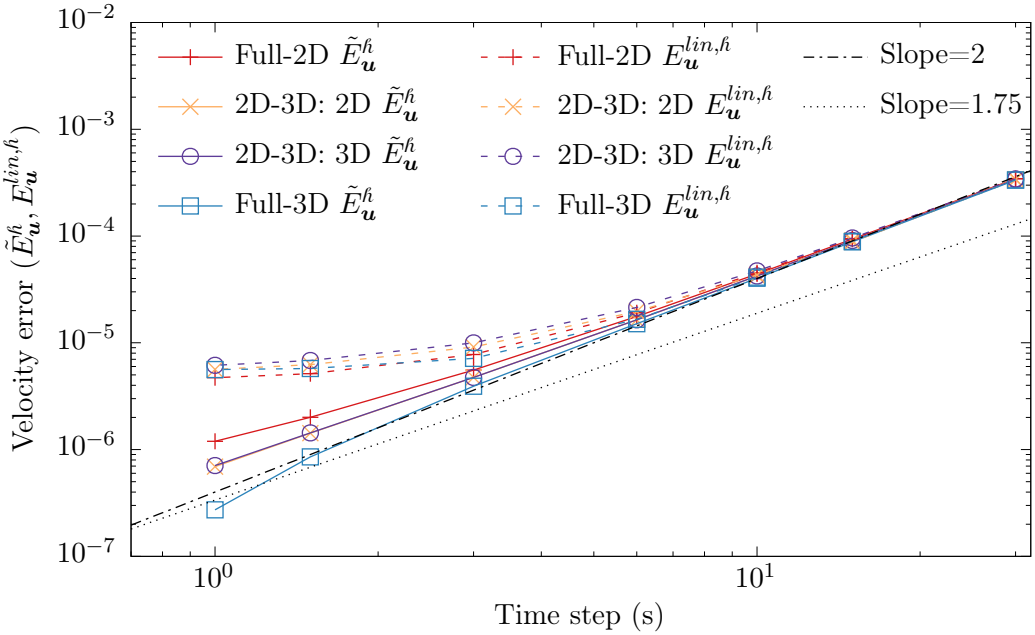

(b) Velocity errors in simulations including SUPG terms

Figure 4.3: Small-amplitude slosh test: Temporal convergence of velocity using mesh 7, $\hbar = 100\,\mathrm{m}$.

suring that the mesh discretization errors are small compared to time discretization errors. This means that a fine mesh should be used for temporal convergence analysis, since for coarse meshes, time step refinements beyond a certain limit result in no improvement in the accuracy due to dominating mesh discretization errors, as seen in Figures 4.4a and 4.4b, which show temporal convergence plots for the fourth mesh of size 800 m. The errors with respect to both the analytical as well as the approximate true solution are seen to flatten out, attributable to mesh discretization errors. In fact, the results of temporal convergence analysis should be used to determine the time step to be used for spatial convergence analysis. This is because the time step in spatial convergence analysis must be small enough so that mesh discretization errors dominate. From the figures, it is deduced that for a time step of 1 s, the mesh discretization errors dominate temporal ones in case of the fourth (and any coarser) mesh, so that this time step is sufficient for use in spatial convergence analysis at least for the coarser meshes. However, from Figures 4.2 and 4.3 for the seventh mesh, $\hbar = 100\,\mathrm{m}$, it is seen for the full-2D and 2D-3D coupled models that the mesh discretization errors are just beginning to become comparable with the time discretization errors, whereas in the full-3D model, the mesh discretization errors are either still insignificant in comparison, or that the approximate true solution needs improvement. In particular, the condition $\|\tilde{\boldsymbol{e}}^{\hbar}\| \gg \|\tilde{\boldsymbol{e}}\|$ required for $\|\boldsymbol{e}^{\hbar}\| \approx \|\tilde{\boldsymbol{e}}^{\hbar}\|$ to hold, as explained in section 4.1.2.2, is likely not satisfied, so that for the seventh mesh at least, $\tilde{\boldsymbol{e}}^{\hbar}$ may not be a reliable approximation to the true error $\boldsymbol{e}^{\hbar}$. Therefore, for the spatial conver-

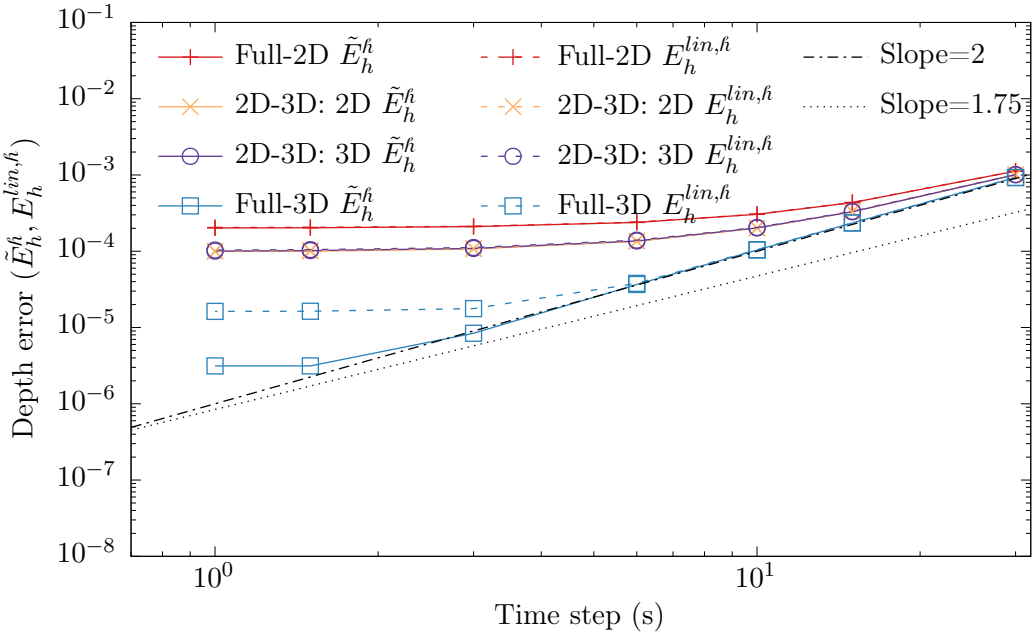

(a) Depth errors in simulations excluding SUPG terms

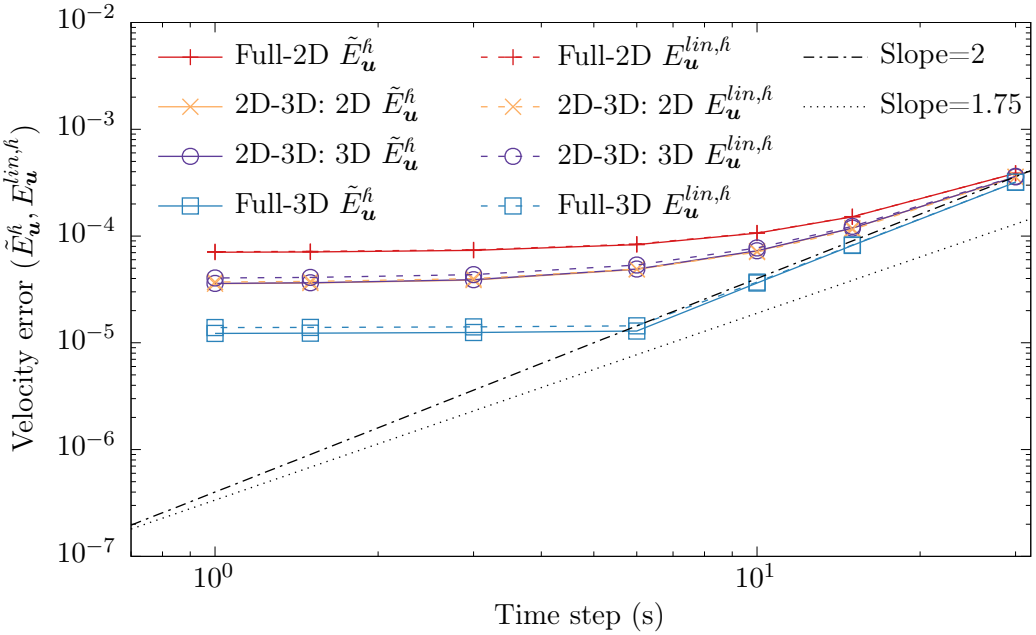

(b) Velocity errors in simulations excluding SUPG terms

Figure 4.4: Small-amplitude slosh test: Temporal convergence of depth (top) and velocity (bottom) using mesh 4, $\hbar = 800\,\mathrm{m}$, excluding SUPG terms.

gence results given in the next section, the rates obtained around the seventh mesh for a time step of 1 s are not representative of the true convergence rate for any of the models, but the results have still been presented for completeness. The slopes around the errors of the fourth mesh of size $\hbar = 800\,\mathrm{m}$ are taken to be representative of the expected asymptotic convergence rates. If a better approximate true solution would have been used, then the slopes around the errors of the finer meshes in the convergence plots would represent the asymptotic convergence rates. However, since the simulation time became prohibitively large, a finer mesh and a smaller time step required for a better approximate true solution were avoided.

4.1.5 Spatial convergence

In case of comparison with the approximate true solution corresponding to the mesh size 50 m and time step 1 s, the errors $\|\tilde{\boldsymbol{e}}^{\hbar}\|$ of seven meshes against the approximate true solution $\tilde{\boldsymbol{s}}$ are obtained and $\tilde{E}_h^{\hbar}$ and $\tilde{E}_{\boldsymbol{u}}^{\hbar}$ are calculated. For comparison with respect to the analytical solution to the linearized SWE (4.7), all eight meshes are used to calculate $E_h^{lin,\hbar}$, and $E_{\boldsymbol{u}}^{lin,\hbar}$, noting that for the eighth mesh with mesh size 50 m, these are respectively $\tilde{E}_h^{lin}$ and $\tilde{E}_{\boldsymbol{u}}^{lin}$ given by (4.14).

Spatial convergence plots for depth and velocity magnitude are shown in Figures 4.5 and 4.6, respectively. The dashed and solid lines in the figures respectively correspond to comparison with analytical and approximate true solutions, and the subfigures on the top and bottom respectively correspond

to simulations with SUPG terms excluded and included during simulations. Following are the observations from the four convergence plots:

- The errors of the 2D-3D coupled models are seen to lie between those of the full-2D and full-3D models for all mesh sizes.
- From Figures 4.5a and 4.6a for simulations excluding SUPG terms, the spatial convergence rates for all three models are observed to be second order for depth as well as velocity, with the exception of depth in the full-3D model which converges at an even higher rate of 2.5.
- From Figures 4.5b and 4.6b for simulations including SUPG terms, the spatial convergence rates for all three models are observed to be nearly second order for depth as well as velocity, with the exception of depth in case of the full-3D model. The convergence rate for depth in the full-3D model is initially seen to be 2.5 but drops to 1.5 from the fifth mesh onward ($\Delta x = \Delta y \leq 400\,\mathrm{m}$), even though the velocity maintains a second order convergence rate. Further analysis is required to determine the reason for this behavior, which has not been done in this work since full-3D models are not the focus herein. It is interesting, however, that the depth in the 2D-3D coupled model maintains a nearly second order convergence rate, even though the rate in the full-3D model is seen to drop to 1.5.

Next, the temporal variation of the error norms is considered. The time-varying depth errors for simulations excluding the SUPG terms are shown in

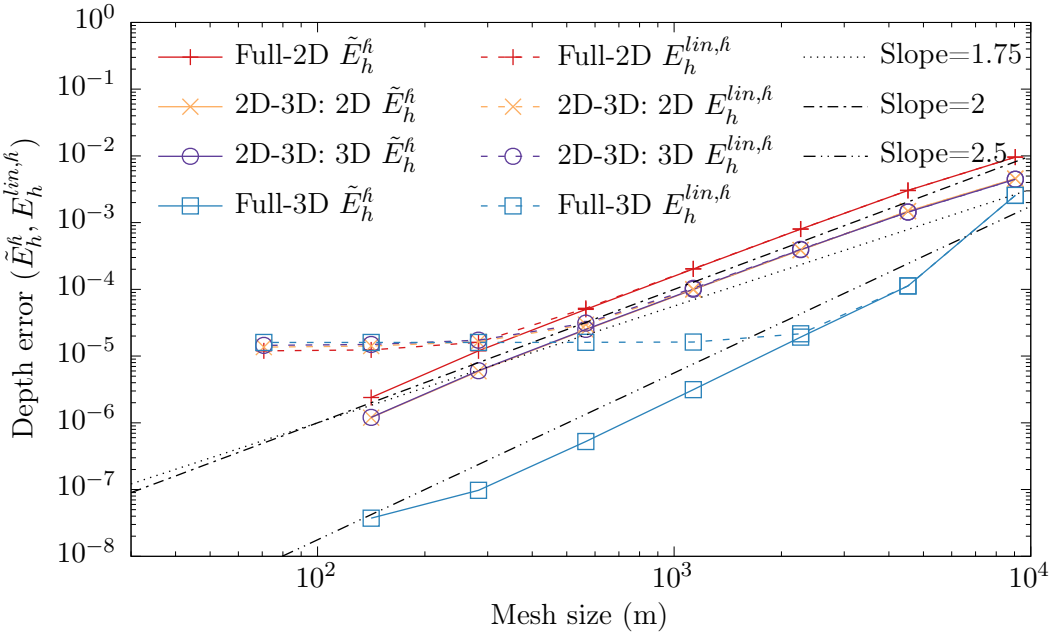

(a) Depth errors in simulations excluding SUPG terms

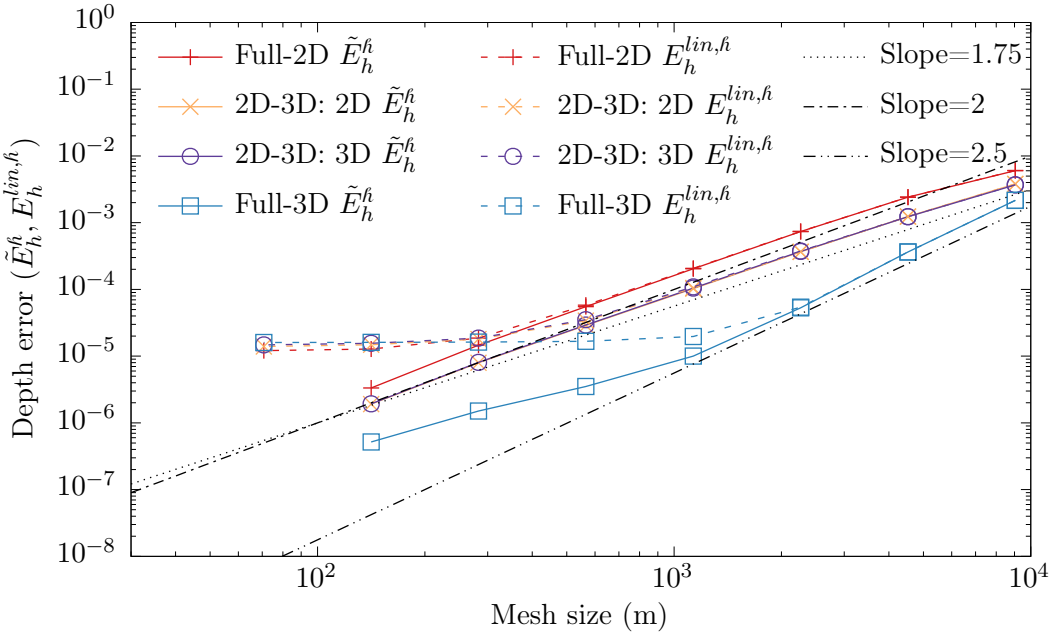

(b) Depth errors in simulations including SUPG terms

Figure 4.5: Small-amplitude slosh test: Spatial convergence of depth using $\Delta t = 1\,\mathrm{s}$.

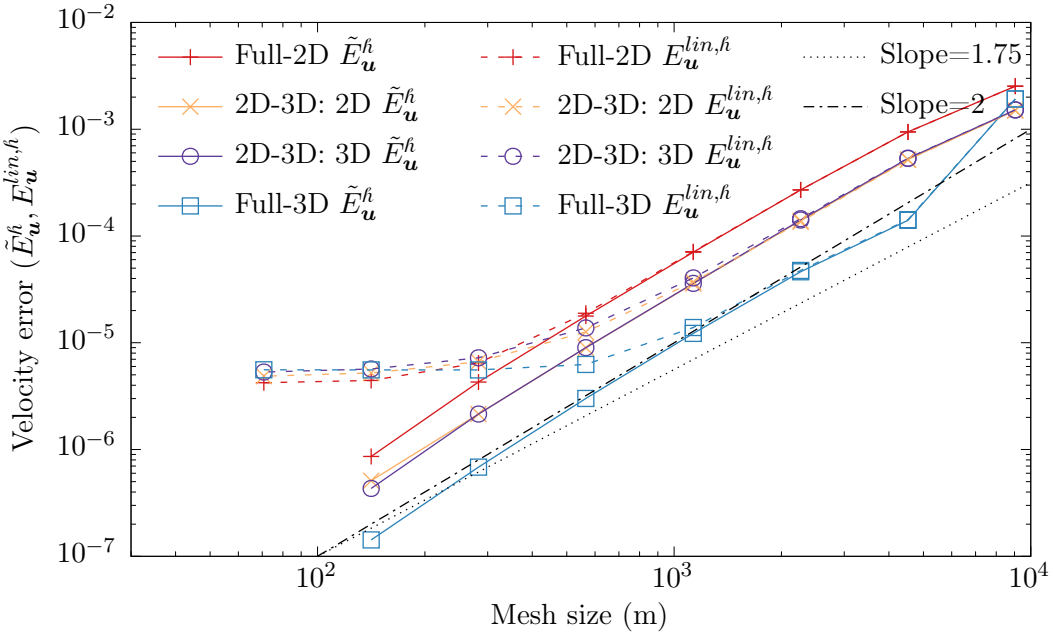

(a) Velocity errors in simulations excluding SUPG terms

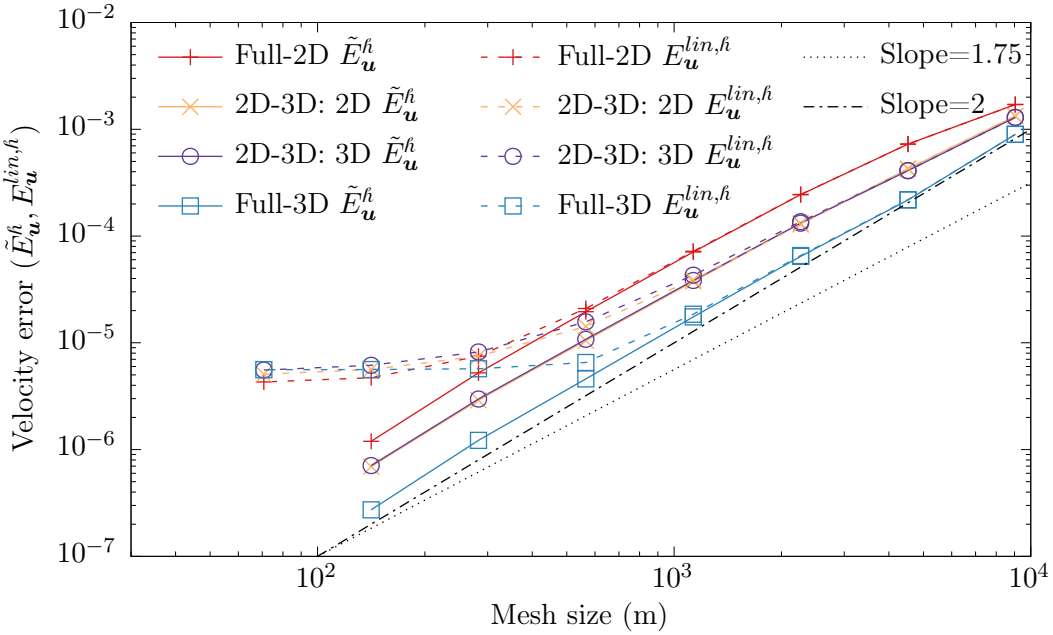

(b) Velocity errors in simulations including SUPG terms

Figure 4.6: Small-amplitude slosh test: Spatial convergence of velocity using $\Delta t = 1\,\mathrm{s}$.

Figure 4.7, and those for simulations including SUPG terms are shown in Figure 4.8. The velocity errors without and with SUPG terms are likewise shown in Figures 4.9 and 4.10. Each figure contains two subfigures that show error norm time series for the fourth and seventh meshes with mesh sizes 800 m and 100 m, respectively. Comparison against analytical as well as approximate true solutions is shown. It is evident from the top subfigures that the analytical solution is good enough to approximate the errors in case of coarse meshes, since the errors $\|\boldsymbol{e}^{lin,\hbar}\|$ and $\|\tilde{\boldsymbol{e}}^{\hbar}\|$ are nearly indistinguishable. It is also seen, as expected, that comparison with the analytical solution for finer meshes becomes misleading, since $\boldsymbol{s}^{\hbar} \nrightarrow \boldsymbol{s}^{lin}$ and $\boldsymbol{e}^{lin,\hbar} \to -\boldsymbol{e}^{lin}$, as explained in section 4.1.2.1. The error norms for the 2D-3D coupled models are seen to lie between the full-2D and full-3D models for most of the duration of the simulations in this case.

4.1.6 Solution behavior

Figures 4.11 to 4.13 show the comparison of surface elevation, x-velocity and surface z-velocity against the analytical solution along the length of the models for the third mesh, $\hbar = 1600$ m. The last 0.5 hours of the simulations are shown at 450 s intervals, corresponding to the final oscillation cycle. The x-velocity is depth-averaged in case of 2D submodels, and at the surface in case of 3D submodels. From the figures, it is seen that the results of all three models agree well with the analytical solution and each other, as expected from the convergence plots of the previous sections. The maximum amplitude of the x-

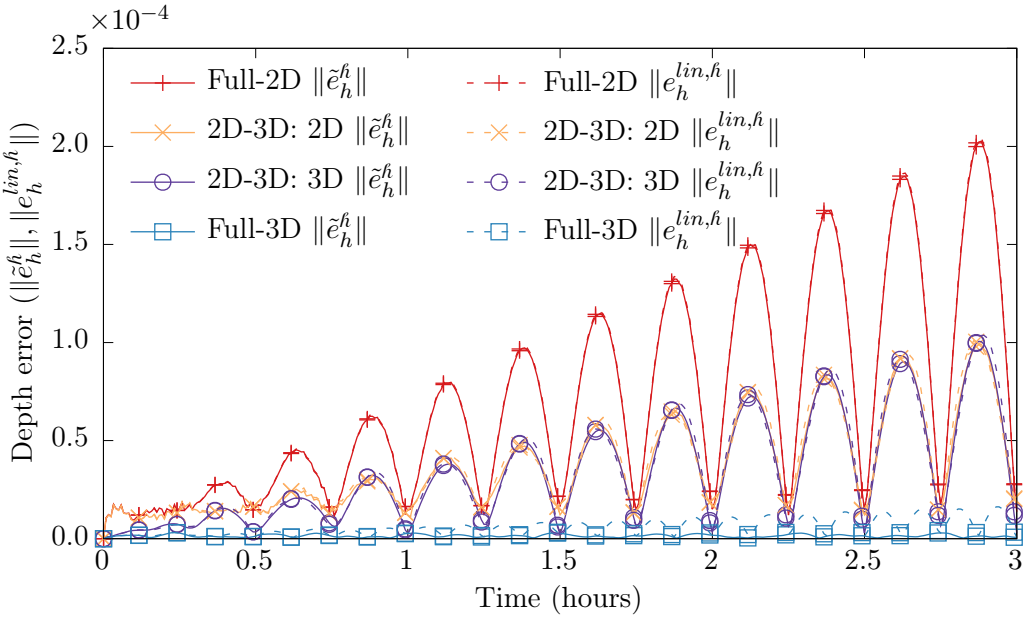

(a) Temporal variation of $\|e_h^{lin,\hbar}\|$ and $\|\tilde{e}_h^{\hbar}\|$ in mesh 4, $\hbar = 800\,\mathrm{m}$

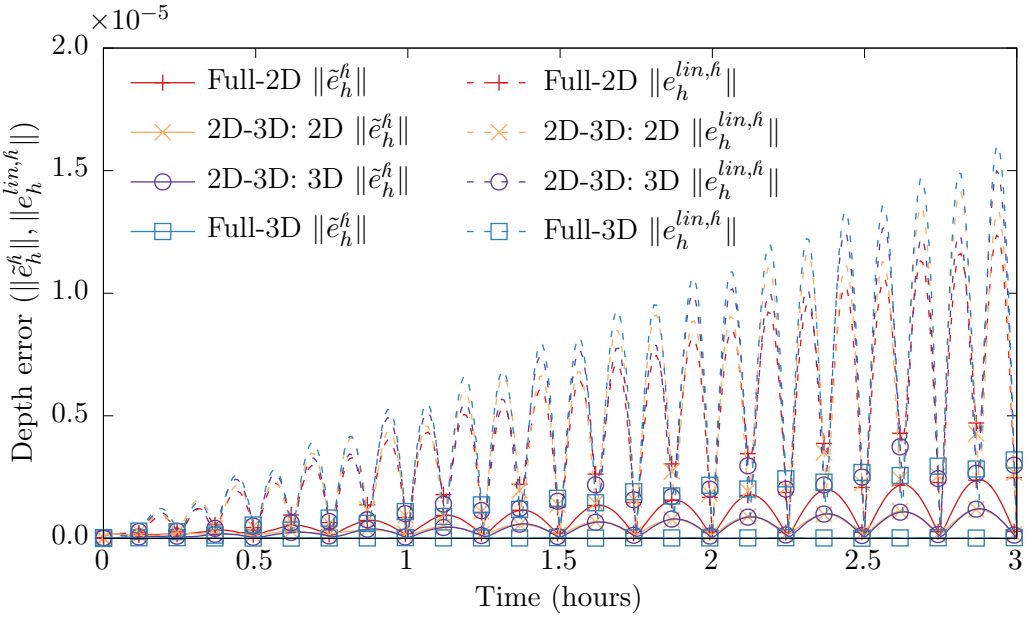

(b) Temporal variation of $\|e_h^{lin,\hbar}\|$ and $\|\tilde{e}_h^{\hbar}\|$ in mesh 7, $\hbar = 100\,\mathrm{m}$

Figure 4.7: Small-amplitude slosh test: Temporal variation of depth errors with SUPG terms excluded, using $\Delta t = 1\,\mathrm{s}$.

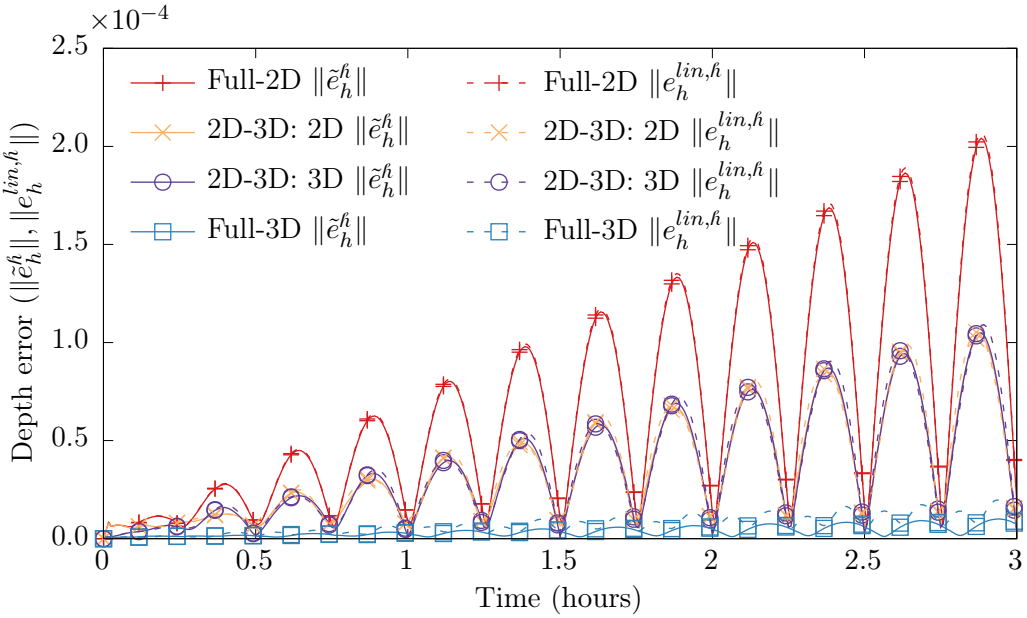

(a) Temporal variation of $\|e_h^{lin,\hbar}\|$ and $\|\tilde{e}_h^{\hbar}\|$ in mesh 4, $\hbar = 800\,\mathrm{m}$

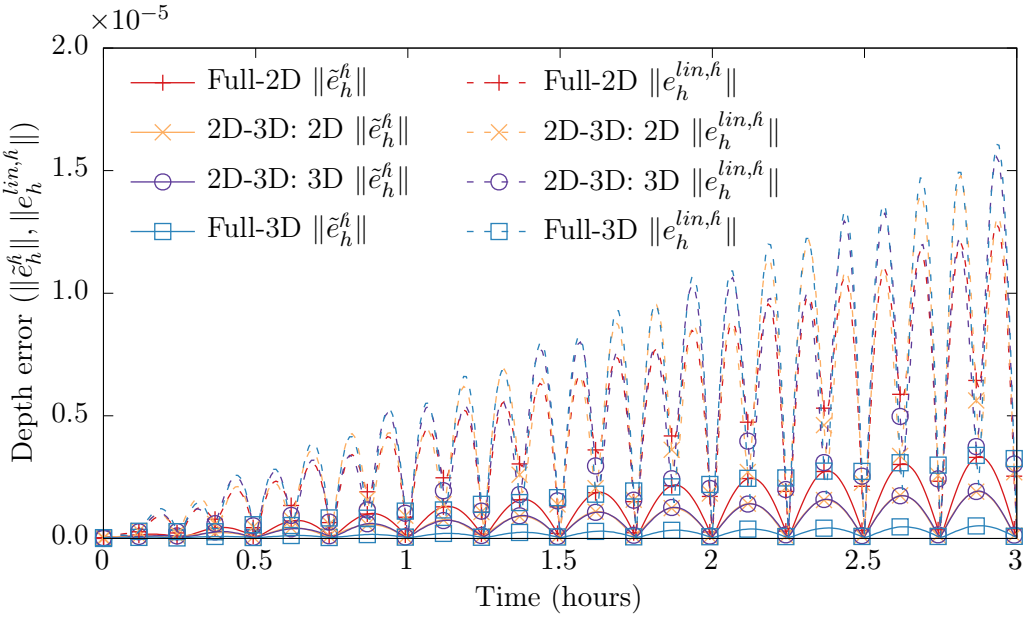

(b) Temporal variation of $\|e_h^{lin,\hbar}\|$ and $\|\tilde{e}_h^{\hbar}\|$ in mesh 7, $\hbar = 100\,\mathrm{m}$

Figure 4.8: Small-amplitude slosh test: Temporal variation of depth errors with SUPG terms included, using $\Delta t = 1\,\mathrm{s}$.

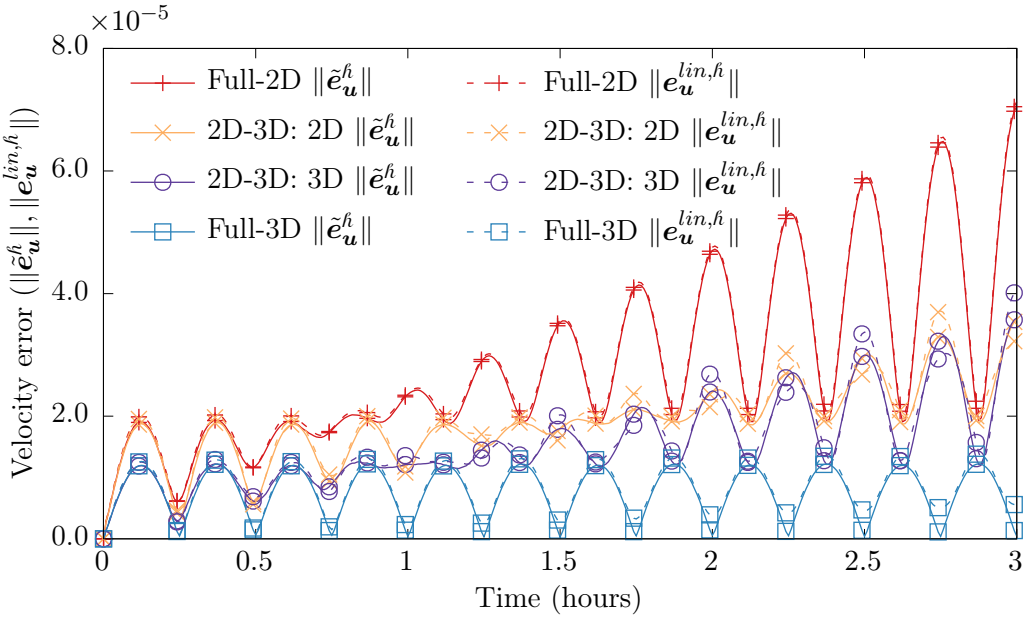

(a) Temporal variation of $\|\boldsymbol{e}_{\boldsymbol{u}}^{lin,\hbar}\|$ and $\|\tilde{\boldsymbol{e}}_{\boldsymbol{u}}^{\hbar}\|$ in mesh 4, $\hbar = 800\,\mathrm{m}$

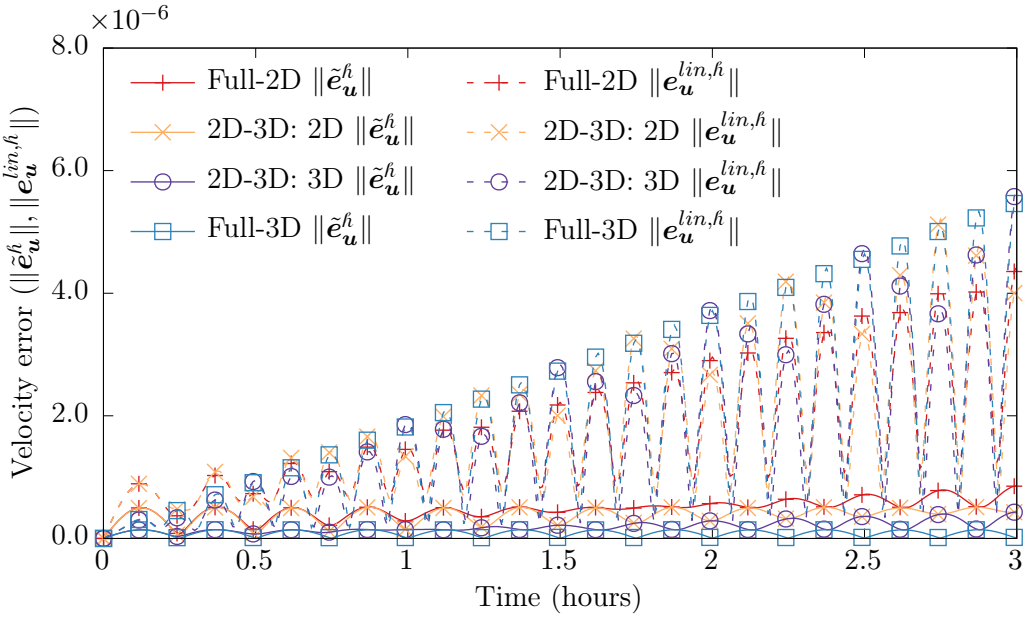

(b) Temporal variation of $\|\boldsymbol{e}_{\boldsymbol{u}}^{lin,\hbar}\|$ and $\|\tilde{\boldsymbol{e}}_{\boldsymbol{u}}^{\hbar}\|$ in mesh 7, $\hbar = 100\,\mathrm{m}$

Figure 4.9: Small-amplitude slosh test: Temporal variation of velocity errors with SUPG terms excluded, using $\Delta t = 1\,\mathrm{s}$.

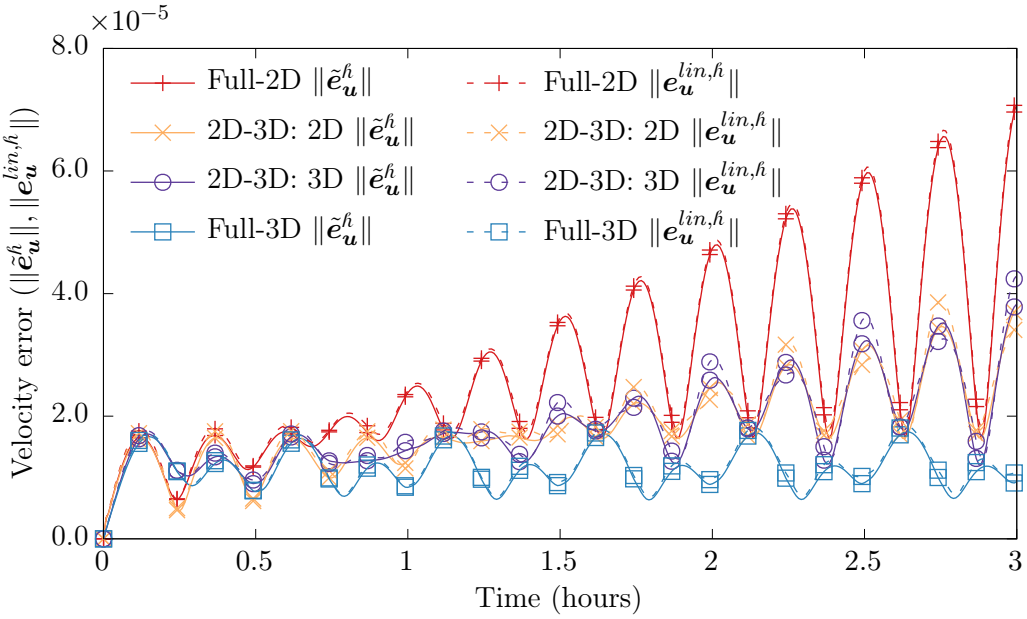

(a) Temporal variation of $\|e_u^{lin,h}\|$ and $\|\tilde{e}_u^h\|$ in mesh 4, $h = 800\,\mathrm{m}$

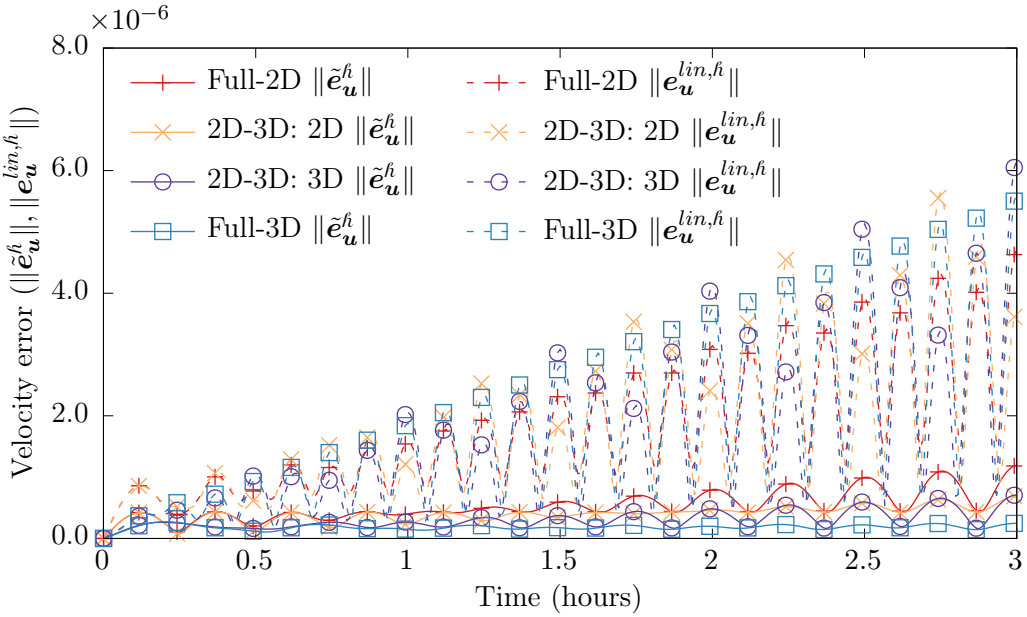

(b) Temporal variation of $\|e_u^{lin,h}\|$ and $\|\tilde{e}_u^h\|$ in mesh 7, $h = 100\,\mathrm{m}$

Figure 4.10: Small-amplitude slosh test: Temporal variation of velocity errors with SUPG terms included, using $\Delta t = 1\,\mathrm{s}$.

velocity, according to the analytical solution, is $a\sqrt{g/H} = 3.448 \times 10^{-3}\,\mathrm{m/s}$, and that of the z-velocity is $a\pi\sqrt{gH}/L = 3.491 \times 10^{-5}\,\mathrm{m/s}$. The observed amplitudes in the models are close to these values.

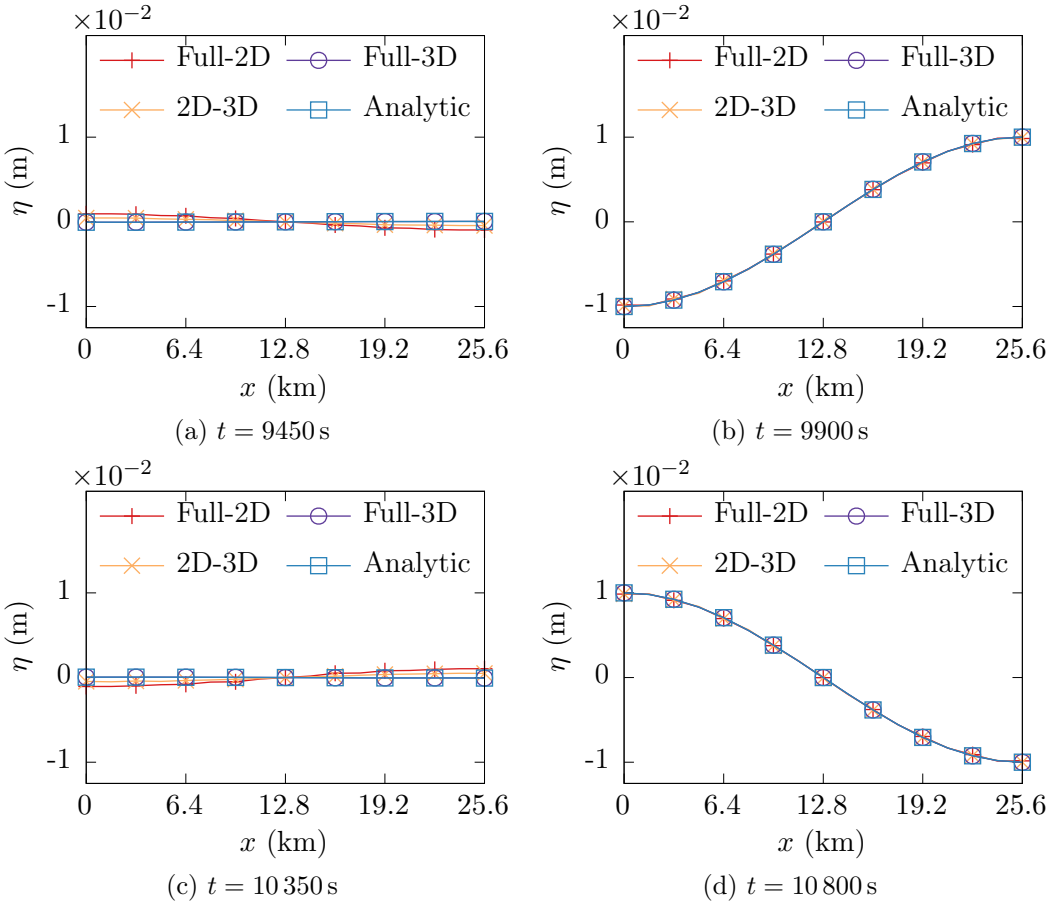

(a) $t = 9450\,\mathrm{s}$ (b) $t = 9900\,\mathrm{s}$

(c) $t = 10\,350\,\mathrm{s}$ (d) $t = 10\,800\,\mathrm{s}$

Figure 4.11: Small-amplitude slosh test: Surface elevation comparison at different times in mesh 3, $\hbar = 1600\,\mathrm{m}$.

Next, the temporal behavior of the solutions at two particular locations in the third mesh, $\hbar = 1600\,\mathrm{m}$, are compared. Surface nodes at the horizontal locations $(12.8, 3.2)\,\mathrm{km}$ and $(19.2, 3.2)\,\mathrm{km}$ are chosen to track the solution. The

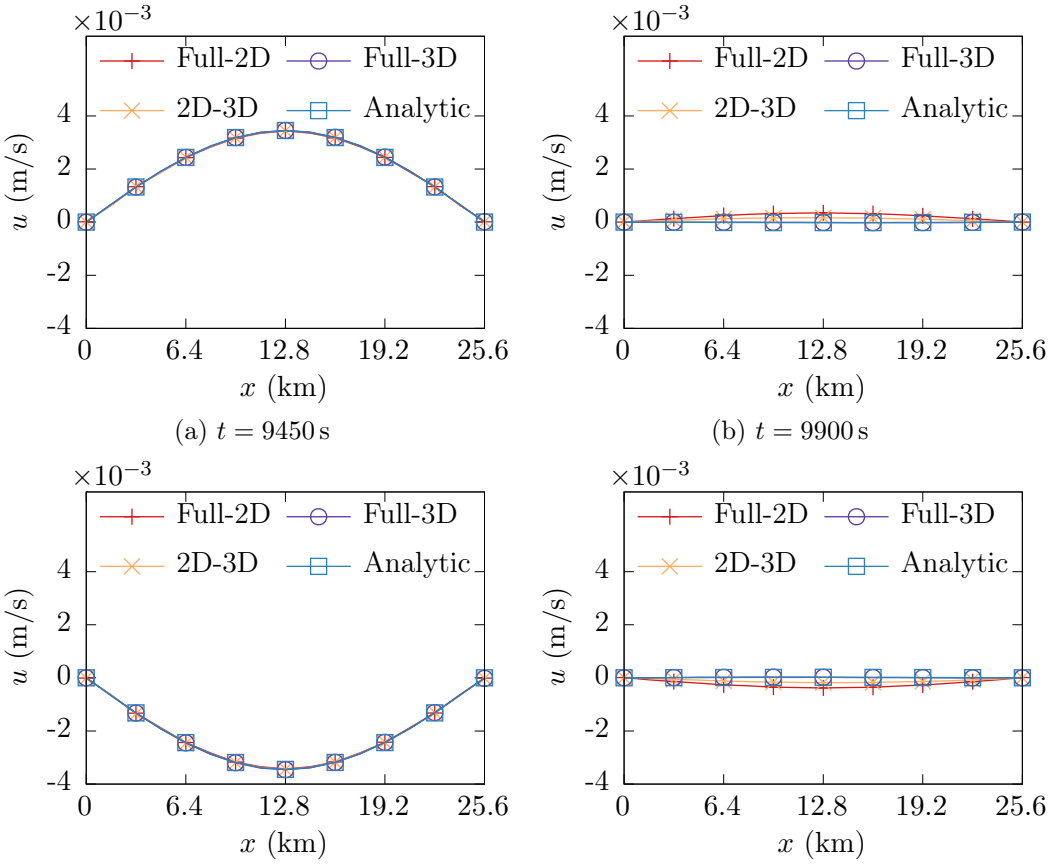

(a) $t = 9450\,\mathrm{s}$ (b) $t = 9900\,\mathrm{s}$

(c) $t = 10\,350\,\mathrm{s}$ (d) $t = 10\,800\,\mathrm{s}$

Figure 4.12: Small-amplitude slosh test: Surface x-velocity comparison at different times in mesh 3, $\hbar = 1600\,\mathrm{m}$.

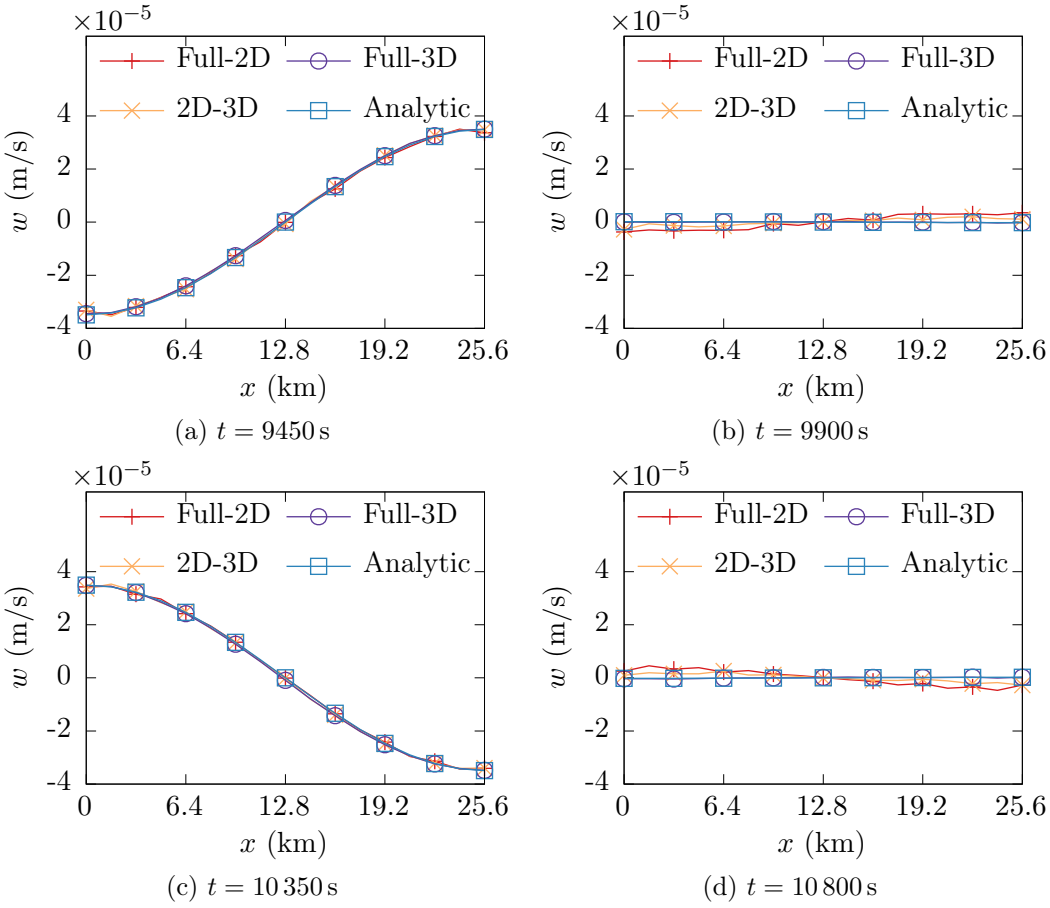

(a) $t = 9450\,\mathrm{s}$ (b) $t = 9900\,\mathrm{s}$

(c) $t = 10\,350\,\mathrm{s}$ (d) $t = 10\,800\,\mathrm{s}$

Figure 4.13: Small-amplitude slosh test: Surface z-velocity comparison at different times in mesh 3, $\hbar = 1600\,\mathrm{m}$.

former node is located right at the 2D-3D interface, whereas the latter node is away from the interface at three-quarters of the domain length L. Figure 4.14 shows the temporal variation of the surface elevation, x-velocity, and z-velocity in the three models, as well as comparison with the analytical solution. The results are seen to agree well with each other. Note the z-velocity solution behavior at the 2D-3D interface at $x = 12.8\,\text{km}$, shown in Figure 4.14c on the left. Although the analytical solution is constant at $0\,\text{m/s}$ and the solutions are close to that, the 3D model captures non-linear effects showing regular oscillations right from the beginning, the full-2D model solution remains nearly zero, whereas the 2D-3D model oscillates irregularly with an amplitude less than that of the full-3D model.

4.1.7 Mass conservation across the 2D-3D interface

A straightforward way to verify mass conservation across the 2D-3D interface in this test case is to calculate the mass of water in each of the two models and check if the sum stays constant in time since there are no sources or sinks. Since the density is constant in this test case, the volume of the water in the mesh can also be used alternatively. Figure 4.15 shows the volume of water in the individual 2D and 3D submodels and their total over the period of 3 hours for the sixth mesh of size $\hbar = 200\,\text{m}$. It is seen from the figure that the individual volumes change with time as expected, but the total volume of water remains constant at $13.5168\,\text{km}^3$, verifying global mass conservation, and in turn, conservation of mass as water moves to and fro across the interface.

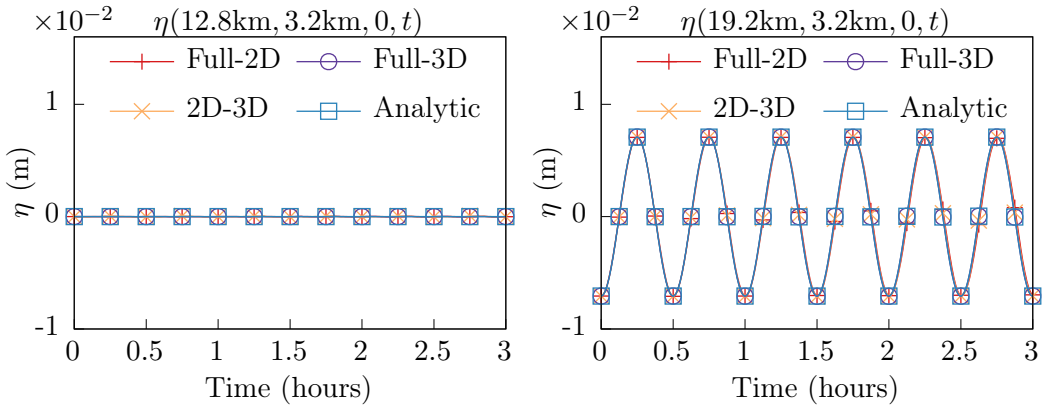

(a) Surface elevation, η (m)

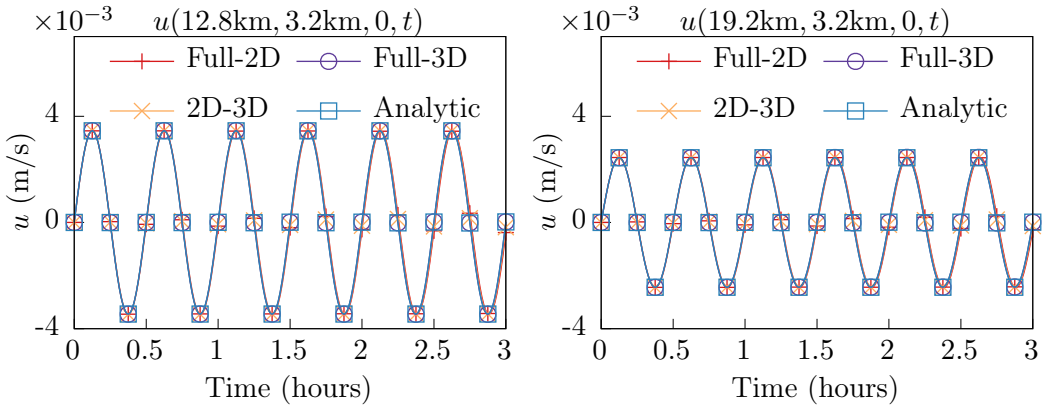

(b) x-velocity, u (m/s)

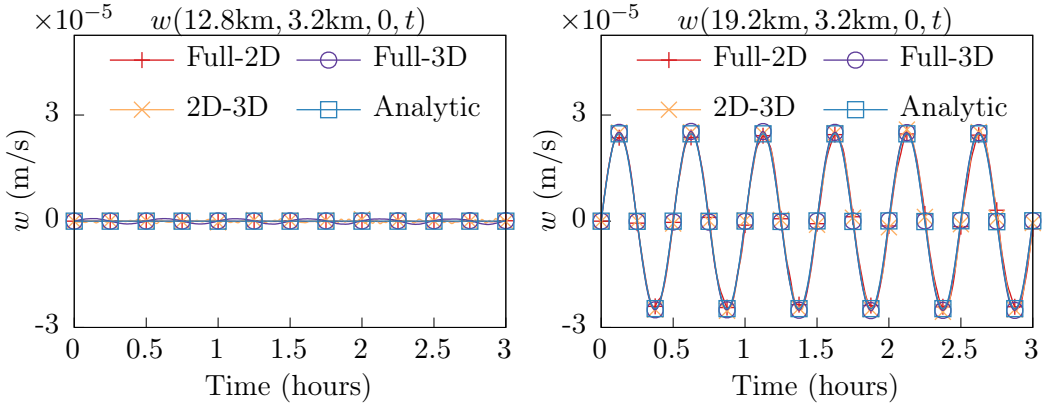

(c) z-velocity, w (m/s)

Figure 4.14: Small-amplitude slosh test: Nodal solutions at $(12.8, 3.2, 0)$ km (left) and $(19.2, 3.2, 0)$ km (right).

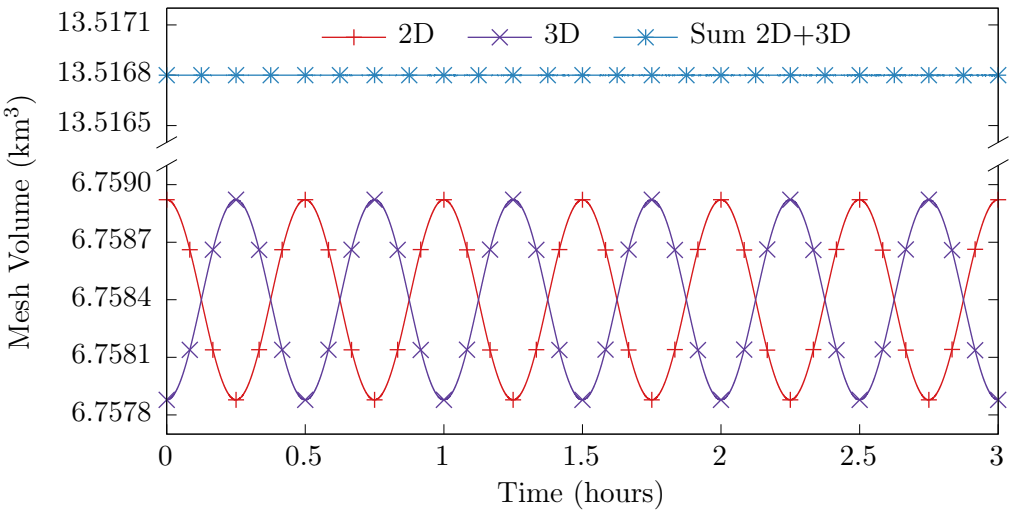

Figure 4.15: Small-amplitude slosh test: Verification of conservation of mass in 2D-3D coupled models using the sixth mesh, $\hbar = 200\,\text{m}$.

4.2 Large-amplitude slosh test case

Next, the same slosh test case from the previous section is considered with two changes, the initial amplitude of depth is increased to $a = 10\,\text{m}$ from its previous value of $0.01\,\text{m}$, and the simulation ending time is decreased to 0.5 hours from 3 hours, which corresponds to 1 oscillation cycle instead of the 6 in the previous case. For this test case, SUPG stabilization becomes necessary since the simulations turn unstable if the SUPG terms are excluded.

Figure 4.16 shows plots of depth and velocity errors against mesh size for this test case. The analytical solution (4.7) is no longer an acceptable approximation to the true solution, since the amplitude of oscillations is not small and advection can no longer be neglected, preventing linearization of

the SWE. This is evident from the figures as well, wherein the errors with respect to the analytical solution are seen to be flat for almost all mesh sizes. Unlike in the small-amplitude case where the temporal errors were reduced for spatial convergence analysis by systematically choosing a time step from temporal convergence analysis, however, no temporal convergence analysis was performed for this test case. As a result, the spatial convergence rates cannot be definitively determined from the convergence plots shown in Figure 4.16. It is likely that a much smaller time step (or an earlier simulation ending time) is required to allow mesh discretization errors to dominate the temporal discretization errors. The convergence rates of the models are seen to be sub-optimal, between 1.25 to 1.5. It is noted that the convergence rates for SUPG are 2 and 1.5 for diffusion-dominated and advection-dominated scenarios of advection-diffusion equations, respectively [4, 48, 65], so it is not surprising that the convergence rates for the shallow water models used herein are sub-optimal. Lastly, it is also noted that unlike in the case of small-amplitude slosh given in section 4.1, only the depth errors of 2D-3D coupled models are seen to exceed both the full-2D as well as full-3D models, but not by a significant amount. The final thing to note is that it may be important for the 3D submodels to have mesh refinements in the vertical direction as well, and not just in the horizontal directions for the large amplitude case, which has not been done herein.

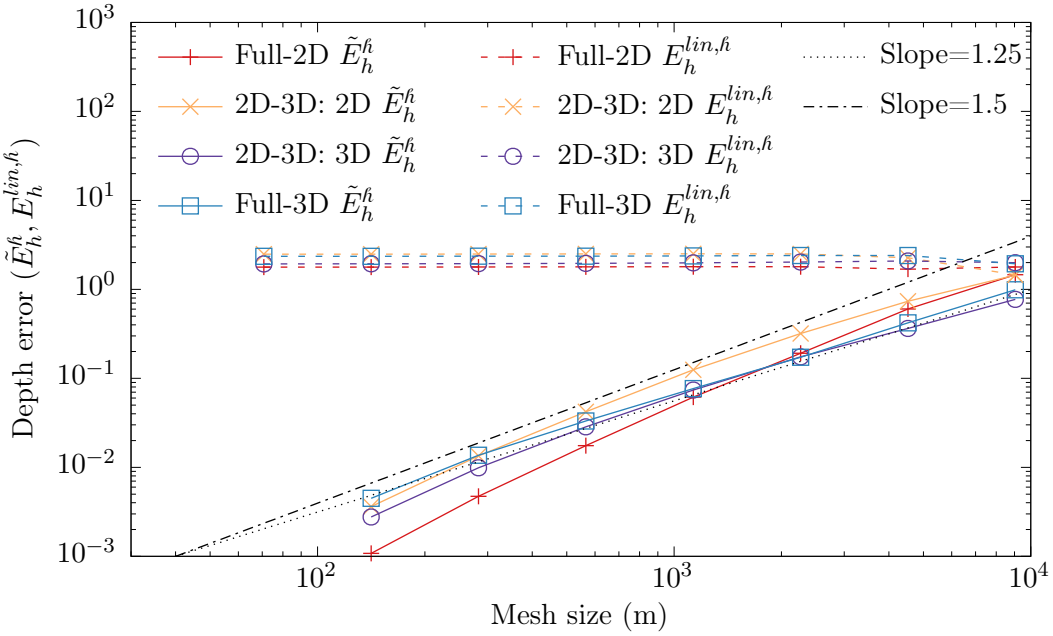

(a) Depth errors in simulations including SUPG terms

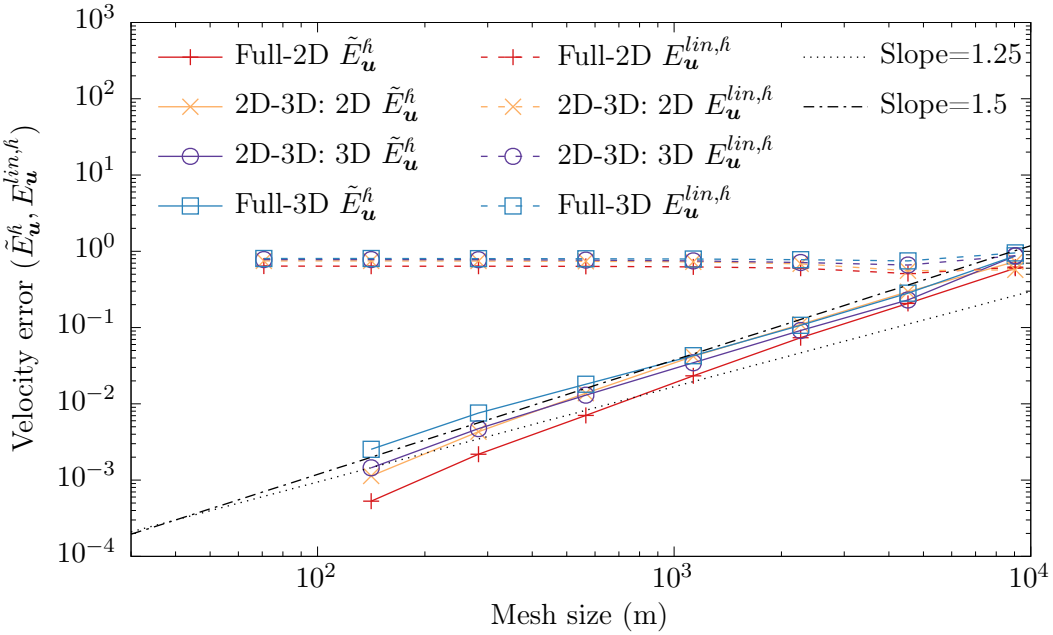

(b) Velocity errors in simulations including SUPG terms

Figure 4.16: Large-amplitude slosh test: Spatial convergence of depth (top) and velocity (bottom) using $\Delta t = 1\,\mathrm{s}$, including SUPG terms.

4.3 Baroclinic flume test case

In this test case, baroclinic flow in a rectangular domain is simulated. This test case violates the recommendation of keeping the 2D-3D interface away from baroclinic regions, explained in section 3.2.1. The purpose of this test case is to observe the behavior of baroclinicity close to the 2D-3D interface, since it may not always be possible in a practical scenario to keep the 2D-3D interface away from baroclinic regions.

The rectangular domain used in this test case is a channel given by $\Omega = (0, 3.2)\,\text{km} \times (0, 0.2)\,\text{km}$. The bed elevation is $b(x, y) = -H = -10\,\text{m}$. The water is initially at rest with a constant depth of $H = 10\,\text{m}$ and salinity of $0\,\text{g/kg}$. The north and south boundaries of the models, $y = \{0, 0.2\}\,\text{km}$, have a no-normal-flow boundary condition. An inflow of $Q = 400\,\text{m}^3/\text{s}$ with a salinity of $1\,\text{g/kg}$ is specified on the western boundary at $x = 0\,\text{km}$. The water surface elevation at the eastern boundary, $x = 3.2\,\text{km}$, is fixed at $0\,\text{m}$. There is no bottom friction, wind, or air pressure.

In this case, the solutions of two 2D-3D coupled models are compared against those of full-2D and full-3D models for verification. The meshes are as shown in Figure 4.17. The first 2D-3D coupled model has the 2D subdomain located on the left/western side and the 3D subdomain on the eastern side. The second 2D-3D coupled model has the opposite placement of the 2D and 3D subdomains as compared to the first 2D-3D coupled model. The two coupled models are respectively referred to as 2D-3D and 3D-2D coupled models in this section. For both the models, the coupling interface is placed midway along

the length at $x = 1.6\,\text{km}$. The horizontal node spacing is $\Delta x = \Delta y = 50\,\text{m}$, and in case of all 3D submodels, the vertical node spacing is $\Delta z = 2.5\,\text{m}$, corresponding to a vertical resolution of 4 element layers. The Smagorinsky coefficient is set to 0.2. A time step of 300 s is used for the simulation, and the simulation ending time set to 4 hours.

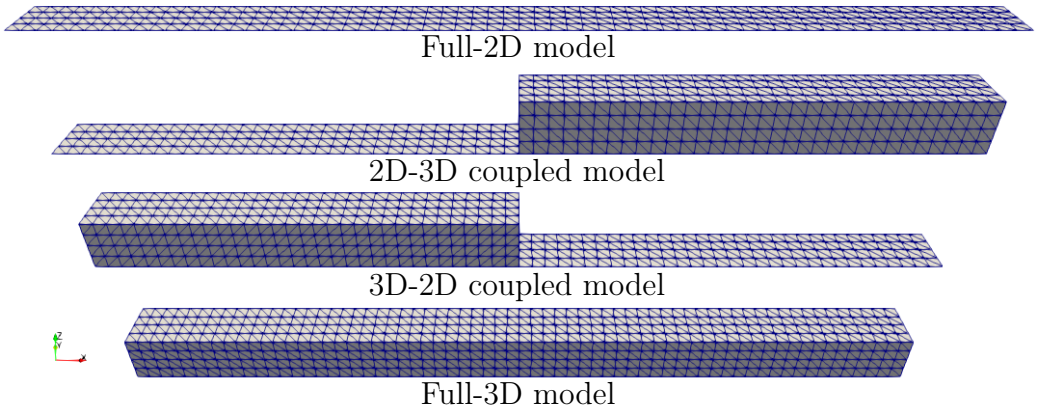

Figure 4.17: Baroclinic flume test case meshes, $\Delta x = \Delta y = 50\,\text{m}$, $\Delta z = 2.5\,\text{m}$ (scaled by a factor of 20 in the z direction).

Since the water is initially at rest whereas the boundary inflow is a non-zero constant right from $t = 0$, transient oscillations are expected in the water depth and velocity, which are damped quickly due to the use of first order time stepping, a larger time step, and viscosity. Also, since the domain initially has fresh water and the water flowing in is saline, a salinity shock travels across the domain from west to east. The steady state solution is a constant water depth of 10 m, uniform horizontal velocity of 0.2 m/s in the x direction, and a uniform salinity of 1 g/kg. The x-velocity and salinity shocks in the solutions are observed, and the steady state values are verified.

Figures 4.18 and 4.19 show the x-velocity and salinity in the models at hourly intervals. These are depth-averaged values in case of 2D submodels, and surface (solid) and bed (dashed) values in case of 3D submodels. Due to baroclinicity, the denser saline water sinks, and salinity and x-velocity shocks travel along the bed in the full-3D and coupled domains, seen by a separation of the dashed and solid lines in all the figures. It is observed that in case of the full-3D and 3D-2D coupled models, the salinity overshoots from what should be its maximum value of 1 g/kg. Some more work is needed to improve the salinity transport in the 3D models, which is out of scope of the current work since it is not a problem pertaining to 2D-3D coupled models. The observations from Figures 4.18 and 4.19 can be divided temporally into three stages.

- Initial stage: This is when the salinity front has just entered the domains and is still far away from the coupling interface. From Figures 4.18a and 4.19a, it is observed that the 2D-3D coupled model initially behaves like the full-2D model, whereas 3D-2D coupled model initially behaves like the full-3D model.

- Intermediate stage: This is when the salinity front is in the vicinity of the coupling interface, before, during, and after crossing it. From Figures 4.18b, 4.18c, 4.19b and 4.19c, it is observed that the coupled models are in a state of transition. In the 2D-3D coupled model, the transition of the salinity and x-velocity front from the 2D domain is

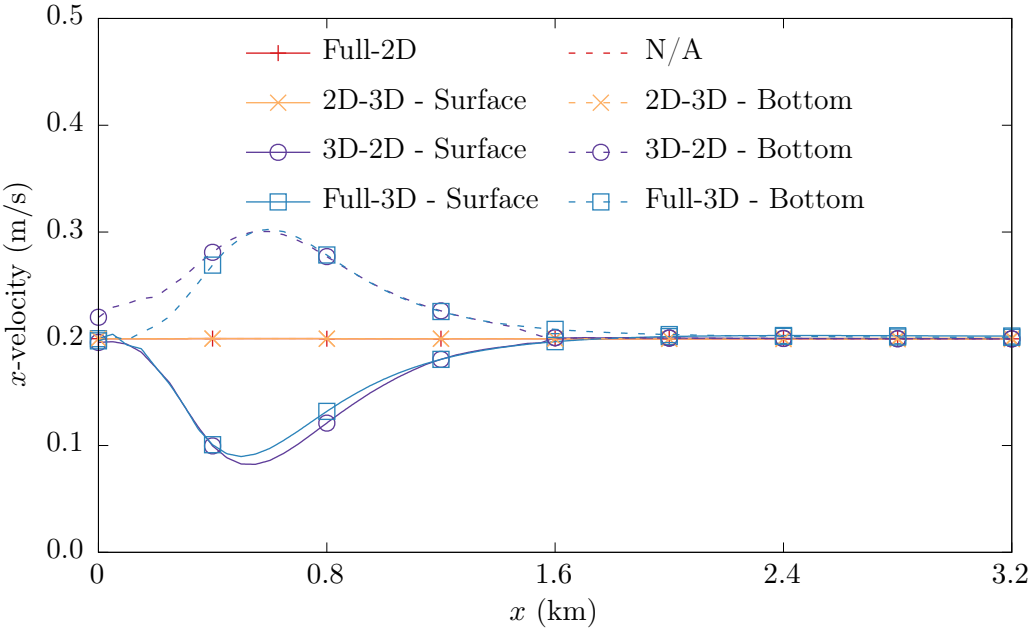

(a) $t = 1\,\text{hour}$

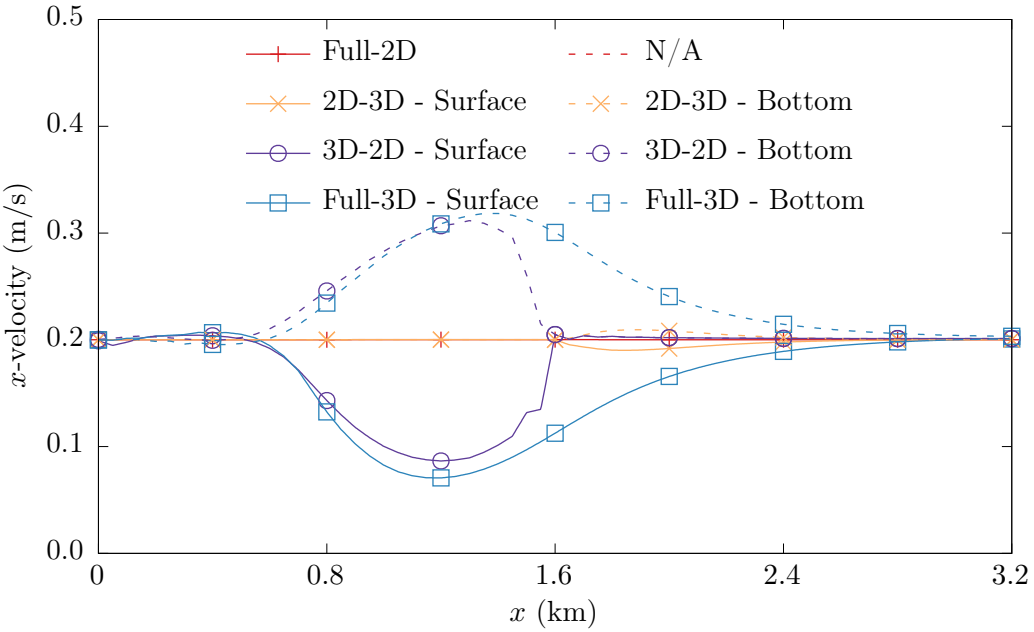

(b) $t = 2\,\text{hours}$

Figure 4.18: Baroclinic flume test: x-velocity in the full-2D, 2D-3D coupled, 3D-2D coupled, and full-3D models at different timestamps.

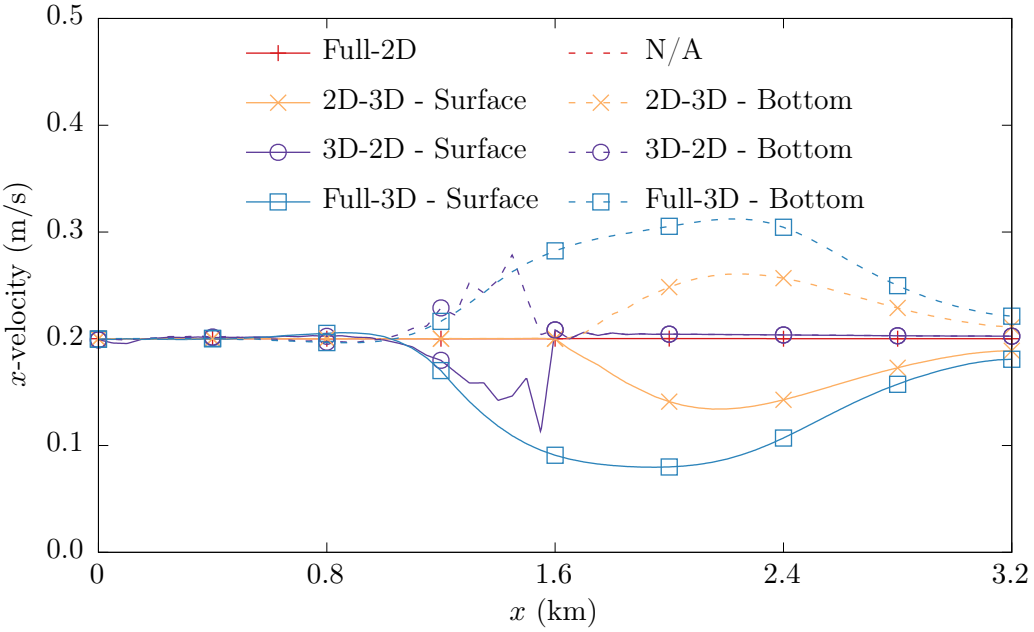

(c) $t = 3$ hours

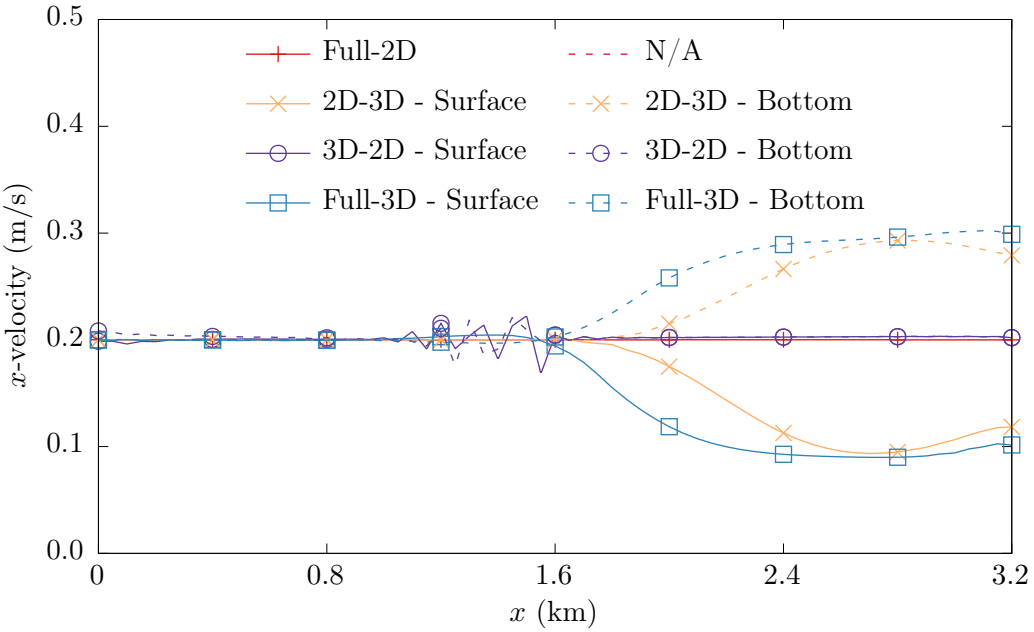

(d) $t = 4$ hours

Figure 4.18: (Cont.) Baroclinic flume test: x-velocity in the full-2D, 2D-3D coupled, 3D-2D coupled, and full-3D models at different timestamps.

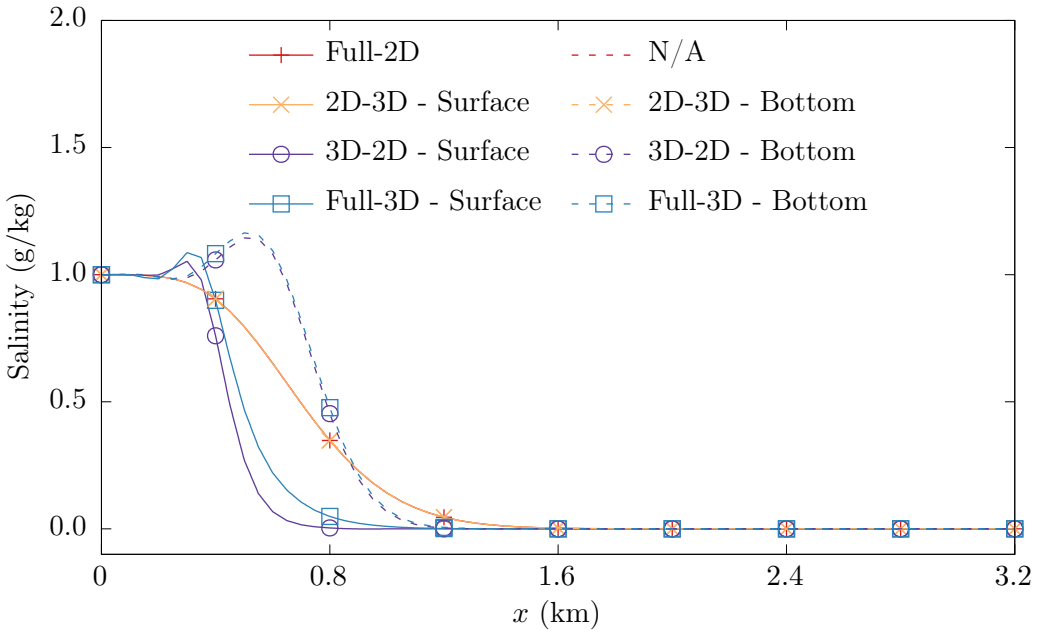

(a) $t = 1\,\text{hour}$

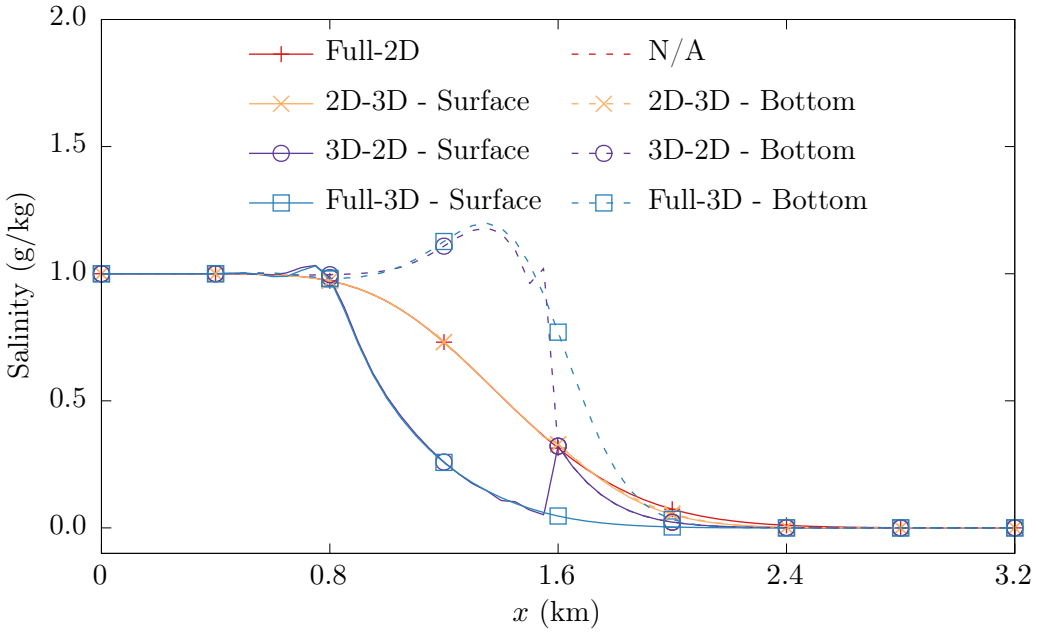

(b) $t = 2\,\text{hours}$

Figure 4.19: Baroclinic flume test: Salinity in the full-2D, 2D-3D coupled, 3D-2D coupled, and full-3D models at different timestamps.

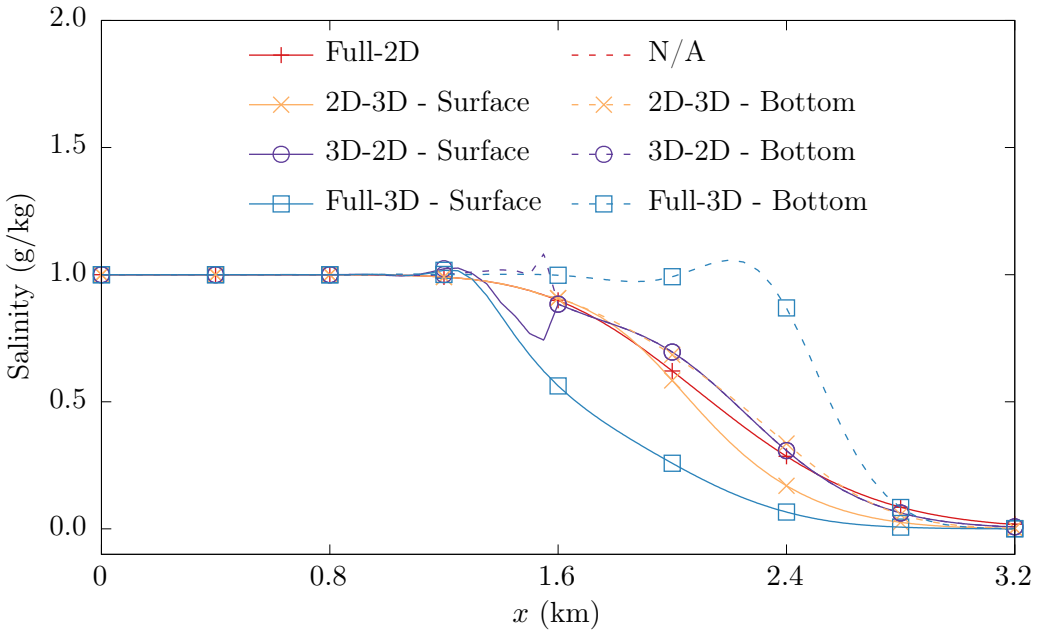

(c) $t = 3$ hours

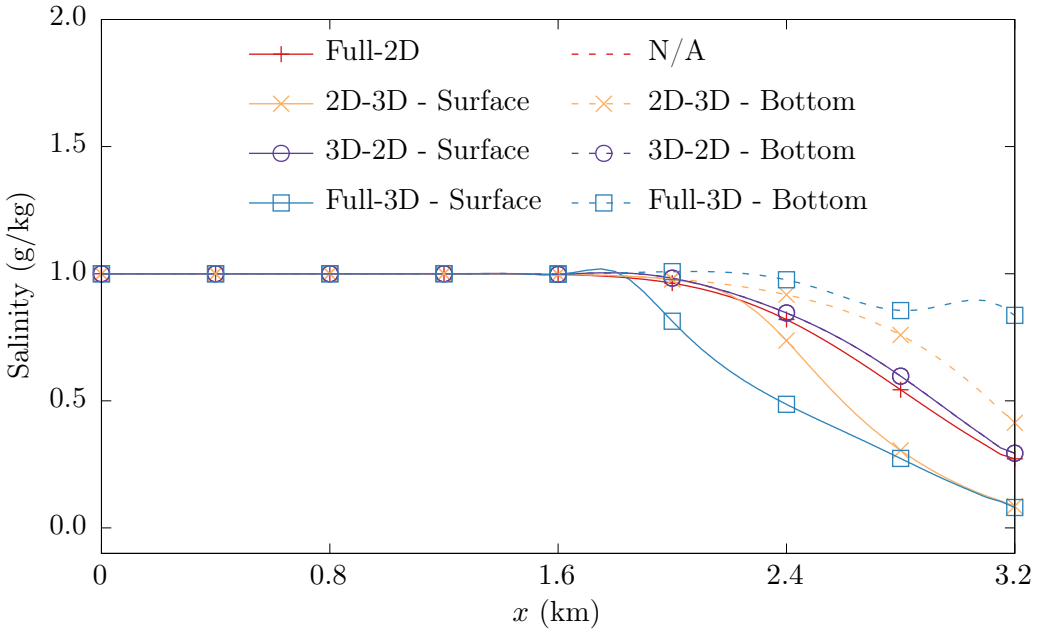

(d) $t = 4$ hours

Figure 4.19: (Cont.) Baroclinic flume test: Salinity in the full-2D, 2D-3D coupled, 3D-2D coupled, and full-3D models at different timestamps.

smooth. In the 3D-2D coupled model, however, the movement of the stratified salinity and x-velocity front from the 3D domain into the 2D domain results in temporary oscillatory behavior in the velocity (but not in the salinity, or the depth which is not shown here). This is precisely the reason why it is important to place the coupling interface away from baroclinic areas. In a practical scenario, however, that may not always be possible, in which case the oscillations can be damped by increasing stabilization in the 3D elements close to the 2D-3D interface. When the salinity front reaches the interface, the salinity near the surface is about $0\,\mathrm{g/kg}$, whereas that near the bed is close to $1\,\mathrm{g/kg}$. Likewise, the x-velocity is also stratified. 2D-3D coupling forces the solution to be constant down a node column, which prevents the salinity and x-velocity front from staying stratified while crossing the interface. This results in a change in the velocities and salinity close to the interface, and as observed here, may lead to oscillations.

- Final stage: This is when the salinity front has fully crossed the coupling interface and is reasonably far away from it. From Figures 4.18d and 4.19d, it is observed that the situation has flipped in comparison with the initial stage, i.e., the 2D-3D coupled model now behaves like the full-3D model, whereas the 3D-2D model behaves like the full-2D model. Also, all the models attain the correct steady state solution on running them for a longer time, which is not shown here. The oscillations in the 3D-2D coupled model are also gone once the salinity front

crosses the coupling interface.

4.4 Lock-exchange test case

Another extreme case of baroclinicity, the lock-exchange experiment, is used to observe the behavior of coupled models with respect to full-2D and full-3D models. As is the case with the baroclinic flume test case, this case also violates the recommendation of placing the 2D-3D interface away from baroclinic areas. Theoretical and experimental investigations of this test case are available in literature [79] but have not been used for comparison herein. In the lock-exchange experiment, a rectangular tank is filled with water to some height. A thin, impermeable membrane is inserted in the middle of the tank vertically to separate the domain into two halves. Different amounts of salt are added on both sides of the membrane, and the water is mixed and allowed to come to rest. A few drops of dilute coloring agent are generally added on one of the sides to allow tracking the movement of the water. This sets up the experiment. On lifting the membrane quickly, the water in the two halves starts mixing due to pressure gradients resulting from density variations in the domain. The difference in salinity in the two halves of the tank results in two salinity and velocity shocks each, traveling in opposite directions along the surface and the bed. Denser water sinks below, and less saline water floats above. The shocks are internal in that the water surface elevation remains constant in the entire domain throughout the experiment, although there is movement of water underneath the surface.

For this test case, the rectangular domain is given by $\Omega = (-1, 1)\,\mathrm{m} \times (-0.1, 0.1)\,\mathrm{m} \times (-0.2, 0.0)\,\mathrm{m}$. The initial condition is water at rest with a constant water depth of $h(x, y, 0) = H = 0.2\,\mathrm{m}$, and initial salinity of $30.0\,\mathrm{g/kg}$ for $x \in (-1, 0)\,\mathrm{m}$ and $10.0\,\mathrm{g/kg}$ for $x \in (0, 1)\,\mathrm{m}$. All the vertical boundaries have a no-normal-flow Neumann boundary condition, $\boldsymbol{u}\cdot\boldsymbol{n} = 0$. The horizontal spacing of nodes in the meshes is $\Delta x = \Delta y = 0.05\,\mathrm{m}$, and in case of 3D submodels, the vertical node spacing is $\Delta z = 0.025\,\mathrm{m}$, corresponding to a vertical resolution of eight element layers. The results of a 2D-3D-2D coupled model are compared to those of full-2D and full-3D models. The 2D-3D-2D coupled model contains one 3D submodel coupled to two 2D submodels on its sides. The 3D submodel corresponds to three-quarters of the domain length, $x \in (-0.75, 0.75)\,\mathrm{m}$, and the two 2D submodels correspond to $x \in (-1.0, -0.75)\,\mathrm{m}$ and $x \in (0.75, 1.0)\,\mathrm{m}$, respectively. The meshes of the models are shown in Figure 4.20.

Manning's bottom friction coefficient is set to 0.0015. The Smagorinsky coefficient is set to 0.2. The salinity diffusivity constant is set to $1 \times 10^{-5}\,\mathrm{m^2/s}$. The salinity drops from $30\,\mathrm{g/kg}$ on the left to $10\,\mathrm{g/kg}$ on the right across 2 element layers around $x = 0\,\mathrm{m}$ in the numerical models, as shown in Figure 4.21. A time step of $0.5\,\mathrm{s}$ is used, and the simulation is run for $48\,\mathrm{s}$. Mesh adaptivity is turned on, allowing maximum of 2 levels of mesh refinement.

Figures 4.22a to 4.22l show the variation of x-velocity and salinity in the models at time intervals of $8\,\mathrm{s}$. In case of 2D submodels, the plots show depth-averaged values, whereas in case of 3D submodels, the plots show the

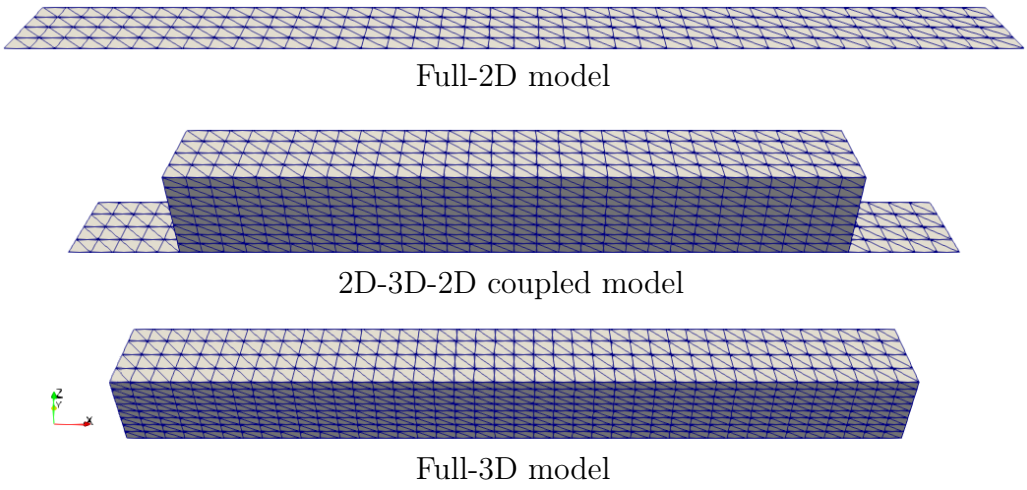

Figure 4.20: Lock-exchange test case meshes, $\Delta x = \Delta y = 0.05\,\text{m}$, $\Delta z = 0.025\,\text{m}$.

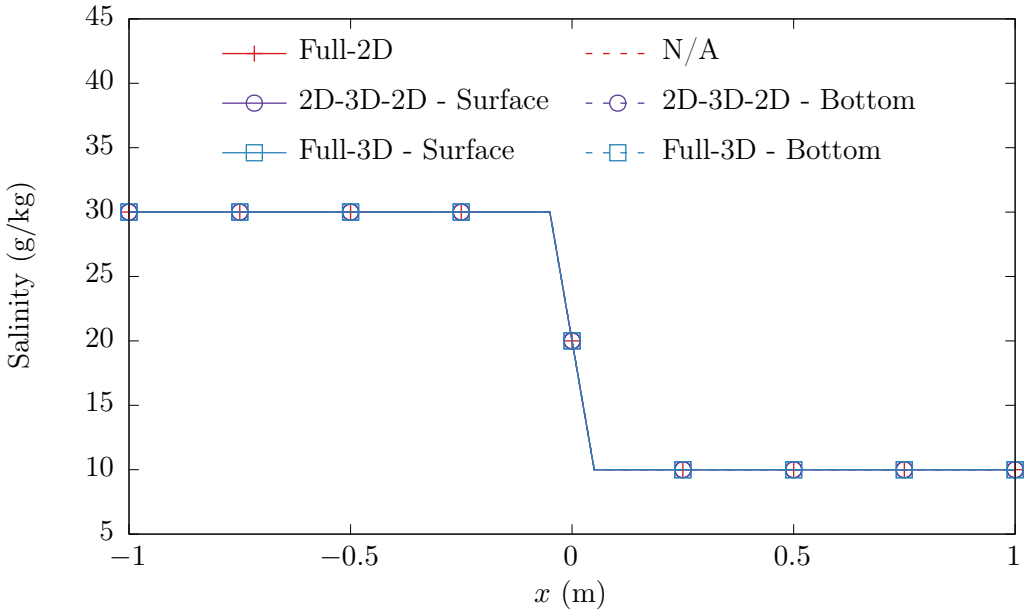

Figure 4.21: Lock-exchange test: Initial condition on salinity in the full-2D, 2D-3D-2D coupled, and full-3D models.

surface (solid) and bed (dashed) solutions. The subfigures on the top of each page show the x-velocity, and those on the bottom show the salinity. Following are the observations from the plots.

- The first observation is that the full-2D model fails to capture baroclinicity, as expected. 2D models cannot simulate pressure gradients arising from density differences down a column, so the solution in the full-2D model stays nearly the same as the initial condition throughout the simulation.

- Initially, when the velocity and salinity shocks are a still far away from both the 2D-3D interfaces, the full-3D and the 2D-3D-2D coupled solutions are nearly identical as they should be, as observed in Figures 4.22a and 4.22b.

- When the stratified shocks reach the 2D-3D interfaces in the 2D-3D-2D coupled models, they cannot pass through since 2D-3D coupling enforces constant solution down a column of nodes, preventing stratification at the interface. It is observed from Figures 4.22c and 4.22d that the 2D-3D-2D coupled solution now lies 'between' the full-2D and the full-3D solution (in say, the L^2 sense and not point-wise).

- In Figures 4.22e to 4.22h, the shocks are observed to be in the process of getting reflected at the domain boundary in case of the full-3D model and at the 2D-3D interfaces in case of the 2D-3D-2D coupled models, seen as a change in sign in the x-velocity.

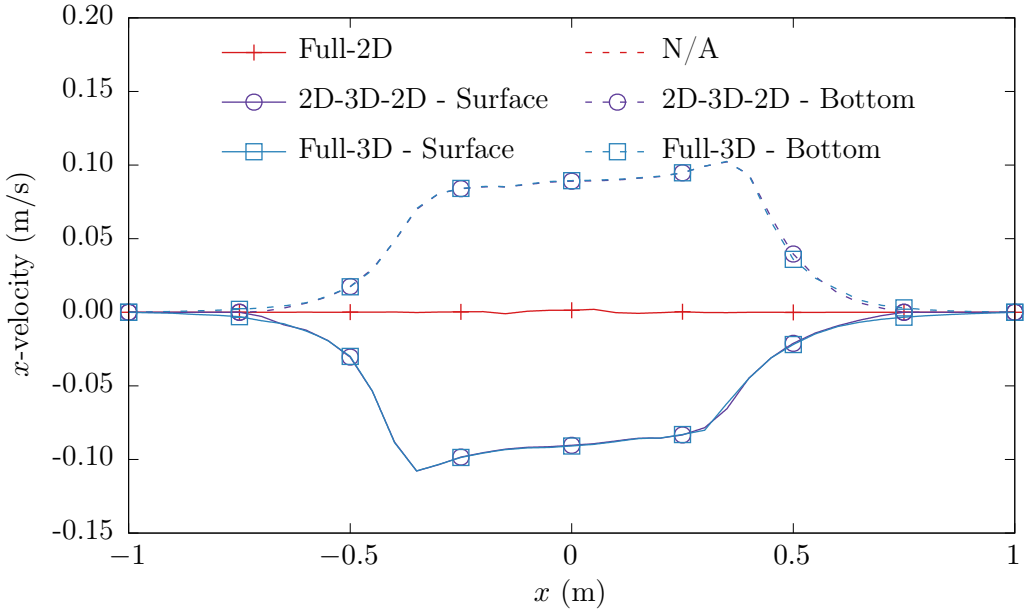

(a) x-velocity at $t = 8\,\mathrm{s}$

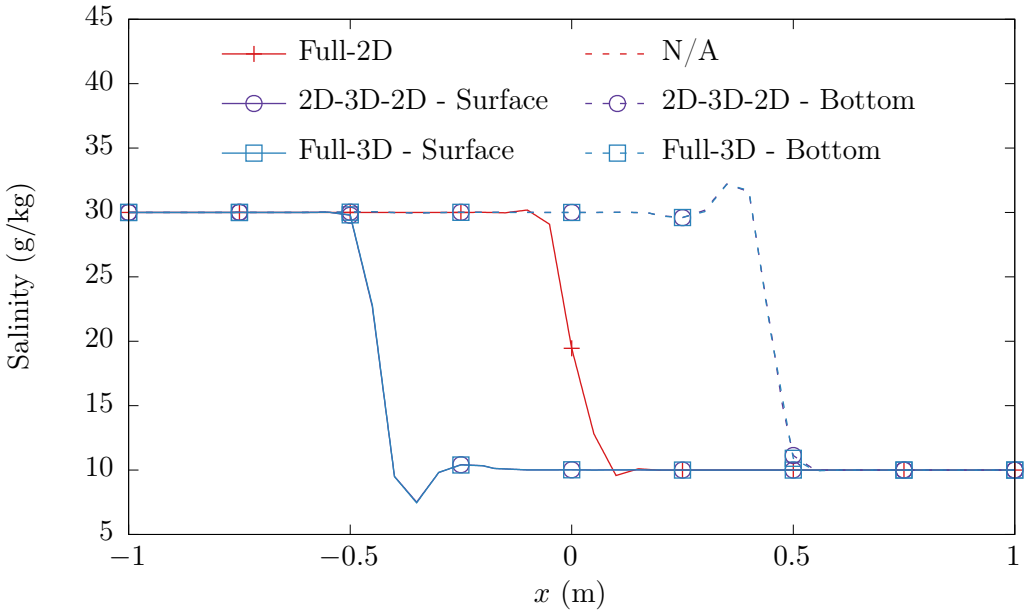

(b) Salinity at $t = 8\,\mathrm{s}$

Figure 4.22: Lock-exchange test: Comparison of solutions in the full-2D, 2D-3D-2D coupled, and full-3D models at different timestamps.

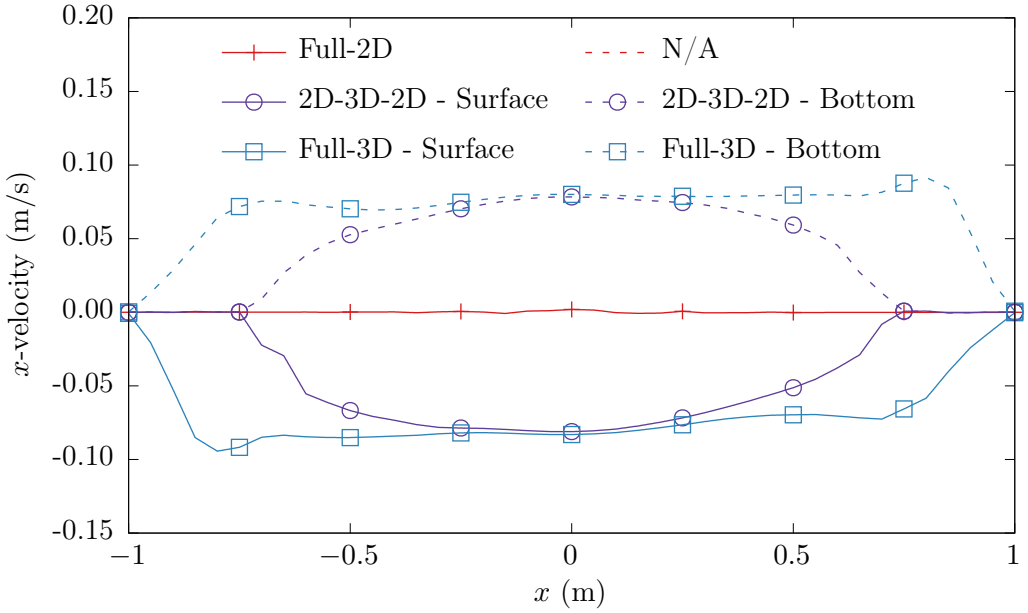

(c) x-velocity at $t = 16\,\mathrm{s}$

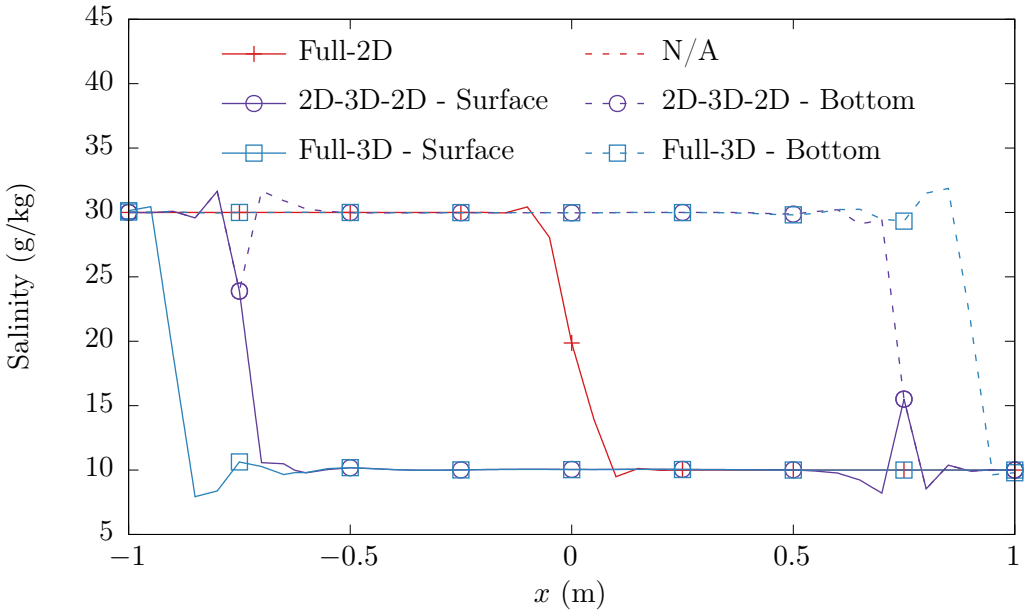

(d) Salinity at $t = 16\,\mathrm{s}$

Figure 4.22: (Cont.) Lock-exchange test: Comparison of solutions in the full-2D, 2D-3D-2D coupled, and full-3D models at different timestamps.

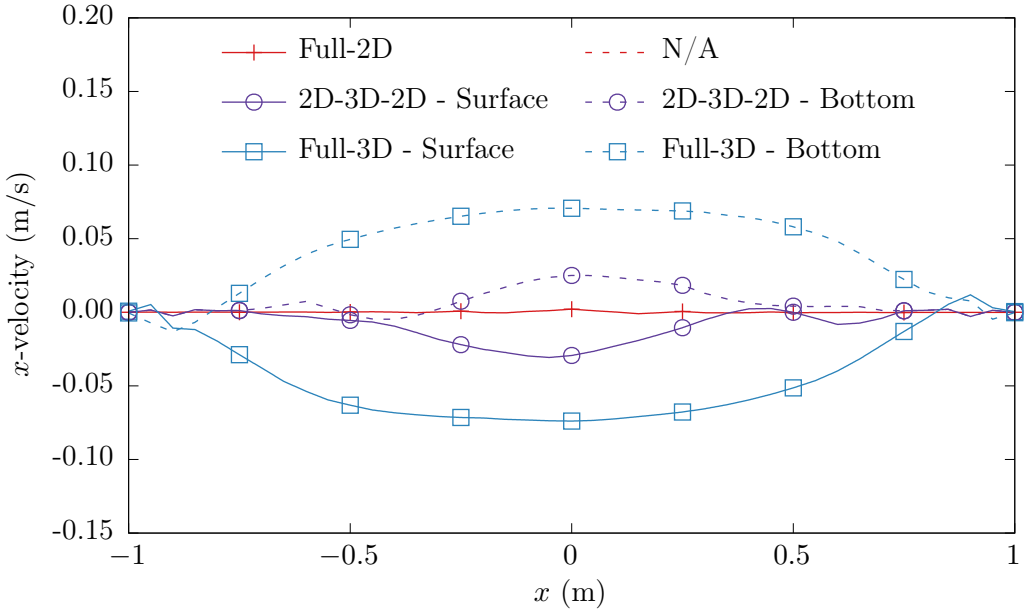

(e) x-velocity at $t = 24\,\mathrm{s}$

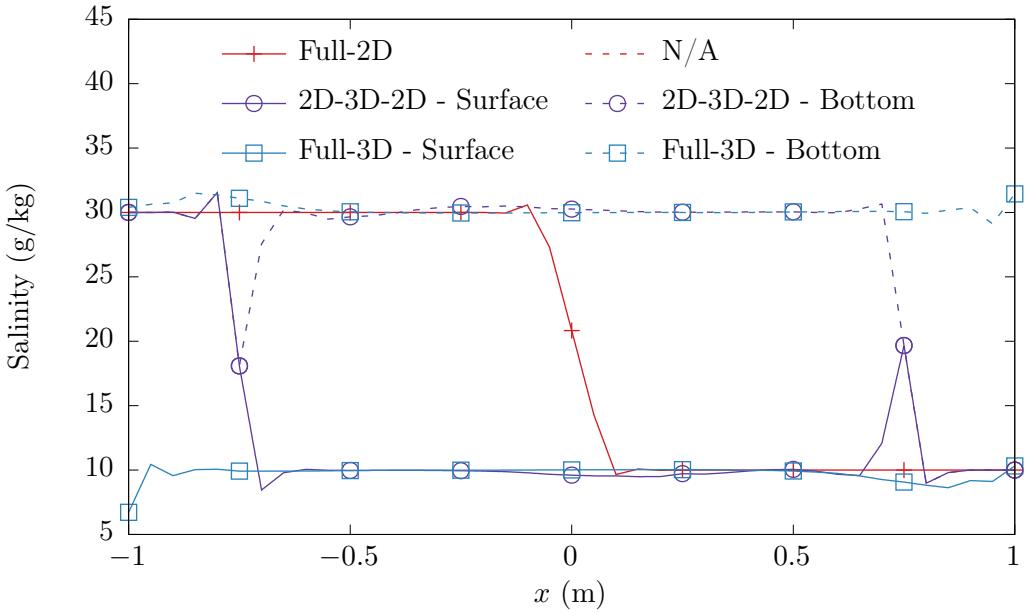

(f) Salinity at $t = 24\,\mathrm{s}$

Figure 4.22: (Cont.) Lock-exchange test: Comparison of solutions in the full-2D, 2D-3D-2D coupled, and full-3D models at different timestamps.

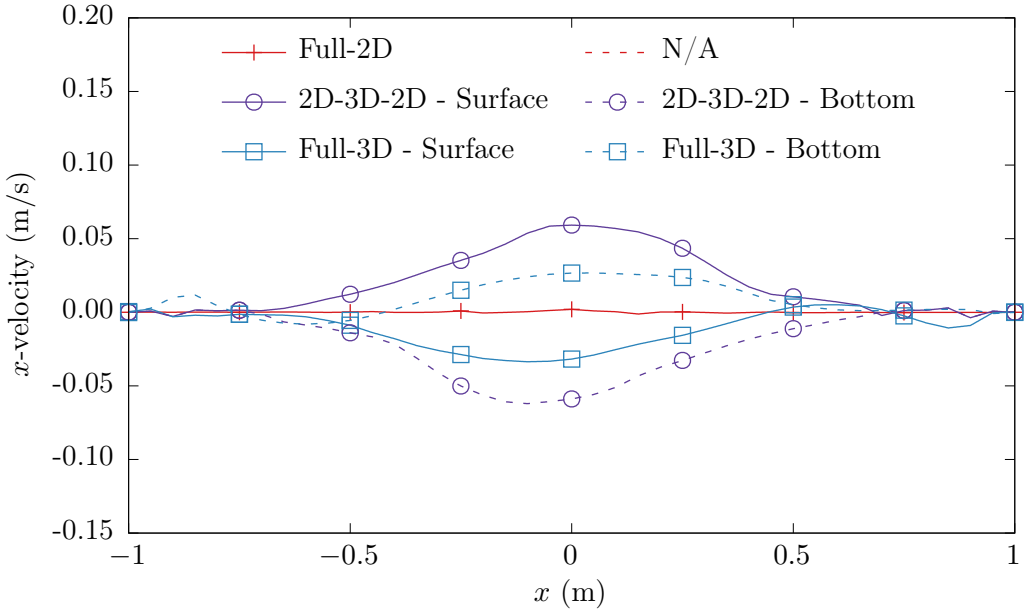

(g) x-velocity at $t = 32\,\mathrm{s}$

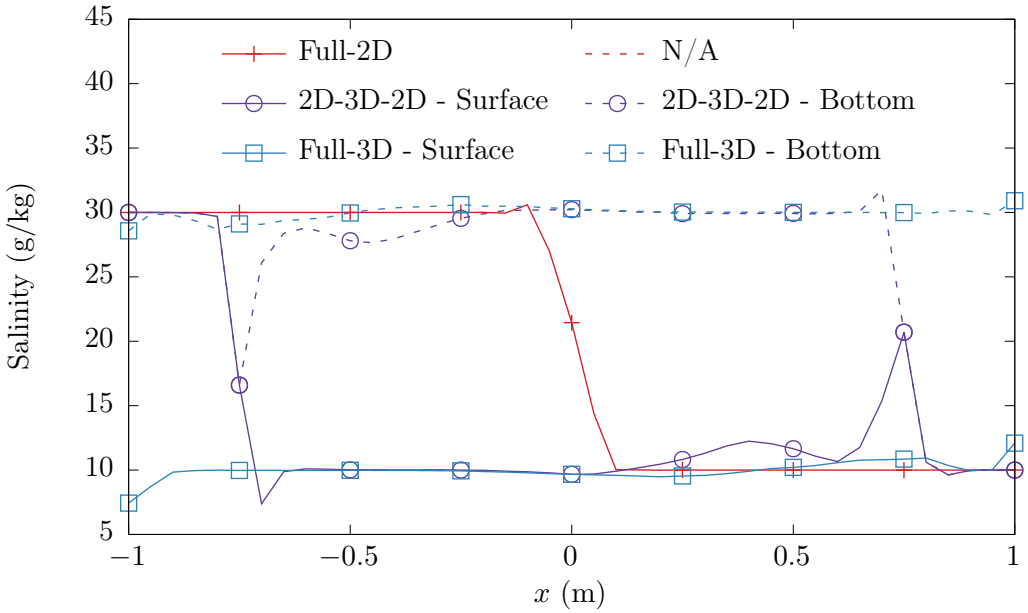

(h) Salinity at $t = 32\,\mathrm{s}$

Figure 4.22: (Cont.) Lock-exchange test: Comparison of solutions in the full-2D, 2D-3D-2D coupled, and full-3D models at different timestamps.

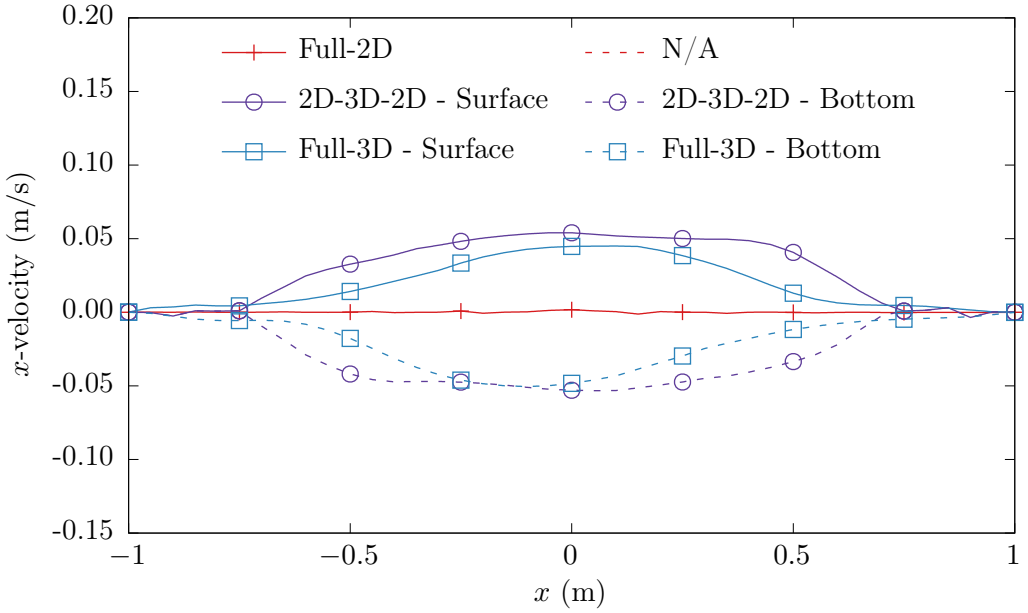

(i) x-velocity at $t = 40\,\mathrm{s}$

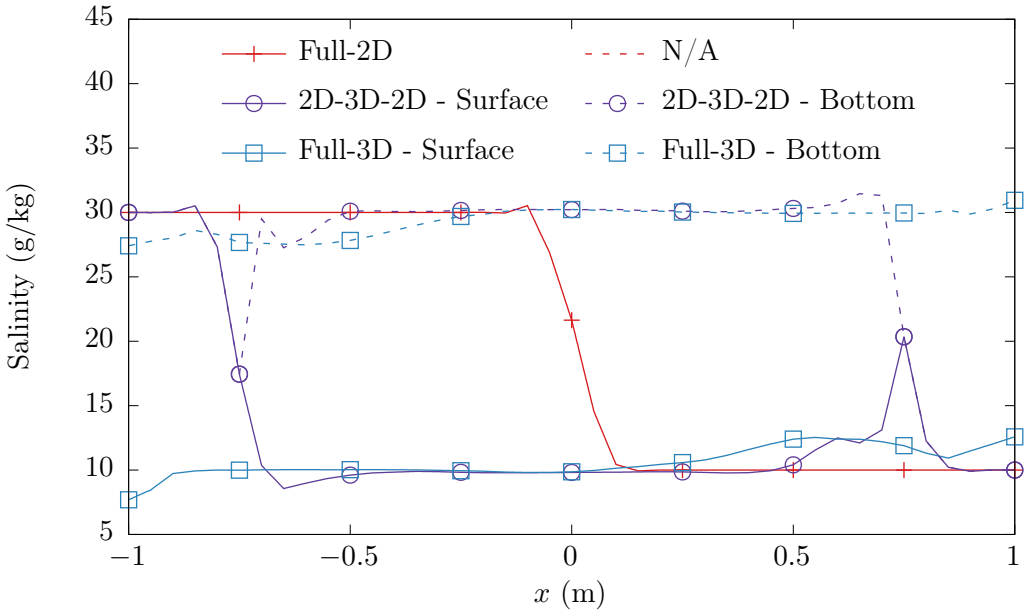

(j) Salinity at $t = 40\,\mathrm{s}$

Figure 4.22: (Cont.) Lock-exchange test: Comparison of solutions in the full-2D, 2D-3D-2D coupled, and full-3D models at different timestamps.

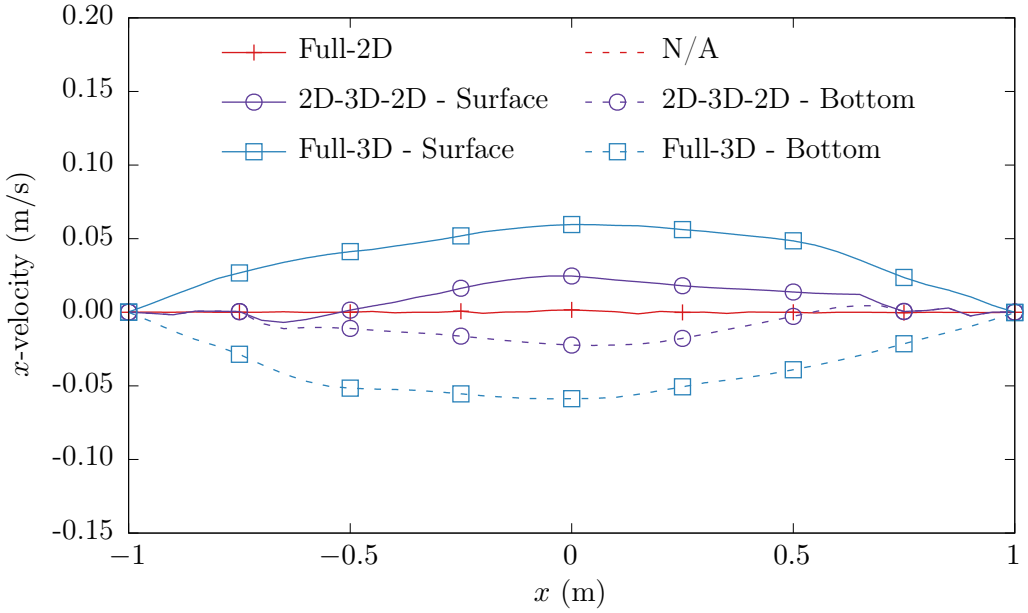

(k) x-velocity at $t = 48\,\mathrm{s}$

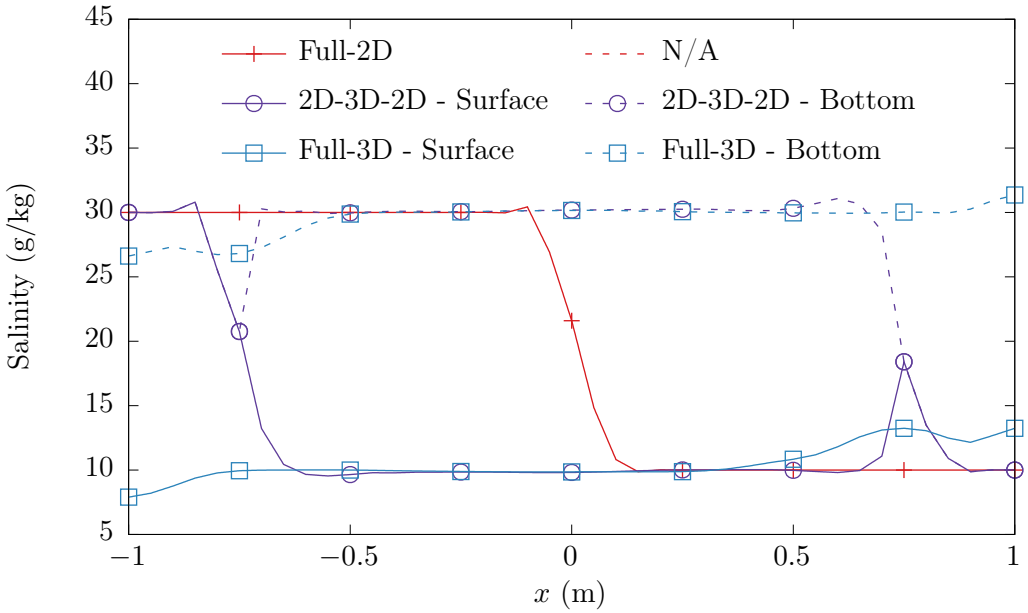

(l) Salinity at $t = 48\,\mathrm{s}$

Figure 4.22: (Cont.) Lock-exchange test: Comparison of solutions in the full-2D, 2D-3D-2D coupled, and full-3D models at different timestamps.

- In Figures 4.22i to 4.22l, the shocks are seen to have reflected, as evident from the bumps in salinity graphs near the domain boundary in case of the full-3D model and the 2D-3D interfaces in case of 2D-3D-2D coupled model.

- It is noticed from the salinity plots that the salinity discontinuity at the 2D-3D interfaces is maintained there in the 2D-3D-2D model, and from the x-velocity plots that the x-velocity in the 2D subdomains remains relatively close to zero. It appears that for this test case, the 2D-3D interfaces effectively act as walls where the velocity and salinity shocks get reflected from instead of passing through. This contrasts with the baroclinic flume test case from the previous section, in which the salinity front is forced to cross the interface due to the general non-zero average horizontal flow of water across the 2D-3D interface.

Having observed the behavior of the models in this test case, the importance of using engineering sense when building coupled models can be seen, since it is as easy to combine the weaknesses of 2D and 3D models as it is to combine their strengths. Instead of a 2D-3D-2D coupled model used here, if a 3D-2D-3D coupled model would have been used with a 2D submodel located in the center and containing the salinity discontinuity, then the solution of that model would remain same as that of the full-2D model. Moreover, this would come at an increased computational cost compared to same solution obtained using the full-2D model. On the other hand, assuming the region and time

range of interest to respectively be the center of the domain and $t \in (0, 16)$ s, the 2D-3D-2D coupled model used here gives results similar to the full-3D model at a reduced computational cost. If, for example, the region of interest would have been the eastern end of the domain, then a 2D-3D coupled model with a 2D model on the (opposite) western end would give acceptable results at a reduced cost. If the time range of interest would have been less than 8 s, then larger 2D regions could have been used in the 2D-3D-2D coupled model. On the other hand, if the time range of interest would have been 48 s, then the results show that the 2D-3D-2D coupled model used here is not an appropriate choice because the coupled solution eventually becomes different from the full-3D solution. Thus, it is important to consider the time range and region of interest when building coupled models and analyzing their solutions.

This concludes the verification of 2D-3D coupled models. The next chapter presents two simple validation tests, followed by another one which demonstrates two applications.

Chapter 5

Validation of 2D-3D coupling

Once verification of a computational code is completed, the next step is to validate it. Validation is important for any scientific software to be used for real-world applications. It ensures that the relevant physics have been included and the correct equations are being used to model the phenomenon under consideration. For the finite element method, validation involves comparison of finite element solutions against real-world experimental or observed data. Validating 2D-3D coupled models in an ocean dynamics setting is a difficult task since building an ocean model for a real-world application involves a lot of complicated steps, such as estimating bottom friction, bathymetry smoothing for maintaining stability, and obtaining atmospheric forcing and tidal data in the right format. The model must be calibrated, which involves trial and error through multiple simulations, given that an inverse modeling framework is currently not implemented in this work. Hence, it is difficult to set up test cases involving real-world measurements, in which 2D-3D coupled models are shown to capture physics that full-2D or full-3D models alone are not able to. On the other hand, it is difficult to find small-scale experimental data for scenarios in which both full-2D and full-3D models are inadequate in some way even where the shallow water equations are applicable, but where 2D-3D coupled models

succeed. As a result, comparison with small-scale experimental data becomes more of a full-2D or a full-3D model validation problem. That is why, the test cases presented in this chapter are only a partial measure of the performance and suitability of 2D-3D coupled models in simulating real-world applications, and validation is not a focus of this work. Instead, two applications are presented in the next chapter to highlight the key capability of coupled models in being able to simulate baroclinic scenarios involving wetting and drying, and in allowing computationally cheaper models in some cases. In this chapter, comparison of results of 2D-3D coupled models with two experiments taken from the literature are presented. The first test case is an experiment of flow around an emergent spur dike [70, 95]. The second one is a partial-breach dam-break experiment [34].

5.1 Emergent spur dike experiment

Spur dikes, also known as groynes, are obstructions constructed on the bank of a river with one end inside the river and another on the bank. They are of practical significance since they reduce the flow speed close to the bank, protecting it from erosion. Multiple experiments of a scaled down model of a channel with an emergent spur dike are given in [70, 95], one of which is used as a validation test case in this section. In this experiment, a plate of width $B = 0.152\,\mathrm{m}$ and thickness $0.03\,\mathrm{m}$ is inserted in a rectangular channel. The domain is given by $(0, 37)\,\mathrm{m} \times (0, 0.92)\,\mathrm{m}$, and the channel has a flat bed at an elevation of $b(x, y) = 0\,\mathrm{m}$. The dike is located at $x = 14.0\,\mathrm{m}$, perpendicular

to the southern boundary and the bed. It is tall enough for the water to flow only around it and not over it. A constant inflow of $Q = 0.0453\,\mathrm{m}^3/\mathrm{s}$ is supplied from the western boundary at $x = 0\,\mathrm{m}$. The measured water depth in the experiment at steady state is $H = 0.189\,\mathrm{m}$ downstream at the eastern boundary at $x = 37\,\mathrm{m}$, where the water is allowed to flow out of. Figure 5.1 shows a 2D-3D-2D coupled model used for simulating this experiment. The

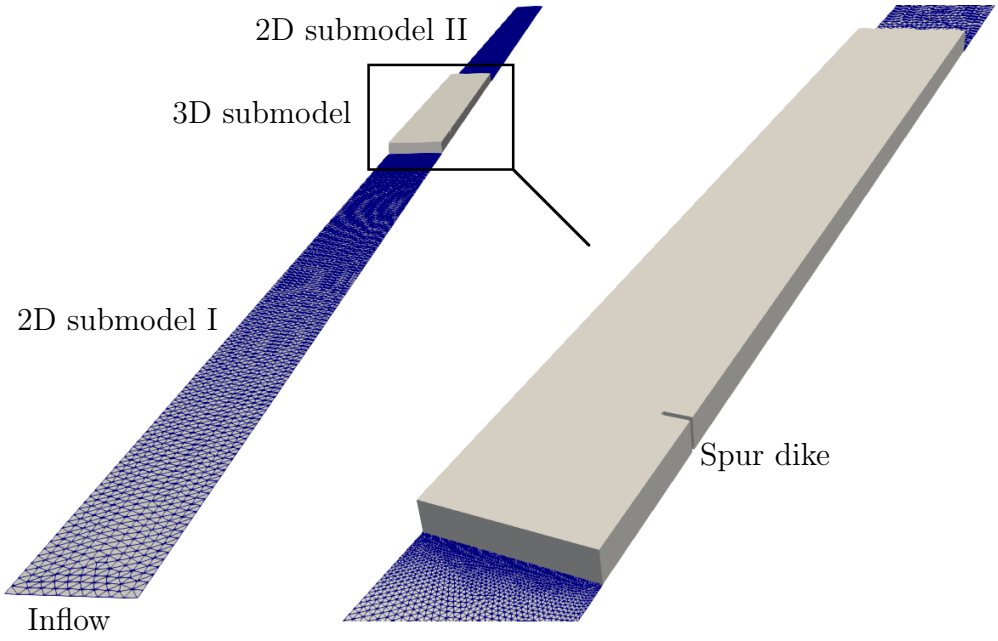

Figure 5.1: Coupled 2D-3D-2D mesh for the spur dike validation case.

3D submodel has a vertical resolution of four element layers. In this numerical model, the boundary conditions are no-normal-flow on the north and south boundaries along the length, inflow Q specified on the western boundary, and water depth fixed at H at the eastern boundary. Initial conditions on the numerical model are water at rest with a constant water depth of $H = 0.189\,\mathrm{m}$.

First order backward Euler time stepping with a time step size of 50 s is used to allow the model to reach steady state sooner. A fine mesh is used to keep mesh discretization errors lower. The simulation achieves steady state at an ending time of 350 s. An isotropic eddy viscosity of 0.001 is used in the 2D submodels, whereas the Smagorinsky scheme is used in the 3D one with the Smagorinsky coefficient set to 0.2. Manning's bottom friction coefficient is set to 0.015. Side-wall friction is ignored.

A vortex is seen downstream in the vicinity of the dike and the wall during the experiment, and there is flow in the upstream direction along a portion of the southern edge. This can be seen in Figure 5.2, which shows the steady-state streamlines in the 3D submodel. There is a location along the southern edge where the x-velocity changes sign, upstream and downstream of which its value is respectively negative and positive. This location is called the reattachment point, and the distance between the spur dike and the reattachment point is called the reattachment length. The average value of the reattachment length over multiple experiments with different inflow and depth values was reported in [70] to be 12 times the width of the spur dike. For the chosen model parameters, a reattachment length of 11.49 times the dike width is obtained for the 2D-3D-2D coupled model.

The x-velocity profiles near the bed and the surface are also compared at different cross-sections of the channel. The eight profile locations are given by $x' = \{2, 4, 6, 8\}B$, and $z = \{0.03, 0.85\}H$, where H is the water depth, B is the dike width, and x' is the distance between the downstream cross-sections

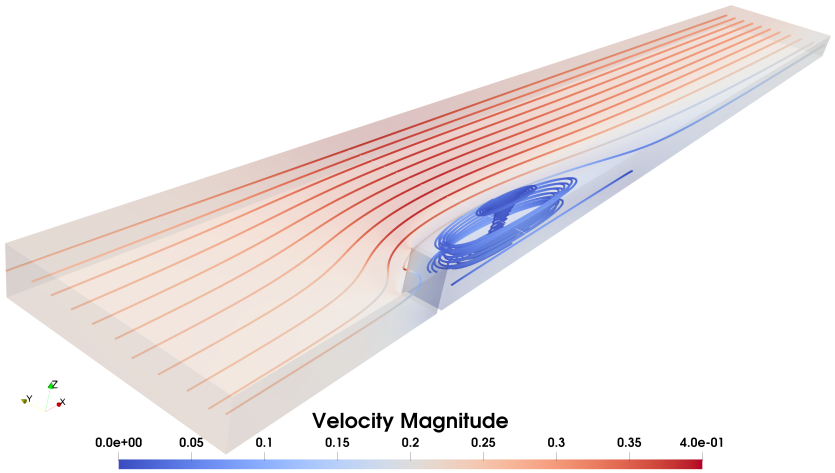

Figure 5.2: Spur dike test: Streamlines showing a vortex downstream of the dike.

and the dike. Figures 5.3 and 5.4 show the comparison between the measured and simulated x-velocity profiles near the bed and the surface, respectively, along lines parallel to the y axis. It is noted that the simulated velocity profiles deviate from the measurements near the wall boundary due to the lack of wall-friction in the current implementation of the shallow water models used herein. The simulated velocity profiles close to the surface are in excellent agreement with measurements, but those near the bed deviate slightly. This could possibly be because the ad hoc value of 0.015 used for the Manning's coefficient may be inappropriate, or due to lack of enough vertical resolution. It is highly unlikely that the problem here is with the coupled model given that the 2D-3D interfaces are far away from the measurement locations.

As mentioned at the beginning of this chapter, this test case is not designed to validate 2D-3D coupled models and is more of a validation of the

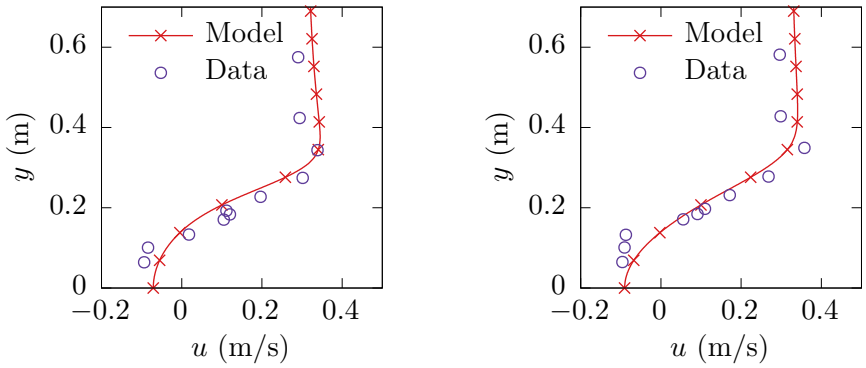

(a) $x'/B = 2$

(b) $x'/B = 4$

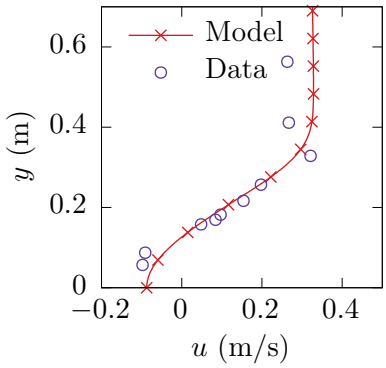

(c) $x'/B = 6$

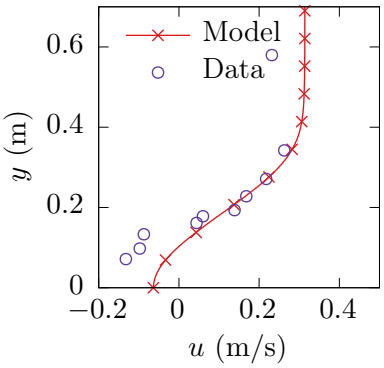

(d) $x'/B = 8$

Figure 5.3: Spur dike test: Measured [70] and computed x-velocity horizontal profiles near the bed, $z = 0.03H$ for different x'/B values.

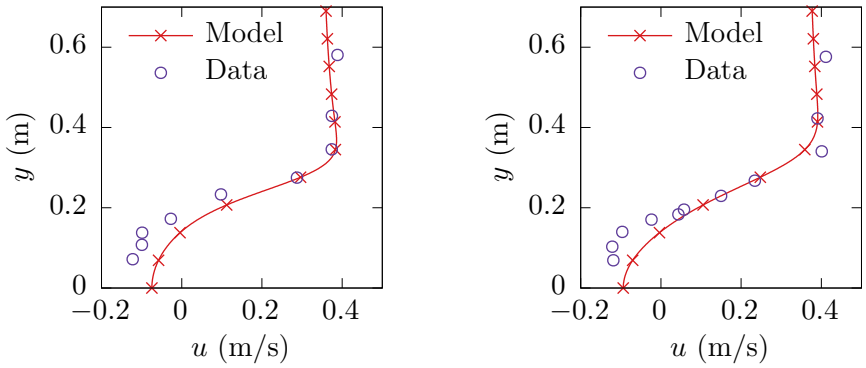

(a) $x'/B = 2$

(b) $x'/B = 4$

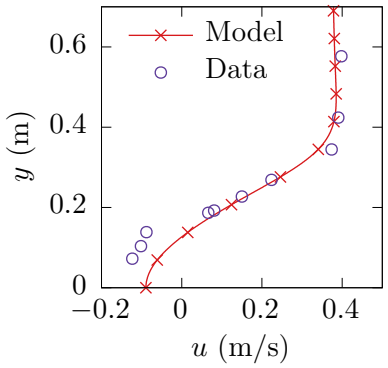

(c) $x'/B = 6$

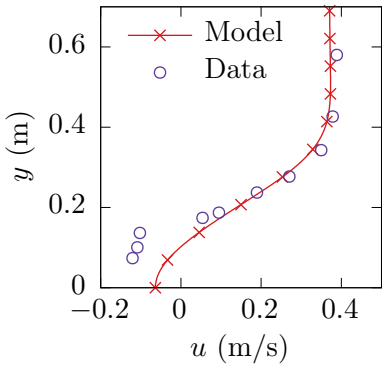

(d) $x'/B = 8$

Figure 5.4: Spur dike test: Measured [70] and computed x-velocity horizontal profiles near the surface, $z = 0.85H$ for different x'/B values.

bottom friction and the Smagorinsky-Lilly turbulence closure methods used in the 3D shallow water models. Nevertheless, this test case does serve an example of how non-critical regions in a full-3D model can be replaced with 2D subdomains to obtain a computationally cheaper model.

5.2 Partial-breach dam-break experiment

Dam-break simulations are a common test to check the stability and shock-capturing capability of shallow water models. In this case, experimental data of a partial-breach dam-break experiment [34] are used for validation. Figure 5.5 shows the full-2D and 2D-3D coupled models used in this test. A full-3D model cannot be used for comparison here since the domain contains a dry area. The domain Ω is a union of four rectangular parts, given by,

$$\Omega_1 = (-3.00, -0.10)\,\mathrm{m} \times (-2.15, 2.15)\,\mathrm{m},$$

$$\Omega_2 = (-0.10, 0.00)\,\mathrm{m} \times (-0.20, 0.20)\,\mathrm{m},$$

$$\Omega_3 = (0.00, 0.10)\,\mathrm{m} \times (-0.20, 0.20)\,\mathrm{m},$$

$$\Omega_4 = (0.10, 8.00)\,\mathrm{m} \times (-2.15, 2.15)\,\mathrm{m}.$$

The positive x axis points along the downstream direction. The gate is located at the common boundary between Ω_2 and Ω_3, along $y \in (-0.2, 0.2)\,\mathrm{m}$ at $x = 0\,\mathrm{m}$. This is seen in the 2D-3D coupled mesh in Figure 5.5 as an apparent discontinuity that spans a width of one element layer in the numerical model. $\Omega_1 \cup \Omega_2$ is the upstream reservoir, $\Omega_3 \cup \Omega_4$ is the initially dry downstream area. There are walls all along the domain boundary. The upstream reservoir is filled with water to a depth of $0.5\,\mathrm{m}$ before conducting the

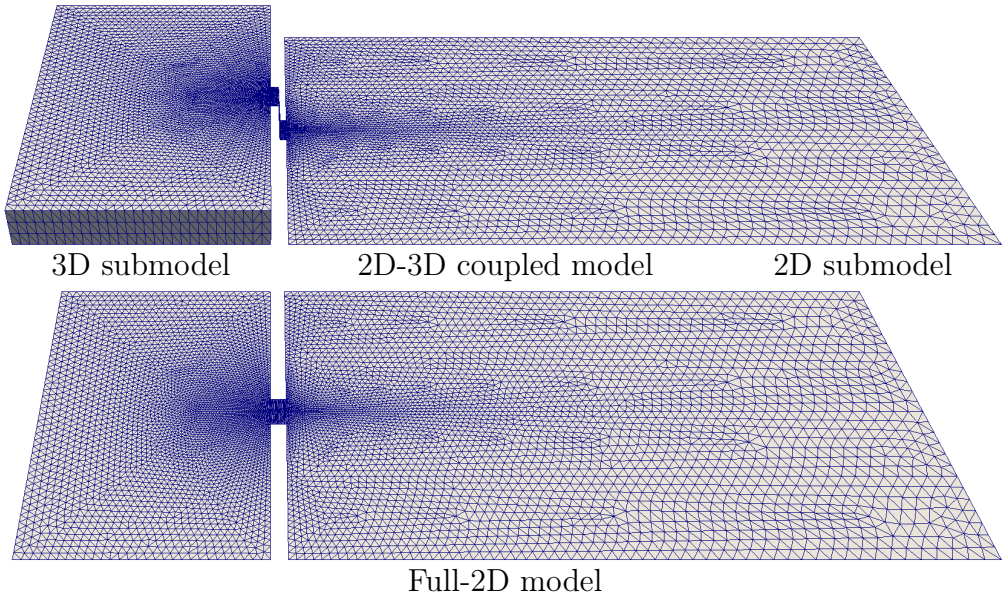

Figure 5.5: Partial-breach dam-break test: 2D-3D coupled (top) and full-2D (bottom) models.

experiment by quickly lifting the dam gate to mimic a dam-break scenario. In the 2D-3D coupled model, Ω_1 is the 3D submodel, and $\Omega_2 \cup \Omega_3 \cup \Omega_4$ is the 2D submodel. The simulation is run for a period of 10 s, using a time step of 0.01 s that can change adaptively without exceeding it. Five levels of mesh adaptivity are allowed downstream of the gate in the 2D subdomain. The Smagorinsky coefficient is set to 0.2 in Ω_1 and a high value of 1.0 in the remaining regions, required for stability. Wetting and drying tolerance is set to 0.03 m. Manning's friction coefficient is set to 0.01. All boundaries have a no-normal-flow Neumann boundary condition. The initial condition is water

at rest, with depth specified as,

$$h(x, y, 0) = \begin{cases} 0.5\,\text{m}, & \text{if } x \leq 0, \\ 0.0\,\text{m}, & \text{if } x > 0. \end{cases}$$

Figures 5.6a to 5.6d show the depth-averaged horizontal velocity magnitude in the 2D domains and the 3D velocity magnitude in the 3D subdomain at 1.5 s time intervals. The full-2D and 2D-3D coupled models appear to be in good agreement with each other in the common 2D region of both the models. In the figures, it is seen that the 3D and 2D submodels of the coupled model show different colors on either side of the 2D-3D interface. This is because the 2D submodel shows only the horizontal velocities, whereas the velocity results of the 3D submodel include a significantly high vertical velocity component of approximately 3 m/s at the 2D-3D interface. In fact, this is an indication that the vertical acceleration is non-negligible. This means that the full-3D vertical momentum equation in the Navier-Stokes equations being reduced to the hydrostatic equation (2.4) through scaling analysis is not an acceptable approximation for this test case. Indeed, dam-break scenarios are often non-hydrostatic and highly nonlinear in nature [13, 14]. The Serre equations [78], also known as the Green-Naghdi equations [36], may be more appropriate for modeling them [60] than the shallow water equations.

This is the reason why both the full-2D and 2D-3D coupled models fail to correctly track the observed location of the flood wave front, which is shown next in Figures 5.7a to 5.7d. The figures show the comparison between the simulated and measured locations of the flood wave front traveling over

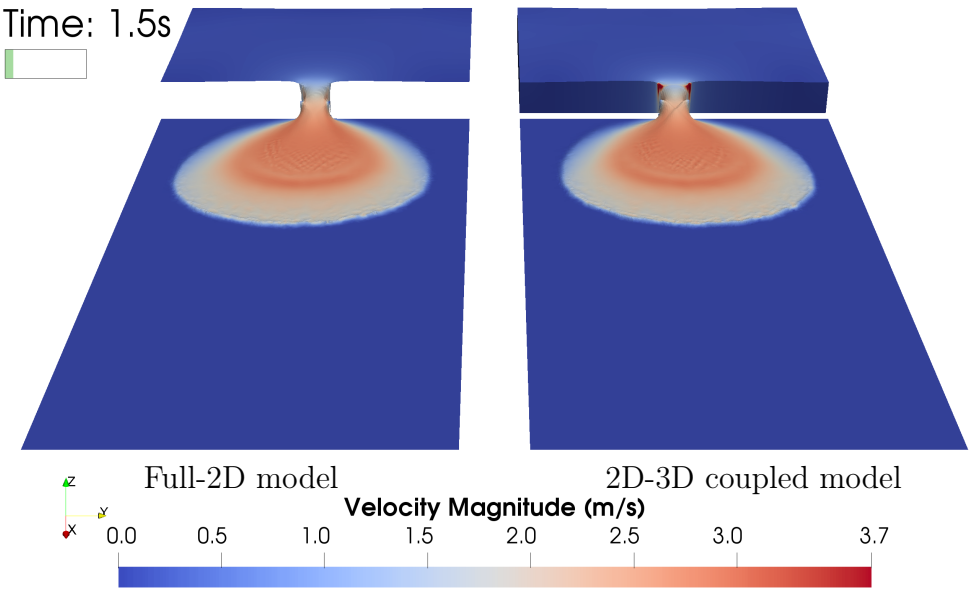

(a) $t = 1.5\,\mathrm{s}$

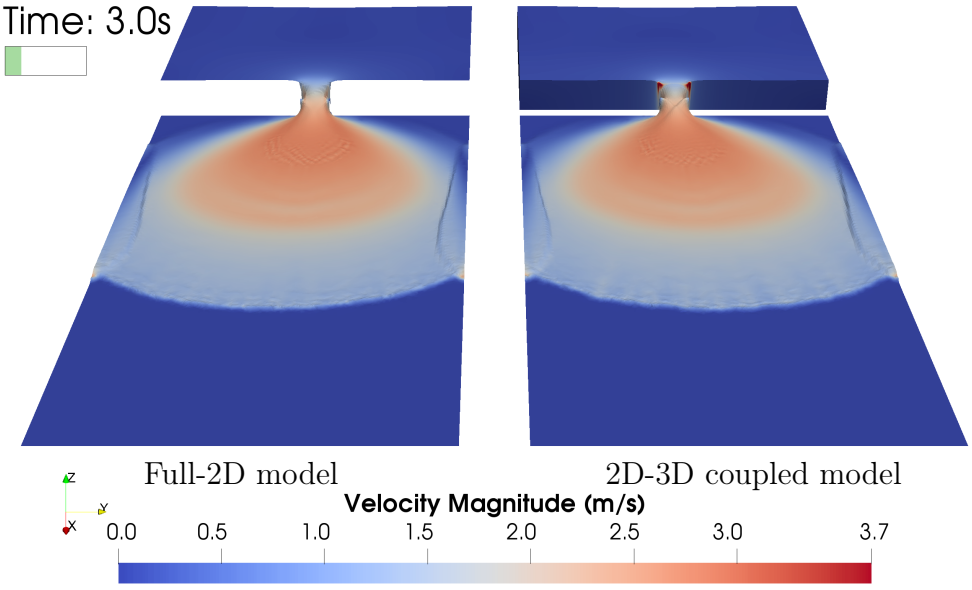

(b) $t = 3.0\,\mathrm{s}$

Figure 5.6: Partial-breach dam-break test: Velocity magnitude comparison between full-2D (left) and 2D-3D coupled (right) models.

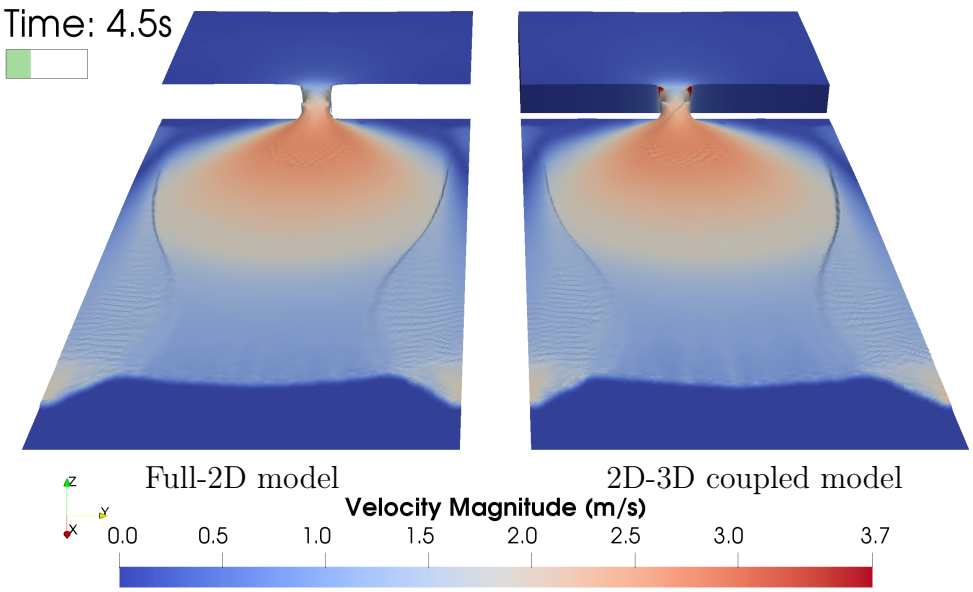

(c) $t = 4.5\,\mathrm{s}$

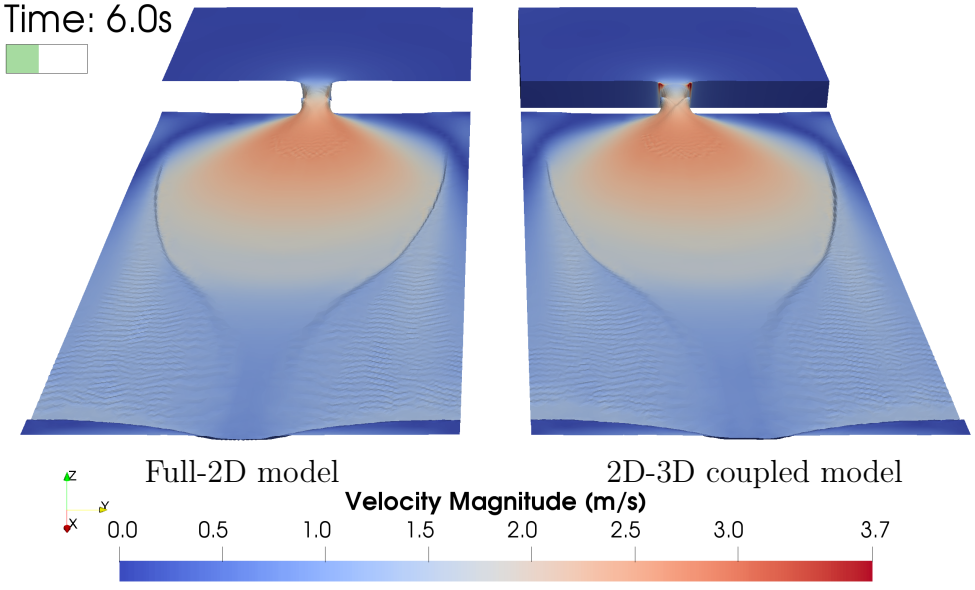

(d) $t = 6.0\,\mathrm{s}$

Figure 5.6: (Cont.) Partial-breach dam-break test: Velocity magnitude comparison between full-2D (left) and 2D-3D coupled (right) models.

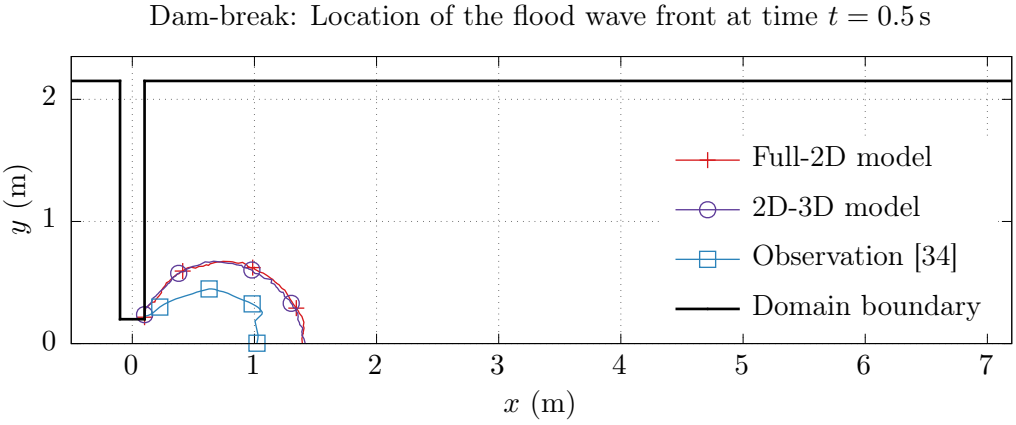

(a) $t = 0.5\,\mathrm{s}$

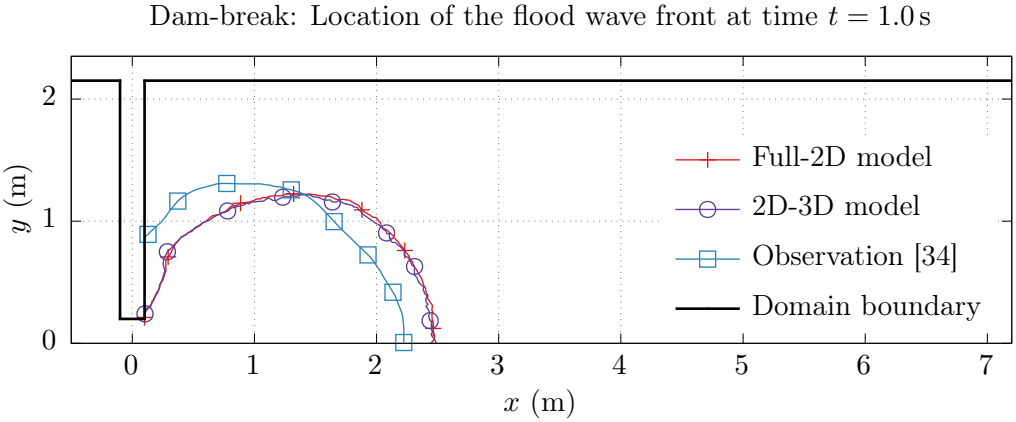

(b) $t = 1.0\,\mathrm{s}$

Figure 5.7: Partial-breach dam-break test: Comparison of the location of the flood wave front against observations [34] at different times.

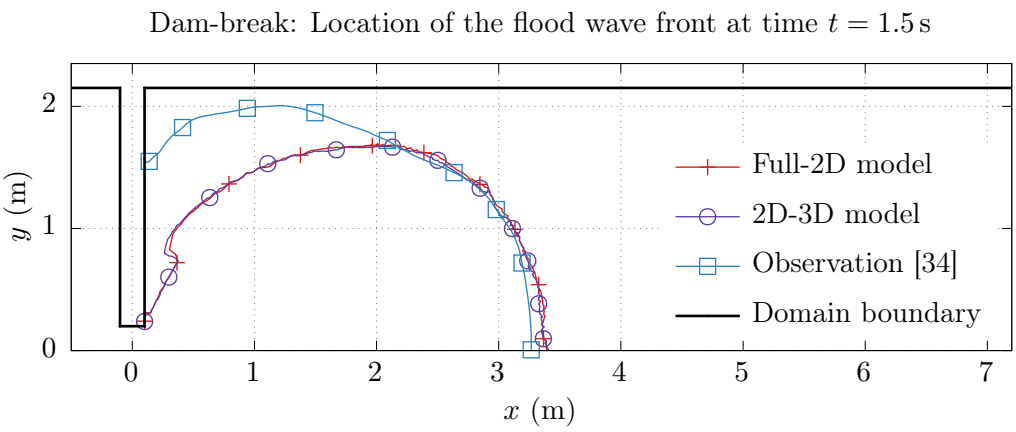

(c) $t = 1.5\,\mathrm{s}$

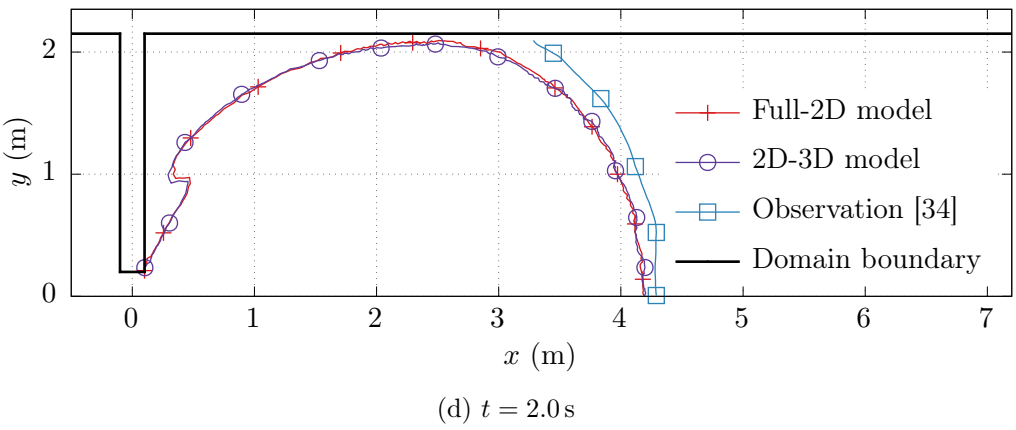

(d) $t = 2.0\,\mathrm{s}$

Figure 5.7: (Cont.) Partial-breach dam-break test: Comparison of the location of the flood wave front against observations [34] at different times.

dry land downstream at $t = \{0.5, 1.0, 1.5, 2.0\}$ s. It is seen that the simulated flood wave is initially faster than the actual flood wave in the experiment, but as the simulation progresses, the simulated wave starts lagging behind the experimentally observed wave front. Trying different values for the Smagorinsky coefficient (0.7, 0.75, 0.9, and 1.0), bottom friction (from 0.005 to 0.025), and wetting-drying tolerance (from 0.001 m to 0.1 m) amounting to over 40 different trial simulations still does not result in a simulation that is able to capture the flood front with an acceptable degree of accuracy.

Lastly, the location of the hydraulic jump at time $t = 6$ s, seen in Figure 5.6d, is compared against that observed during the experiment, extracted by digitizing one of the figures given in [34] showing the average measured surface y-velocity for the time interval $t \in (5, 6)$ s. The hydraulic jump observed in the experiment occurs after the non-hydrostatic flood front has passed further downstream, so that the hydrostatic assumption is likely valid in that region of the domain. The locations of the hydraulic jump in the full-2D and 2D-3D coupled simulations compare well with the experiment, as seen in Figure 5.8.

The validation test cases presented in this chapter are, to a significant extent, just a validation of full-2D and full-3D models and are unable to address the specific added capabilities of 2D-3D coupled models. The next chapter, therefore, presents two applications demonstrating the capabilities of coupled models in order to lay the groundwork for their further validation in the future.

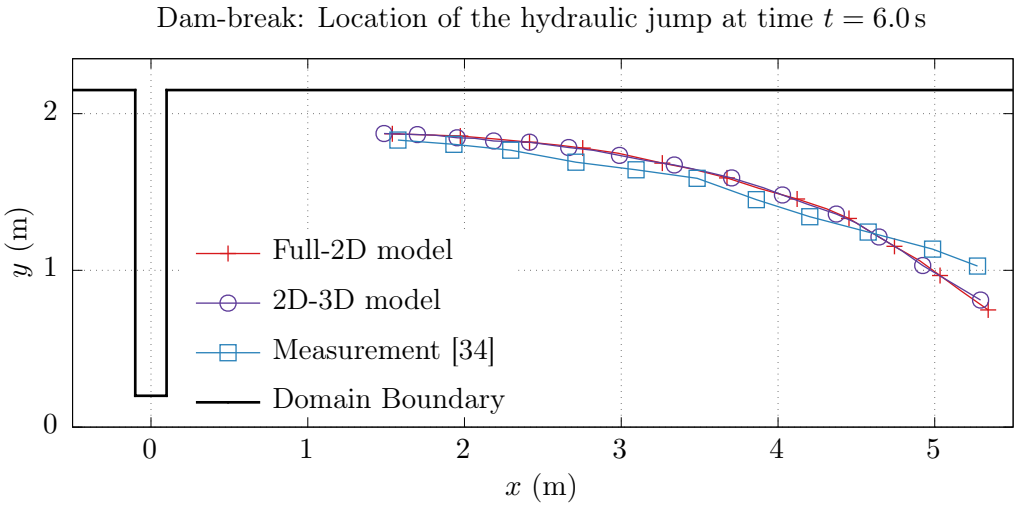

Figure 5.8: Partial-breach dam-break test: Comparison of the location of the hydraulic jump in the full-2D and 2D-3D coupled models against measurements [34] at time $t = 6\,\mathrm{s}$.

Chapter 6

Applications of 2D-3D coupled models

From the verification and validation tests given in the previous chapters, it is seen that 2D-3D coupled models produce results similar to solely 2D or 3D models in general. Thus, coupled models inherently satisfy all of the validation cases of 2D models and some of the tests of 3D models. Some of the validation tests of the 2D and 3D models used herein are given in [5, 6, 55, 74, 89]. However, as mentioned at the beginning of the previous chapter, it is difficult to find small-scale experiments that allow validating the added capability of handling baroclinicity as well as wetting-drying using coupled models. Real-world measurements that would allow such validation in an ocean dynamics setting may be available, but are time-consuming to set up. Therefore, this chapter presents ad hoc applications of 2D-3D coupled models for demonstrating their capabilities and providing valuable insight into what data would be needed to enable their conclusive validation in the future. Separate 2D and 3D simulations are also run to enable comparison, though they are not a substitute for rigorous validation against real-world scenarios. Coupled models are used to simulate flow in an idealized estuary and in Galveston Bay. Both the test cases involve wetting-drying and baroclinicity with the density of water being dependent on salinity. The 3D models involved cannot handle wetting-drying

but can simulate vertical mixing due to baroclinicity, whereas the 2D models involved can handle wetting-drying but do not have vertical mixing. The 2D-3D coupled models can handle both in relevant regions.

6.1 Idealized estuary application

Consider an idealized estuary, with a river in the east flowing into an ocean in the west. The y axis is aligned with the north, and the domain shown in Figure 6.1 (not drawn to scale) is symmetric about the x-z plane. The bathymetry is divided into piecewise linear regions shown as triangles and quadrilaterals in the figure. The domain is 300 km long and 100 km wide. The bed elevation at the deep ocean boundary on the left (edge AD in the figure) is -200 m. The ocean coastline initially corresponds to $x = 100$ km (edges BG and EI), and a portion of the riverbank corresponds to $y = \pm 1.51$ km (edges GO and IQ). The bed elevation at the river inflow end along $y \in (-1.49, 1.49)$ km at $x = 300$ km on the right (edge LN) is -5 m. The node coordinates and bathymetry are given in Table 6.1.

The initial conditions are water at rest with a constant water surface elevation of 0.0 m, and salinity of 35 g/kg in the entire domain. The north and south boundaries (edges AC and DF in the figure) and the eastern boundary except for the river (edge LN) have no-normal-flow Neumann BCs. A constant inflow of 29 800 m^3/s with a salinity of 1 g/kg is specified as river inflow from the east. An elevation time-series is specified at the deep ocean, given by,

$$\eta(t) = a(1 - \cos(2\pi t/T)), \tag{6.1}$$

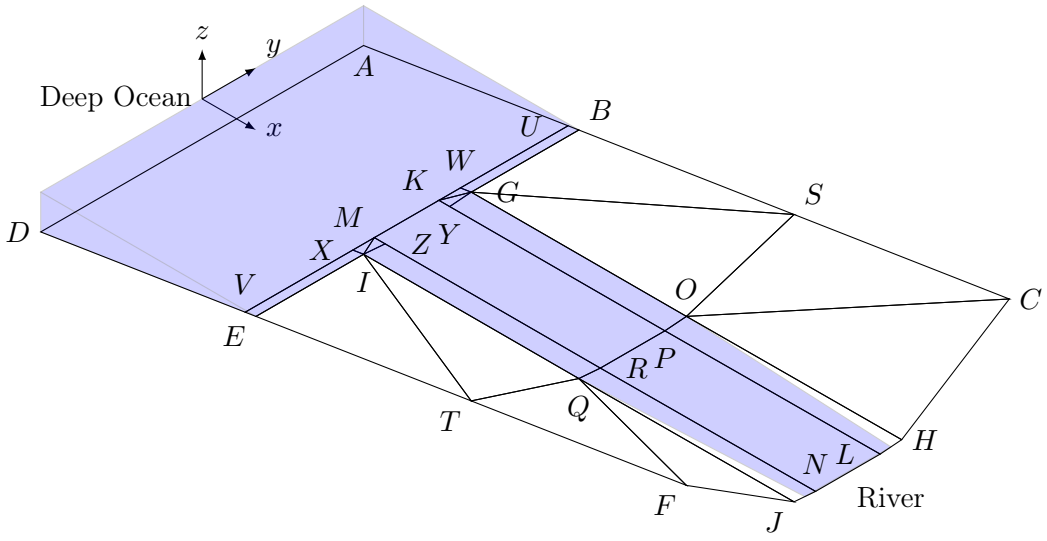

Figure 6.1: The idealized estuary domain. (Figure not drawn to scale.)

Table 6.1: Node locations and bathymetry of the idealized estuary.

Point[1]	Location (km, km, m)
A	(0, 50 , −200)
B	(100, 50 , 0)
C	(300, 50 , 400)
G	(100, 1.51, 0)
H	(300, 1.51, 5)
K	(95, 1.49, −10)
L	(300, 1.49, −5)
O	(200, 1.51, 0)
P	(200, 1.49, −10)
S	(200, 50 , 200)
U	(95, 50 , −10)
W	(95, 1.51, −10)
Y	(100, 1.49, −10)

[1] Symmetric about x-z plane; See Figure 6.1.

where the amplitude a is 0.5 m and the time period T is 1 day.

The results obtained from three models shown in Figure 6.2 are compared. The first model is a full-2D model covering the entire domain. The second one is a 2D-3D coupled model covering the entire domain, with the 3D submodel given by *A-U-W-K-Y-P-R-Z-M-X-V-D*, and the 2D submodel covering the remaining region, including all wetting-drying areas. The third model can be considered equivalent to what would be a 3D-only model given by *A-U-W-K-Y-P-L-N-R-Z-M-X-V-D*, with no-normal-flow Neumann boundary conditions on all boundaries except the deep ocean and river inflow ones. However, it is actually another 2D-3D coupled model with the 3D region being the same as that in the second model, and the 2D region given by *P-L-N-R*. The reason for using a 2D-3D coupled model instead of the aforementioned 3D-only model is to save computational cost since the river region has a very fine mesh, and because the main region of interest in this application is where the river meets the ocean, close to points K and M. With this understanding, the third model is referred to as a 3D-only model for the rest of this section to distinguish it from the second model which is referred to as the 2D-3D coupled model. The 3D submodels have a vertical resolution of 3 element layers. A 10-day simulation is run with a time step of 0.5 hours.

Figures 6.3a to 6.3d show the surface and depth-averaged salinity in the 3D and 2D regions, respectively, at time intervals of 2.5 days. Since relatively freshwater flows into an initially saline domain, it leads to shocks traveling along the river. The shocks reach the ocean at $t \approx 2.5$ days as seen in Fig-

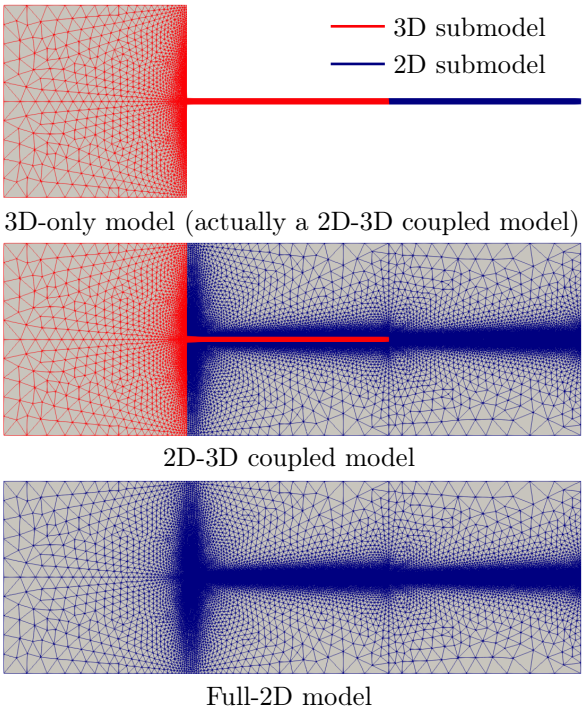

Figure 6.2: Idealized estuary meshes: Full-2D (bottom), 2D-3D coupled (center), and 3D-only (top) models. The 3D-only model is a 2D-3D coupled model without wetting-drying areas, and is a computationally cheaper replacement for an actual 3D-only model.

ure 6.3a. After that, they travel along the $\pm y$ directions near the coast till they reach the no-normal-flow BC on the north and south boundaries, as seen in the remaining subfigures.

Vertical mixing is seen to occur close to the coast in the 3D submodels, as shown in Figures 6.4a and 6.4b for two timestamps, $t = \{5, 10\}$ days. The figures show the movement of salt using balls with trailing lines. The balls represent the current position of salt, and the trailing lines represent the path it has traveled over the preceding 9 hours. Vertical mixing close to the mouth also relates with the x-velocity varying significantly over the depth, with negative values at the surface and positive values at the bed in this case. This is shown in Figure 6.5 for two timestamps, $t = \{5, 10\}$ days. The top and bottom subfigures respectively show the surface and bed x-velocities in the 3D subdomains. The x-velocity shown in the 2D subdomains is depth-averaged. The results of the 3D and 2D submodels in the coupled model are comparable to the respective regions in the 3D-only and full-2D models.

Wetting-drying is seen in the full-2D and 2D-3D models. Figures 6.6a to 6.6d show the comparison of the water surface elevation at four locations in the models over time, two of which correspond to the horizontal locations of points G and K in Figure 6.1. The top subfigures show the temporal variation in the full-2D and 2D-3D models at two locations along $x = 100\,\text{km}$, where the coastline initially lies; the 3D-only model does not extend to these two locations. The bottom subfigures show the surface elevation in all three models at two other locations along $x = 95\,\text{km}$, which corresponds to the 2D-

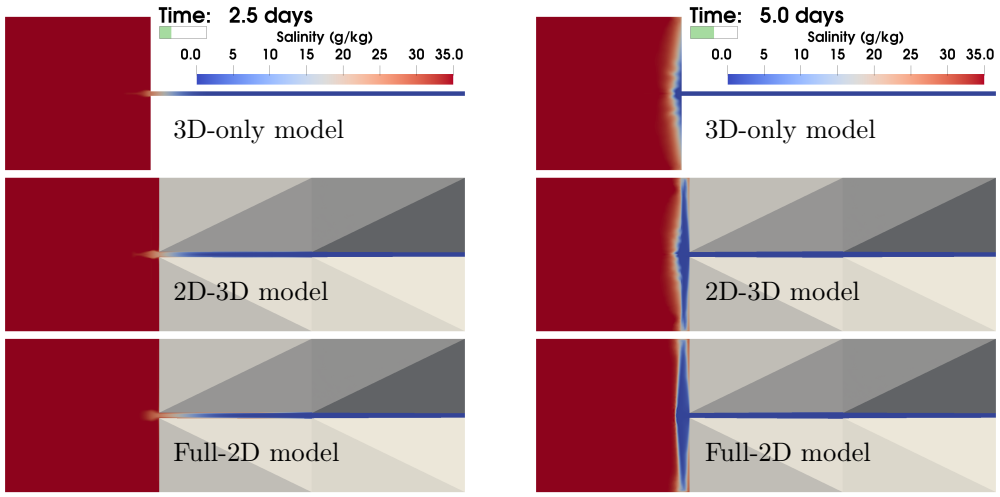

(a) $t = 2.5\,\text{days}$

(b) $t = 5.0\,\text{days}$

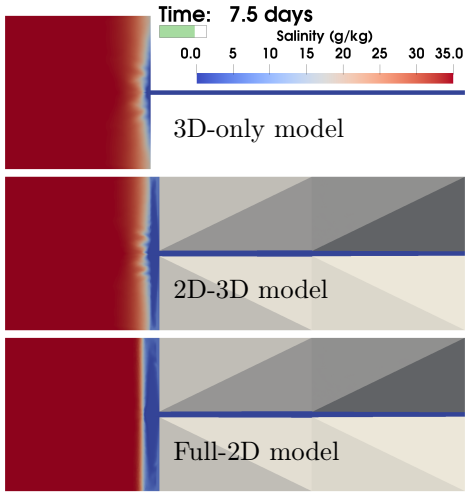

(c) $t = 7.5\,\text{days}$

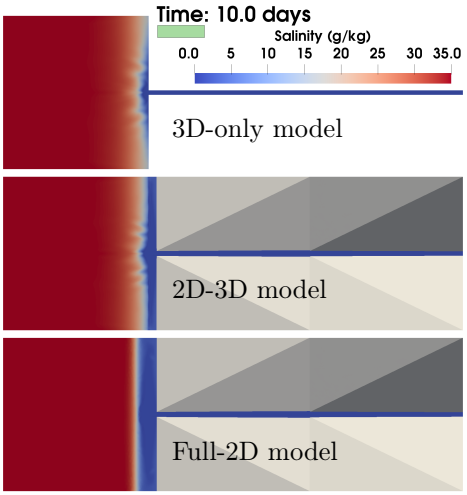

(d) $t = 10.0\,\text{days}$

Figure 6.3: Idealized estuary: Salinity in the full-2D, 2D-3D coupled, and 3D-only models.

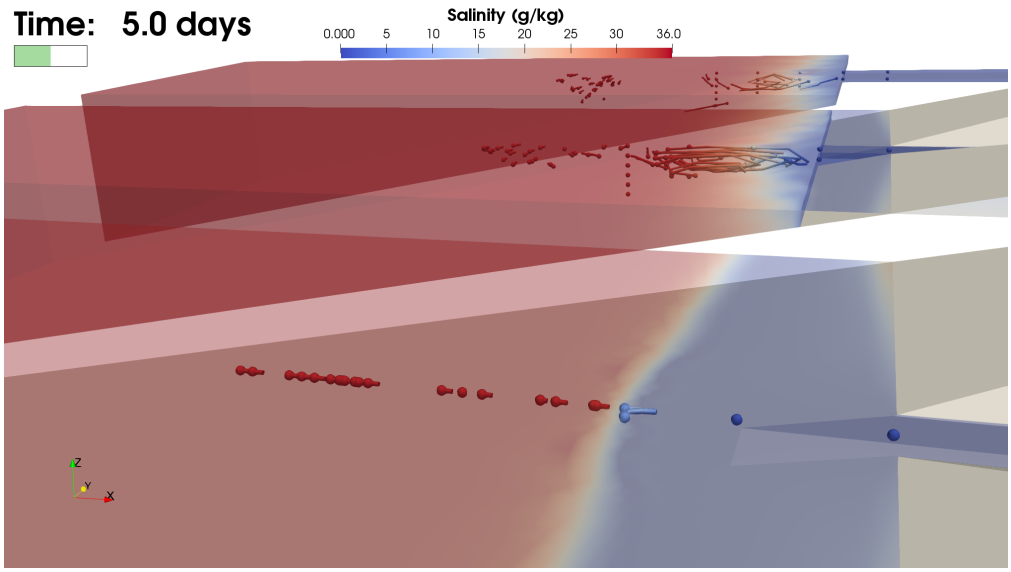

(a) $t = 5.0\,\text{days}$

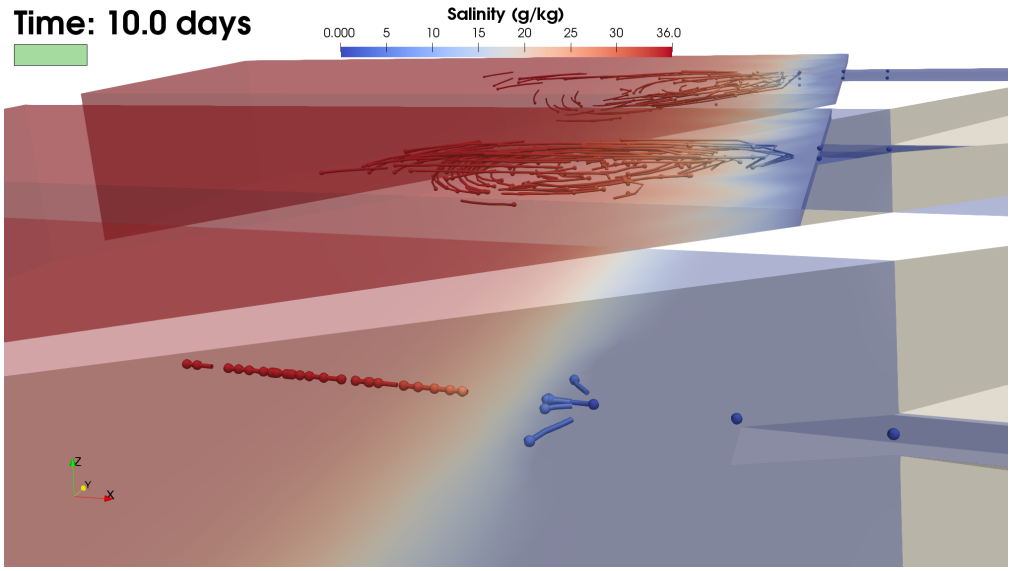

(b) $t = 10.0\,\text{days}$

Figure 6.4: Idealized estuary: Movement of salt in the full-2D (bottom), 2D-3D coupled (center), and 3D-only (top) models.

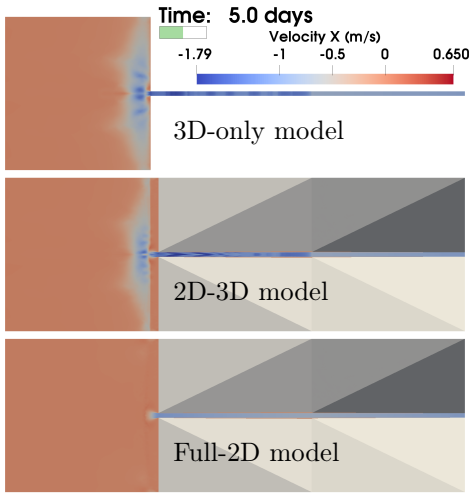

(a) Surface x-velocity at $t = 5.0$ days

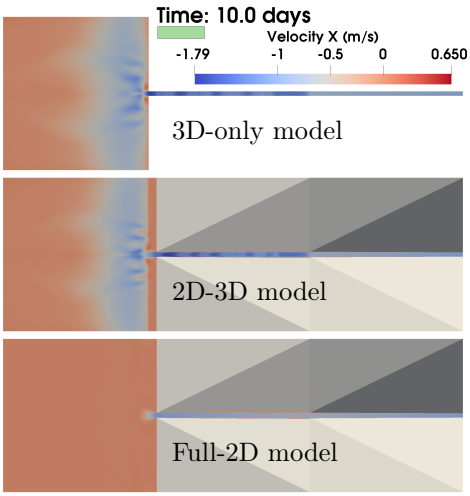

(b) Surface x-velocity at $t = 10.0$ days

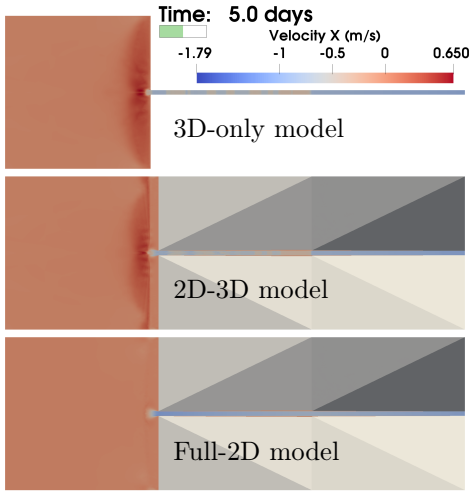

(c) Bed x-velocity at $t = 5.0$ days

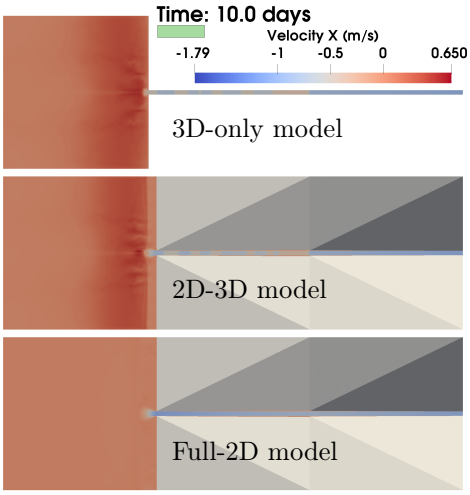

(d) Bed x-velocity at $t = 10.0$ days

Figure 6.5: Idealized estuary: x-velocity at the surface (top) and the bed (bottom) in the full-2D, 2D-3D coupled, and 3D-only models.

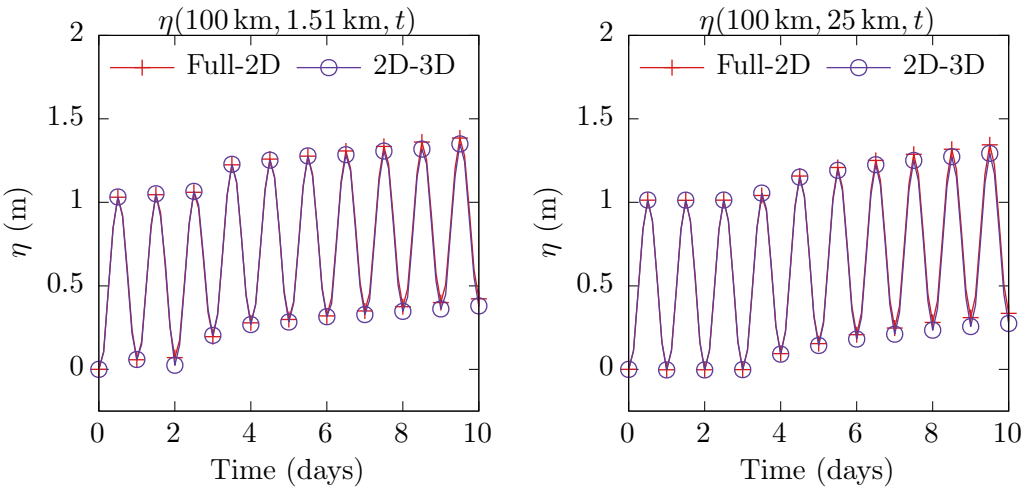

(a) Surface elevation at $(100, 1.51)$ km

(b) Surface elevation at $(100, 25)$ km

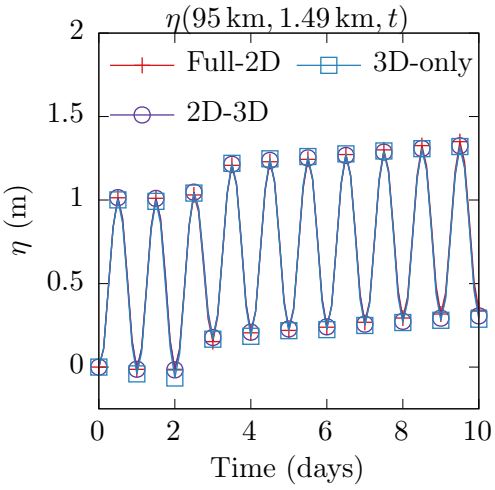

(c) Surface elevation at $(95, 1.49)$ km

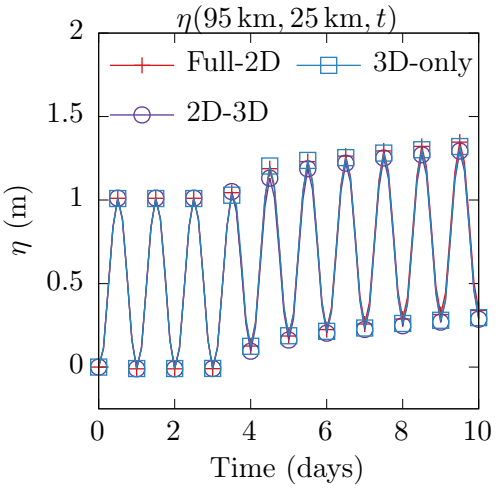

(d) Surface elevation at $(95, 25)$ km

Figure 6.6: Idealized estuary: Surface elevation in the models at four different locations, two close to the wetting-drying coastline (top) and two along the 2D-3D interface (bottom).

3D interface location in the coupled model. The surface elevation results of the models compare well with each other.

Figures 6.7 and 6.8 respectively show the x-velocity and salinity along $x \in (80, 100)\,\text{km}$ at $y = 0\,\text{km}$. The location is along the centerline of the model, close to the mouth of the river. Figures 6.9 and 6.10 respectively show the y-velocity and salinity along $y \in (-50, 50)\,\text{km}$ at $x = 92\,\text{km}$, which is parallel to the 2D-3D interface location of $x = 95\,\text{km}$ in the coupled model. The results show surface and depth-averaged values respectively in the 3D and 2D submodels, as may be the case. The coupled model shows results that are similar yet different compared to the full-2D and 3D-only models, as it should. The presence of substantially large 2D and 3D subdomains allows the coupled model to differentiate itself from the full-2D and 3D-only models.

That is not to say that the presented 2D-3D coupled solution is the best one. For example, engineering sense would suggest that vertical mixing, in reality, would extend right up to the coastline in this case, which cannot be seen in the coupled model in Figure 6.4 since that region is a 2D subdomain. Also, in Figure 6.5, the red and blue regions near the interface corresponding to positive and negative bed and surface x-velocities would likely also extend up to the coastline in a full-3D model with wetting-drying (if one could be implemented), instead of ending at the 2D-3D interface as seen. A better coupled model could be used to capture these effects to the maximum extent by placing the 2D-3D interface as close to the coastline as possible while ensuring that the depth along the interface does not drop to zero at any time during

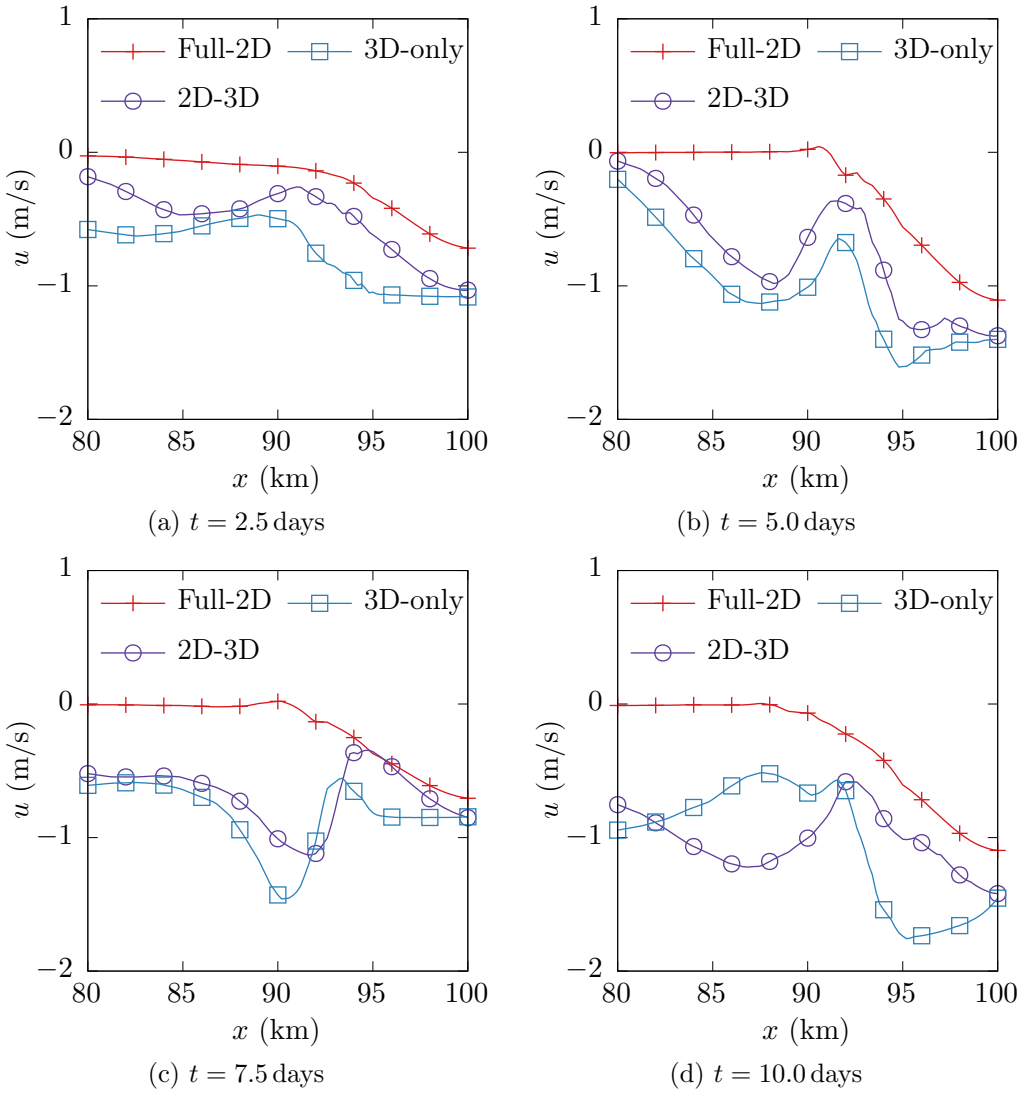

(a) $t = 2.5$ days

(b) $t = 5.0$ days

(c) $t = 7.5$ days

(d) $t = 10.0$ days

Figure 6.7: Idealized estuary: x-velocity in the full-2D, 2D-3D coupled, and 3D-only models along $x \in [80, 100]$ km at $y = 0$ km.

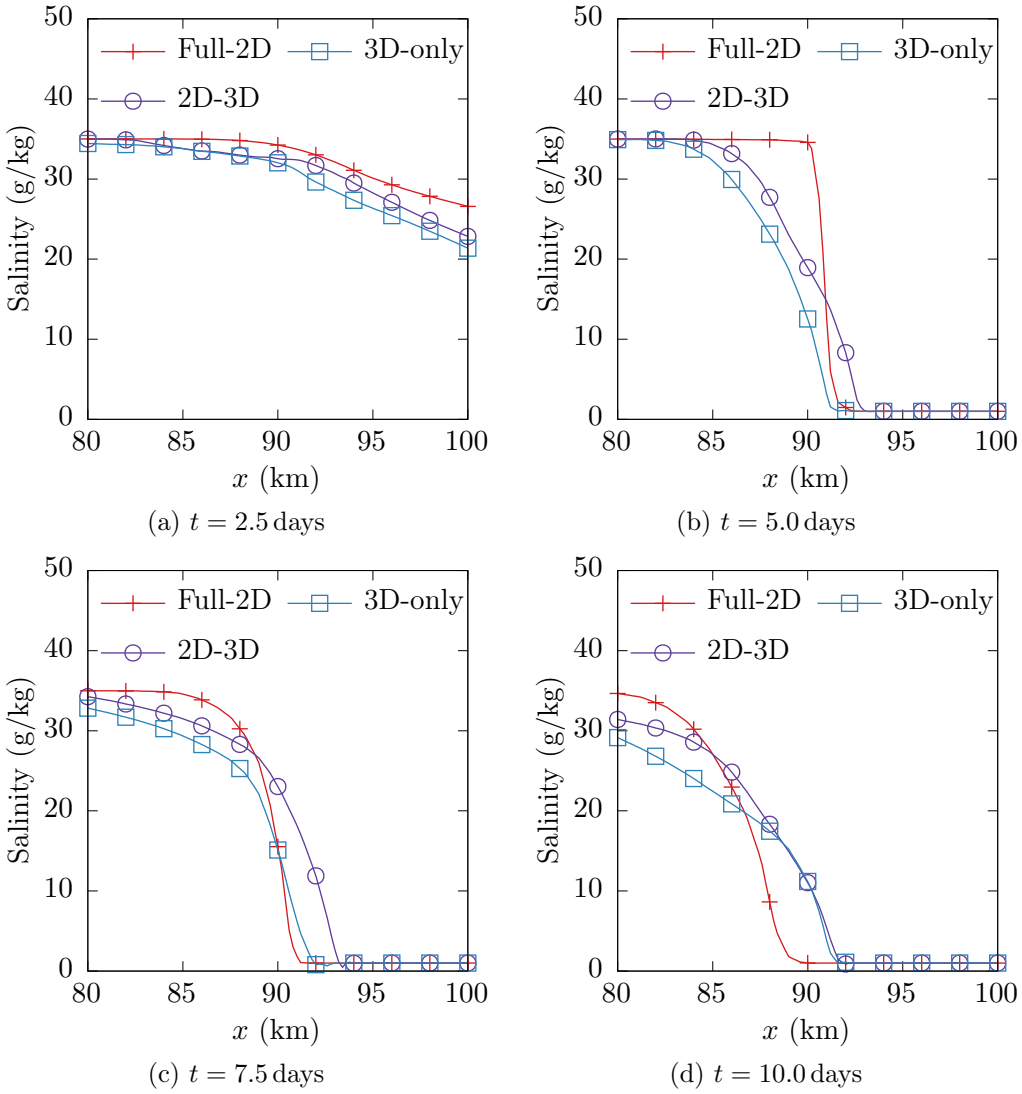

(a) $t = 2.5$ days (b) $t = 5.0$ days

(c) $t = 7.5$ days (d) $t = 10.0$ days

Figure 6.8: Idealized estuary: Salinity in the full-2D, 2D-3D coupled, and 3D-only models along $x \in [80, 100]$ km at $y = 0$ km.

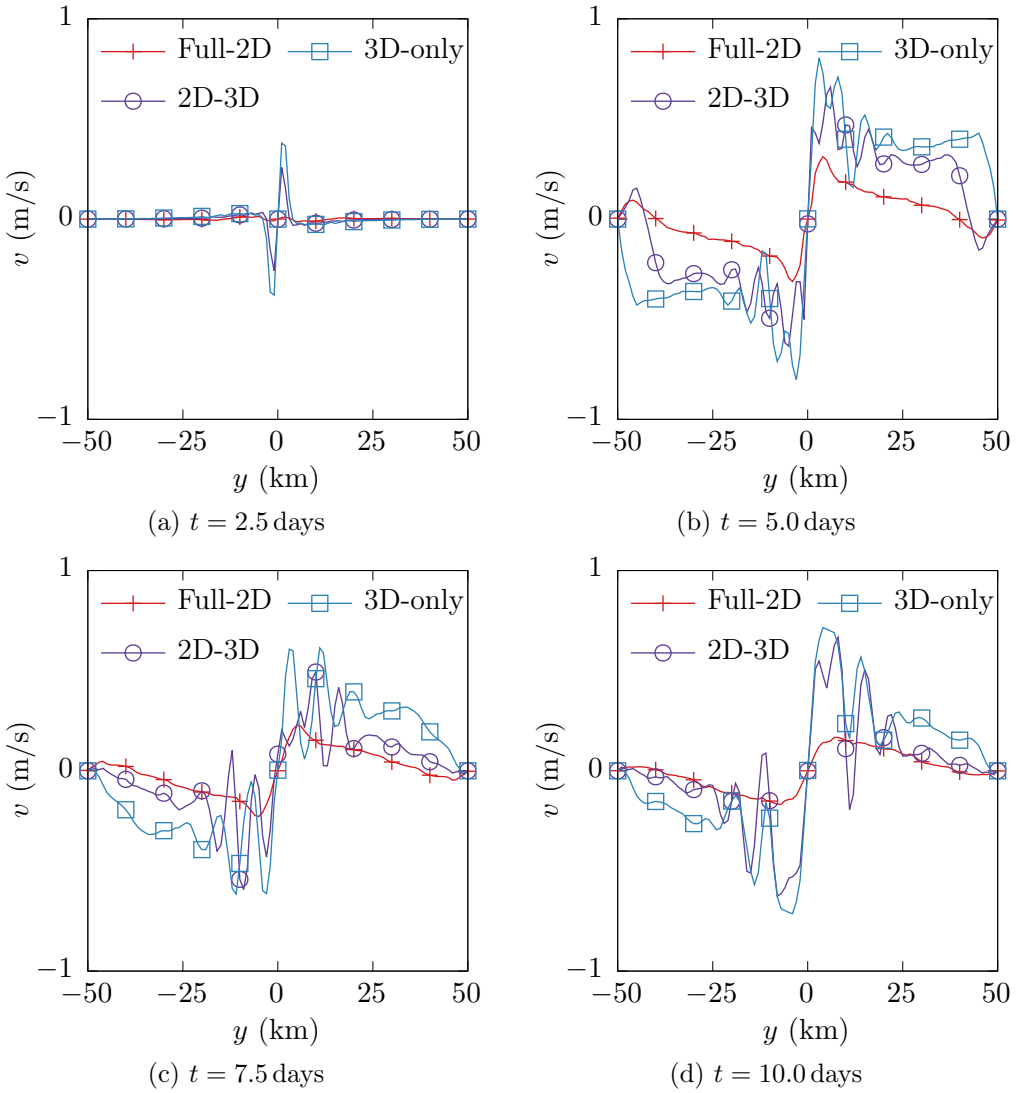

(a) $t = 2.5$ days (b) $t = 5.0$ days

(c) $t = 7.5$ days (d) $t = 10.0$ days

Figure 6.9: Idealized estuary: y-velocity in the full-2D, 2D-3D coupled, and 3D-only models along $y \in [-50, 50]$ km at $x = 92$ km.

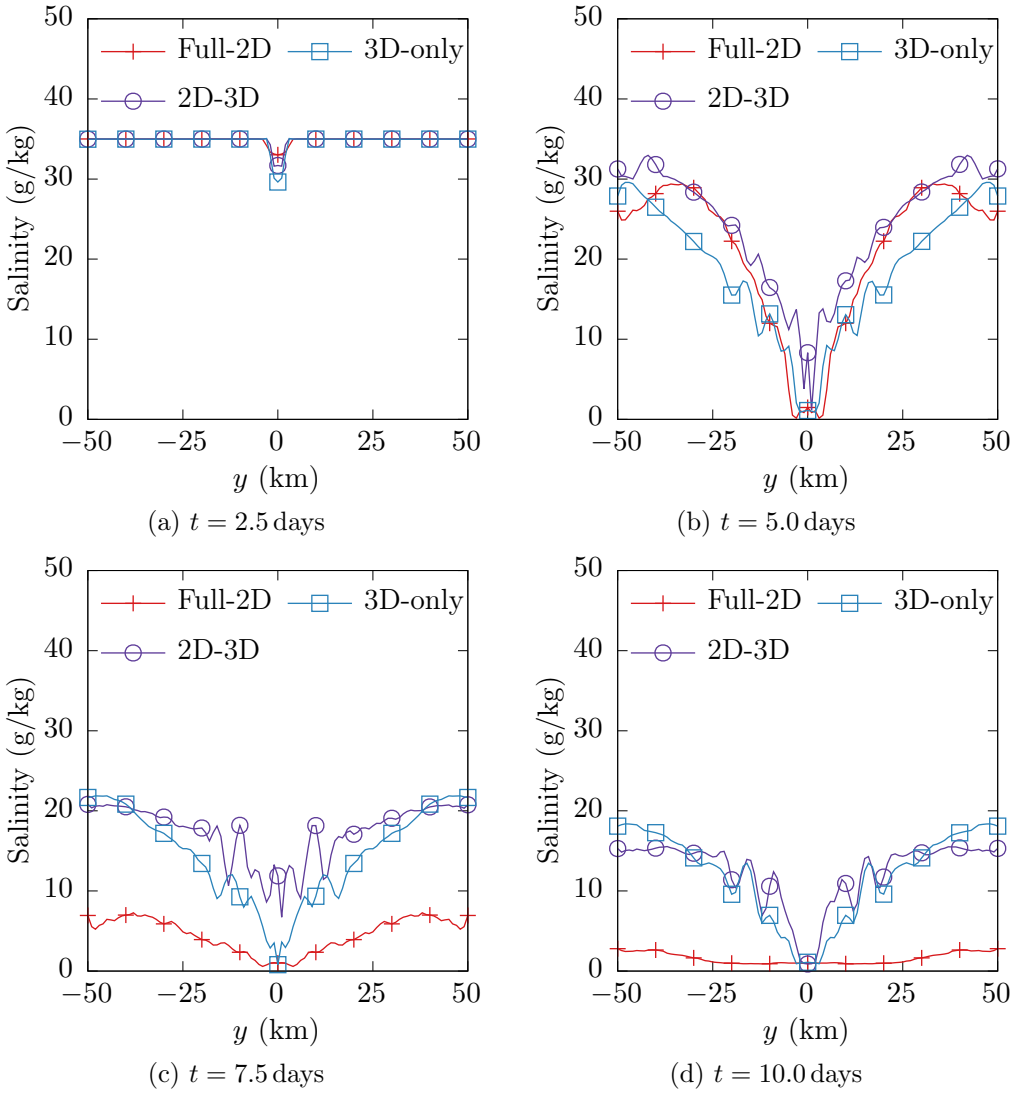

(a) $t = 2.5$ days (b) $t = 5.0$ days

(c) $t = 7.5$ days (d) $t = 10.0$ days

Figure 6.10: Idealized estuary: Salinity in the full-2D, 2D-3D coupled, and 3D-only models along $y \in [-50, 50]$ km at $x = 92$ km.

the simulation.

This test case demonstrates that coupled models can capture wetting and drying as well as baroclinicity. Given the lack of availability of full-3D models that can handle wetting-drying, coupled models would give the best available solution in such scenarios when used properly. The results of the 3D-only model, which is actually another 2D-3D coupled model here, demonstrate how a coupled model may be used to selectively replace certain 3D regions with 2D subdomains to reduce computational cost. The next test case presents an application of coupled models to Galveston Bay.

6.2 Galveston Bay application

An application of coupled models to an ad hoc baroclinic Galveston Bay test case with wetting-drying is presented in this section. The results of a 2D-3D coupled model are again compared with an equivalent full-2D model and a 3D-only model. The bathymetry of Galveston Bay is shown in Figure 6.11, and the meshes used in this application are shown in Figure 6.12.

The 3D submodels are extruded from a portion of the full-2D mesh and have a vertical resolution of three element layers throughout the domain. As was the case in the previous application, the 3D-only model does not have wetting-drying areas. Moreover, the western branch of the bay has not been modeled in the 3D-only model, as seen in Figure 6.12. Since it is a significant area, the 3D-only model is not a good representative of an actual 3D model of the bay. The 3D Galveston Bay model shown in Figure 2.2 is more appropriate

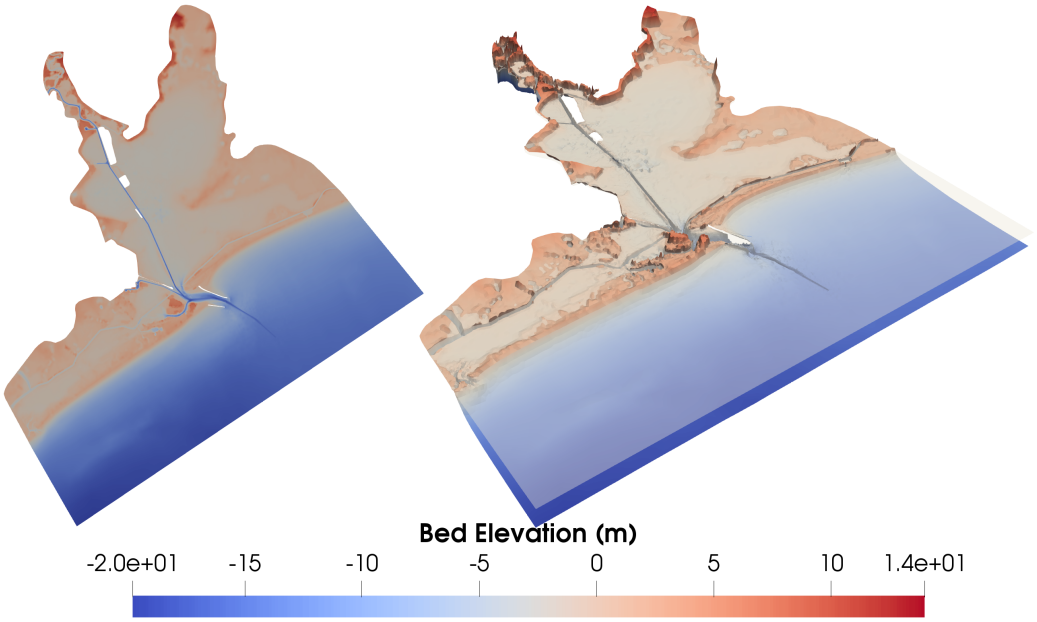

Figure 6.11: Galveston Bay bathymetry (left) and 3D view (right). The 3D view is scaled by a factor of 100 in the z direction.

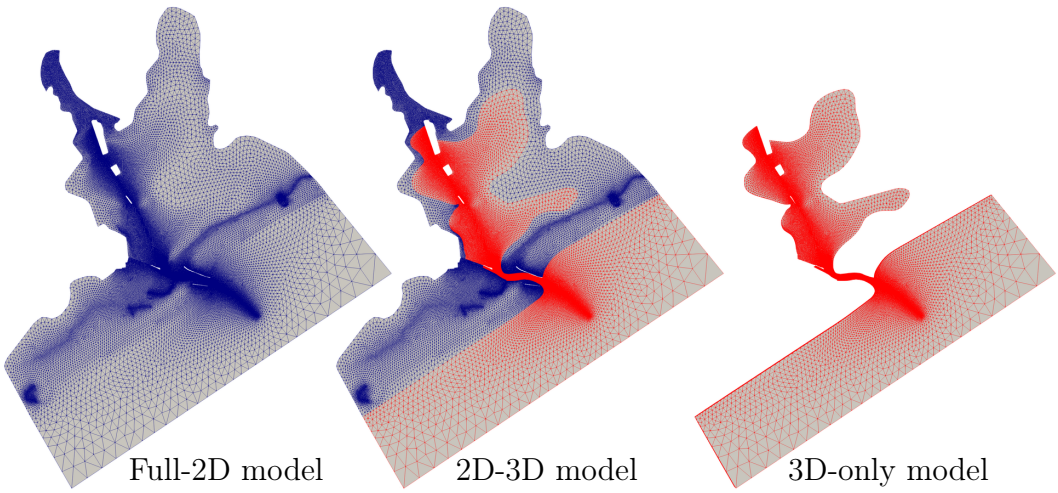

Figure 6.12: Galveston Bay meshes: Full-2D (left), 2D-3D coupled (center), and 3D-only (right) models.

but has not been used herein.

The initial conditions on the models are shown in Figure 6.13. The water is initially at rest, and the water surface is flat at an elevation of 0 m. An initial salinity distribution is specified in the three models, with the salinity being constant along the depth in the 3D submodels. The boundary conditions are no-normal-flow everywhere for all models, except at their south-east deep-ocean boundary where the water surface elevation is specified as (6.1), with amplitude $a = 0.5$ m and time period $T = 1$ day, same as that in the previous test case. The salinity at the deep ocean boundary is fixed at 35 g/kg. Wind and air pressure are not included in this test case. An isotropic eddy viscosity with a value of 0.01 is used in all the 2D subdomains, whereas the 3D submodels use a Smagorinsky coefficient of 0.2. Manning's bed friction coefficient is set to 0.025 throughout the domain. A time step of 0.5 hours is used for the simulations, allowed to change adaptively. The simulation ending time is set to 3 days.

Over the three-day duration, water repeatedly enters and leaves the bay through the inlet, respectively in the first and second halves of each day. The inlet area between the islands in the middle of the domain is observed to have significant salinity-related activity. Since the interface passes right through it, this application is an example of a real-world scenario in which the interface must be placed in a baroclinic region due to lack of other alternatives.

Figures 6.14a to 6.14f plot the water surface elevation results at half-day intervals. The surface elevation in the 2D-3D coupled model agrees well

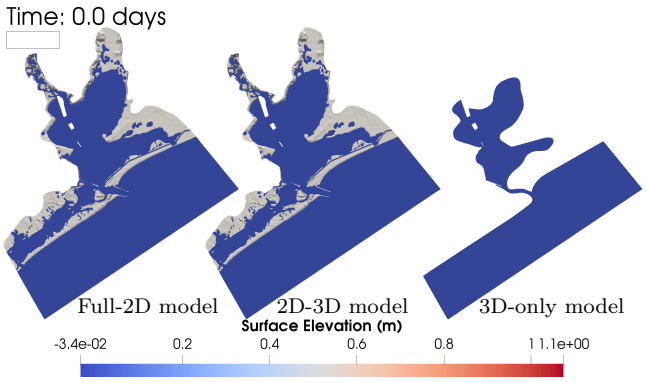

(a) Water surface elevation at $t = 0.0$ days

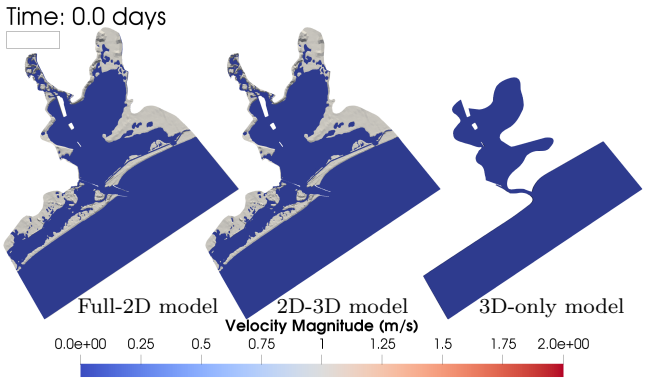

(b) Velocity magnitude at $t = 0.0$ days

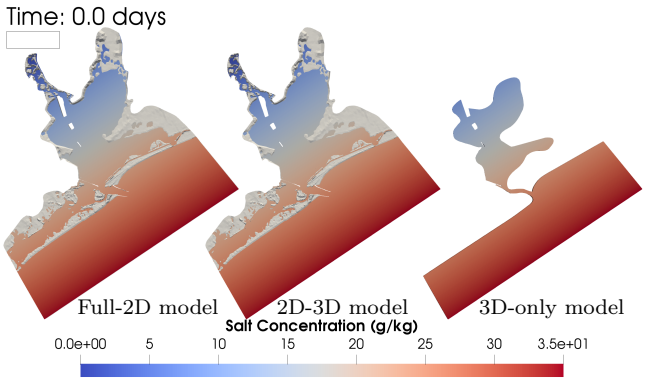

(c) Salinity at $t = 0.0$ days

Figure 6.13: Galveston Bay: Initial conditions (constant along the z direction in 3D submodels).

with the full-2D model, including the wetting-drying pattern. In the 3D-only model, the surface elevation in the bay appears to have been overestimated compared to that seen in the full-2D and coupled models. This is because the western area of the bay has not been modeled in the 3D-only model, so the water piles up inside the bay instead of allowing some of it to enter the western bay. Moreover, the 3D-only model has no-normal-flow boundary conditions everywhere except for the deep ocean, so the water level inside the bay builds up, whereas in the full-2D and 2D-3D models, the water is allowed to move onto dry land, preventing the build-up to some extent. In order to get better water surface elevation results with the 3D-only model, the domain boundary must be moved closer to the coastline and the western bay must be modeled.

Figures 6.15a to 6.15f plot the velocity magnitude results at half-day intervals. The 3D submodels show the surface velocity, whereas the 2D submodels show the depth-averaged velocity. The surface velocities shown in the coupled and 3D-only models at the inlet are more than double the depth-averaged velocity computed in the full-2D model. If the depth-averaged velocities are calculated from the 3D velocities in the coupled and 3D-only models (not shown for brevity), it is seen that the full-2D model underestimates even the depth-averaged velocity at the inlet. The surface velocity results at the inlet in the coupled and 3D-only models agree well with each other, although the velocity jets that come out from the inlet are seen to have slightly different orientations and extent in all the three models.

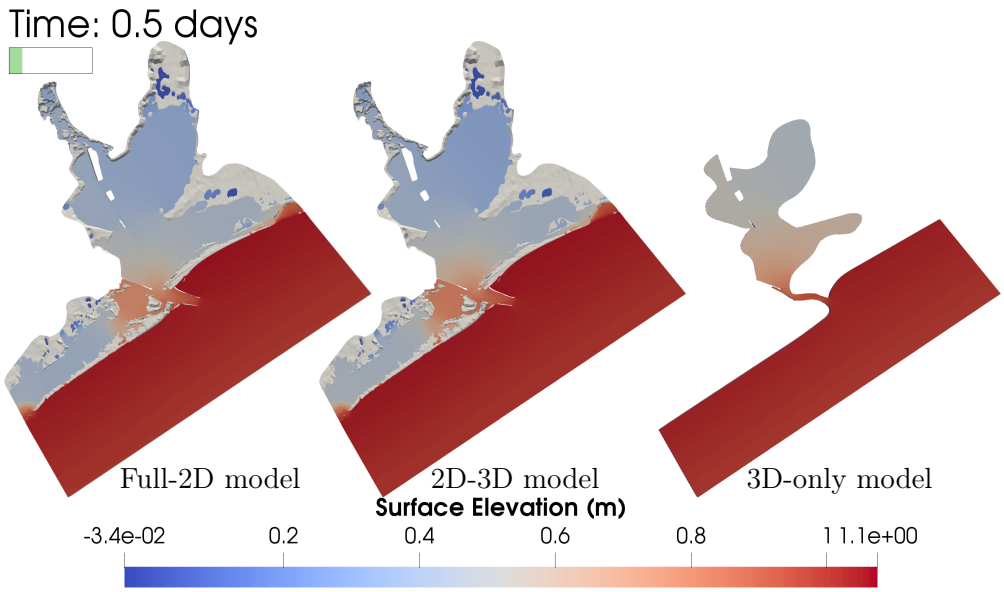

(a) $t = 0.5$ days

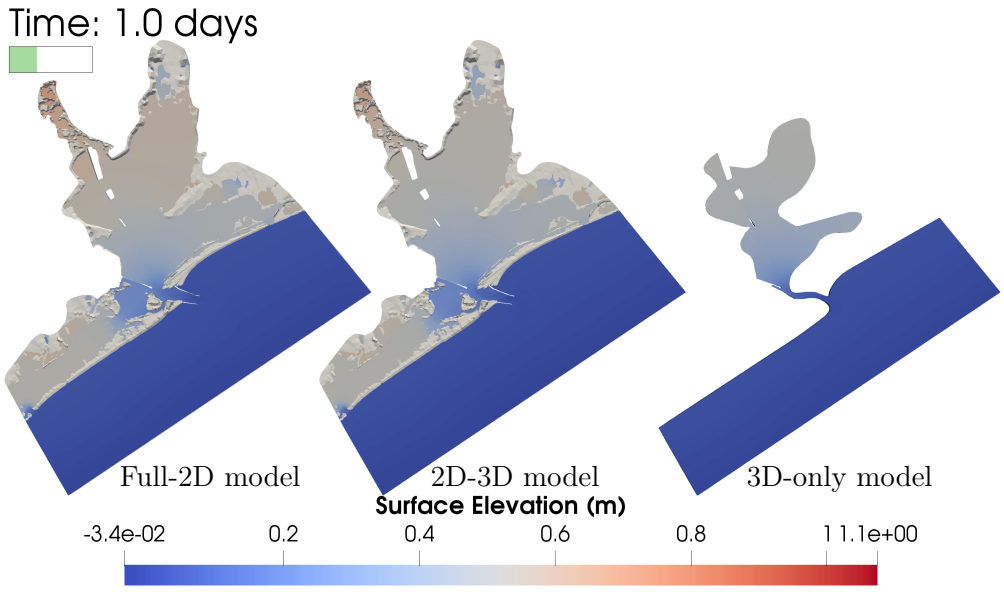

(b) $t = 1.0$ day

Figure 6.14: Galveston Bay: Comparison of surface elevation in the full-2D (left), 2D-3D coupled (center), and 3D-only (right) models.

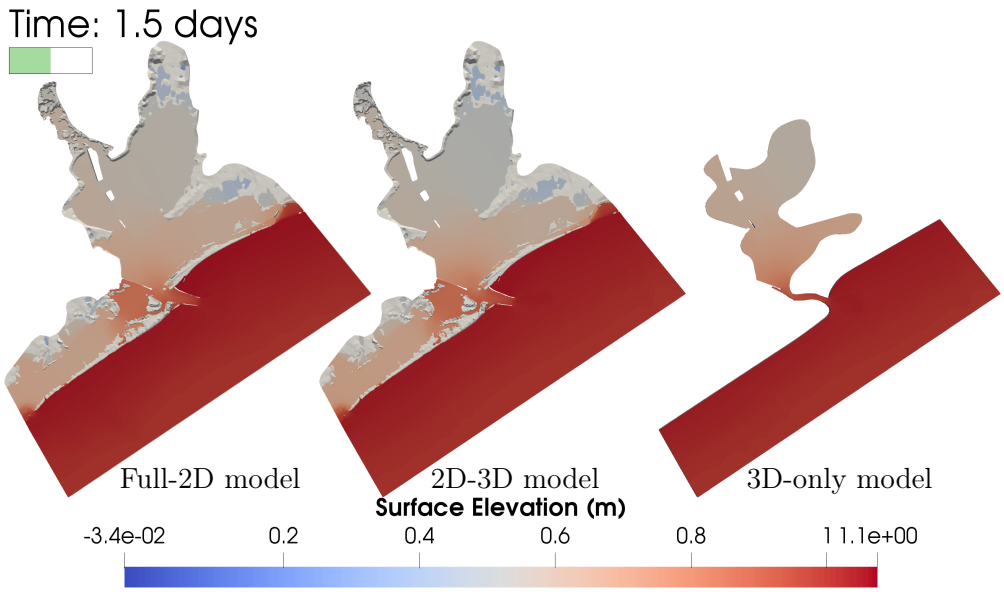

(c) $t = 1.5$ days

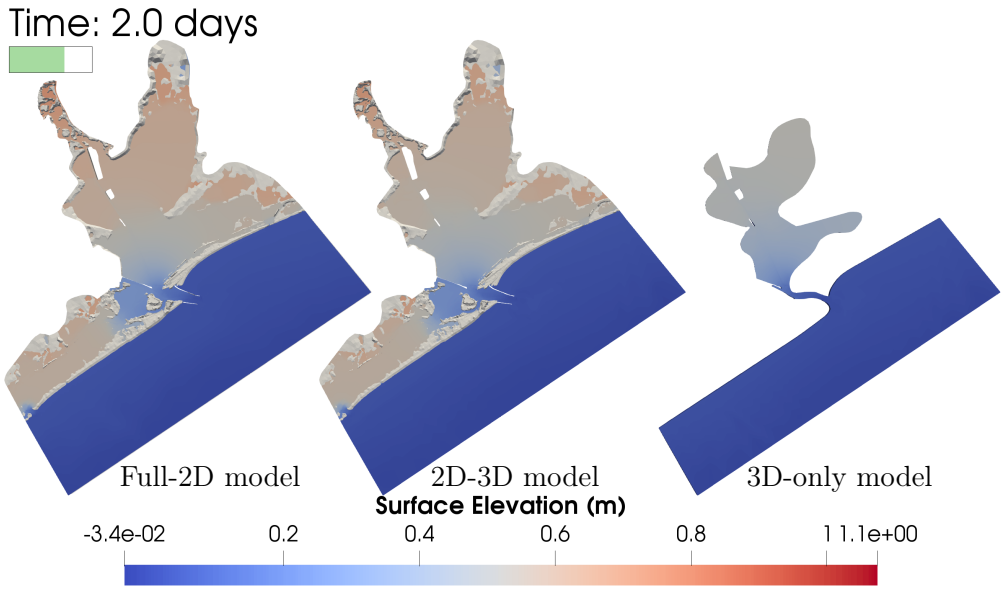

(d) $t = 2.0$ days

Figure 6.14: (Cont.) Galveston Bay: Comparison of surface elevation in the full-2D (left), 2D-3D coupled (center), and 3D-only (right) models.

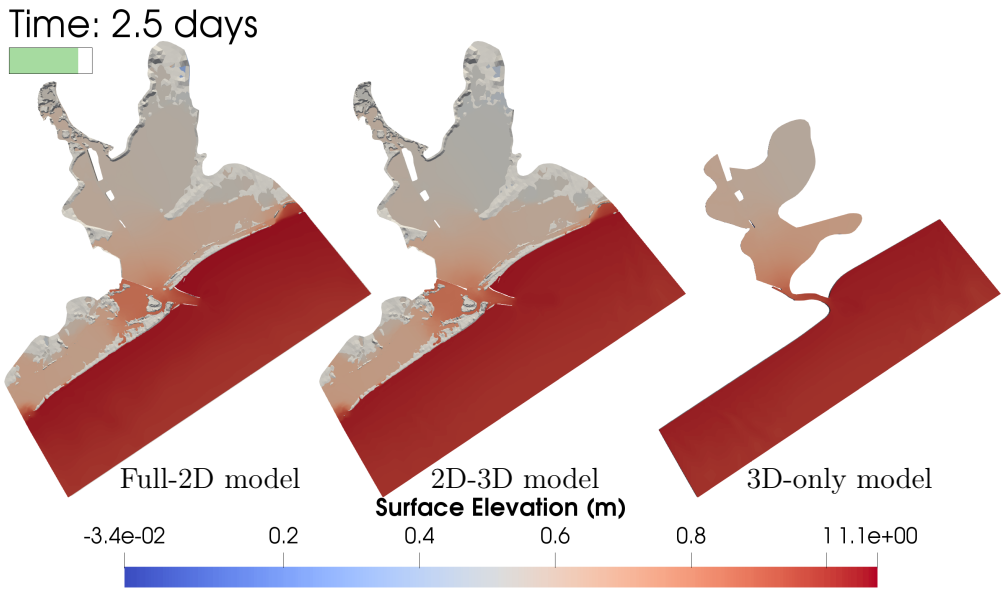

(e) $t = 2.5$ days

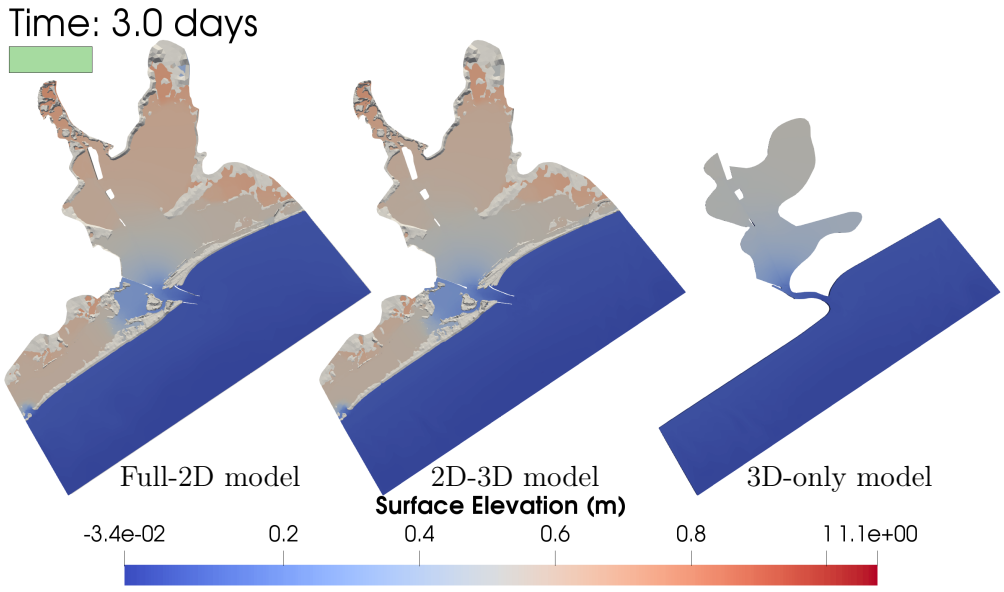

(f) $t = 3.0$ days

Figure 6.14: (Cont.) Galveston Bay: Comparison of surface elevation in the full-2D (left), 2D-3D coupled (center), and 3D-only (right) models.

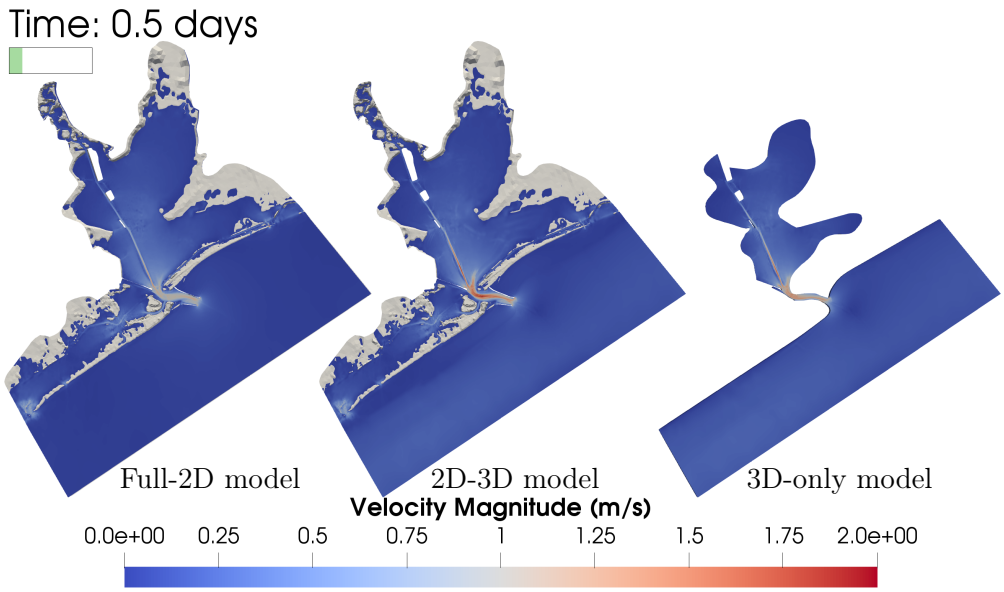

(a) $t = 0.5$ days

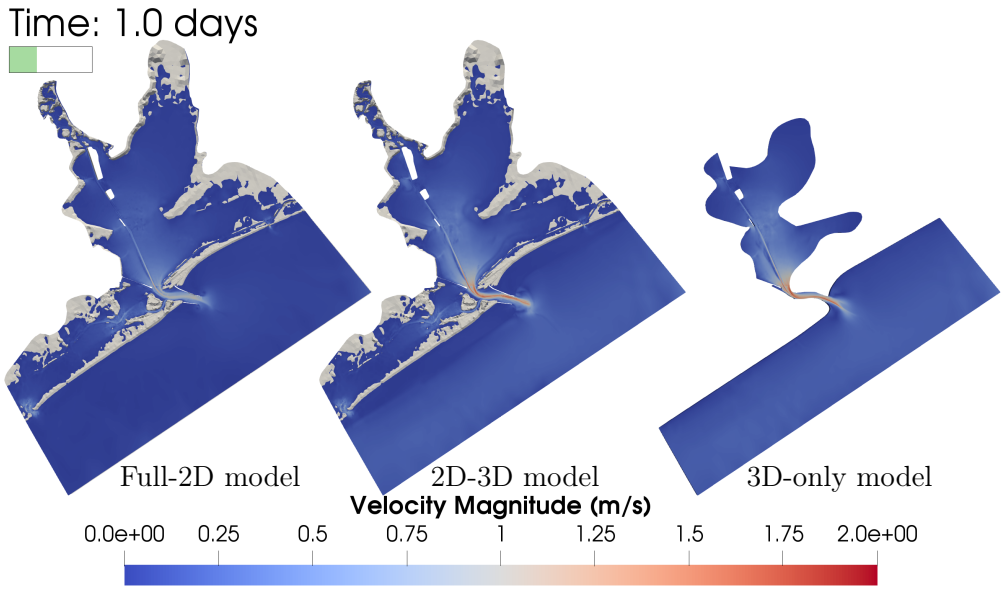

(b) $t = 1.0$ day

Figure 6.15: Galveston Bay: Comparison of velocity in the full-2D (left), 2D-3D coupled (center), and 3D-only (right) models.

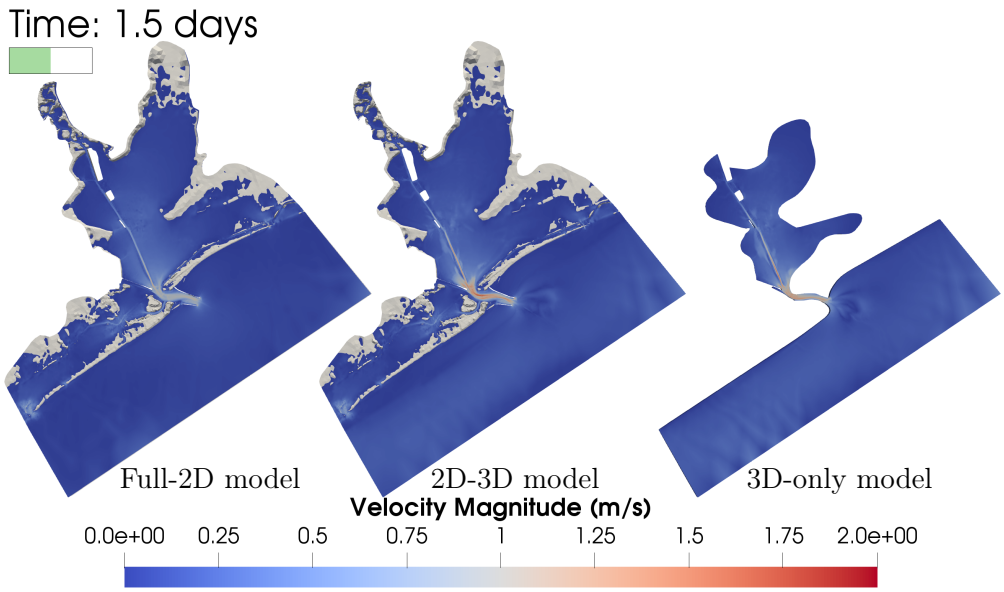

(c) $t = 1.5$ days

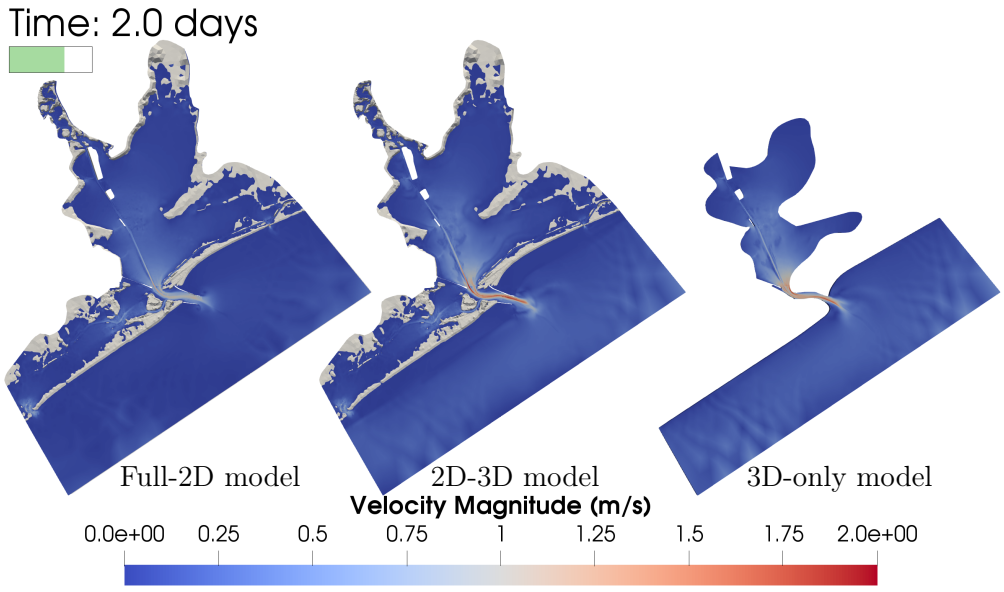

(d) $t = 2.0$ days

Figure 6.15: (Cont.) Galveston Bay: Comparison of velocity in the full-2D (left), 2D-3D coupled (center), and 3D-only (right) models.

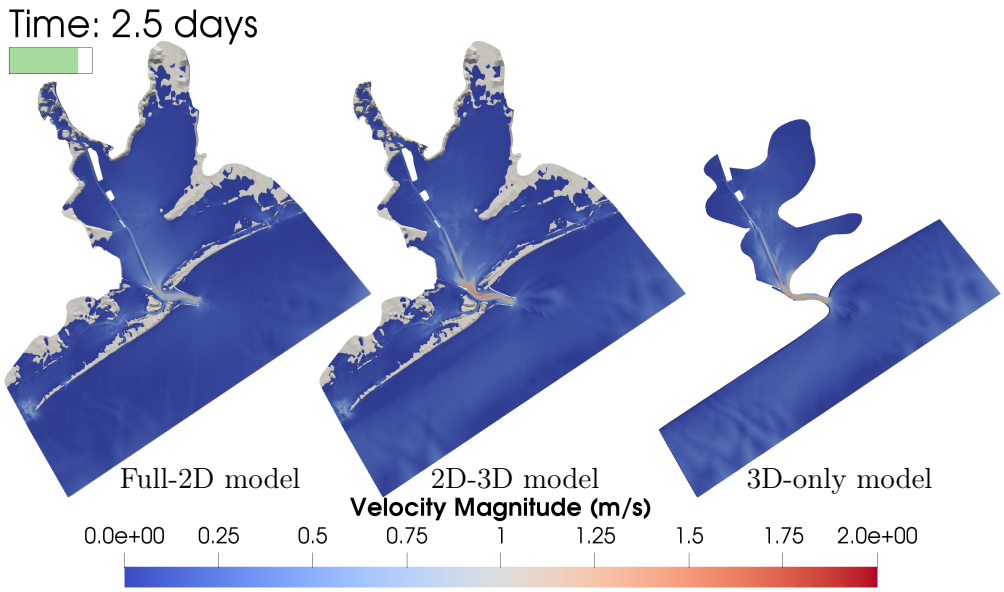

(e) $t = 2.5$ days

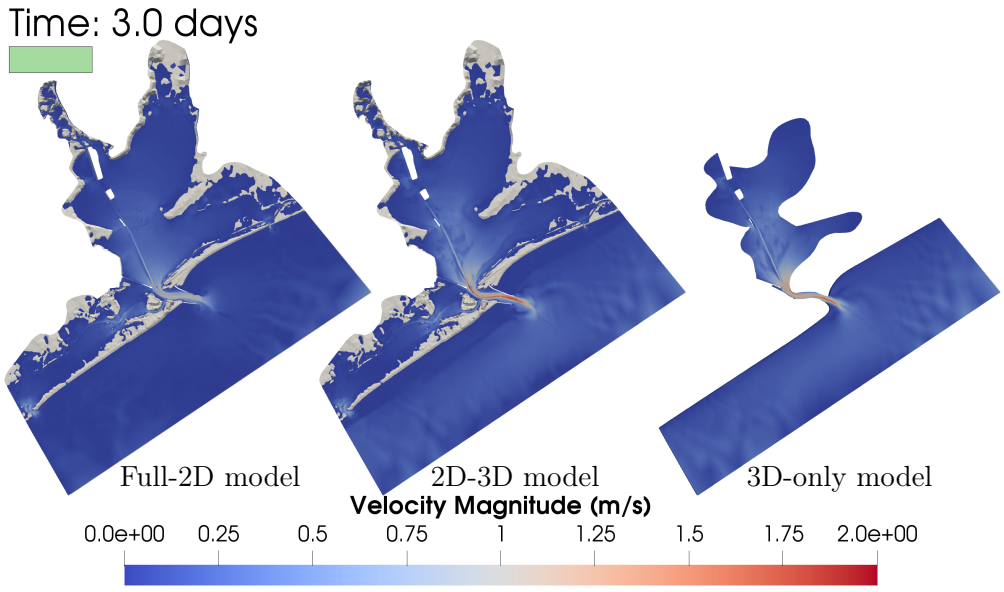

(f) $t = 3.0$ days

Figure 6.15: (Cont.) Galveston Bay: Comparison of velocity in the full-2D (left), 2D-3D coupled (center), and 3D-only (right) models.

Two eddies are generated in all the models on the sides of the inlet at the deep-ocean end whenever water leaves the bay. This is seen in Figures 6.15b, 6.15d and 6.15f upon closer inspection. Similar eddies were also reported in [51] for an idealized coastal inlet scenario.

Lastly, Figures 6.16a to 6.16f show the salinity results at half-day intervals. The 3D submodels show surface salinity, whereas the 2D submodels show depth-averaged salinity. Qualitatively, the results in the three models are seen to agree reasonably well. The eddies on the deep-ocean side of the inlet mentioned above are more visible in the salinity results. On post-processing the results to observe the salinity behavior close to the inlet — similar to the way Figures 6.4a and 6.4b were generated in the previous test case — vertical mixing is also seen in the 3D submodels, although the mixing patterns are complex and are not shown herein for brevity.

Through numerous test cases in this and the previous chapters, 2D-3D strongly coupled models are observed to be conservative, stable, accurate, and convergent, in line with the theory. They are seen to be capable of simulating complex phenomena in scenarios where full-2D and full-3D models are inadequate, but where the shallow water equations are still applicable. They also enable computationally cheaper 3D models in certain scenarios when used sensibly. The next chapter continues to demonstrate the benefits of coupling models in a different context by presenting the results of weakly coupled atmospheric, hydrodynamic, and hydrologic models.

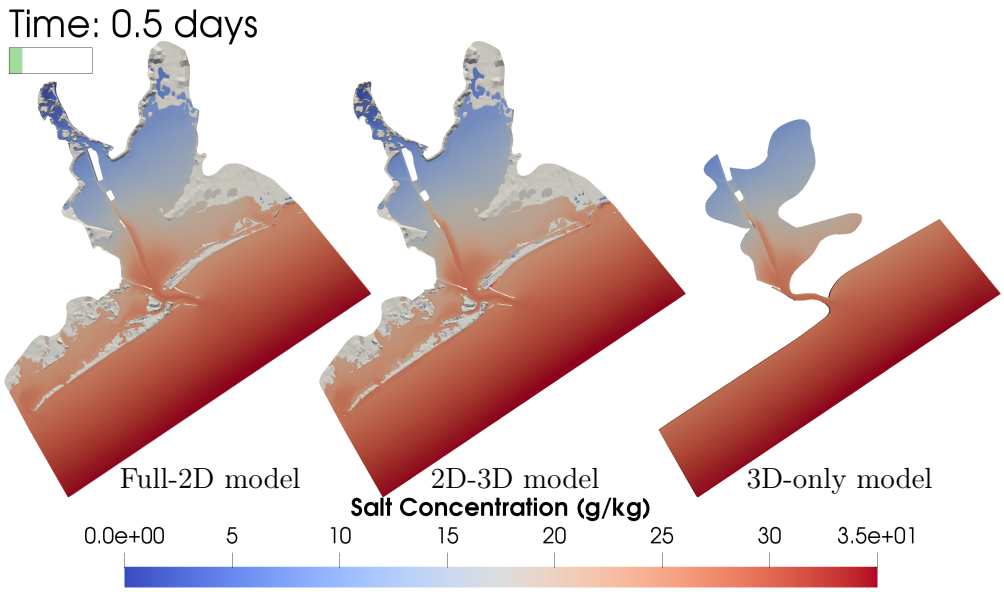

(a) $t = 0.5$ days

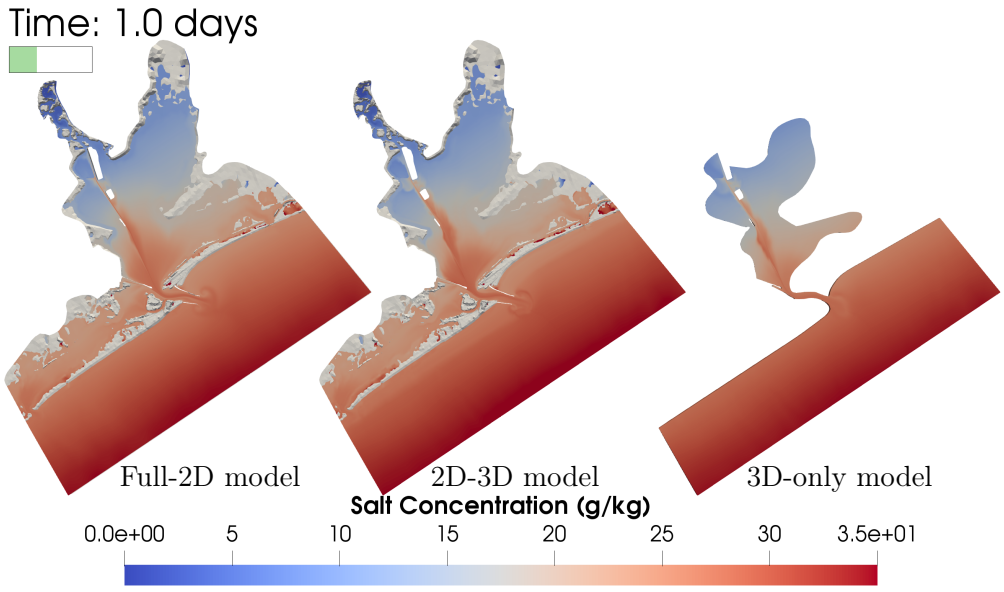

(b) $t = 1.0$ day

Figure 6.16: Galveston Bay: Comparison of salinity in the full-2D (left), 2D-3D coupled (center), and 3D-only (right) models.

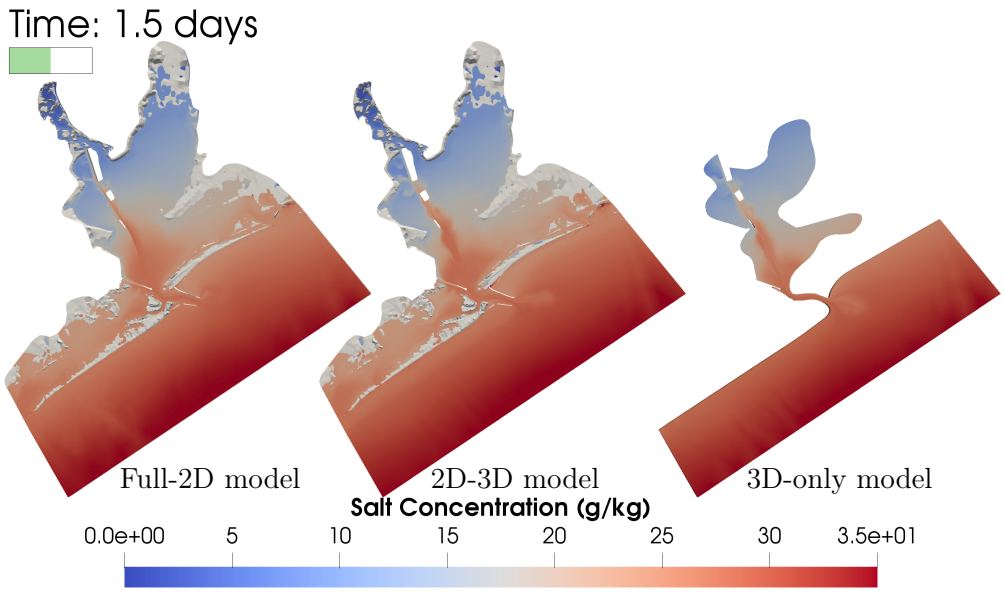

(c) $t = 1.5$ days

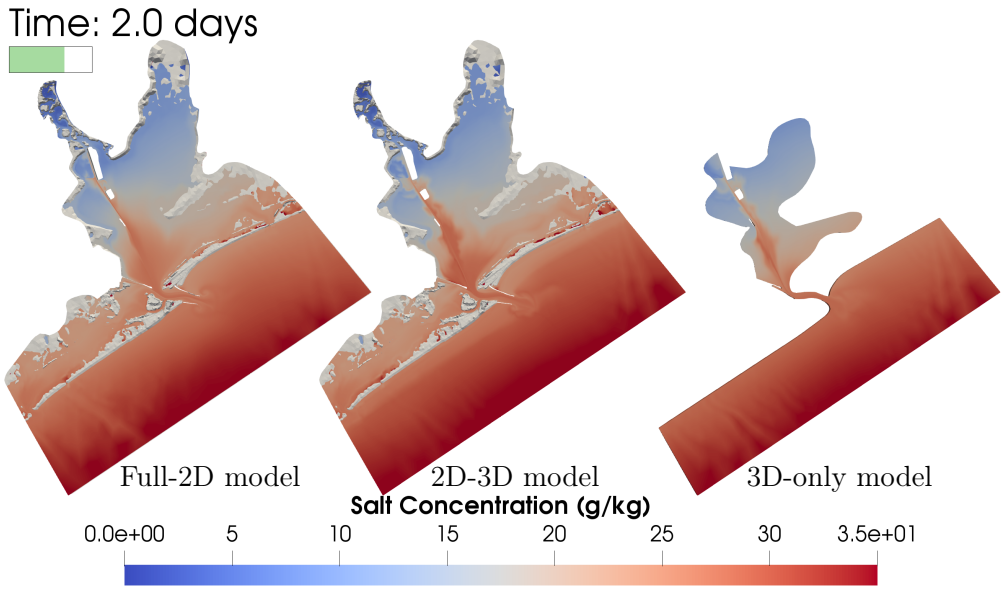

(d) $t = 2.0$ days

Figure 6.16: (Cont.) Galveston Bay: Comparison of salinity in the full-2D (left), 2D-3D coupled (center), and 3D-only (right) models.

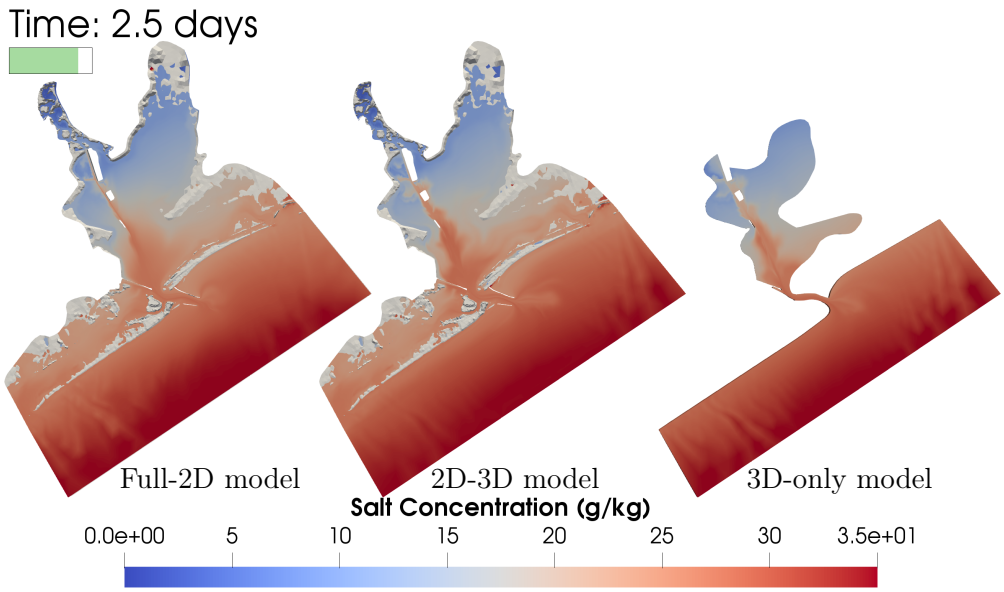

(e) $t = 2.5$ days

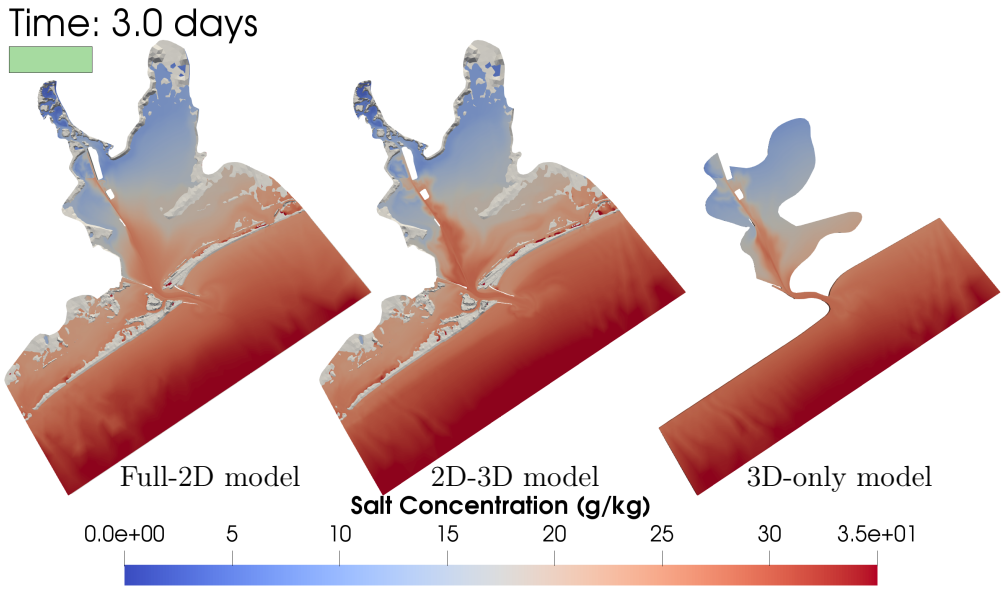

(f) $t = 3.0$ days

Figure 6.16: (Cont.) Galveston Bay: Comparison of salinity in the full-2D (left), 2D-3D coupled (center), and 3D-only (right) models.

Chapter 7

Weakly coupled atmospheric, hydrodynamic, and hydrologic models

The majority of attempts at simulating compound flooding events resulting from combined impacts of coastal and pluvial floods such as those during Hurricane Harvey of 2017 [99] often leave out the effects of one of them [61]. Both aspects contribute significantly in exacerbating the impacts of such extreme events and cannot be ignored. Commonly used general-purpose commercial finite element or other computational software are rarely suitable for handling such extreme events, whereas specialized computational software that do handle them are often designed with specific physics in mind. Addition of new physics in such software is seldom easy. If, instead of pursuing that difficult option, the capabilities of multiple software designed to do their respective jobs are leveraged, it may save significant effort in development, verification, validation and testing. Shallow water models such as AdH or ADCIRC and overland flow models such as GSSHA or HEC-RAS can be weakly coupled to each other and driven by one way coupling from atmospheric models such as NAM or GFS to simulate compound flooding events. This chapter presents preliminary work in coupling AdH, GSSHA, and NAM.

7.1 Python interface

While coupling multiple software, accommodations must be made for the possibility that they may have been written using different programming languages, or that the source codes may not be available or modifiable. A framework that minimizes changes to existing software and instead adds a separate layer of functions to access the software functionality must be built in such scenarios. To that end, a programming language compatible with multiple languages is important. The Python programming language is currently one of the fastest growing in the world by several metrics [1, 67, 88]. Using an application programming interface (API) or an application binary interface (ABI), Python can be coupled to various other programming languages such as Fortran, C, and C++, which most existing high-performance computing codes use. Although Python is significantly slower in terms of performance, it is much faster to set up a coupling software in Python than it is using any of C, C++ or Fortran. Particularly since it is expected that minimal computation time will be spent in Python and maximal in the software being coupled, a small hit on the performance is acceptable compared to the significant amount of development time that would otherwise be needed.

Having a Python interface for software can be especially advantageous for users at any level of skill in the software being coupled and/or Python, given the growing community of Python users and a rich set of freely available libraries that are hassle-free to download and install. The interface of a (non-Python) software is meant to allow users to run it through Python, giving

them access to and control over its data structures and functions. Following are some of the possible uses of a Python interface from the perspectives of software developers and users.

- Software developers:
  - Unit/integration testing of the software can be automated.
  - Creating proof of concepts for addition of new functionalities to the software is possible using a Python interface.
  - Coupling to other software (whose source code may be available for use but not for extensive changes) becomes easier with a Python interface in place, as has been done in the work presented in this chapter.
- Software users:
  - Creating a pipeline for post-processing results after a simulation is run becomes possible with a Python interface, as the simulation results can be stored in Python memory for the user to manipulate after the simulation runs. This can be used to automate plot generation, for example.
  - A Python interface would also help in adding new I/O options, such as reading in different mesh formats or writing output in different formats. The eXtensible Data Model and Format (XDMF) and

Visualization Toolkit (VTK) formats, for example, have Python interfaces of their own, which can be taken advantage of for I/O.

- A Python interface can allow users to extend the capabilities of software beyond those that are currently supported. For example, a significant part of the convergence analysis of the slosh test case presented in section 4.1 was done using the newly added AdH Python interface, which was not something the AdH source code had been designed for.

In the present work, `ctypes` [71, 92], which is part of the standard Python library, was used to create Python interfaces for AdH and GSSHA. Python can access most data structures and functions of AdH and GSSHA through `ctypes` on compiling them as shared libraries. After building the respective Python interfaces, a new coupling code was created. The code simply imports the AdH and GSSHA python interfaces, calls their functions from Python, allowing them to run, and performs *in-memory* modifications of the model boundary conditions without using any sort of file input/output for exchanging information. Unfortunately, the work gone into the Python interfaces and the coupling code is more of software engineering than it is research, which is why the numerous options for, and the process of building Python interfaces are not discussed herein. Only the weak coupling between the atmospheric, hydrodynamic, and hydrologic models — NAM, AdH, and GSSHA — is presented next.

7.2 The atmospheric model – NAM

Before beginning the coupling between AdH and GSSHA, a source of precipitation and wind datasets must first be chosen in order to drive the models. Keeping in mind that short turn-around times of results are required for actionable decision support during extreme events, typically within a 24-hour time window, the North American Mesoscale Forecast System (NAM) [63] is chosen in this work for obtaining meteorological forcing. NAM is a major atmospheric model run by the National Centers for Environmental Prediction (NCEP). It is based on [45, 73], and solves the primitive equations for the atmosphere. It includes non-hydrostatic effects and temperature transport. It produces analysis and forecast results over multiple grids at various horizontal resolutions. NAM models are run 4 times daily at 00, 06, 12, and 18 hours Coordinated Universal Time (UTC). NAM creates forecasts for the following domains in each execution of the production run:

- Full North American 12 km parent domain to 84 hours, and
- Four fixed nested domains run to 60 hours at 3 km resolution, which are all one-way nested inside the parent 12 km domain:
  - Contiguous United States (CONUS),
  - Alaska,
  - Hawaii,
  - Puerto Rico, and

– One very high-resolution nest run to 36 hours at 1.5 km horizontal resolution that is placed at different locations each cycle.

In general, atmospheric models are run on supercomputers, and obtaining source code access is not easy. Since NAM forecasts to 84 hours are available every 6 hours [63], and since only one-way coupling from NAM to the hydrodynamic and hydrologic models is needed, the output files of NAM are used to obtain forcing data. Additionally, NAM analysis files going back more than a decade are also available at time intervals of 1, 2, 3, and 6 hours [63]. The gridded binary (GRIB2) [25] output files of the 12 km resolution CONUS grid [62] shown in Figure 7.1 are used herein. Daily availability of NAM fore-

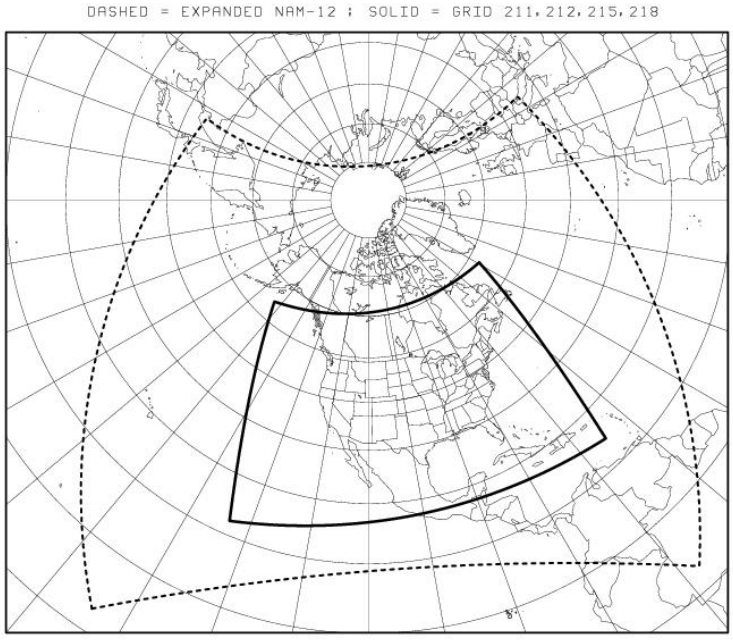

Figure 7.1: NAM 12 km CONUS domain (solid line) [62].

casts is one of the reasons of choosing NAM as the atmospheric model herein. The second reason for that is the availability of external libraries to interpret the output files, such as the *wgrib2* library [33] used in this work. The sustained wind velocity 10 m above the surface, and the accumulated precipitation datasets from the GRIB2 output files of NAM are used as forcing in AdH shallow water and GSSHA diffusive wave models, respectively. The output datasets over the NAM grid are interpolated onto AdH and GSSHA domains using nearest-neighbor interpolation in space and linear interpolation in time.

7.3 Coupling hydrodynamic and hydrologic models

Weak coupling is generally software-dependent, and existing boundary condition options must be worked with unless the source codes are available and allowed to be significantly modified. It is also important to understand the limitations of the software being coupled and the scenarios in which they are applicable. As mentioned in section 1.2, AdH solves the 2D shallow water equations and supports velocity/elevation Dirichlet/Neumann boundary conditions. The equations are applicable for flow in the ocean and even watersheds. However, when used for overland flow routing in watersheds, shallow water models are computationally expensive to solve since an extremely fine mesh and small time step must be used. Neglecting the inertial acceleration terms in the depth-averaged horizontal momentum equations (2.7) and (2.8), instead, leads to the diffusive wave equations. These equations are only valid for flow over gentle slopes and low Froude number, $\mathrm{Fr} = U/\sqrt{gH} \ll 1$.

GSSHA [31, 32] solves the diffusive wave equations, wherein the well-known empirical Manning's formula is used to relate the depth and discharge in the equations with each other. It uses the finite volume method with explicit time stepping to solve these equations. It also has options for coupling the overland flow model with groundwater/infiltration, which has not been used herein. The 2D watershed models in GSSHA support specification of depth on the boundary of the domain to allow them to get flooded laterally. In case of coupled 2D/1D diffusive wave simulations, the watershed empties from a single 1D stream outlet cell, which accepts either a hydraulic slope or a depth time series specified as a boundary condition. For the preliminary work presented herein, AdH and GSSHA domains are assumed to be non-overlapping except for a shared boundary called the AdH-GSSHA interface. The 1D stream outlet cell of a GSSHA watershed is weakly coupled to a connected boundary of an AdH 2D shallow water model. Coupling using the first type of GSSHA boundary condition, for which the water depth on the GSSHA 2D domain boundary must be specified, is planned for future work. There are three main topics that need to be considered when coupling AdH and GSSHA: type of weak coupling and order of runs, time-stepping, and type of boundary conditions being exchanged.

7.3.1 Types of weak coupling and order of runs

The current implementation of coupling is simple in terms of theory. As mentioned in section 1.2, Gauss-Seidel and Gauss-Jacobi type iterations

are two broad ways of weakly coupling models [97]. Gauss-Seidel iterations are used in this case, although implementing Gauss-Jacobi iterations with the current work in place is not too difficult. Using Gauss-Seidel style weak coupling also means that the models are solved in a specific order every time step. In the current case, since there are just two models involved, the model that is being solved first is called the driving model and the model that is solved second is referred to as the driven model. The driving model is so named since it initiates the exchange of boundary conditions first. Modification of BCs can be one-way, in which case only the driving model always modifies the BCs of the driven model, or two-way, so that both driving and driven model modify the BCs of each other. The driving model typically runs ahead in time compared to the driven model, so the solution of the current time step of the driving model always decides the BCs of the current time step of the driven model. In case of one-way coupling, it is possible to essentially run the driving model to completion first, apply boundary conditions on the driven model next, and then run it to completion. In case of bi-directional exchange of information, however, both models must be run in lock-step fashion. If at least one Gauss-Seidel iteration is used in weak two-way coupling, then the driven model also affects the BCs of the driving model for the current time step, and the driving model must be solved again. However, at the end of the Gauss-Seidel iterations, the final solution of the driven model always decides the BCs of the driving model for the next time step. In the case of zero Gauss-Seidel iterations as is used herein, resetting or backtracking the solutions of

the models within the current time step is not required. This is of particular importance when legacy codes are involved, which may or may not allow easily resetting the solution. In summary, the case of weak two-way coupling with zero Gauss-Seidel iterations used herein corresponds to the following steps being undertaken every time step in the given order.

1. The driving model is solved first, which may be multiple times if the time step sizes of the coupled models are different.

2. The current solution of the driving model is used to determine and apply BCs on the driven model for the current coupling interval.

3. The current time interval of the driven model is solved next, which may also be multiple times if the time step sizes of the coupled models differ.

4. The current time interval solution of the driven model is used to determine and modify the BCs of the driving model for the next coupling interval.

5. The time step is incremented and the entire process is repeated.

Thus, in the current implementation of two-way coupling, the driven model also drives the driving model but with the BC application lagged by a time interval. Based on that, Table 7.1 summarizes the terminology for the four types of coupling implemented, viz., GDA, ADG, GDADG, and ADGDA. The types of coupling are one-way or two-way, with the driving model being AdH

Table 7.1: Implemented types/modes of AdH-GSSHA coupling.

Coupling Name	Coupling Type	Meaning
GDA	One-way	GSSHA driving AdH
ADG	One-way	AdH driving GSSHA
GDADG	Two-way	GSSHA driving AdH driving GSSHA
ADGDA	Two-way	AdH driving GSSHA driving AdH

Table 7.2: BC influence in different types of coupling.

Coupling Name	Coupling Type	BC Influence AdH to GSSHA	BC Influence from GSSHA to AdH
GDA	One-way	None	Current to current
ADG	One-way	Current to current	None
GDADG	Two-way	Current to next	Current to current
ADGDA	Two-way	Current to current	Current to next

or GSSHA. For example, GDADG mode is two-way coupling with GSSHA being the driving model and AdH being the driven model. It is expected that the results of ADGDA and GDADG coupling would be similar except for a time-lag. Table 7.2 states how the solutions of one model influence the BCs of the other with respect to coupled time intervals. For example, 'current to current' BC influence from AdH to GSSHA in ADG coupling means that the AdH solution of the current interval defines GSSHA BCs for solving its current interval.

7.3.2 Time-stepping procedure

The models are allowed to start or end at different times and are allowed to use different time step sizes. This allows subcycling, which means that one

or both the models may be solved for multiple time steps before information is exchanged between them. The models are run in lockstep fashion even in one-way coupling so that the current times of both the models remain as close to each other as possible while marching forward in time. The strategy for developing the time-stepping algorithm is based on Table 7.2. Let $\mathcal{A}$ be the driving model and $\mathcal{B}$ be the driven model. Let $\Delta t_{\mathcal{A}}$ and $\Delta t_{\mathcal{B}}$ be the time step sizes of $\mathcal{A}$ and $\mathcal{B}$. Let $t^0_{\mathcal{A}}$ and $t^0_{\mathcal{B}}$ be the starting times, and $t^e_{\mathcal{A}}$ and $t^e_{\mathcal{B}}$ be the ending times of the whole simulation. Let $t^{0i}_{\mathcal{A}}$ and $t^{0i}_{\mathcal{B}}$ be the intermediate starting times, and $t^{ei}_{\mathcal{A}}$ and $t^{ei}_{\mathcal{B}}$ be intermediate ending times of a coupling interval, which must be calculated so that $\mathcal{A}$ and $\mathcal{B}$ run for the intervals $(t^{0i}_{\mathcal{A}}, t^{ei}_{\mathcal{A}})$ and $(t^{0i}_{\mathcal{B}}, t^{ei}_{\mathcal{B}})$, respectively, at a time. The following conditions need to be satisfied while time-stepping.

- Model $\mathcal{A}$ stays ahead of model $\mathcal{B}$, i.e., $t^{0i}_{\mathcal{A}} \geq t^{0i}_{\mathcal{B}}$ for all timestamps i, possibly except for the starting times, $t^0_{\mathcal{A}}$ and $t^0_{\mathcal{B}}$. If $t^0_{\mathcal{B}} + \Delta t_{\mathcal{B}} \leq t^0_{\mathcal{A}}$, then $\mathcal{B}$ runs first with whatever BCs it has been supplied with, until it is one time-step behind $\mathcal{A}$, so that $t_{\mathcal{B}} + \Delta t_{\mathcal{B}} > t^0_{\mathcal{A}} \geq t_{\mathcal{B}}$. Although $\mathcal{B}$ runs first in this case, it is still the driven model since it stays behind $\mathcal{A}$.

- At the beginning of any coupling interval being solved for, model $\mathcal{A}$ must take at least one time step forward, so that $t^{ei}_{\mathcal{A}} \geq t^{0i}_{\mathcal{A}} + \Delta t_{\mathcal{A}}$.

- In order to maintain lockstep time-stepping, $t^{ei}_{\mathcal{A}}$ and $t^{ei}_{\mathcal{B}}$ must be calculated so that $t^{ei}_{\mathcal{B}} + \Delta t_{\mathcal{B}} > t^{ei}_{\mathcal{A}} \geq t^{ei}_{\mathcal{B}}$. This works irrespective of which model has a larger time step or an earlier starting time.

- If the ending time of one of the models, $t^e_{\mathcal{A}}$ or $t^e_{\mathcal{B}}$, is reached, the choice implemented herein is to set the BC of the remaining model to a constant value for the remainder of the simulation. A no-normal-flow Neumann BC is used in AdH, whereas in case of the GSSHA water depth BC, the depth is set to its last encountered value at the interface.

Note that the mathematically rigorous way would likely be to force starting and ending times of both the models to be the same. The above way of dealing with starting and ending times is non-rigorous and debatable. All examples presented later have the same starting and ending times but have different AdH and GSSHA time step sizes. These conditions are used to design the `while` loop that calls the AdH and GSSHA functions for running the models and the Python functions for calculating and applying BCs.

7.3.3 Modification of boundary conditions

AdH currently allows time series of either water surface elevation or velocity/flow to be applied as a BC on any portion of its model boundary. GSSHA allows only a depth time series to be specified on the watershed outlet cell as a Dirichlet boundary condition. Therefore, the straightforward way to couple AdH and GSSHA is for the AdH model boundary to always supply the GSSHA model outlet cell with depths, and for the GSSHA outlet cell to always supply AdH with inflow/outflow. In one-way ADG coupling, the BC on the AdH side of the coupling interface must be specified by the user and that on the GSSHA side is calculated from the AdH solution. In one-way

GDA coupling, the BC on the GSSHA side is user-specified and that on the AdH model is calculated from the GSSHA solution. In two-way GDADG and ADGDA coupling, the boundary conditions on both AdH and GSSHA domains are calculated and cannot be user-specified.

An important consideration for deciding how to translate BCs between the models is that the GSSHA model 1D stream outlet cell and the AdH 2D model coupled boundary cross-sections may not necessarily match. For example, a GSSHA watershed stream may directly be emptying into an ocean modeled in AdH, with different cross-sections on either side of the AdH-GSSHA interface. It is also possible that the models do not even have the same depth at the coupling interface. Therefore, the water surface elevations across the interface are assumed to be continuous at the initial time $t = 0$, even though the depths may not be so. The *change* in the water depth in the AdH model over a coupled time interval is added to the water depth of the outlet cell in GSSHA for use as a boundary condition. Whether that change in depth should be calculated as the maximum, minimum, or average change, or if some other aggregation method should be used over the coupled AdH boundary portion currently remains unexplored. For now, the average AdH depth at the coupled boundary, defined as,

$$h_{\text{avg}} = \int_{\partial\Omega_{\text{cpl}}} h \, d\partial\Omega_{\text{cpl}} \Big/ \int_{\partial\Omega_{\text{cpl}}} d\partial\Omega_{\text{cpl}} \, , \tag{7.1}$$

where $\partial\Omega_{\text{cpl}}$ is the coupled boundary portion on the AdH side, is kept track of and used to change the GSSHA outlet cell depth BC. On the other hand,

Table 7.3: Continuity of water surface elevation and conservation of mass in AdH-GSSHA coupling.

Coupling Name	Continuity of Water Surface Elevation	Conservation of mass
GDA	Ignored/not possible	Satisfied at all times[1]
ADG	Satisfied at all times[1]	Ignored/not possible
GDADG	Satisfied in a time-lagged way	Satisfied at all times[1]
ADGDA	Satisfied at all times[1]	Satisfied in a time-lagged way

[1] 'All times' here means over each coupled time interval.

to ensure mass conservation, the total outflow from the GSSHA model over a coupled time interval is kept track of and is used to modify the interface BC of AdH for the current or next time interval depending on the coupling type. Lastly, since GSSHA and AdH can run at different time steps, the BCs are interpolated linearly in time where required. Thus, in order to calculate the actual values of the BCs that are applied on and exchanged between the models, two key aspects of the solutions have been considered: continuity of the water surface elevation and conservation of mass. Table 7.3 mentions which of continuity and conservation are maintained in the different types of coupling. Strictly speaking, 'time-lagged' continuity or conservation across the coupling interface mentioned in the table is actually a small discontinuity. It is a result of truncation errors arising from avoiding multiple Gauss-Seidel iterations. Even if multiple iterations were to be used, either the mass flux or the water surface elevation is bound to be discontinuous, although it is expected that the discontinuity would be much smaller on using multiple iterations.

7.4 Verification

Three verification test cases are presented in this section. The first test case checks continuity of water surface elevation and conservation of mass across the AdH-GSSHA coupling interface, and confirms the information given in Table 7.3. The flood in this test case also happens to effectively act as a compound flooding event. The second coupling test case gives an example of stability problems that may arise in some cases. The third test case involves an AdH model using a relatively large time step and having a wetting-drying region close to the coupling interface. Test cases involving large GSSHA time step sizes are not presented herein because even GSSHA-only 2D/1D overland flow simulations using large time steps were found to be unstable, likely because GSSHA currently has only explicit time stepping options. It is noted that more rigorous testing particularly for analyzing stability is needed, which is left for future work.

7.4.1 Continuity, conservation, and compound flooding

An easy way to confirm that mass is being conserved is to let outflow from any GSSHA watershed fill up a coupled AdH model that has no-normal-flow boundary conditions on its entire boundary except for the portion coupled to GSSHA. To that end, a simple 2D rectangular AdH domain is coupled to a watershed taken from the GSSHA tutorial and test suite, available online for download [54], shown in Figure 7.2. The AdH domain is given by $\Omega = (0, 600)\,\mathrm{m} \times (0, 48)\,\mathrm{m}$ and has a flat bed. The initial conditions on the

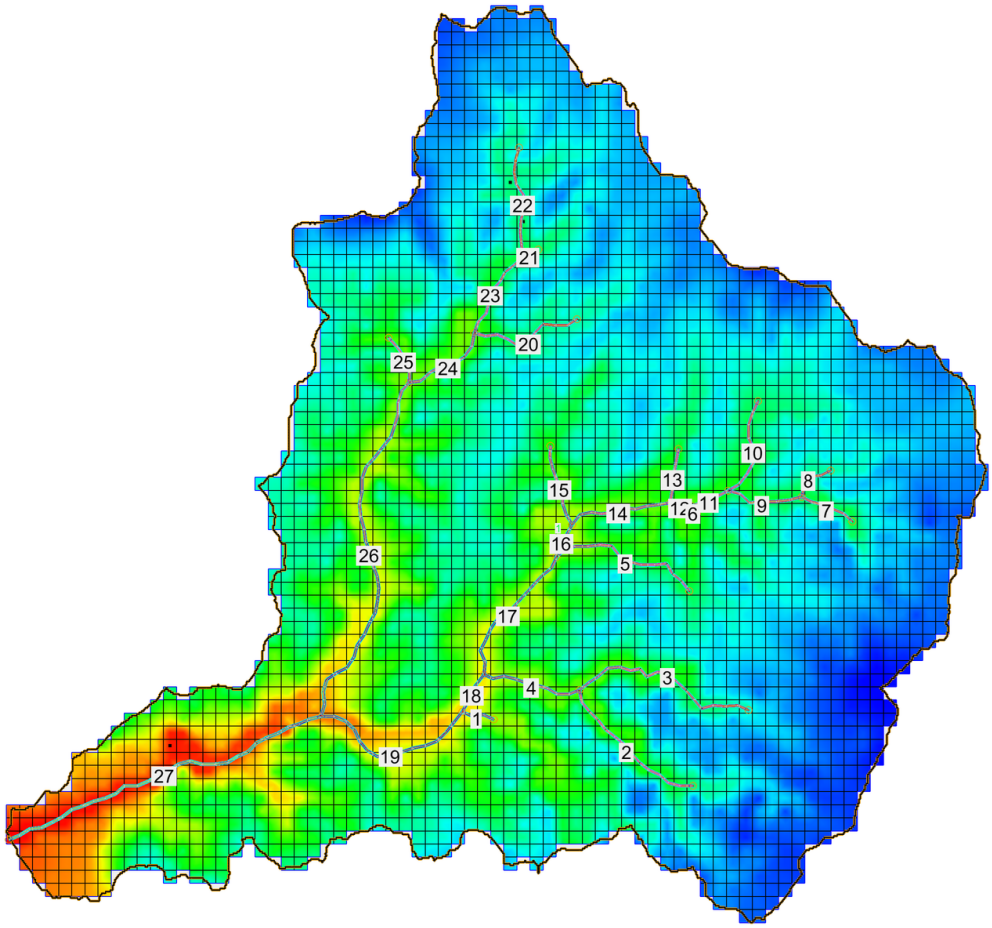

(a) GSSHA 2D/1D diffusive wave model

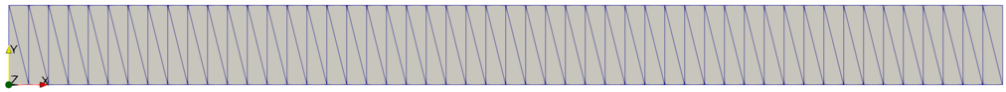

(b) AdH 2D shallow water model

Figure 7.2: GSSHA and AdH coupled domains (shown at different scales). The western/left edge of the AdH domain is coupled to the 1D stream outlet cell of the GSSHA watershed in the south-west.

domain are water at rest with a uniform initial depth of 20 m. Four levels of mesh adaption are allowed. Manning's bottom friction coefficient is set to 0.002 and the Smagorinsky coefficient is set to 0.25. There is no wind or atmospheric pressure in the AdH model. Its entire boundary has no-normal flow BCs, except for its western edge at $x = 0$ m, which is coupled to the GSSHA watershed outlet cell. The watershed has an area of 22.39 km^2 and is initially dry. The initial condition on the GSSHA 1D channels is water at rest, with a flat water surface such that the depth at the outlet cell is 2 m. Most of the channel regions are initially dry. Manning's bed friction coefficient is set to 0.03 in the watershed. All four types of coupling given in Table 7.1 are tested. In GDA coupling, the BC on the GSSHA outlet cell is a constant depth of 2.0 m and the depth on the AdH side is ignored. In ADG coupling, the BC on the coupled AdH edge is no-normal-flow, with the outflow from GSSHA being ignored. In the two-way GDADG and ADGDA coupling modes, both the models calculate the BCs to be applied on each other at the interface.

A uniform rainfall of 40 mm/hour is applied for a duration of 2 hours over the domain. The simulations are run for a duration of 5 hours. The time steps of GSSHA and AdH are set to 0.25 s and 100 s, respectively. As mentioned in section 7.3.3, although the interface depths of 20.0 m at the AdH boundary and 2.0 m at the GSSHA watershed outlet are different, the water surface elevations are treated as continuous at the starting time $t = 0$. The initial water surface elevation η at the interface is treated as $\eta = 0$.

Two sets of coupled simulations are run, and the information given in

Table 7.3 is tested. The first set of simulations excludes overbank flow physics in GSSHA, and the second one includes it. When overbank flow physics in GSSHA is turned on, it allows the water accumulating in the 1D streams to spill back onto the 2D overland cells when the streams get flooded beyond a specified limit on the depth. Incorporating this effect is generally important for compound flooding events, which is why these results have been included. The depth limit for the stream cells to be considered as flooded is different for different streams in the watershed. It is 8.0 m close to the watershed outlet. For this test case, it is found that in two-way coupled simulations with overbank physics excluded, the water depth in the GSSHA outlet cell exceeds this value by about 6 m, so the set of simulations including overbank flow physics is important.

Figures 7.3 and 7.4 show the results of simulations excluding and including overbank flow physics, respectively. The top subfigures show the variation of the water surface elevation in GSSHA (solid lines) and AdH (dashed lines) at the AdH-GSSHA coupling interface for GDA, ADG, GDADG, and ADGDA runs. Likewise, the bottom subfigures show the cumulative volume of water that flows out of GSSHA as calculated by GSSHA, and the same that flows into AdH as calculated by AdH, for the four coupling types. In the graphs, the water surface elevation is continuous, and mass is conserved across the AdH-GSSHA interface in a given type of coupling if and only if the dashed line with the corresponding marker is (nearly) coincident with the solid line having the same marker.

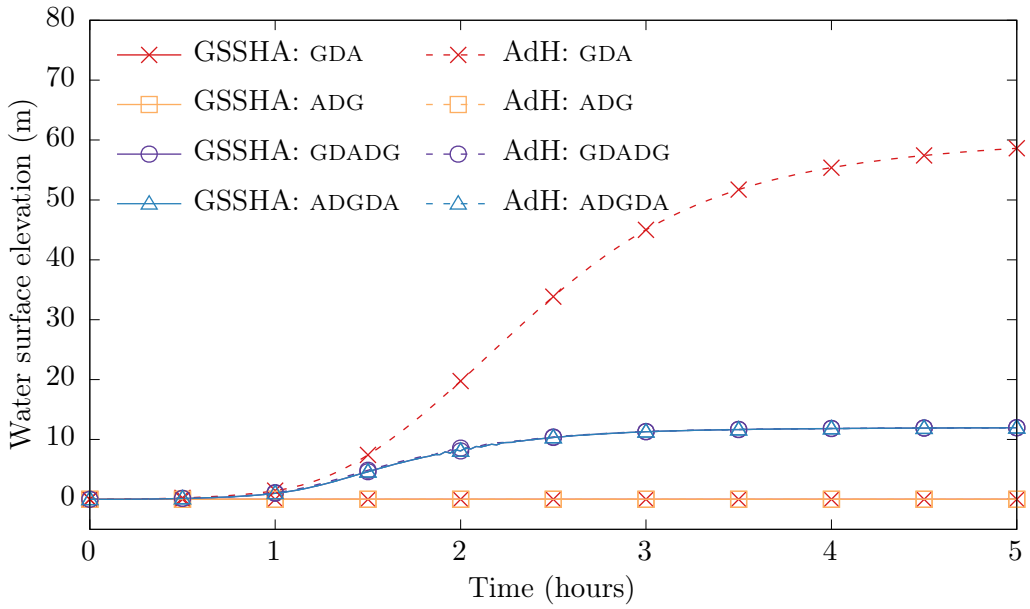

(a) Checking continuity of water surface elevation in AdH-GSSHA coupling

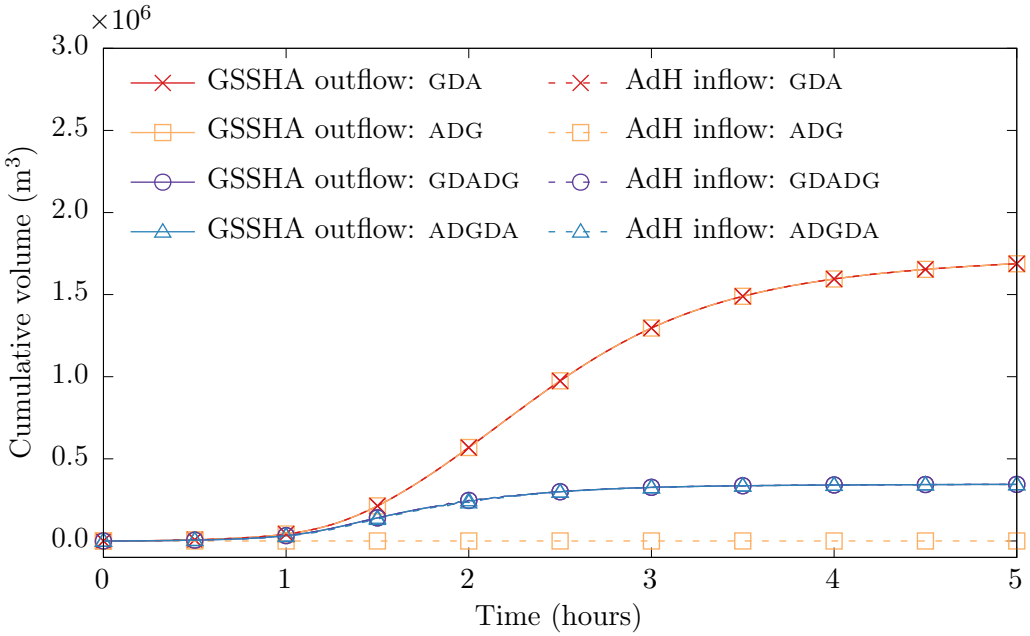

(b) Checking conservation of mass in AdH-GSSHA coupling

Figure 7.3: Verification of continuity of water surface elevation and conservation of mass for simulations excluding overbank flow physics in GSSHA.

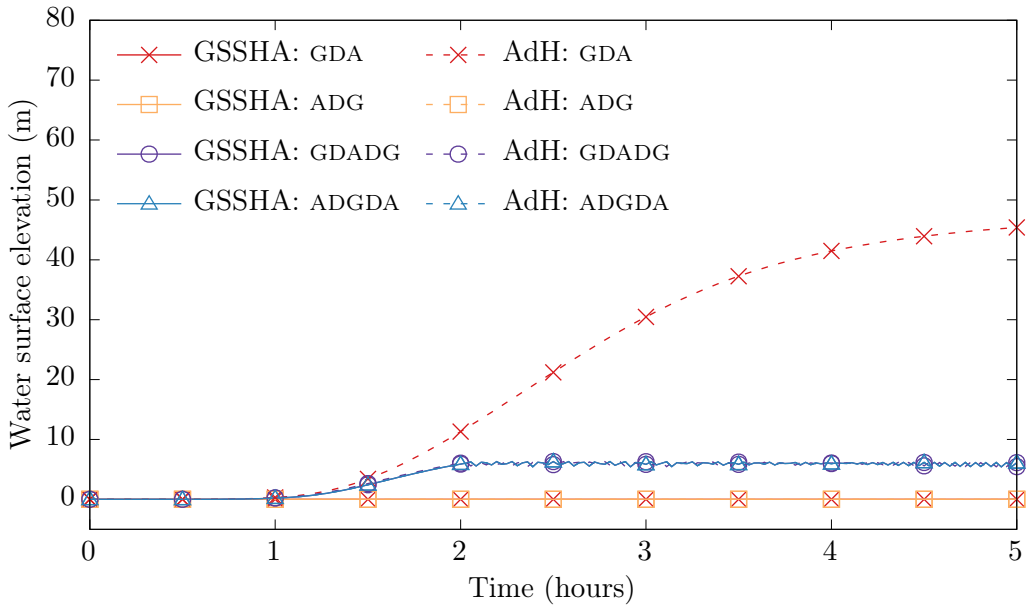

(a) Checking continuity of water surface elevation in AdH-GSSHA coupling

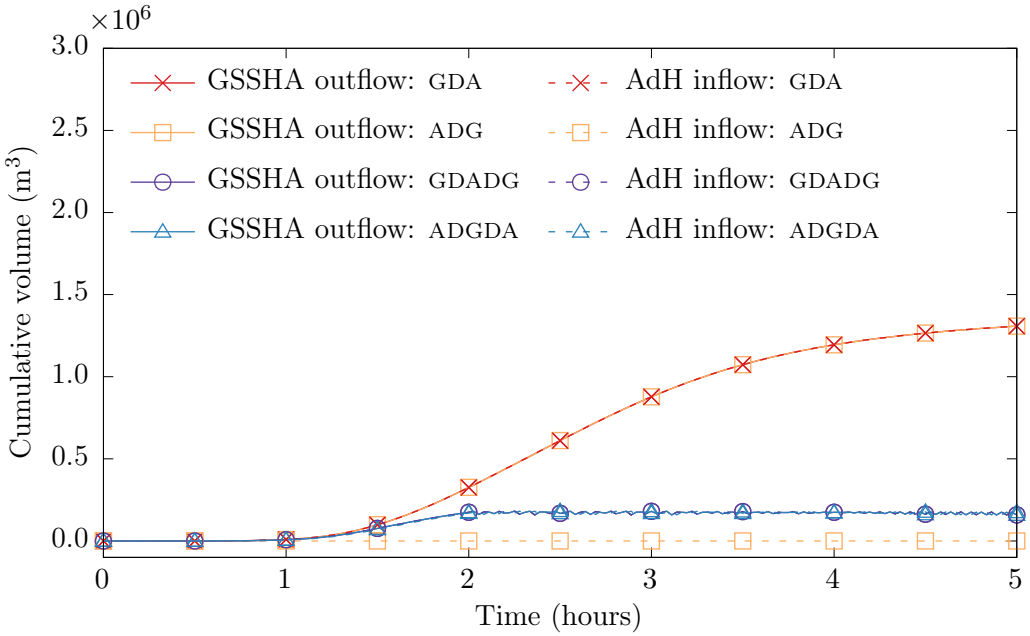

(b) Checking conservation of mass in AdH-GSSHA coupling

Figure 7.4: Verification of continuity of water surface elevation and conservation of mass for simulations including overbank flow physics in GSSHA.

From Figures 7.3a and 7.4a, it is observed that the water surface elevation is discontinuous in GDA coupling, and continuous in a time-lagged manner in GDADG coupling. It is continuous for ADG and ADGDA coupling. On the other hand, from Figures 7.3b and 7.4b, it is seen that mass is not conserved in ADG coupling, and is conserved in a time-lagged sense in ADGDA coupling. Mass is conserved in case of GDA and GDADG coupling. Thus, the information given in Table 7.3 is successfully verified using this test case.

The results of the simulations also indicate how a compound flooding event would be captured using two-way coupled simulations. It is observed from Figures 7.3b and 7.4b that the cumulative volume of water that flows out of the GSSHA watershed is significantly lower in the two-way coupled simulations than in the one-way runs. This is because in two-way coupling, the rise in the water surface elevation in the AdH domain causes backwater effects in the GSSHA domain. This results in water piling up in the watershed instead of flowing out freely, effectively becoming a compound flooding event. The compound flooding behavior in two-way coupling is further confirmed from Figures 7.5a and 7.5b, which show the water depths over the watershed at $t = \{2.5, 5.0\}$ hours in GDADG coupling. The results of simulations including and excluding overbank flow physics are both shown in the figures. The water is seen to remain collected in the watershed behind the outlet cell during the second half of the simulation, even after the rainfall stops at $t = 2$ hours. In the one-way coupled simulations (not shown in the figures), the watershed is close to dry at the end of the runs, and the stream depths are much lower.

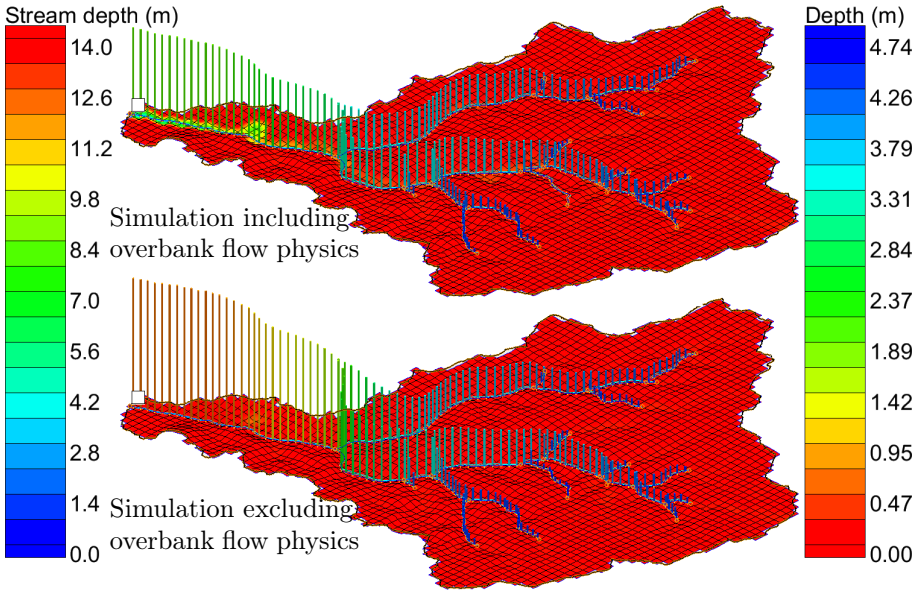

(a) $t = 2.5$ hours

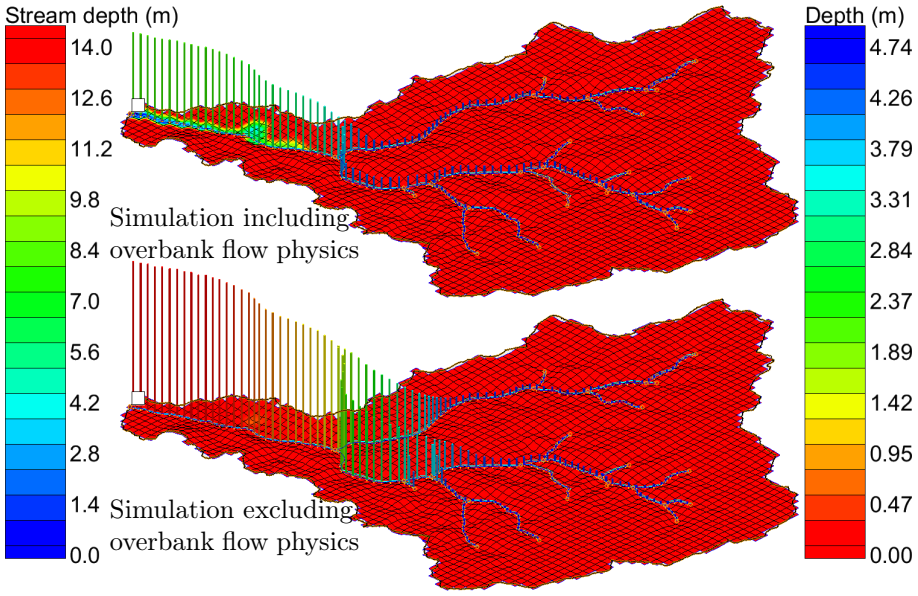

(b) $t = 5.0$ hours

Figure 7.5: Compound flooding effect in GDADG coupling: Comparison of 2D overland and 1D stream depths in simulations including (top) and excluding (bottom) overbank flow physics, at two different times.

On comparing simulations excluding overbank flow physics with those including it, significant differences are observed. As seen in the figures, in two-way coupled simulations excluding overbank flow, the water depth at the GSSHA outlet cell rises to 14 m. However, in simulations with overbank flow included, the depth at the outlet cell rises to and stays around its overbank flooding limit of 8 m. Moreover, as seen in Figure 7.5, the 2D overland cells close to the outlet get flooded to a depth of over 4 m, which is not seen in simulations excluding overbank flow physics. It is also noted that the cumulative volume of water that flows out of GSSHA is lower for the simulation including overbank flow physics. This indicates that more water remains piled up in the watershed in that case, indicating that the flooding is worse in that simulation. The final observation is that some oscillations are seen in two-way coupled simulations when overbank effects are included, evident from Figure 7.4. The GSSHA manual [32] states that including overbank flow physics can induce instabilities in the watershed models. Oscillations may also occur due to other reasons, however, as seen in the next verification test case.

7.4.2 Test case with stability problems

A test case in which oscillations are seen even when overbank flow physics is not in effect is presented in this section. The same GSSHA model from the previous section with overbank flow physics turned on is used. A different AdH model is utilized, given by $\Omega = (-12, 12)\,\mathrm{m} \times (0, 12)\,\mathrm{m}$, with a flat bed and an initial depth of 2 m. The western boundary of the AdH model

at $x = -12\,\text{m}$ is coupled to the GSSHA watershed outlet cell. The eastern boundary at $x = 12\,\text{m}$ has a constant water depth of 2 m specified as a BC. The north and south boundaries at $y = \{0, 12\}\,\text{m}$ have a no-normal-flow boundary condition. Manning's friction coefficient in the AdH domain is set to 0.002, and the Smagorinsky coefficient is set to 0.25. Four levels of mesh adaption are allowed. The time steps in GSSHA and AdH are respectively set to 0.5 s and 30 s. The four types of coupled simulations are run for 5 hours again.

Figures 7.6a and 7.6b respectively plot the temporal variation of depth and x-velocity in AdH at the AdH-GSSHA interface. One-way ADG and GDA coupled modes are seen to be vastly different as expected, since nothing happens in the AdH model in ADG coupling due to lack of any feedback to and forcing on it. Both the two-way coupled models are seen to exhibit oscillatory behavior. Even though overbank flow physics is turned on in the results shown in the figures, the oscillations seen in them are not due to that. This is because turning off the overbank flow effects does not remove the oscillations. Moreover, they are seen even at the beginning of the simulations when the depths in the channels are much smaller than their flooding limits. Using a larger time step of 300 s in AdH instead of 30 s used here removes the oscillations, although the results are not shown here for brevity. In two-way coupling, it is seen that when the outflow rate from GSSHA is relatively stable, small changes in the outflow can cause immediate changes in the AdH depth, which can in turn lead to increasingly larger feedback to both the models, resulting in oscillatory behavior. When larger time steps are used in AdH, it allows the outflow

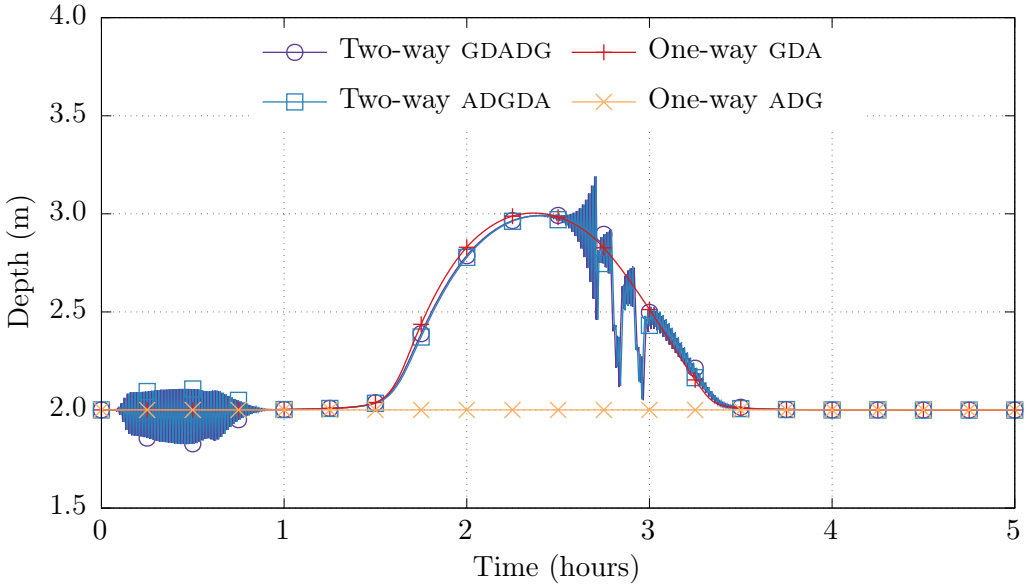

(a) Depth in AdH at the AdH-GSSHA interface

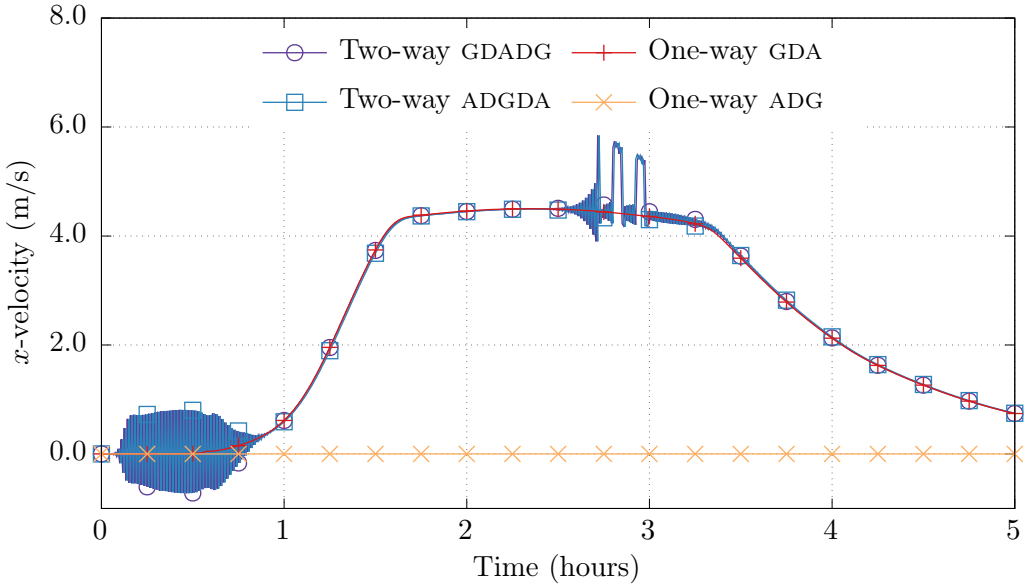

(b) x-velocity in AdH at the AdH-GSSHA interface

Figure 7.6: Depth and x-velocity in AdH at the AdH-GSSHA interface in all four types of coupling, for a relatively small AdH time step size of 30 s.

to get changed significantly in some direction in fewer (but larger) time steps, essentially skipping the oscillations. Another possible reason in case of the second set of oscillations during the peak outflow in this test case could be that the flow is close to the supercritical limit, with the Froude number becoming $\mathrm{Fr} = U/\sqrt{gh} \approx 4.5/\sqrt{9.81 \times 3.0} = 0.83$. It even crosses the 1.0 threshold during the oscillations, causing hydraulic jumps to momentarily appear in AdH, characterized by short periods of decreased depth and increased velocity in the figures. The oscillations stabilize when the GSSHA outflow drops significantly and flow returns to being subcritical. As mentioned in section 7.3, it is important to note that the diffusive wave equations are valid only for $\mathrm{Fr} \ll 1$, which is violated in this test case. Given the high velocities, it is seen that using a large value of 1.0 for the Smagorinsky coefficient also removes the oscillations. Since there are multiple scenarios in which the oscillations are seen to go away, the reason for the instability in this test case is currently unknown. More tests are needed to understand the stability aspects of shallow water and diffusive wave coupling.

Next, the outflow hydrograph of GSSHA in Figure 7.7a is compared to the inflow hydrograph of AdH shown in Figure 7.7b to confirm mass conservation. The AdH inflow hydrograph shown is only approximate, obtained by multiplying the coupled boundary width of 12 m with the depth and velocity shown in Figure 7.6. The depth and velocity vary along the coupled boundary, so the approximate AdH inflow hydrograph does not exactly match the GSSHA outflow hydrograph in the figures. The results again confirm the mass

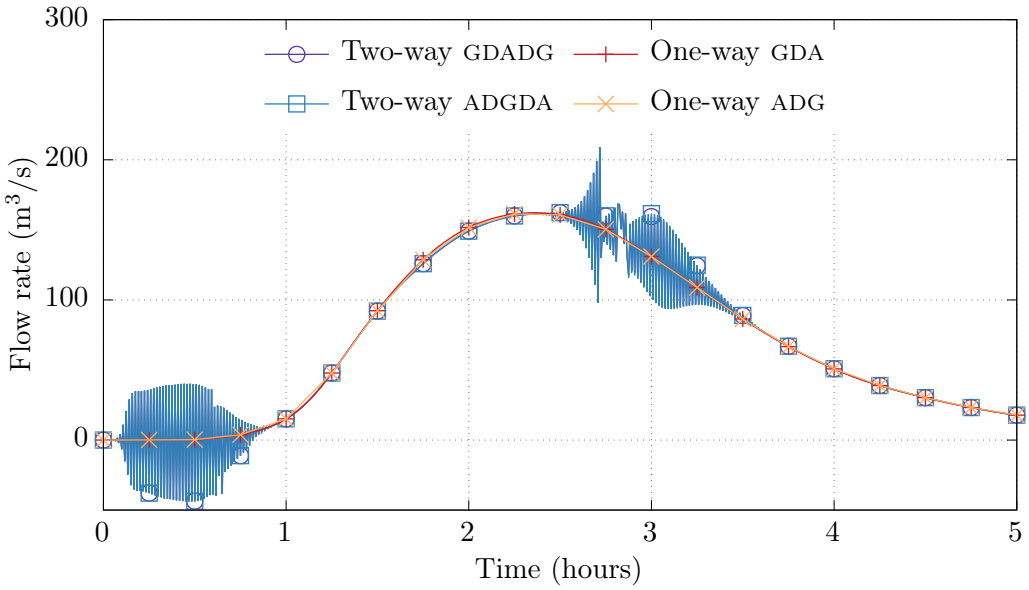

(a) Outflow hydrograph obtained from GSSHA

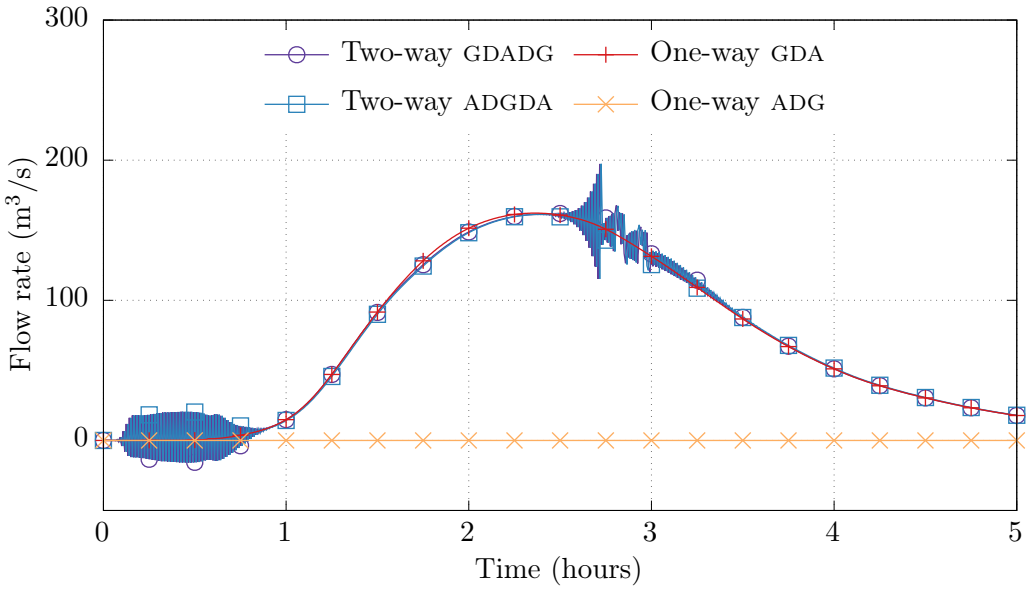

(b) AdH inflow hydrograph calculated approximately from Figure 7.6

Figure 7.7: Hydrographs at the AdH-GSSHA interface in all four types of coupling for a relatively small AdH time step size of 30 s.

conservation information given in Table 7.3. Note that unlike in the previous verification test case, this simulation does not show compound flooding effects because the water depth at the interface does not rise significantly, as seen in Figure 7.6a. Another indicator is that the results of two-way coupled models are unchanged as compared to those of the GDA simulation, except for the oscillations.

7.4.3 Test case with wetting-drying in the shallow water model

In this test case, the same GSSHA model from the previous section is used, but a different AdH model that has wetting-drying is utilized. The AdH domain is a channel given by $\Omega = (0, 40)\,\mathrm{m} \times (-8, 8)\,\mathrm{m}$, and has a trapezoidal cross-section. The flat bed portion of the cross-section is $y \in (-4, 4)\,\mathrm{m}$, and the sides have a slope of $\Delta\mathrm{y} : \Delta\mathrm{z} = 1 : 2$. The initial conditions are water at rest, with a flat water surface such that the depth is 2 m along the centerline, $y = 0\,\mathrm{m}$. Part of the western boundary, $y \in (-4, 4)\,\mathrm{m}$ at $x = 0\,\mathrm{m}$, is coupled to the GSSHA watershed outlet cell. The boundary condition on the eastern boundary at $x = 40\,\mathrm{m}$ is fixed water surface elevation such that the depth at the centerline is 2 m, same as the initial condition. Manning's bottom friction coefficient is set to 0.03, up to 4 levels of mesh adaption are allowed, the Smagorinsky coefficient is set to 1.00, and the wetting-drying tolerance in AdH is set to 0.1 m. There is no wind or atmospheric pressure in the AdH model. The time steps in AdH and GSSHA are set to 300 s and 0.5 s, respectively, and the coupled simulations are run for 5 hours.

Figures 7.8a and 7.8b show the depth and x-velocity in the AdH model in the middle of the AdH-GSSHA interface, whereas Figures 7.9a and 7.9b show the GSSHA outflow and approximate AdH inflow hydrographs. The mass conservation behavior given in Table 7.3 is confirmed yet again since the outflow and inflow hydrographs match well. The flow turns supercritical in this case too, with the Froude number being $\text{Fr} = U/\sqrt{gh} \approx 6/\sqrt{9.81 \times 3.25} = 1.06$. The Froude number is even higher for the wetting-drying elements which have a lower depth. This is the likely reason why reducing the Smagorinsky coefficient causes AdH to become unstable in this case without oscillations at the AdH-GSSHA interface. The key focus in this test case, however, is that wetting-drying close to the AdH-GSSHA interface (and not at it) works without problems related to coupling at least. Another important thing to note is that although the outflow hydrographs remain unchanged between the previous and current test cases, as observed by comparing Figures 7.7 and 7.9, the results of the depth and x-velocity shown in Figures 7.6 and 7.8 are seen to be significantly different. It shows, as expected, that the cross-section modeled in AdH at the AdH-GSSHA interface may significantly change the results in the coupled models, at least at the AdH-GSSHA interface. It remains to be seen if the results are also different far away from the AdH-GSSHA interface, or if the effects diminish away from it.

This concludes the verification of the weakly coupled shallow water and diffusive wave models used herein. The next section presents an application of coupling between NAM, AdH, and GSSHA. Separate verification tests were run

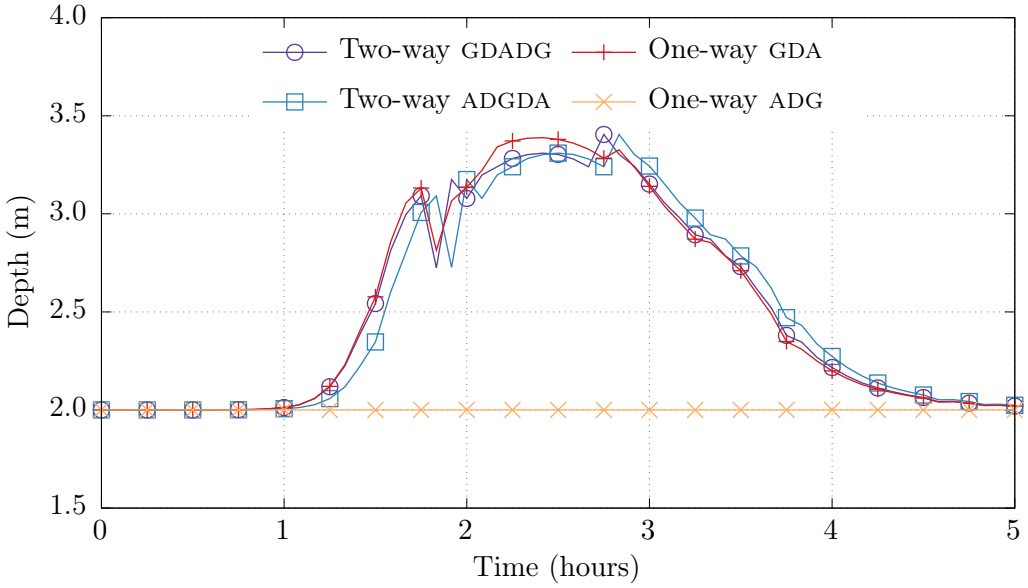

(a) Depth in AdH at the AdH-GSSHA interface

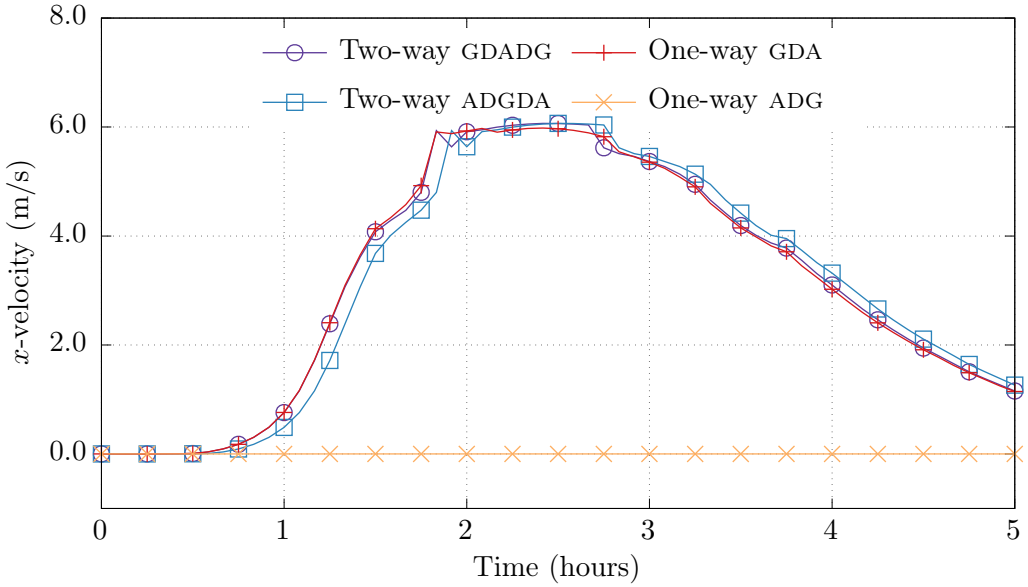

(b) x-velocity in AdH at the AdH-GSSHA interface

Figure 7.8: Depth and x-velocity in AdH at the AdH-GSSHA interface in all four types of coupling for a relatively large AdH time step size of 300 s.

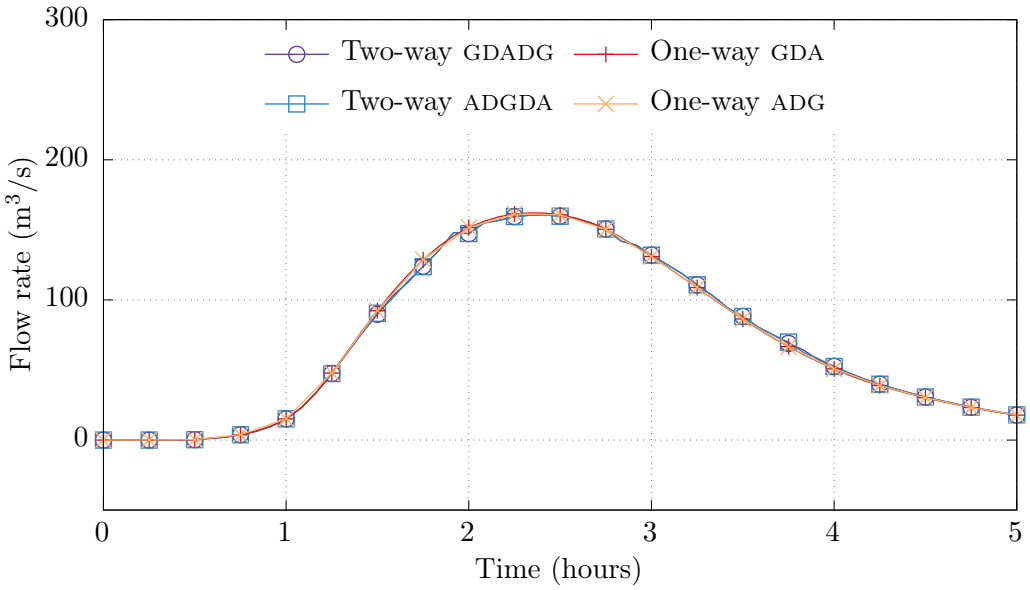

(a) Outflow hydrograph obtained from GSSHA solution

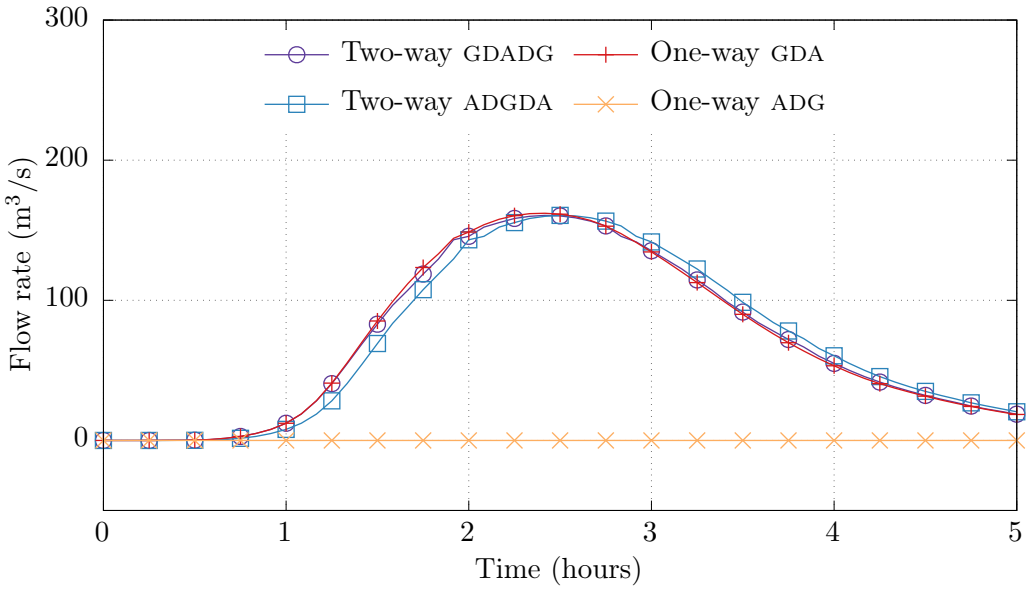

(b) Approximate inflow hydrograph obtained from AdH solution

Figure 7.9: Hydrographs at the AdH-GSSHA interface in all four types of coupling for a relatively large AdH time step size of 300 s.

to ensure that the data from NAM output files were being read into AdH and GSSHA correctly; these tests are not presented herein since one-way coupling from atmospheric models is already common, and no new information is gained in verifying NAM-AdH and NAM-GSSHA coupling.

7.5 Application: Flooding due to Hurricane Harvey

Hurricane Harvey caused record amounts of precipitation and flooding from 25^{th} to 30^{th} of August 2017, in south-east Texas, United States. Harvey dropped between 26 to 47 inches of rainfall across Harris County over a period of 4 days [53]. In particular, in the Brays Bayou watershed located in south-west Harris County, the rainfall at different locations during that time was between 29 to 35 inches [53]. Figure 7.10 shows the various watersheds located within Harris County. Figure 7.11 shows the Brays Bayou watershed, including its various streams and waterways. The watershed is important because it is located close to downtown Houston. It covers an area of approximately $329\,\text{km}^2$. Brays Bayou flows eastward to meet the Houston Ship Channel, which is connected to Galveston Bay further in the east. An ad hoc application involving a GSSHA model of the Brays Bayou watershed coupled to an AdH Galveston Bay model, with both being driven by atmospheric forcing from NAM is presented to simulate the flooding due to Hurricane Harvey.

A preliminary, uncalibrated GSSHA model of the watershed is used, shown in Figure 7.12. Overbank flow physics is turned off. The initial conditions on the channels are water at rest, with a flat water surface such that the

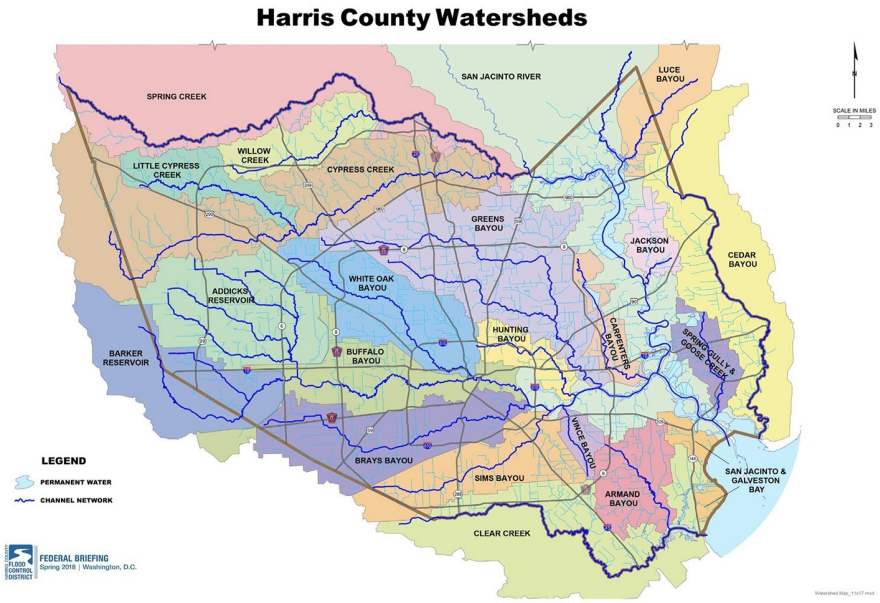

Figure 7.10: Harris County watersheds [29].

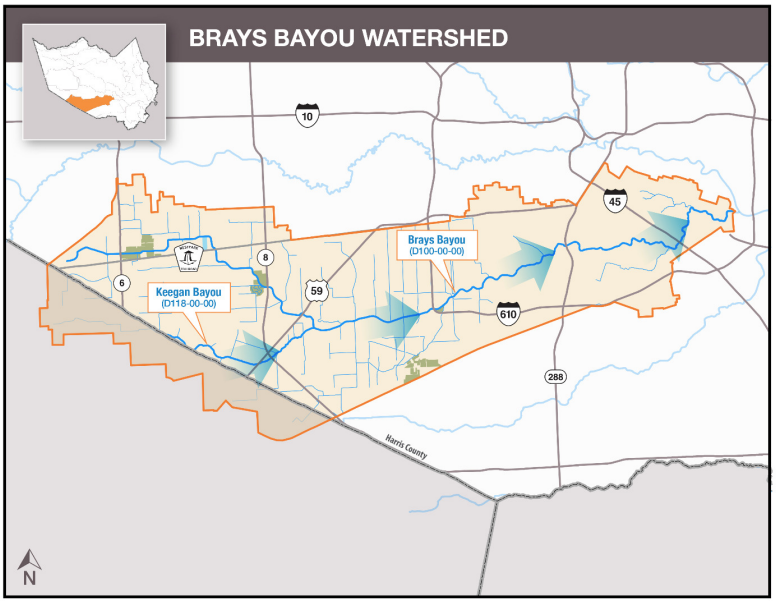

Figure 7.11: Brays Bayou watershed [27].

depth at the watershed outlet is 3 m, chosen arbitrarily. Most of the channels are dry. The 2D overland region is also initially dry. The NAM grid is approximated locally as a Cartesian grid about the latitude-longitude, (29.687646N, 264.486509E), before supplying GSSHA with rainfall data. The rainfall from NAM gets interpolated onto 9 regions over the watershed, as shown in Figure 7.13. These regions have approximately square boundaries, which result from using nearest-neighbor interpolation for distributing the rainfall from NAM onto the GSSHA watershed. Figure 7.14a shows the accumulated rainfall contained in the NAM output files over these 9 regions, ordered from top to bottom, left to right. In comparison, the observed accumulated rainfall data obtained from the Harris County Flood Warning System (HCFWS) [28] are shown in Figure 7.14b. From the figures, it is clear that NAM underestimated the accumulated rainfall over the watershed by about 10 inches, which is 30% of the observed rainfall of 29 to 35 inches [28, 53]. With such a high level of discrepancy, it would be impossible to accurately simulate the flooding during this event using the rainfall from NAM, no matter how good the models are. However, it is important to note that HCFWS data are observations that are only available *after* the event has passed, and therefore cannot be used for quick turn-around forecasts *before* the event when the need for them is maximum. Forecast data from atmospheric models are the only option available for use in predicting flooding before a hurricane makes landfall.

The AdH full-2D Galveston Bay model from section 6.2 is used as the shallow water model. The Smagorinsky coefficient is set to 0.2, Manning's

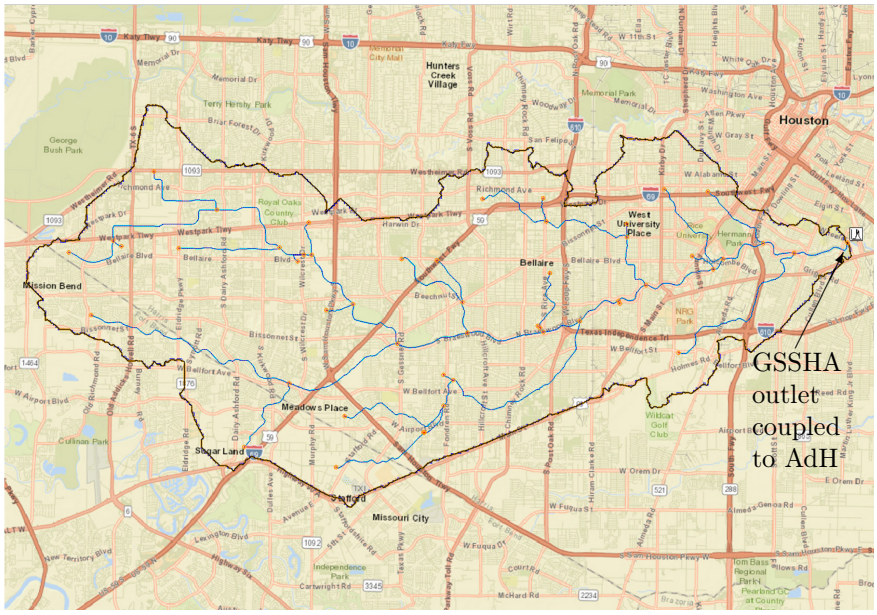

Figure 7.12: Modeled domain of the Brays Bayou watershed.

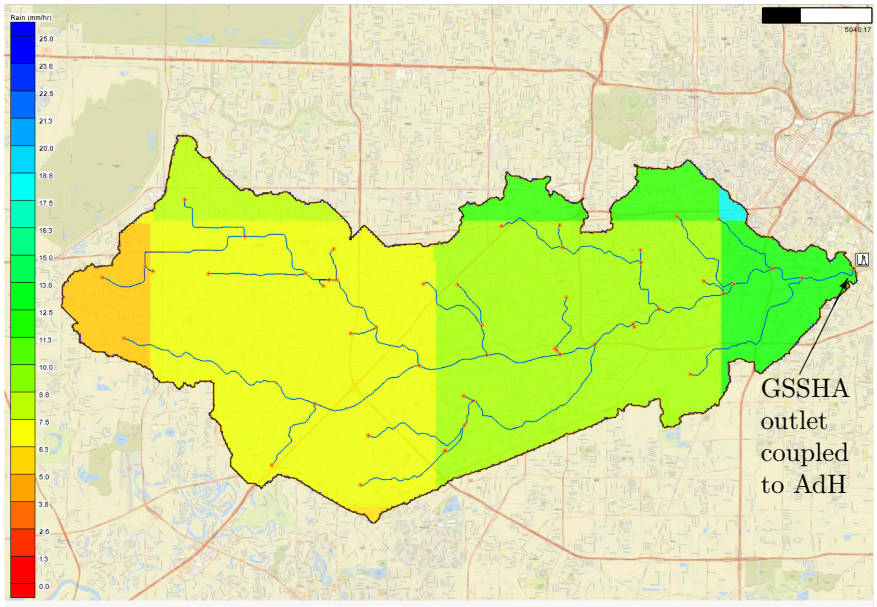

Figure 7.13: Voronoi cells resulting from nearest-neighbor interpolation of NAM rainfall over the Brays Bayou watershed.

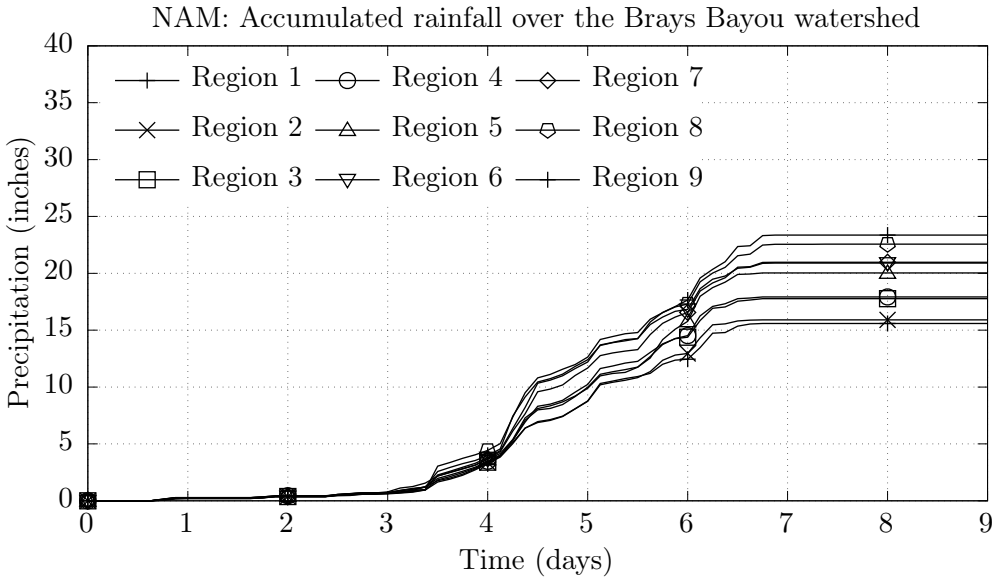

(a) Accumulated rainfall contained in NAM output files

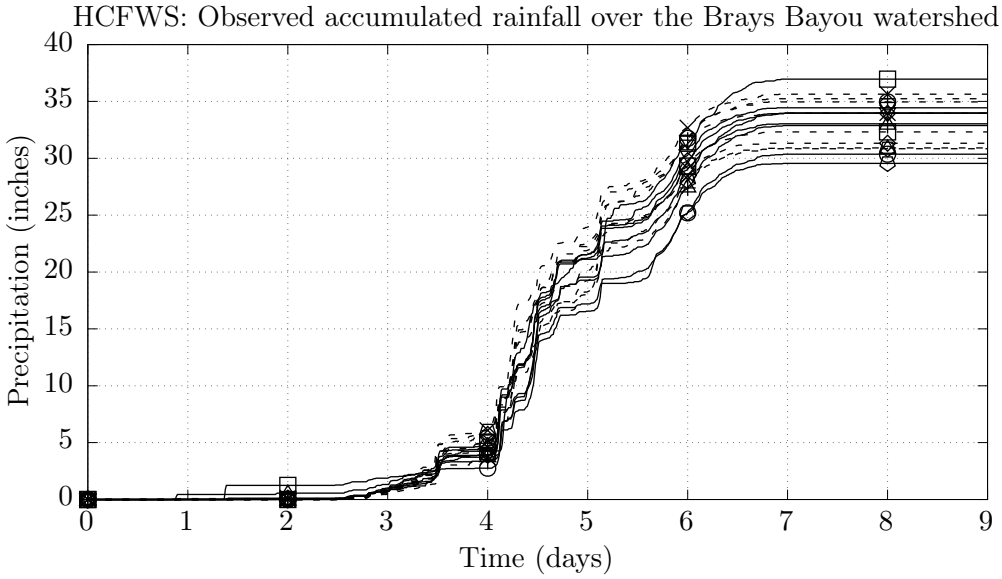

(b) Observed accumulated rainfall over 16 locations in the Brays Bayou watershed [28].

Figure 7.14: Accumulated rainfall: Comparison with NAM output files over actual observations [28] in the Brays Bayou watershed. Time $t = 0$ corresponds to August 23, 2017, 0000 hours UTC.

bed friction coefficient is set to 0.025, and wetting-drying tolerance is set to 0.2 m. Initial conditions on the model are water at rest with a flat water surface. Boundary conditions are no-normal-flow across the entire boundary except for two portions, one coupled with GSSHA, and the other in the deep ocean. The observed mean sea level at the Galveston Bay entrance, North Jetty, TX, Station ID #8771341, from the National Oceanic and Atmospheric Administration (NOAA) Tides and Currents website, is used [66] as a water surface elevation boundary condition on the south-eastern deep sea boundary. The observed and predicted elevation data for the duration of the simulation are shown in Figure 7.15. In a real-world hurricane scenario, the entire Gulf of Mexico must be modeled instead of just Galveston Bay to accurately forecast water surface elevations close to it; observations are not available for use before the event. In order to save modeling and computational time, however, only a model of the bay is used herein with the observed water surface elevation as forcing. The winds in AdH are read in from the NAM output files. Figure 7.16 shows the spatially varying wind from NAM over Galveston Bay. The snapshot corresponds to day 7 of the simulation. The roughly square divisions seen are a result of nearest-neighbor interpolation of the NAM data onto the shallow water grid.

There are about 20 miles of waterway between the GSSHA model outlet cell at the intersection of Brays Bayou and Martin Luther King (MLK) Jr. Boulevard shown in Figure 7.12, and the coupled AdH boundary at the Houston Ship Channel near Galveston Bay shown in Figure 7.16, that have not

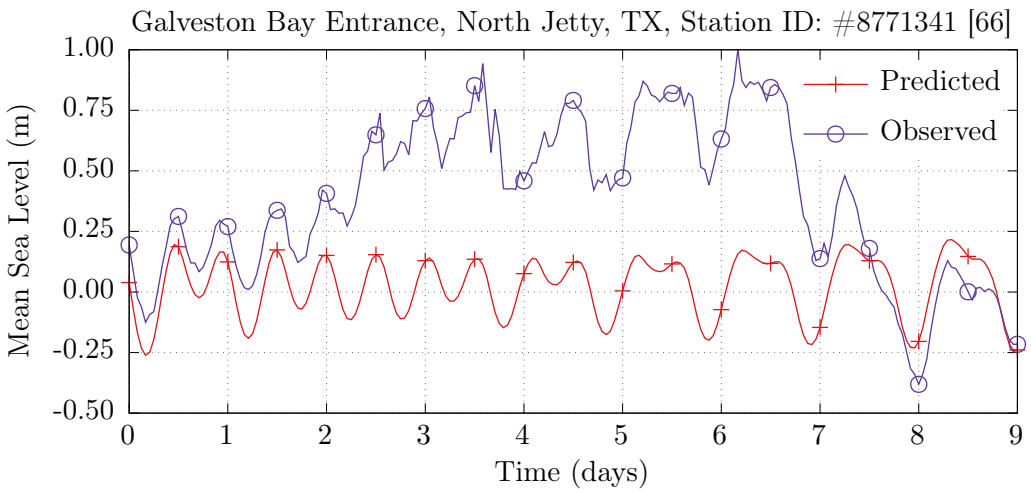

Figure 7.15: Mean sea level at Galveston Bay Entrance, North Jetty, TX, during Hurricane Harvey [66], starting from August 23, 2017, 0000 hours UTC.

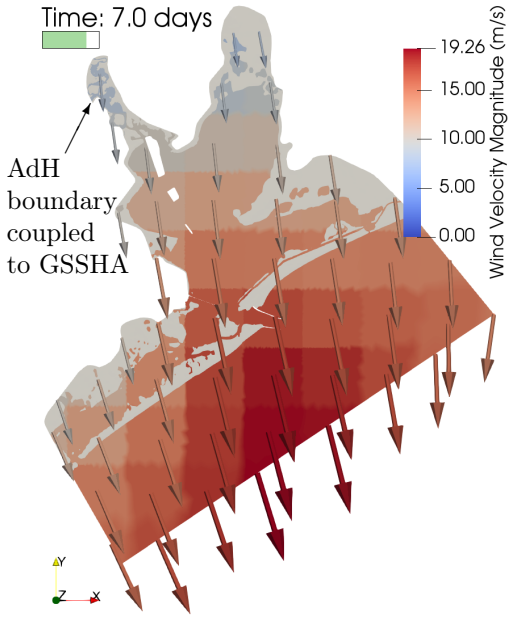

Figure 7.16: Snapshot of wind over the Galveston Bay domain supplied by NAM on day 7 of the simulation.

been modeled. The GSSHA watershed outlet cell is coupled to two connected boundary edges of the AdH model formed by three nodes numbered 37547, 37577, and 37608 in the model, with initial depths of 14.78 m, 5.23 m, and 3.61 m, respectively. Each edge is 265.5 m in length, so that the initial cross-section area on the AdH side of the interface is 3830 m^2. On the GSSHA side, at the coupled 1D stream outlet cell, the cross-section is trapezoidal, having a bottom width of 22.86 m and a side-slope of $\Delta\text{width} : \Delta\text{height} = 4 : 1$, so that its area is given by $(22.86h + 4h^2)$ in this case, where h is the depth in the outlet cell. At the beginning of the simulation, the GSSHA outlet cross-section area is 104.6 m^2, which is much smaller than the 3830 m^2 area on the AdH side. This difference is used for some sanity checks later.

The simulation ending time is set to 9 days, starting from August 23, 0000 hours to September 1, 0000 hours, UTC. The time steps of the GSSHA and AdH models are set to 0.25 s and 0.5 hours, respectively. Two sets of multiple simulations are run. One set uses rainfall supplied by NAM shown in Figure 7.14a, and the other uses the observed rainfall data from HCFWS shown in Figure 7.14b. In both the cases, the winds in AdH are read in from NAM. Each set of simulations contains four different runs,

1. A GSSHA-only run with a hydraulic slope of 0.001 specified on the 1D stream outlet cell as a boundary condition,

2. A GSSHA-only run with a constant water depth of 3 m specified as a boundary condition on the 1D stream outlet cell,

3. A one-way coupled ADG run, with the AdH model forcing the water surface elevation in the GSSHA outlet cell, ignoring the outflow from GSSHA, and using a no-normal-flow boundary condition on its coupled boundary instead, and

4. A two-way coupled GDADG run.

Figures 7.17 and 7.18 respectively show the surface elevation and velocity magnitude in AdH at the AdH-GSSHA interface in ADG and GDADG coupling simulations. The top and bottom subfigures respectively show the results of runs using NAM and HCFWS rainfall. Given the substantial differences in the rainfall inputs to GSSHA, the results of NAM and HCFWS rainfall simulations also differ. Figure 7.17 additionally shows the water surface elevation at the GSSHA watershed outlet cell. Except for small differences seen due to different output time resolutions, it is verified that the surface elevations in GSSHA and AdH match at the interface. It is also seen that the water surface elevations in the ADG and GDADG runs start to differ after about 3.5 days, seen as a departure between solid and dashed lines. This is when the outflow from GSSHA starts to affect the AdH solution at the interface in GDADG simulations, whereas that outflow is ignored in one-way ADG runs. Much lower velocities are seen at the interface nodes in the ADG mode than in the GDADG mode in Figure 7.18 due to the same reason.

Next, the GSSHA outflow hydrographs in all the simulations are compared with US Geological Survey (USGS) gauge data. The gauge is #08075110

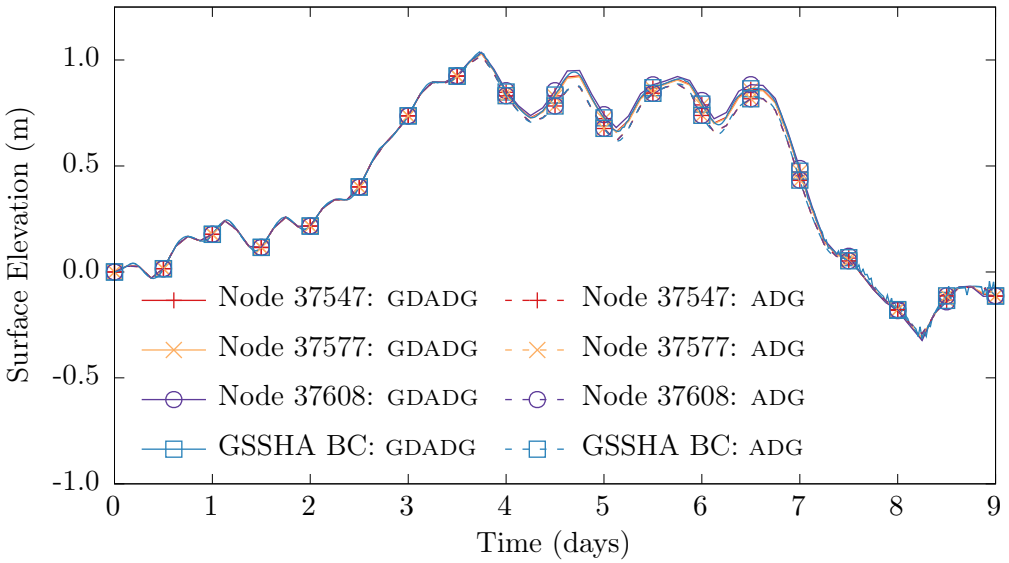

(a) Simulations using NAM rainfall

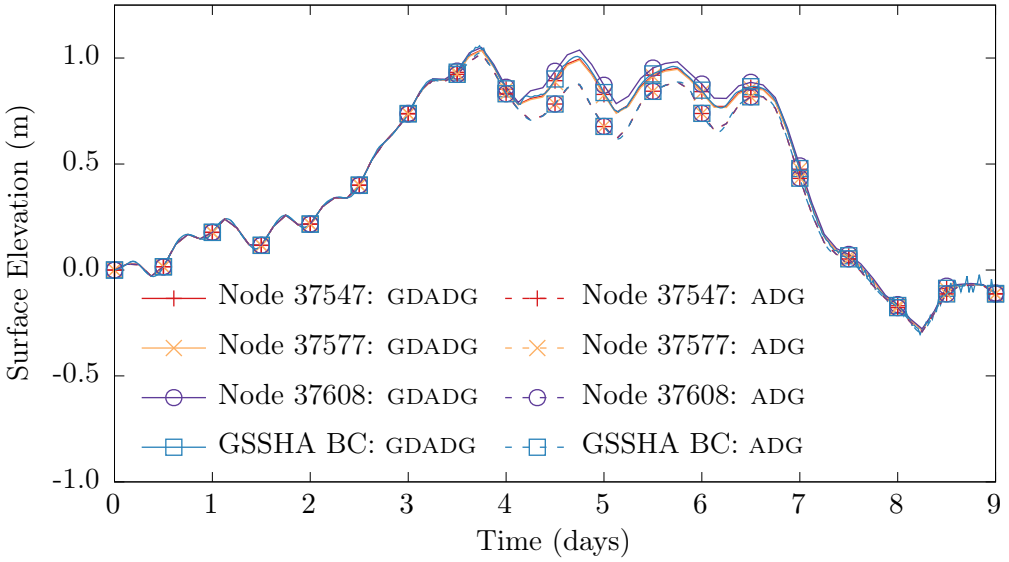

(b) Simulations using HCFWS rainfall

Figure 7.17: Temporal variation of water surface elevation at the coupled interface in simulations using NAM and HCFWS rainfall input.

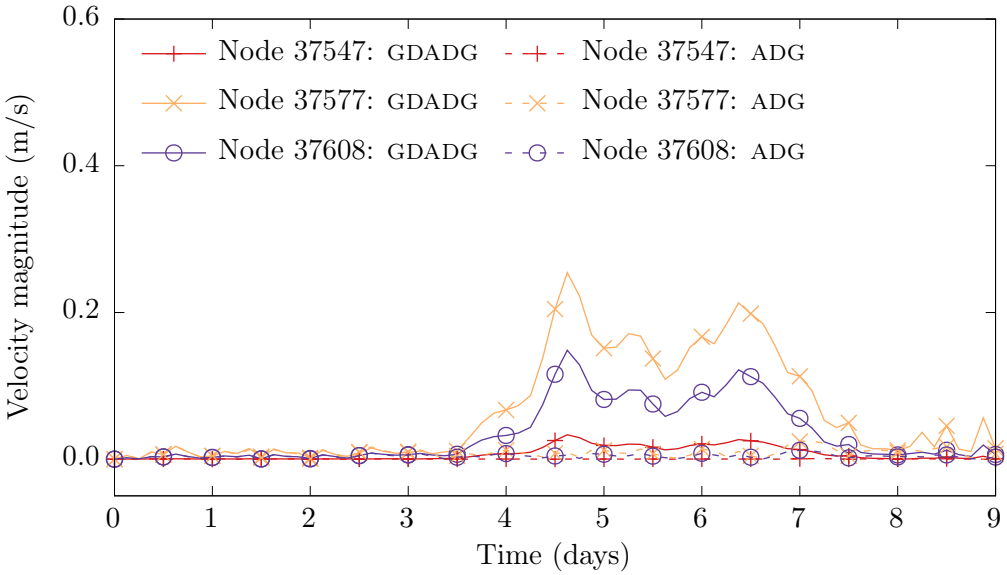

(a) Simulations using NAM rainfall

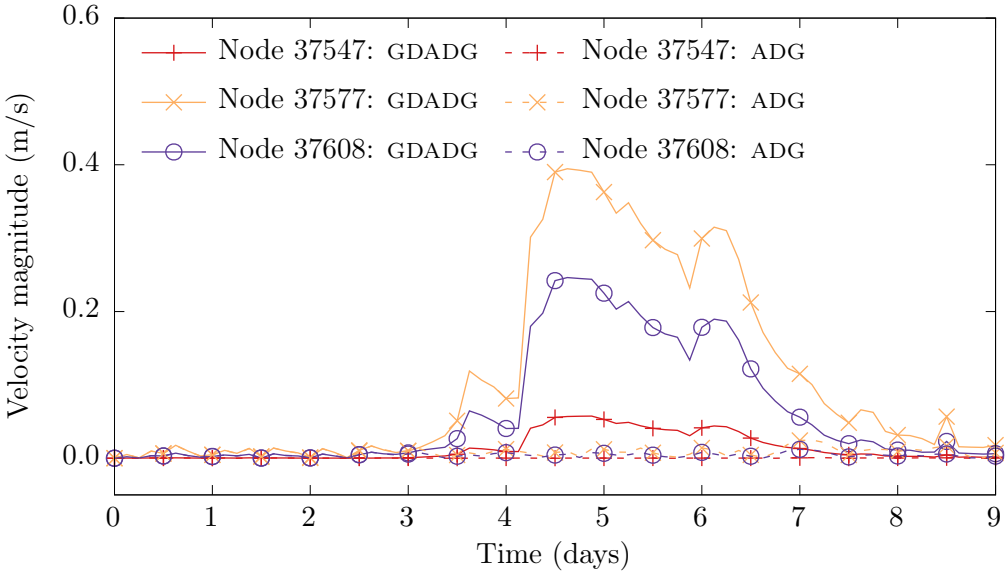

(b) Simulations using HCFWS rainfall

Figure 7.18: Temporal variation of velocity magnitude at the coupled interface in simulations using NAM and HCFWS rainfall input.

Brays Bayou at MLK Jr. Boulevard, Houston, TX [83]. Figure 7.19 shows a comparison of the hydrographs obtained in the two sets of simulations. As expected, the hydrographs of simulations using NAM and HCFWS rainfall are significantly different from each other given the substantially different inputs. The results of simulations using the rainfall data from NAM are seen to be inaccurate, which is expected given the large errors in them compared to actual observations. Using the rainfall observations from HCFWS gives significantly better results. In that case, the hydrographs of the ADG and GDADG simulations as well as the GSSHA-only run with a constant depth BC reasonably match the observed outflow at the USGS gauge, except for an overestimation of the peak outflow by about 20% between the fourth and fifth days. The GSSHA-only run with a hydraulic slope BC is only able to capture the general trend of the hydrographs but remains inaccurate. For a given rainfall input, NAM or HCFWS, the hydrographs of ADG and GDADG simulations are observed to be similar to each other as well as to that of the GSSHA-only simulation with a constant depth BC, indicating that the flooding in Brays Bayou was possibly not a compound flooding event. However, it may be misleading to conclude that from the hydrographs alone. Field observations [53] point to significant backwater flooding in many of the tributaries of Brays Bayou due to high flows in the bayou. Also, according to USGS gauge measurements [83], the water level in Brays Bayou at MLK Jr. Boulevard rose by over 9 m, whereas the water level is seen to have risen by a mere 1 m in Figure 7.17. Therefore, although the effects of storm surge were possibly not directly felt in

the watershed, backwater effects due to downstream flooding were significant. It is possible that including other physics such as overbank flow or groundwater may give better results. Modeling the correct cross-section in AdH at the interface and the 20 miles of waterways between the watershed outlet and Galveston Bay that were avoided herein may also be important. This is seen in the verification tests in the previous two sections which show how the surface elevations at the AdH-GSSHA interface are different for different AdH models even though the GSSHA model remains the same. Therefore, modeling the correct cross-section is likely crucial to get the water levels at the interface right. Overall, the key takeaway as far as NAM-AdH-GSSHA coupling is concerned is that if the precipitation data from NAM were accurate and comparable to the actual observations, then the coupled models would have been able to predict at least the outflow hydrographs relatively well.

One might question the need of two-way coupled models in this case given that the ADG simulation and the GSSHA-only run with a constant depth BC appear to do well. However, it is important to note that a two-way coupled model accounts for the outflow from the diffusive wave model into the shallow water domain, which is otherwise unavailable in a hurricane storm surge simulation using only a shallow water model. For example, noting that the ADG run would give the same results in the AdH domain as an AdH-only simulation would, it is seen in Figure 7.18 that the ADG runs cannot account for the inflow from GSSHA whereas GDADG simulations can. On the other hand, if the water surface elevation in AdH would have risen significantly enough like

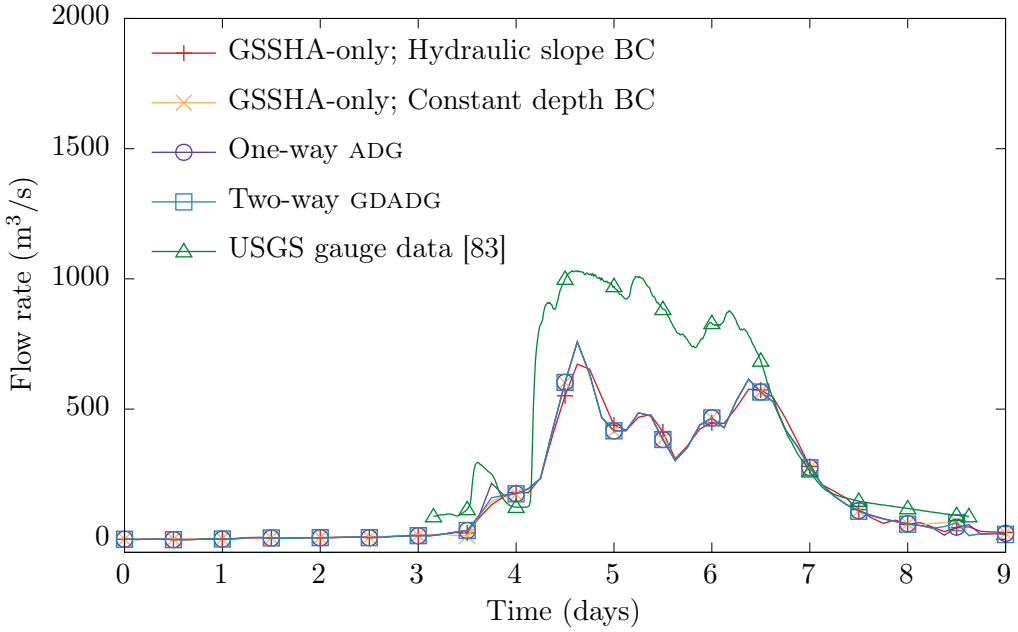

(a) Simulations using rainfall from NAM

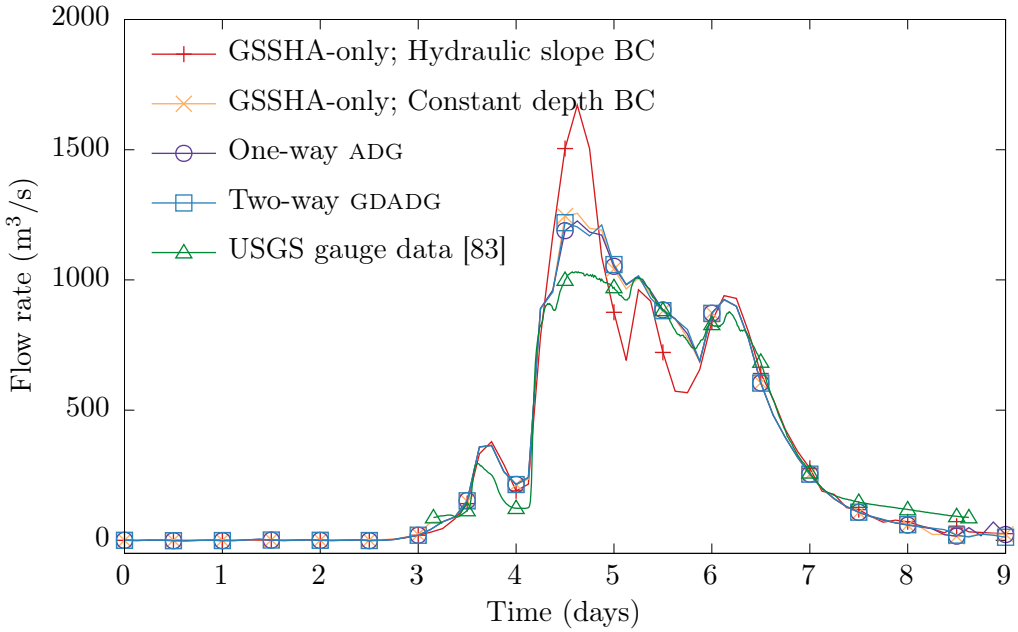

(b) Simulations using rainfall from HCFWS

Figure 7.19: Brays Bayou at MLK Jr. Boulevard: Comparison of obtained outflow hydrographs in different simulations against observations [83].

in the first verification test given in section 7.4.1, then GSSHA-only or GDA simulations would not be able to capture the compound flooding effect whereas two-way coupled simulations would do so. Therefore, two-way coupled models do hold importance, although it may not be obvious from the hydrograph results alone.

Having confirmed from Figure 7.17 that the surface elevations are continuous across the AdH-GSSHA interface in ADG and GDADG coupling, the final step is a sanity check to confirm that mass is being conserved across the interface in the two-way coupled simulations. Figure 7.20 zooms into the Houston Ship Channel in Galveston Bay to show the water velocity in AdH resulting from the outflow from GSSHA. The image corresponds to the fifth day of the GDADG simulation with HCFWS rainfall as input. As seen in Figure 7.19b, the outflow from GSSHA at that time is $1059\,\mathrm{m}^3/\mathrm{s}$. The interface cross-section area in AdH at that time, with depths calculated from Figure 7.17b, is $((14.78 + 0.83) + 2 \times (5.23 + 0.82) + (3.61 + 0.87)) \times 265.5/2 \approx 4273\,\mathrm{m}^2$. For conserving mass, the average speed of water flowing into AdH at that time should therefore be $(1059\,\mathrm{m}^3/\mathrm{s})/(4273\,\mathrm{m}^2) \approx 0.248\,\mathrm{m/s}$. Although from Figure 7.20, it looks as though the velocity at the AdH-GSSHA interface is about $0.55\,\mathrm{m/s}$, that value is only *close to* and *not at* the interface. The average inflow speed at the interface should be calculated from Figure 7.18b as $(0.05 + 2 \times 0.36 + 0.22)/4 = 0.248\,\mathrm{m/s}$, which is the same as the expected value. Therefore, the velocities seen in Figures 7.18 and 7.20 make sense, and mass is conserved across the AdH-GSSHA interface in the GDADG simulations

at least at that time.

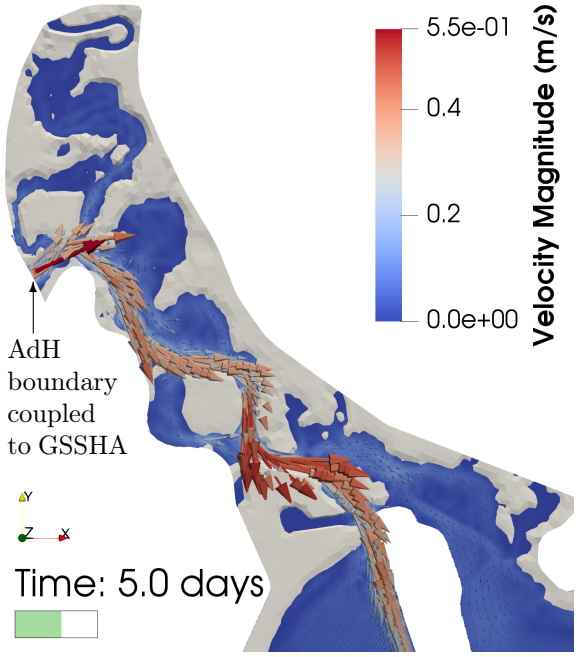

Figure 7.20: Velocity in the Houston Ship Channel close to the AdH-GSSHA interface in the GDADG coupled simulation using HCFWS rainfall data.

Chapter 8

Summary and conclusions

This dissertation focused on coupling different computational models to enable simulations that capture physics which the individual models are otherwise incapable of handling on their own. The major focus of this work was strong coupling between 2D and 3D shallow water and transport finite element models for enabling computationally cheaper 3D models and simulation of scenarios involving baroclinicity as well as wetting-drying. The second part of the work presented multi-software weak coupling between atmospheric, shallow water, and diffusive wave models to enable quick turn-around forecasts during extreme events such as hurricanes. A summary of the work, discussion of results, and conclusions are given in the following sections.

8.1 Coupled shallow water models

Strong coupling of 2D and 3D shallow water and transport models under a conformity requirement was seen to be a generalization of the usual finite element method, in the sense that analogous 2D-2D and 3D-3D strongly coupled models were observed to be exactly the same as usual full-2D and full-3D models. The conformity requirement imposed in coupling 2D and 3D

models indicated a particular choice of trial and test spaces during spatial discretization that naturally led to a monolithic system of equations being solved once at each time step. Conformity was shown to guarantee continuity of solution and conservation of mass and momentum across the 2D-3D coupling interface at all locations and at all times. A vertical velocity stage for 2D models was newly added to enable coupling of 2D and 3D vertical velocity calculations as well, improving past work which gave insufficient treatment to the same. The coupled shallow water models were verified and validated, and applications were presented to demonstrate their capabilities. In most cases, the coupled models were compared to full-2D and full-3D/3D-only models.

Four verification test cases were first presented, viz., the small- and large-amplitude slosh, baroclinic flume, and lock-exchange. Conservation of mass across the 2D-3D interface was verified in the small-amplitude slosh test case by checking that the sum of total volumes of water in the 2D and 3D domains was nearly constant throughout the duration of one of the simulations. For the small-amplitude slosh test case using second order implicit time-stepping, the L^2 error temporal convergence rates of full-2D, 2D-3D coupled, and full-3D models were verified to be second order. The L^2 error spatial convergence rates of all the models with SUPG terms excluded were also observed to be optimal at second order. For simulations with SUPG terms included, the spatial convergence rates for all the models were observed to be slightly lower. The error norms of the 2D-3D coupled models were observed to lie between those of full-2D and full-3D models for most of the time steps

in all the meshes for the small-amplitude slosh test case. Things were different, however, for the advection-dominated large-amplitude slosh test case, for which suboptimal spatial convergence rates between 1.25 to 1.5 were obtained for all the models, which is not unusual for SUPG [4, 48, 65]. Moreover, for this test case, it is likely that vertical mesh refinements, which were not done, would also be required to obtain a better convergence rate in the full-3D and 2D-3D coupled models. Overall, it was observed from the slosh test cases that:

1. The L^2 error convergence rates of 2D-3D strongly coupled models were no worse than the lower rate of convergence between full-2D and full-3D coupled models, and

2. Temporally, the L^2 error norms of the coupled models were either between or comparable to those of the full-2D and full-3D models.

On satisfactory verification with the slosh test case, the limits of 2D-3D coupled models were tested in baroclinic scenarios violating the base recommendation of placing the 2D-3D interface far away from baroclinicity; this was done since practical scenarios may force the placement of the interface in a baroclinic region. In the baroclinic flume test case, 2D-3D and 3D-2D coupled models were compared with full-2D and full-3D models. It was observed as expected that the 2D and 3D subdomains in the coupled models respectively behaved like the full-2D and full-3D models in the initial and final stages of the 2D-3D and 3D-2D coupled simulations when the salinity front was far away from the 2D-3D interface. The coupled models were in a state of transition

when the front was crossing the interface. The salinity front was seen to pass smoothly across the interface into the 3D region from the 2D subdomain in the 2D-3D coupled model. However, temporary velocity oscillations were seen in the 3D-2D coupled model, in which the stratified salinity front passing from the 3D domain into the 2D domain could no longer remain stratified due to the nature of coupling. It is possible that the temporary oscillations are an unavoidable trade-off for violating the 2D-3D interface location recommendation. Next, an extreme scenario of a lock-exchange test case was used to compare the results of a 2D-3D-2D coupled model against those of full-2D and full-3D models. Unlike in the full-3D and 2D-3D-2D coupled models, the solution in the full-2D model remained almost the same as the specified initial conditions throughout the simulation since 2D models cannot handle baroclinic mixing. As was the case with the baroclinic flume test case, the behavior of the 2D-3D-2D coupled model was initially similar to that of the full-3D model when the salinity and velocity shocks were far away from the 2D-3D interfaces. Unlike the baroclinic flume case, however, the shocks in lock-exchange test did not pass through the 2D-3D interfaces and were reflected back as if the interfaces were walls. The results of the coupled model were still better than the full-2D model.

Strongly coupled 2D-3D models were then validated against experimental data of the spur dike and partial-breach dam-break tests, giving acceptable results. These test cases were more of a validation of full-2D and full-3D models than of 2D-3D coupled models. Given the verification and validation results,

however, the following are expected to hold.

1. In test cases where 2D and 3D models are both successfully validated, 2D-3D coupled models would give acceptable results as well.

2. In tests where exactly one of the 2D or 3D models fails validation and the other succeeds, such as the lock-exchange test case, it would be possible to construct coupled models that would either pass or fail depending on the region of interest, location of the interface, and arrangement of the submodels.

3. In test cases where the shallow water equations are applicable but both 2D and 3D shallow water models fail validation, such as wetting-drying in a baroclinic scenario, 2D-3D coupled models would do better.

The first two points above can be concluded from all the presented tests. The only way to decisively draw the third conclusion is to perform actual validation in a scenario in which the shallow water equations are applicable but the 2D and 3D shallow water models are both inadequate. However, it is difficult to find small scale experimental data that can be used validate that case. It is also hard to compare results for the last scenario against real world measurements, since creating a model, gathering data, and tuning model parameters for large scale test cases is time-consuming and not a focus of this work. In order to lay the groundwork for rigorous validation of the third scenario in the future, two applications involving wetting-drying as well as baroclinicity were presented.

The first application was an idealized estuary test case, and the second one was a Galveston Bay test. In both the test cases, the solutions of the 2D-3D coupled models were seen to be similar yet different compared to those of the full-2D and 3D-only models. The coupled models were seen to be able to capture baroclinic mixing as well as wetting-drying, whereas the full-2D and 3D-only models could not handle at least one of them. In the idealized estuary case, the water surface elevations in the models close to the wetting-drying coastline and at the 2D-3D interface were observed to be in good agreement with each other. The surface salinity, and the surface and bed x-velocities in the coupled model were seen to be similar to those in the full-2D and 3D-only models in the relevant regions. In the Galveston Bay test case, the overall behavior of the solutions in the 2D-3D coupled model were observed to be qualitatively like those of the full-2D and 3D-only models in the respective regions.

In summary, the results of all the test cases show that strongly coupled 2D-3D shallow water and transport models are accurate, stable, and conserve mass and momentum across the 2D-3D interface at all times and at all locations along the interface. They are a viable alternative to implementing wetting-drying in 3D models, can capture baroclinicity as well as wetting-drying, and can reduce the computational cost of 3D models by allowing replacement of unimportant regions with 2D subdomains. Future work in 2D-3D coupled shallow water models can be to validate them rigorously, and to explore the possibility of allowing the solutions to vary within coupled

node columns instead of having to force them to remain constant. Coupling between 3D and multi-layer 2D shallow water models can also be explored.

8.2 Coupled atmospheric, hydrodynamic, and hydrologic models

Preliminary coupling between atmospheric, shallow water, and diffusive wave models was presented to simulate compound flooding events such as those during hurricanes. The atmospheric model solving the primitive equations was NAM, the hydrodynamic model solving the 2D shallow water equations was AdH, and the hydrologic model solving the 2D/1D coupled diffusive wave equations was GSSHA. The 1D stream outlet cell of a GSSHA watershed was weakly coupled to a portion of the AdH 2D shallow water domain boundary, enabling one/two-way exchange of flux and water surface elevation data between them. NAM was coupled one-way to the models through its GRIB2 format output files to drive precipitation over GSSHA watersheds and winds over AdH domains. The AdH and GSSHA models were solved in Gauss-Seidel format without any iterations, requiring them to be solved one after the other, once within each time step. The latest available solutions were utilized to modify the interface boundary conditions. Four types of coupling were implemented, GDA, ADG, GDADG, and ADGDA, with the former two being one-way and the remaining ones being two-way. Iterations were avoided since they involved having to backtrack solutions, which would potentially mean dealing with resetting thousands of variables in GSSHA. Backtracking solutions

within a time-step is non-trivial for users not involved in the development of the software being coupled, unless the functionality to do so is already built-in.

Three verification test cases and one application were presented. The first test case was for checking continuity of water surface elevation and conservation of mass across the AdH-GSSHA coupling interface in accordance with the information given in Table 7.3. The results confirmed that the water surface elevation was continuous in ADG coupling and mass was conserved in GDA coupling; mass was not conserved in ADG coupling and the water surface elevation was discontinuous in GDA coupling, as expected. In two-way GDADG and ADGDA coupling modes, the water surface elevation was continuous, and mass was conserved across the AdH-GSSHA interface, with one of them unavoidably being time-lagged. This hypothetical test case also happened to act as a compound flooding event that only the two-way coupled models were able to capture. This was evident from the following two factors.

1. The water surface elevation in the AdH domain rose significantly in GDA and two-way coupled simulations, but the backwater effects of that on the watershed were only captured in GDADG and ADGDA coupling.

2. The total outflow volume from the GSSHA watershed was significantly reduced in the two-way coupled simulations, which meant that the watershed remained flooded.

The next verification test case focused on stability problems encountered in two-way coupled simulations. Using smaller time steps in AdH re-

sulted in temporary oscillations in two-way coupled models in this test case. Using either a larger AdH time step size or a larger value of the Smagorinsky coefficient removed the oscillations. It was observed that during periods of relatively stable watershed outflow rates, the models gave increasing feedback to each other in quick succession, leading to oscillations. These oscillations were temporary in this test case, but in some other tests not presented herein, the time steps of the models got adaptively reduced to prohibitively small values, or the depth at the interface dropped to zero. There could be many possible reasons why the instabilities are seen, such as not using multiple Gauss-Seidel iterations, not modeling matching cross-sections on the AdH and GSSHA sides, or the diffusive wave equations being invalid at the location of the interface so that the approximation of neglecting the acceleration terms in the momentum equation becomes inappropriate. More work is needed to find the root cause of the oscillations.

The third verification test case ensured that wetting-drying in the vicinity of the coupling interface was not a problem. More importantly, this and the previous test cases showed how modeling different cross-sections on the AdH side of the interface led to different depth and velocity solutions there. The outflow hydrographs between the two test cases, however, appeared to remain unchanged in spite of that, indicating that the AdH model in these two test cases did not cause backwater flooding effects that would otherwise alter the hydrographs as well. More work needs to be done to determine how important it is to model matching cross-sections in the models at the interface, and how

it affects that solutions at and away from the interface.

Next, an application of NAM-AdH-GSSHA coupling to simulate flooding due to Hurricane Harvey of August 2017 was presented. A GSSHA model of the Brays Bayou watershed was coupled to an AdH Galveston Bay model. The models were not calibrated and had little resemblance to the real-world scenario due to numerous factors. The first reason was that the watershed and the bay are physically separated by about 20 miles of land and waterway that were not modeled in this application. The second reason was that the area of the coupled cross-section on the AdH side was over 35 times larger than that on the GSSHA side, causing a significant reduction in the water level rise and the velocity at the interface. The last and the most important factor was that NAM underestimated the rainfall by about 30% compared to the observations, leading to inaccurate results in the NAM-AdH-GSSHA coupled simulations. However, the hydrograph results in runs using observed rainfall data from HCFWS instead of precipitation from NAM were in good agreement with USGS gauge data. Although the results of the coupled atmospheric/hydrodynamic/hydrologic framework appeared to be unsatisfactory, the problem was clearly the precipitation input from NAM and not the coupling methodology, at least as far as the hydrograph was concerned. Moreover, given that observations cannot be used before an event has passed since they are only available during or after the event, only forecasts such as those from NAM that are available prior to such events can be used in emergency planning. Therefore, the application showed that given a reasonably accurate

forecast from an atmospheric model, the coupled models would have produced a match on the hydrograph, demonstrating their ability in producing quick turn-around forecasts.

The NAM-AdH-GSSHA coupling presented herein needs more work, testing and validation before being used. In particular, lateral flooding effects from 2D overland flow model boundaries must also be added to the coupling options. The stability of the models and the effects of modeling different cross-sections on either side of the interface must be thoroughly investigated in the future. In spite of shortcomings, however, this work demonstrates the capability of weakly coupled atmospheric, hydrodynamic, and hydrologic models in producing forecasts of compound flooding events.

8.3 Conclusion

The overall conclusion of this work is that coupling existing, well-tested and validated models is the key to capturing physics that the individual models cannot in general. This is seen in 2D and 3D shallow water and transport coupling, wherein 2D and 3D models cannot handle baroclinicity and wetting-drying respectively, but 2D-3D coupled models can when used sensibly. This is also observed in case of coupled shallow water and diffusive wave models, which are able to capture the interaction of floods downstream and upstream of the coupled interface. When coupled with an atmospheric model that gives accurate wind and precipitation forecasts, the coupled models would be able to capture compound flooding effects during hurricanes, which most models are

currently incapable of doing. Thus, coupled atmospheric, hydrodynamic, and hydrologic models hold importance in being able to simulate complex physical phenomena that the individual models may be incapable of.

Index

Bibliography

[1] PYPL Popularity of Programming Language Index. http://pypl.github.io/PYPL.html. Accessed: 2019-09-15.

[2] K. Anastasiou and C. T. Chan. Solution of the 2D shallow water equations using the finite volume method on unstructured triangular meshes. *International Journal for Numerical Methods in Fluids*, 24(11):1225–1245, 1997.

[3] Andrea Balzano. Evaluation of methods for numerical simulation of wetting and drying in shallow water flow models. *Coastal Engineering*, 34(1):83–107, 1998.

[4] Rutherford C. Berger and R. L. Stockstill. Finite-element model for high-velocity channels. *Journal of Hydraulic Engineering*, 121(10):710–716, 1995.

[5] Rutherford C. Berger, Jr. *Free-surface flow over curved surfaces.* PhD thesis, The University of Texas at Austin, 1992.

[6] Rutherford C. Berger, Jr. A finite element scheme for shock capturing. http://www.dtic.mil/get-tr-doc/pdf?AD=ADA270182, Aug 1993. Accessed: 2019-09-15.

[7] Alfredo Bermudez, Alain Dervieux, Jean-Antoine Desideri, and M.Elena Vazquez. Upwind schemes for the two-dimensional shallow water equations with variable depth using unstructured meshes. *Computer Methods in Applied Mechanics and Engineering*, 155(1):49–72, 1998.

[8] Eric S. Blake and David A. Zelinsky. Tropical cyclone report: Hurricane Harvey (AL092017). https://www.nhc.noaa.gov/data/tcr/AL092017_Harvey.pdf, May 2018. Accessed: 2019-09-15.

[9] Alan F. Blumberg and George L. Mellor. *A Description of a Three-Dimensional Coastal Ocean Circulation Model*, pages 1–16. American Geophysical Union (AGU), 2013.

[10] C. A. Brebbia and P. W. Partridge. Finite element simulation of water circulation in the north sea. *Applied Mathematical Modelling*, 1(2):101–107, 1976.

[11] A. N. Brooks and T. J. R. Hughes. Streamline upwind/Petrov-Galerkin formulations for convection dominated flows with particular emphasis on the incompressible Navier-Stokes equations. *Computer Methods in Applied Mechanics and Engineering*, 32(1):199–259, 1982.

[12] Shintaro Bunya, Ethan J. Kubatko, Joannes J. Westerink, and Clint Dawson. A wetting and drying treatment for the runge-kutta discontinuous Galerkin solution to the shallow water equations. *Computer Methods in Applied Mechanics and Engineering*, 198(17):1548–1562, 2009.

[13] Francisco Nicolás Cantero-Chinchilla, Oscar Castro-Orgaz, Subhasish Dey, and Jose Luis Ayuso. Nonhydrostatic dam break flows. I: Physical equations and numerical schemes. *Journal of Hydraulic Engineering*, 142(12):04016068, 2016.

[14] Francisco Nicolás Cantero-Chinchilla, Oscar Castro-Orgaz, Subhasish Dey, and Jose Luis Ayuso-Muñoz. Nonhydrostatic dam break flows. II: One-dimensional depth-averaged modeling for movable bed flows. *Journal of Hydraulic Engineering*, 142(12):04016069, 2016.

[15] Vincenzo Casulli. Semi-implicit finite difference methods for the two-dimensional shallow water equations. *Journal of Computational Physics*, 86(1):56–74, 1990.

[16] Vincenzo Casulli and Ralph T. Cheng. Semi-implicit finite difference methods for three-dimensional shallow water flow. *International Journal for Numerical Methods in Fluids*, 15(6):629–648, 1992.

[17] National Hurricane Center. 2017 update to the costliest US tropical cyclones. https://www.nhc.noaa.gov/news/UpdatedCostliest.pdf, Jan 2018. Accesssed: 2019-09-15.

[18] Changsheng Chen, Hedong Liu, and Robert C. Beardsley. An unstructured grid, finite-volume, three-dimensional, primitive equations ocean model: Application to coastal ocean and estuaries. *Journal of Atmospheric and Oceanic Technology*, 20(1):159–186, 2003.

[19] Yongcan Chen, Zhiyong Wang, Zhaowei Liu, and Dejun Zhu. 1D–2D coupled numerical model for shallow-water flows. *Journal of Hydraulic Engineering*, 138(2):122–132, 2012.

[20] Gajanan Krishna Choudhary. Algebraic coupling of 2D and 3D shallow water finite element models. Master's report, The University of Texas at Austin, 2017.

[21] Clint Dawson and Vadym Aizinger. A discontinuous Galerkin method for three-dimensional shallow water equations. *Journal of Scientific Computing*, 22(1):245–267, Jun 2005.

[22] Clint Dawson and Jennifer Proft. Discontinuous and coupled continuous/discontinuous Galerkin methods for the shallow water equations. *Computer Methods in Applied Mechanics and Engineering*, 191(41):4721–4746, 2002.

[23] Clint Dawson and Juha H. Videman. A streamline diffusion finite element method for the viscous shallow water equations. *Journal of Computational and Applied Mathematics*, 251:1–7, 2013.

[24] A. Decoene and J. F. Gerbeau. Sigma transformation and ALE formulation for three-dimensional free surface flows. *International Journal for Numerical Methods in Fluids*, 59(4):357–386, 2009.

[25] Clifford H. Dey, Charles Sanders, Jean Clochard, John Hennessy, and Simon Elliott. *Guide to the WMO Table Driven Code Form Used for the*

Representation and Exchange of Regularly Spaced Data in Binary Form: FM 92 GRIB Edition 2. World Meteorological Organization (WMO), Geneva, Jan 2003. Accessed: 2019-09-15.

[26] J. C. Dietrich, C. J. Trahan, M. T. Howard, J. G. Fleming, R. J. Weaver, S. Tanaka, L. Yu, R. A. Luettich, C. N. Dawson, J. J. Westerink, G. Wells, A. Lu, K. Vega, A. Kubach, K. M. Dresback, R. L. Kolar, C. Kaiser, and R. R. Twilley. Surface trajectories of oil transport along the northern coastline of the Gulf of Mexico. *Continental Shelf Research*, 41:17–47, 2012.

[27] Harris County Flood Control District. The Brays Bayou watershed. https://www.hcfcd.org/projects-studies/brays-bayou/. Accessed: 2019-09-15.

[28] Harris County Flood Control District. Harris County Flood Warning System. https://www.harriscountyfws.org/?View=full. Accessed: 2019-09-15.

[29] Harris County Flood Control District. Federal briefing 2018. https://www.hcfcd.org/media/2493/hcfcdfederalbriefing2018.pdf, 2018. Accessed: 2019-09-15.

[30] K Djadel, A Ern, and S Piperno. Discontinuous Galerkin methods for the shallow-water equations with bathymetric terms and dry areas. In P. Wesseling, E. OÃśate, and J. PÃľriaux, editors, *ECCOMAS CFD 2006:*

Proceedings of the European Conference on Computational Fluid Dynamics, pages 1–12, Egmond aan Zee, Netherlands, 2006. Delft University of Technology.

[31] Charles W. Downer and Fred L. Ogden. Gssha: Model to simulate diverse stream flow producing processes. *Journal of Hydrologic Engineering*, 9(3):161–174, 2004.

[32] Charles W. Downer and Fred L. Ogden. Gridded Surface Subsurface Hydrologic Analysis (GSSHA) User's Manual; Version 1.43 for Watershed Modeling System 6.1. Technical report, Coastal and Hydraulics Lab, Engineer Research and Development Center, Vicksburg, MS, 2006.

[33] Wesley Ebisuzaki, Reinoud Bokhorst, John Howard, Jaakko Hyvätti, Dusan Jovic, Daniel Lee, Kristian Nilssen, Karl Pfeiffer, Pablo Romero, Manfred Schwarb, Gregor Schee, Arlindo da Silva, Niklas Sondell, Sam Trahan, and Sergey Varlamov. *wgrib2: A Utility to Read and Write GRIB2 Files*. Climate Prediction Center, National Weather Service, NCEP, NOAA. Accessed: 2019-09-15.

[34] Mohamed Elkholy, Lindsey Ann LaRocque, M. Hanif Chaudhry, and Jasim Imran. Experimental investigations of partial-breach dam-break flows. *Journal of Hydraulic Engineering*, 142(11):04016042, 2016.

[35] Lisa R. Gaddis and Peter J. Mouginis-Mark. Mississippi river outflow patterns seen by Seasat radar. *Geology*, 13(4):227, 1985.

[36] A. E. Green and P. M. Naghdi. A derivation of equations for wave propagation in water of variable depth. *Journal of Fluid Mechanics*, 78(2):237–246, 1976.

[37] Mourad Heniche, Yves Secretan, Paul Boudreau, and Michel Leclerc. A two-dimensional finite element drying-wetting shallow water model for rivers and estuaries. *Advances in Water Resources*, 23(4):359–372, 2000.

[38] C. W. Hirt. An arbitrary Lagrangian-Eulerian computing technique. In Maurice Holt, editor, *Proceedings of the Second International Conference on Numerical Methods in Fluid Dynamics*, pages 350–355, Berlin, Heidelberg, 1971. Springer Berlin Heidelberg.

[39] C. W. Hirt, A. A. Amsden, and J. L. Cook. An arbitrary Lagrangian-Eulerian computing method for all flow speeds. *Journal of Computational Physics*, 14(3):227–253, 1974.

[40] M. S. Horritt. Evaluating wetting and drying algorithms for finite element models of shallow water flow. *International Journal for Numerical Methods in Engineering*, 55(7):835–851, 2002.

[41] Thomas J. R. Hughes, Wing Kam Liu, and Thomas K. Zimmermann. Lagrangian-Eulerian finite element formulation for incompressible viscous flows. *Computer Methods in Applied Mechanics and Engineering*, 29(3):329–349, 1981.

[42] Thomas J. R. Hughes, Guglielmo Scovazzi, and Tayfun E. Tezduyar. Stabilized methods for compressible flows. *Journal of Scientific Computing*, 43(3):343–368, Jun 2010.

[43] Arieh Iserles. *A First Course in the Numerical Analysis of Differential Equations*. Cambridge Texts in Applied Mathematics. Cambridge University Press, 2 edition, 2008.

[44] M. Iskandarani, D. B. Haidvogel, and J. C. Levin. A three-dimensional spectral element model for the solution of the hydrostatic primitive equations. *Journal of Computational Physics*, 186(2):397–425, Apr 2003.

[45] Z. I. Janjic. A nonhydrostatic model based on a new approach. *Meteorology and Atmospheric Physics*, 82(1):271–285, Jan 2003.

[46] Akhilesh Kumar Jha, Juichiro Akiyama, and Masaru Ura. First- and second-order flux difference splitting schemes for dam-break problem. *Journal of Hydraulic Engineering*, 121(12):877–884, 1995.

[47] Y.W. Jiang and Onyx W.H. Wai. Drying-wetting approach for 3D finite element sigma coordinate model for estuaries with large tidal flats. *Advances in Water Resources*, 28(8):779–792, 2005.

[48] Claes Johnson, Alfred H Schatz, and Lars B Wahlbin. Crosswind smear and pointwise errors in streamline diffusion finite element methods. *Mathematics of Computation*, 49(179):25–38, 1987.

[49] M. Kawahara, T. Kodama, and M. Kinoshita. Finite element method for tsunami wave propagation analysis considering the open boundary condition. *Computers & Mathematics with Applications*, 16(1):139–152, 1988.

[50] C. Knock and S.C. Ryrie. A varying time step finite-element method for the shallow water equations. *Applied Mathematical Modelling*, 18(4):224–230, 1994.

[51] Ethan J. Kubatko, Joannes J. Westerink, and Clint Dawson. *hp* discontinuous galerkin methods for advection dominated problems in shallow water flow. *Computer Methods in Applied Mechanics and Engineering*, 196(1):437–451, 2006.

[52] Igor Kukavica and Mohammed Ziane. On the regularity of the primitive equations of the ocean. *Nonlinearity*, 20(12):2739–2753, Oct 2007.

[53] Jeff Lindner and Steve Fitzgerald. Memorandum - Hurricane Harvey storm and flood information, Jun 2018.

[54] Aquaveo LLC. Watershed Modeling System (WMS) tutorials. https://www.aquaveo.com/software/wms-learning-tutorials. Accessed: 2019-09-15.

[55] Tate O. McAlpin, Gaurav Savant, Gary L. Brown, S. Jarrell Smith, and Raymond S. Chapman. Hydrodynamics of Knik Arm: Modeling study.

Journal of Waterway, Port, Coastal, and Ocean Engineering, 139(3):232–246, 2013.

[56] Morgan McKee. Effects of storm surge and nutrient loading on coastal wetland soil processes: Implications for ecosystem function. Master's thesis, Louisiana State University, 2014.

[57] Edie Miglio, Alfio Quarteroni, and Fausto Saleri. Finite element approximation of quasi-3D shallow water equations. *Computer Methods in Applied Mechanics and Engineering*, 174(3):355–369, 1999.

[58] Hseng Tseng Ming and Chia R. Chu. Two-dimensional shallow water flows simulation using TVD-MacCormack scheme. *Journal of Hydraulic Research*, 38(2):123–131, 2000.

[59] Florian Mintgen and Michael Manhart. A bi-directional coupling of 2D shallow water and 3D Reynolds-averaged Navier-Stokes models. *Journal of Hydraulic Research*, 56(6):771–785, 2018.

[60] Dimitrios Mitsotakis, Boaz Ilan, and Denys Dutykh. On the Galerkin/ finite-element method for the Serre equations. *Journal of Scientific Computing*, 61(1):166–195, Oct 2014.

[61] Hamed R. Moftakhari, Gianfausto Salvadori, Amir AghaKouchak, Brett F. Sanders, and Richard A. Matthew. Compounding effects of sea level rise and fluvial flooding. *Proceedings of the National Academy of Sciences*, 114(37):9785–9790, 2017.

[62] National Centers for Environmental Prediction (NCEP). NAM CONUS 12 km resolution grid. https://www.emc.ncep.noaa.gov/mmb/namgrids/g212.12km.jpg. Accessed: 2019-09-15.

[63] National Centers for Environmental Prediction (NCEP). North American Mesoscale Forecast System. https://www.ncdc.noaa.gov/data-access/model-data/model-datasets/north-american-mesoscale-forecast-system-nam. Accessed: 2019-09-15.

[64] Ionel Michael Navon. Finite-element simulation of the shallow-water equations model on a limited-area domain. *Applied Mathematical Modelling*, 3(5):337–348, 1979.

[65] Koichi Niijima. Pointwise error estimates for a streamline diffusion finite element scheme. *Numerische Mathematik*, 56(7):707–719, Jul 1989.

[66] National Oceanic and Atmospheric Administration. Galveston Bay Entrance, North Jetty, TX, Station ID: 8771341. https://tidesandcurrents.noaa.gov/waterlevels.html?id=8771341&units=metric&bdate=20170823&edate=20170831&timezone=GMT&datum=MSL&interval=h&action=. Accessed: 2019-09-15.

[67] S. O'Grady. RedMonk programming language rankings for January 2019. https://redmonk.com/sogrady/2019/03/20/language-rankings-1-19. Accessed: 2019-09-15.

[68] N. A. Phillips. A cordinate system having some special advantages for numerical forecasting. *Journal of Meteorology*, 14(2):184–185, 1957.

[69] Donald W. Pritchard. A summary concerning the newly adopted Practical Salinity Scale, 1978, and the International Equation of State of Seawater, 1980. 1982.

[70] Nallamuthu Rajaratnam and Benjamin A. Nwachukwu. Flow near groin-like structures. *Journal of Hydraulic Engineering*, 109(3):463–480, 1983.

[71] The Python Language Reference. *ctypes – A foreign function library for Python*. Python Software Foundation. Accessed: 2019-09-15.

[72] Jean-François Remacle, Sandra Soares Frazão, Xiangrong Li, and Mark S. Shephard. An adaptive discretization of shallow-water equations based on discontinuous Galerkin methods. *International Journal for Numerical Methods in Fluids*, 52(8):903–923, 2006.

[73] Eric Rogers, Geoffrey DiMego, Thomas Black, Michael Ek, Brad Ferrier, George Gayno, Zavisa Janjic, Ying Lin, Matthew Pyle, Vince Wong, Wan-Shu Wu, and Jacob Carley. The NCEP North American mesoscale modeling system: Recent changes and future plans. In *Preprints, 23rd Conference on Weather Analysis and Forecasting/19th Conference on Numerical Weather Prediction*, 2009.

[74] Gaurav Savant and Tate O. McAlpin. Tidal hydrodynamics in the lower

Columbia river estuary through depth averaged Adaptive Hydraulics modeling. *Journal of Engineering*, page 416914, 2014.

[75] Hermann Amandus Schwarz. *Ueber einen Grenzübergang durch alternirendes Verfahren.* Zürcher u. Furrer, 1870.

[76] Antonia Sebastian, Kasper Lendering, Baukje Kothuis, Nikki Brand, Sebastiaan N. Jonkman, Pieter van Gelder, Maartje Godfroij, Bas Kolen, Tina Comes, and Stef Lhermitte. Hurricane Harvey report: A fact-finding effort in the direct aftermath of Hurricane Harvey in the Greater Houston region, Oct 2017.

[77] Antonia Sebastian, Jennifer Proft, J. Casey Dietrich, Wei Du, Philip B. Bedient, and Clint N. Dawson. Characterizing hurricane storm surge behavior in Galveston Bay using the SWAN+ADCIRC model. *Coastal Engineering*, 88:171–181, 2014.

[78] François Serre. Contribution à l'étude des écoulements permanents et variables dans les canaux. *La Houille Blanche*, (3):374–388, 1953.

[79] J. O. Shin, S. B. Dalziel, and P. F. Linden. Gravity currents produced by lock exchange. *Journal of Fluid Mechanics*, 521:1–âĂŞ34, 2004.

[80] Stefan Alfred Sicklinger. *Stabilized Co-Simulation of Coupled Problems Including Fields and Signals.* Dissertation, Technische Universität München, München, 2014.

[81] Joseph Smagorinsky. General circulation experiments with the primitive equations. *Monthly Weather Review*, 91(3):99–164, 1963.

[82] Pavel Solin, Karel Segeth, and Ivo Dolezel. *Higher-order finite element methods*. Chapman and Hall/CRC, 2003.

[83] United States Geological Survey. USGS gage data for hurricane Harvey: Gage 08075110, Brays Bayou at MLK Jr Blvd, Houston, TX. https://nwis.waterdata.usgs.gov/nwis/uv?cb_00060=on&cb_00065=on&format=gif_default&site_no=08075110&period=&begin_date=2017-08-23&end_date=2017-08-31. Accessed: 2019-09-15.

[84] R. C. Sutcliffe. A contribution to the problem of development. *Quarterly Journal of the Royal Meteorological Society*, 73(317-318):370–383, 1947.

[85] Shinsuke Takase, Kazuo Kashiyama, Seizo Tanaka, and Tayfun E. Tezduyar. Space-time SUPG formulation of the shallow-water equations. *International Journal for Numerical Methods in Fluids*, 64(10-12):1379–1394, 2010.

[86] Allen M. Teeter, Billy H. Johnson, Charlie Berger, Guus Stelling, Norman W. Scheffner, Marcelo H. Garcia, and T.M. Parchure. Hydrodynamic and sediment transport modeling with emphasis on shallow-water, vegetated areas (lakes, reservoirs, estuaries and lagoons). *Hydrobiologia*, 444(1):1–23, Feb 2001.

[87] William Carlisle Thacker. Some exact solutions to the nonlinear shallow-water wave equations. *Journal of Fluid Mechanics*, 107:499–508, 1981.

[88] TIOBE. Tiobe Index for September 2019. https://www.tiobe.com/tiobe-index. Accessed: 2019-09-15.

[89] Corey J. Trahan, Gaurav Savant, Rutherford C. Berger, Matthew Farthing, Tate O. McAlpin, Lucas Pettey, Gajanan Krishna Choudhary, and Clint N. Dawson. Formulation and application of the adaptive hydraulics three-dimensional shallow water and transport models. *Journal of Computational Physics*, 374:47–90, 2018.

[90] Torbjørn Utnes. A finite element solution of the shallow-water wave equations. *Applied Mathematical Modelling*, 14(1):20–29, 1990.

[91] Geert Jan van Oldenborgh, Karin van der Wiel, Antonia Sebastian, Roop Singh, Julie Arrighi, Friederike Otto, Karsten Haustein, Sihan Li, Gabriel Vecchi, and Heidi Cullen. Attribution of extreme rainfall from hurricane Harvey, August 2017. *Environmental Research Letters*, 12(12):124009, Dec 2017.

[92] Gaël Varoquaux, Valentin Haenel, Emmanuelle Gouillart, Zbigniew Jędrzejewski-Szmek, Ralf Gommers, Fabian Pedregosa, Olav Vahtras, Pierre de Buyl, Gert-Ludwig Ingold, Nicolas P. Rougier, Pauli Virtanen, Akihiro Uchida, Christophe Combelles, Nicolas Pettiaux, Robert Cimrman, aespaze, Nelle Varoquaux, Didrik Pinte, Philip Gillißen, reverland, Ozan Çağlayan, Maximilien Riehl, Olivier Verdier, Wes Turner,

kikocorreoso, Stefan van der Walt, Sergio Oller, Robert Gieseke, Lars, and yasutomo57jp. SciPy-lecture-notes: Release 2015.1 beta. https://doi.org/10.5281/zenodo.31521, Sep 2015. Accessed: 2019-09-15.

[93] Cornelis Boudewijn Vreugdenhil. *Numerical methods for shallow-water flow*, volume 13. Springer Science & Business Media, 2013.

[94] Thomas Wahl, Shaleen Jain, Jens Bender, Steven D. Meyers, and Mark E. Luther. Increasing risk of compound flooding from storm surge and rainfall for major US cities. *Nature Climate Change*, 5(12):1093–1097, 2015.

[95] Sam S. Y. Wang, Partick J. Roache, Richard A. Schmalz, Yafei Jia, and Peter E. Smith. *Verification and Validation of 3D Free-Surface Flow Models*. American Society of Civil Engineers, 2008.

[96] Mary Fanett Wheeler. A priori L_2 error estimates for Galerkin approximations to parabolic partial differential equations. *SIAM Journal on Numerical Analysis*, 10(4):723–759, 09 1973.

[97] Qun Zhang and Song Cen. 3 - The coupling methods. In *Multiphysics Modeling*, Elsevier and Tsinghua University Press Computational Mechanics Series, pages 125 – 156. Academic Press, Oxford, 2016.

[98] Lianyuan Zheng, Changsheng Chen, and Hedong Liu. A modeling study of the satilla river estuary, Georgia. I: Flooding-drying process and water

exchange over the salt marsh-estuary-shelf complex. *Estuaries*, 26(3):651–669, June 2003.

[99] Jakob Zscheischler, Seth Westra, Bart J. J. M. van den Hurk, Sonia I. Seneviratne, Philip J. Ward, Andy Pitman, Amir AghaKouchak, David N. Bresch, Michael Leonard, Thomas Wahl, and Xuebin Zhang. Future climate risk from compound events. *Nature Climate Change*, 8(6):469, 2018.

Vita

Gajanan Krishna Choudhary was born in Ras Al Khaimah, United Arab Emirates in 1991. He eventually moved to Pune, India, where he received training in mathematics, physics and chemistry at Bhaskaracharya Pratishthana and M. Prakash Academy in Pune. He received the Bachelor of Technology degree in Civil Engineering from the Indian Institute of Technology (IIT) Kharagpur, India. He worked at Indian Register of Shipping, Mumbai, in its Research and Rule Development division for a year. He joined the University of Texas at Austin in August 2014 for pursuing graduate studies in Engineering Mechanics. He loves playing drums, singing along while listening to music, and watching anime.

E-mail address: gajanan@utexas.edu /
gajananchoudhary91@gmail.com

This dissertation was typeset with LaTeX[†] by the author.

[†]LaTeX is a document preparation system developed by Leslie Lamport as a special version of Donald Knuth's TeX Program.